EFFECT OF COLD WORKING AND ISOCHRONAL ANNEALING PROCESSING PARAMETERS ON SPECIAL GRAIN BOUNDARY FRACTIONS IN COMMERCIAL PURITY NICKEL

BY

BRENDAN M. GUYOT

A Thesis
Submitted to the Faculty of Graduate Studies
In Partial Fulfillment of the Requirements for the Degree of

MASTER OF SCIENCE

Department of Mechanical and Industrial Engineering
University of Manitoba
Winnipeg, Manitoba

THE UNIVERSITY OF MANITOBA

FACULTY OF GRADUATE STUDIES

*****

COPYRIGHT PERMISSION PAGE

EFFECT OF COLD WORKING AND ISOCHRONAL ANNEALING PROCESSING PARAMETERS ON SPECIAL GRAIN BOUNDARY FRACTIONS IN COMMERCIAL PURITY NICKEL

BY

Brendan M. Guyot

A Thesis/Practicum submitted to the Faculty of Graduate Studies of The University

of Manitoba in partial fulfillment of the requirements of the degree

of

Master of Science

ABSTRACT

It has been known for decades that thermomechanical processing, through cold working and annealing heat treatments, can effectively manipulate the type and distribution of grain boundaries in many FCC metals. This processing technique has been used to increase the fraction of 'special' low energy grain boundaries (Fsp) and disrupt the random boundary connectivity in a wide variety of metals, including nickel alloys. Unfortunately, the exact types and distribution of grain boundaries as well as other characteristics of an 'optimum' microstructure are not well defined since many researchers have placed emphasis on different microstructural features.

The focus of the present study was to study the effects of cold rolling and isochronal annealing processing parameters on both the fraction of special boundaries and the random boundary connectivity in commercially pure nickel. Secondary objectives were to determine which processing schedules were most effective at increasing Fsp and disrupting the random boundary connectivity.

Commercially pure nickel was chosen for this study since alloying elements play important roles in the resulting strain distributions after deformation as well as the grain boundary movement during subsequent annealing. By eliminating the complexities associated with alloying elements, the results from this study will serve as a baseline for comparison to more complex superalloys, such as IN-718.

To study the interacting effects of processing on microstructural characteristics, the following three variables were chosen, while holding all others constant:

- Percent reduction in thickness by cold rolling
- Annealing temperature
- Number of cycles of sequential cold rolling and annealing

It was found that one cycle of 5% strain by cold rolling, followed by annealing at 900°C for 10 minutes produced the highest increase in Fsp from the as-received fraction of 35% to 65%. Other effective processing schedules were similar, involving 1 to 3 cycles of low strain and high temperature anneals. Also effective were slightly higher strained samples that were annealed at slightly lower temperatures, for example, 3 cycles of 10%, and annealed at 800°C produced an Fsp of 63%. It was concluded, however, that processing with low strain and high temperature anneals were most effective at breaking up the random boundary connectivity.

ACKNOWLEDGEMENTS

I would like to thank my advisor, Dr. N. L. Richards, for giving me the opportunity to work on this research project, and also for his valuable guidance. Also deserving recognition and thanks are NSERC for financial support, Dr. M. C. Chaturvedi for providing an excellent research laboratory, technicians Mike Boskwick, John Van Dorp, and Dan McCooeye in the metallurgy lab, as well as the Department of Mechanical and Industrial Engineering. I would also like to gratefully thank my parents, Dennis and Charlene, and my girlfriend Meghan, for their endless patience, love, support, and encouragement.

TABLE OF CONTENTS

LIST OF FIGURES

Optical Micrographs:

LIST OF TABLES

Chapter 1 INTRODUCTION

The demand for temperature and corrosion resistant materials is ever increasing as technology pushes the limits of current material capabilities. Research has been accelerating over the years to develop improved material properties, cheaper and more efficient manufacturing routes as well as longer component lives.

Nickel-base alloys are used extensively for applications such as aircraft turbine blades, vanes, combustors, and exhaust frames due to their ability to retain mechanical properties at up to 0.8 of their melting point. The careful selection of alloy can yield excellent service performance including high temperature tensile strength, creep rupture strength, fatigue resistance, as well as hot corrosion and oxidation resistance.

Until recently, alloying, including solid-solution and precipitation hardening, with the addition of coatings have been among the few methods of tailoring the properties of a metal for a given application. Directionally solidified and single crystal components offer excellent properties for some applications, such as turbine blades, but their costs remain extremely high. This gives significance to the development of new techniques of improving polycrystalline material properties without the associated costs of the aforementioned methods.

To control the microstructure, thermomechanical processing, consisting of straining followed by annealing, has been researched for about 25 years now and is proving the ability to significantly alter the type and distribution of grain boundaries in certain metals. Since many material properties are structure dependant, the ability to manipulate and control the grain boundary types and distribution gives considerable control over the bulk mechanical, physical and chemical properties of the metal.

Although property improvements have been reported in many experiments, the process by which the grain boundary structures change during annealing is very complex due to the high number of process variables interacting, and is thus not fundamentally understood. Since many of the processing schedules described in the literature for increasing the fraction of special boundaries are empirically derived, it makes it very difficult to design and select a processing route for a specific metal or alloy. Predictions of the final grain boundary types and distributions for a given processing schedule are challenging since each metal and alloy system is unique.

To gain a more fundamental understanding of the key process related characteristics controlling grain boundary types and distributions in nickel-based superalloys, this thesis examines three process variables in the relatively simple system of commercially pure nickel. By using a pure metal, it should be possible to eliminate the effects of grain boundary precipitation reactions known to exist in superalloys and permit the evaluation of the process characteristics controlling the types of grain boundaries.

Chapter 2 LITERATURE REVIEW

2.1 Introduction

The concept of exploiting grain boundaries for their beneficial properties was first introduced by Watanabe in 1984 [1]. He was also the first to describe the frequency of occurrence and distribution for various types and orientations of grain boundaries within a metal by its Grain Boundary Character Distribution, or GBCD. Since then, many researchers have acknowledged the significance of the GBCD in controlling bulk material properties in polycrystalline metals, which has led to studies on the properties of different types of grain boundaries and the associated processing methods capable of manipulating their fractions.

There are essentially five main research groups studying this topic, namely:

(1) Palumbo, Aust, Lin, et al. focused on increasing absolute special boundary fractions to 50-70% through thermomechanical processing for intergranular degradation resistance and other property improvements. Processing usually consisted of high strain, with high temperature, short time anneals to invoke recrystallization.

(2) Randle, et al. has studied twinning and grain growth in nickel, and also the effect of low strain and long time anneals on the relative coherence of $\Sigma3$ boundaries in nickel. Recrystallization was usually not active in processing, but rather slight reorientations of the grains to facilitate ‘fine tuning’.

(3) Kumar, King, Schwartz, et al. explored the effects of thermomechanical processing on random boundary connectivity and GBCD in both copper and nickel alloys in attempt to optimize the GBCD (Fsp>80%).

(4) Watanabe, et al. focused on the importance of low energy boundaries in the GBCD to improve the bulk material properties, as well as structure dependant properties of different type of grain boundaries and creep in polycrystalline metals.

(5) Was, et al. studied intergranular cracking and creep in thermomechanically processed and grain boundary modified Ni-16Cr-9Fe.

It is important to note that many of the thermomechanical treatments described in the literature seem to lack scientific methodology in their selection since most of them are empirically derived. Furthermore, several authors have reported drastically different processing routes and suggested different kinetics for the evolution of the modified grain boundary structure. These researchers also emphasized the importance of different microstructural features of the modified structure, for example, absolute special fractions. These shortcomings combine to justify the need for additional research on this constantly developing technology. A fundamental understanding of the effects of processing parameters and their interactions remains unclear.

This chapter first summarizes several important issues such as factors effecting recrystallization in metals, followed by types of grain boundaries, thermomechanical processing techniques, and finally property improvements reported in the literature.

2.2 Recrystallization and Grain Growth in Nickel

The recrystallization and grain growth experienced by a metal is driven primarily by stored energy within the material as well as thermal energy supplied by annealing heat treatments. These processes involve many variables and each metal or alloy will exhibit different behavior for a given circumstance. These variables must be acknowledged in order to study them and put their collective effects on the final structure of a processed metal or alloy into perspective. The structure of a cold worked metal and the associated energetic considerations involved must be considered to understand the recrystallization and grain growth behavior.

2.2.1 Cold Worked Structure

Plastic deformation resulting from an imposed strain results in movements of an increasing number of dislocations, point defects and stacking faults. These dislocations hinder further straining of the lattice and result in a hardened structure. The structure that results from cold work is the subject of continuous research since it is complex and not well understood.

Factors that affect the structure of deformed metals include the stacking fault energy, solute concentration, deformation temperature, strain rate, grain size, and the type of deformation process. Stacking faults are interfacial defects that occur when an atomic plane is stacked out of the normal sequence. Nickel has an FCC structure where the stacking sequence ABC|ABC|A becomes ABC|ACB|CA as a result of a twin fault as seen in figure 2.2.1. Metals with relatively low stacking fault energies tend to produce wide stacking faults, while solute atoms cause local lattice distortions and can obstruct dislocation movement which greatly affects the deformed structure. The stacking fault energies for a selection of different metals can be observed in figure 2.2.2.

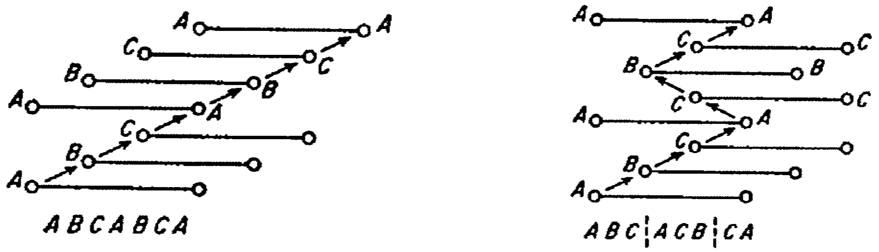

(a) (b)

Figure 2.2.1 Normal FCC stacking sequence (a) and stacking fault due to a twin (b) [2].

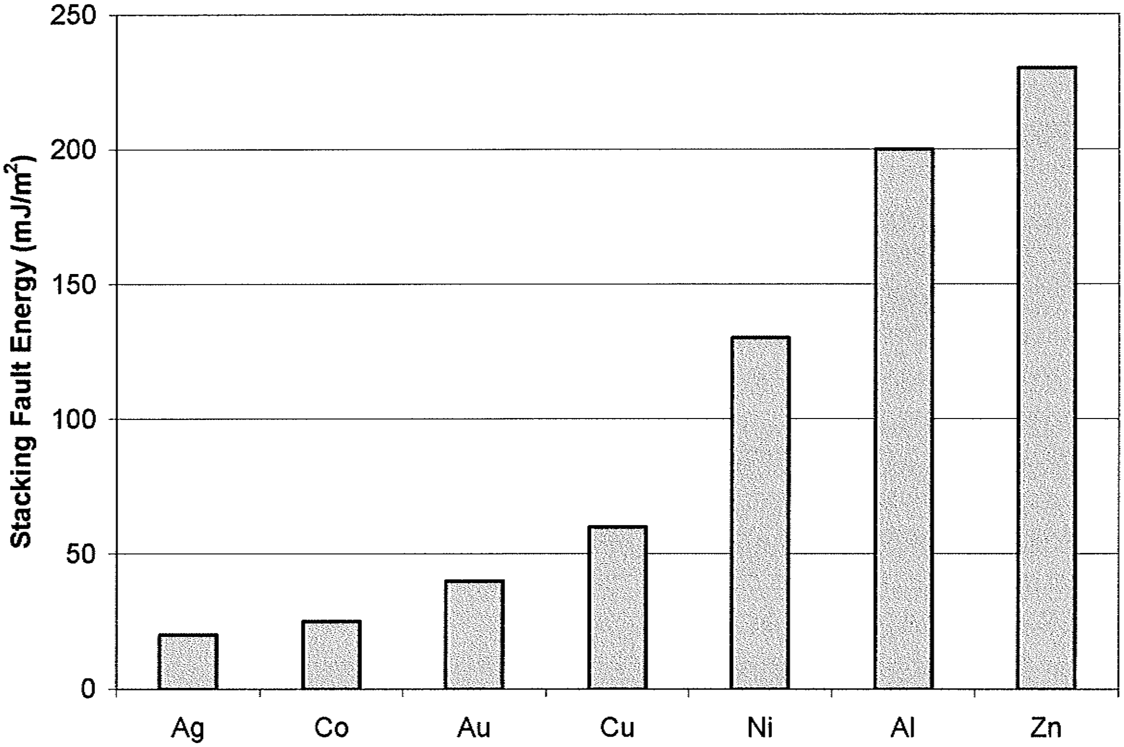

Figure 2.2.2 Stacking fault energies for a variety of metals. Data from [3].

The deformation temperature can have a substantial impact on the dislocation density and distribution that result. Lower temperatures and higher strain rates often result in increased dislocation density. Fine grain metals have more dislocations and higher energies than coarse grain ones, therefore the structure will be dependant on the grain size. Finally, the process type (such as cold rolling or forging) determines the strain distribution and consequently the amount of deformation at a given point.

2.2.2 Energy Considerations

During deformation, a large portion of the mechanical energy is dissipated as heat, but a certain fraction remains stored within the metal. This stored energy is of great importance since it represents the disorder resulting from the deformation and provides a driving force for recovery and recrystallization. The amount of stored energy increases as the strain imposed on the metal increases until the limiting value for the particular metal is reached.

Annealing an adequately cold worked metal provides the necessary driving force to initiate changes in the structure of the deformed metal. During the preliminary stages of annealing, recovery mechanisms are operative where the metal retains its basic characteristics, but the density and distribution of defects within it change.

Further annealing results in recrystallization whereby new strain-free grains nucleate, grow, and interact with each other. As first pointed out by Cahn in 1949, the nucleation process likely does not occur on an atom to atom basis, but rather on small regions that are already present in the deformed metal [4]. It should be noted that the principal difference between nucleation in recrystallization and in other types of structural transformations, such as solidification, is that in other transformations, atomic arrangements characteristic of a new structure do not already exist and nucleation must occur on an atom by atom basis [4]. This suggests that the orientation of the recrystallized grains are determined by the orientation of those from which it came, however different theories of nucleation exist for specific circumstances, such as the nucleated growth and nucleated orientation models and research is continuing in this area [4].

A minimum amount of deformation must be imposed on a metal for recrystallization to occur during annealing at a given temperature for a given length of time. Smaller amounts of deformation which result in less stored energy require higher annealing temperatures for recrystallization, but increasing the time decreases the required amount of deformation.

The mechanical properties of metals usually do not change substantially until recrystallization begins. This is due to the difficulty associated with dislocation rearrangement processes in the deformed structure. The rate of property changes that occur during recrystallization is usually high at the start of recrystallization and then slows down as time progresses. This is due to the high number of nucleation sites available at the onset of recrystallization and the subsequent reduction in this number as the nuclei grow and impinge on each other.

2.2.3 Recrystallization

The process of recrystallization is extremely important to materials processing, not only to allow the material to soften and restore its ductility, but to control the final microstructure. There are six main variables that govern the recrystallization behavior of metals [2]. They are:

1) amount of deformation
2) annealing temperature
3) annealing time
4) initial grain size
5) composition
6) amount of recovery prior to the start of recrystallization

These variables are not independent of each other and the recrystallization behavior for a given metal will depend on the combination of the aforementioned variables. The relationship between the variables can be summarized by the following eight points as outlined by R.F. Mehl [5]:

1. A minimum amount of deformation is needed to cause recrystallization.

2. The smaller the degree of deformation, the higher the temperature required to cause recrystallization.

3. Increasing the annealing time decreases the recrystallization temperature. (However, temperature is far more important than time. Doubling the annealing time is approximately equivalent to increasing the annealing temperature 10°C. This is a result of the temperature T in the exponential term of the Arrhenius equation.)

4. The final grain size depends chiefly on the degree of deformation and to a lesser extent on the annealing temperature. The greater the degree of deformation and the lower the annealing temperature, the smaller the recrystallized grain size.

5. The larger the original grain size, the greater the amount of cold-work required to produce an equivalent recrystallization temperature.

6. The recrystallization temperature decreases with increasing purity of the metal. Solid-solution alloying additions always raise the recrystallization temperature.

7. The amount of deformation required to produce equivalent recrystallization behavior increases with increased temperature of working.

8. For a given reduction in cross section, different metalworking processes, such as rolling, drawing, etc., produce somewhat different effective deformations. Therefore, identical recrystallization behavior may not be obtained.

The recrystallization behavior can be studied by observing the microstructural changes after annealing, and also by performing hardness tests to determine the deviation from the annealed condition. Microstructural observation provides valuable information on the stage of recrystallization, but does not offer quantitative measurements as does hardness testing. During annealing, the hardness of the deformed metal will decrease as the stored energy is released and the dislocation density decreases. This behavior is illustrated by the strength curve (which is usually proportional to hardness) in the figure below.

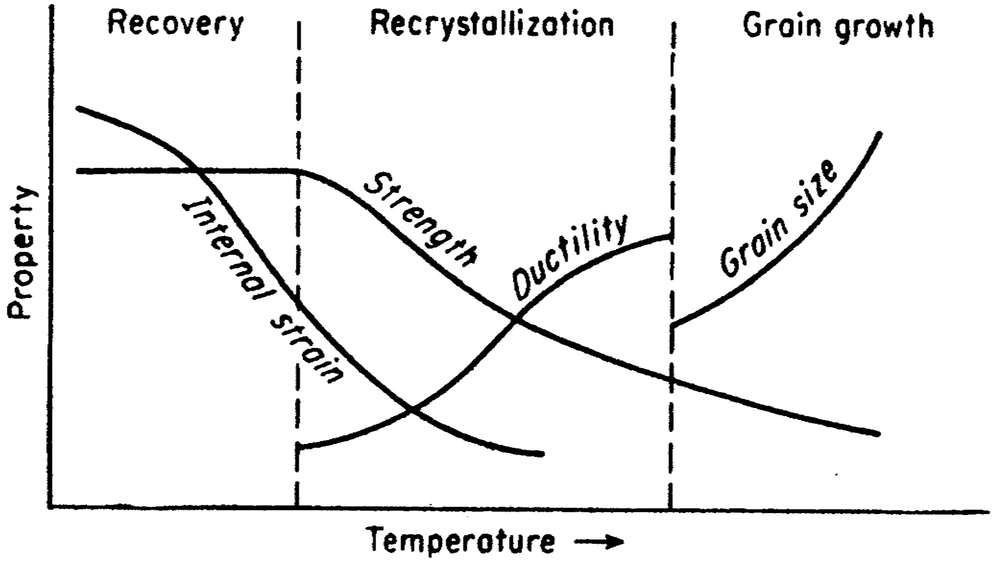

Figure 2.2.3 Schematic drawing indicating recovery, recrystallization, and grain growth and chief property changes in each region [2].

Other methods used to study recrystallization include electron back-scatter diffraction (EBSD), x-ray analysis, differential thermal analysis (DTA), resistivity, and internal friction, but the lack of standardization between testing methods complicates accurate characterization. The EBSD method is gaining interest since it is capable of providing very localized characterization of strain. The sample volume for EBSD is three orders of magnitude less than microhardness indentation measurements [6].

Recrystallization studies show that it progresses in a sigmoidal fashion with respect to time as seen in figure 2.2.4. The initial stage is represented by an incubation period whereby new grains nucleate until a slow rate of change begins due to growth. This rate of change increases over time due to an increasing number of nucleating and growing grains. This process slows down once the deformed structure is consumed by a completely new set of recrystallized grains.

The recrystallization behavior has been analytically modeled by Johnson, Mehl, Avrami, and Kolmogorov (JMAK analysis) [7] where the fraction recrystallized, f_{rex} is given by:

$$f_{rex} = 1 - \exp(-rt^{n})$$

where t is time, r is a function of the nucleation rate, and the JMAK exponent n is a function of both nucleation and growth rates. This analysis is based on the assumptions that the recrystallized nuclei form randomly and that growth of nuclei is isotropic. These assumptions often lead to the inaccuracy of this model. Attempts at modification of the JMAK analysis have been made by Doherty et al. [8], to include variable nucleation rates during recrystallization. Recently, a modeling approach using a Monte Carlo simulation has been developed by Radhakrishnan, et al [9].

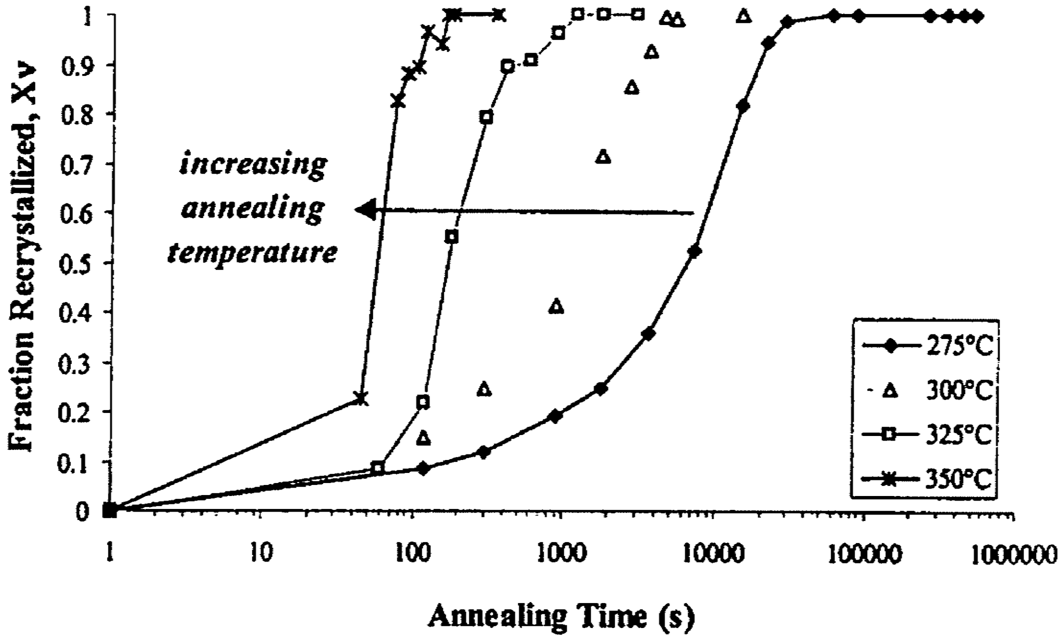

Figure 2.2.4 Isothermal annealing curves for cold worked aluminum alloy AA6061 [10].

2.2.4 Grain Growth

Once recrystallization is complete, the new set of strain-free grains are at a minimum size that is determined by such factors as the composition, amount of deformation, as well as annealing time and temperature. Although the relatively high energy state of the deformed structure has been brought down to a lower energy state associated with a new set of grains, the system is still only partially stable. It remains energetically favorable for the grains to grow since a reduction in grain boundary area per unit volume reduces the energy of the structure, again provided the necessary thermal driving force is present.

The main factors affecting grain growth are annealing time and temperature, solutes and particles, specimen size, and texture. Grain growth is characterized by the migration of grain boundaries through the existing grain network until an equilibrium condition is reached. Grain boundary mobility will increase with temperature, but is hindered by solute atoms and particles within the grain boundary structure [for example 11, 12, 13, 14]. The driving force for grain growth is decreased by the presence of low angle boundaries since they already exist at a relatively low energy state.

Grain growth in nickel usually obeys an Arrhenius-type equation of the following form:

$$D = (k_o\, e^{-Q/RT}\, t)^n$$

where D is the grain diameter, k_o and R are constants, T is the annealing temperature, Q is the activation energy for grain boundary migration (approximately $2\text{x}10^5$ J/Mol for nickel), t is the annealing time, and n is the grain growth exponent that depends on both the purity and annealing temperature. A recent study on grain growth in commercially-pure nickel [15] has found that the grain growth exponent to be approximately equal to 0.16, which differs from the theoretical value of 0.5.

2.3 Grain Boundary Designed Structure

The concept of 'grain boundary design and control' was first introduced almost 20 years ago [1], and since then, much effort has been committed to investigating its implications and capabilities. Researchers have studied a wide range of topics, including grain boundary properties in different environments, for example [16-20], structural dependence of intergranular fracture [1, 14, 21-27], annealing twin formation and movement [28, 29, 30], as well as bulk property improvements due to grain boundary engineering [for example 1, 31].

As mentioned in the introduction, Watanabe [1] was the first to describe the fraction of different types of special grain boundaries in polycrystalline materials by its 'grain boundary character distribution' (GBCD). The importance of this relatively new microstructural characterization parameter has been emphasized repeatedly by Watanabe, leading to the conclusion that the GBCD is *"the most important microstructural parameter controlling the bulk mechanical properties of polycrystalline solids"* [23].

Most of Watanabe's work has been focused on the structure dependence on intergranular fracture in polycrystalline solids. This was initiated by the discovery that low energy boundaries (low angle and low-Σ boundaries) have special properties and were more resistant to creep fracture than random boundaries [1, 14, 21-27]. Additional research was performed on the effect of GBCD on ductility and toughness [24], as well as the significance of GBCD to recrystallization, grain growth and texture [25]. More recent work has included the importance of random boundary connectivity in the prevention of intergranular crack propagation [26].

2.3.1 High and Low Angle Boundaries (HAB and LAB)

Low angle grain boundaries are a simple arrangement of dislocations that are considered a substructure that exists within the grains of a metal. They are characterized by very slight orientation differences (less than 10-15°) between adjacent grains, and relatively low energies. If two cubic crystals at a misorientation θ were joined together as seen in figure 2.3.1(a), there would be local lattice distortions to produce a continuous grain boundary, as seen in figure 2.3.1(b). Since the misfit cannot be accommodated completely, some of the atom planes must end on the grain boundary. These are edge dislocations and each is denoted by an upside down "T" in the figure.

If the grain boundary lies normal to the axis of rotation, the other type of low angle boundary forms from screw dislocations and is called a twist boundary as seen in figure 2.3.2.

High angle boundaries are those with large misorientations (more than 10-15 degrees) between adjacent grains and relatively high energy. As the degree of misorientation increases the distance between dislocations becomes smaller. High angle boundaries are considered a less perfect fit of the joined atoms of two lattices since the high degree of misorientation results in 'gaps' at the boundary. This additional area is usually occupied by impurity atoms which can have a detrimental effect on bulk material properties.

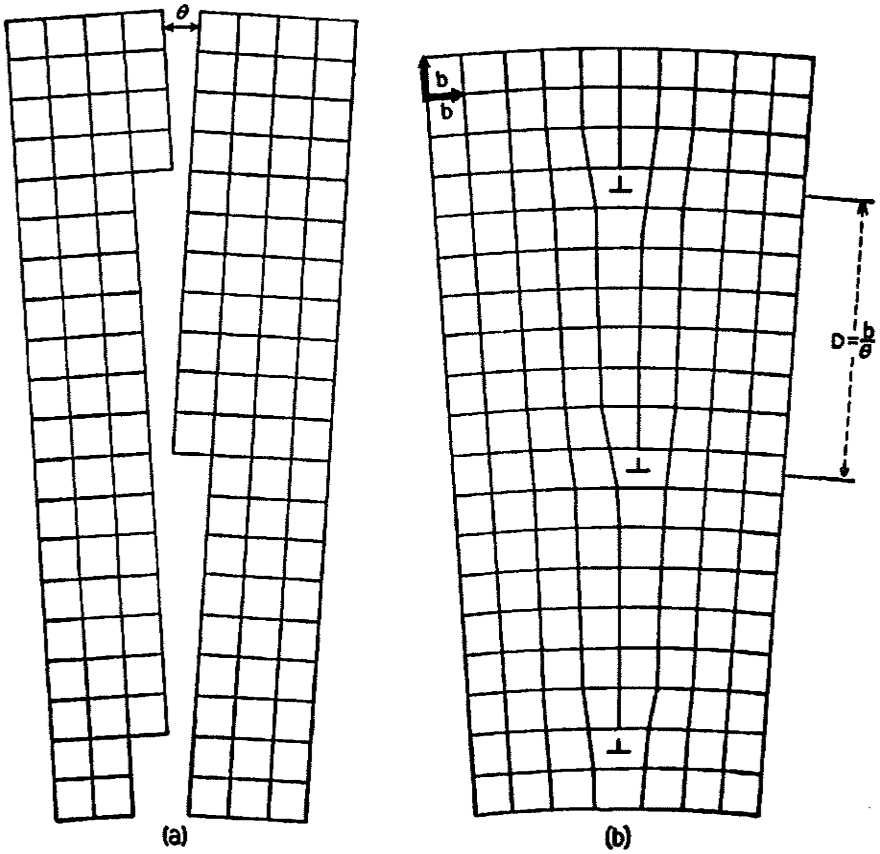

Figure 2.3.1 Diagram of a low angle tilt boundary. (a) two crystals, (b) dislocation structure after joining [2].

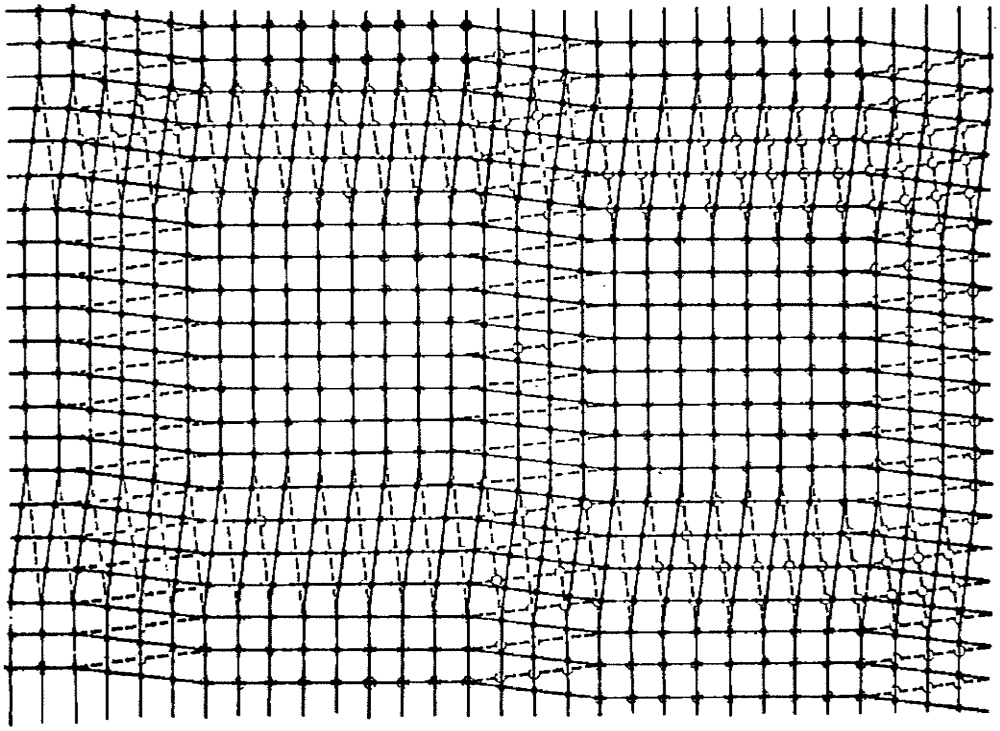

Figure 2.3.2 Diagram of a low angle twist boundary. Open circles represent atoms of one grain; full circle, atoms of the other [32].

2.3.2 The Coincident Site Lattice (CSL) Grain Boundary

A 'special' grain boundary is one which can be described in terms of the coincident site lattice (CSL) framework [33-35], whereby the boundary is assigned a Σ value, or the reciprocal of the number of coincident lattice sites shared by two adjoining grains. These boundaries exist for certain axes and angles of misorientation [33].

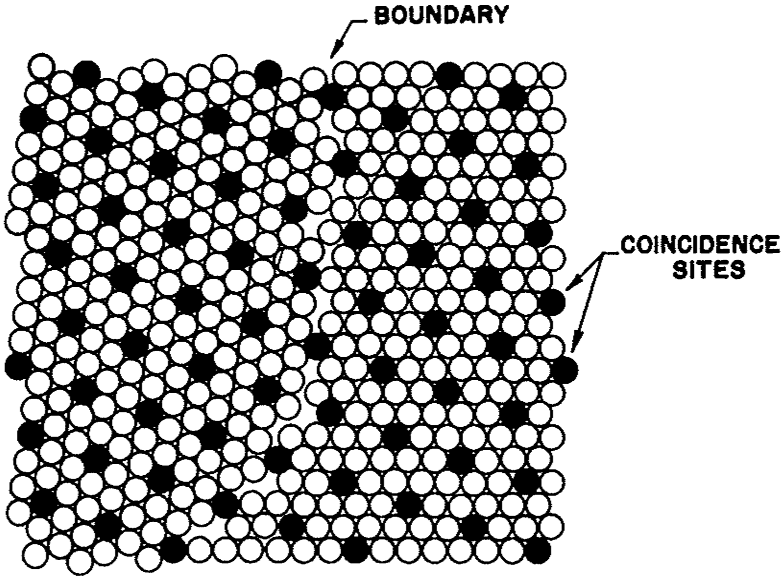

Figure 2.3.3 Schematic representation of a CSL boundary. Black dots represent atoms that are located at lattice sites coincident to both grains [36].

Interest has been focused on methods for increasing low-Σ boundaries ($\Sigma \leq 29$) since numerous studies [for example 1, 14, 16, 31, 37] have shown that they have improved properties over random boundaries, which is discussed in section 2.5. Specifically, much attention has been given to twin boundaries (Σ3s) and twin related variants ($\Sigma 3^n$) since materials with low to medium stacking fault energies readily form twins during annealing. The classification of boundaries as either "special" or "non-special" may appear somewhat oversimplified, however, this method has proven useful in studying the property improvements of metals as they relate to the GBCD.

Generally, FCC metals with relatively low SFE that have been processed to enhance the fraction of special grain boundaries have large fractions of Σ3 grain boundaries. Processed materials also have increased fractions of Σ9 and Σ27 boundaries since they are geometrically related to $\Sigma 3$ grain boundaries [38, 39]. As a guideline, it has been estimated that there will be approximately 1/5 as many $\Sigma 9$ boundaries as there are $\Sigma 3$ boundaries, while the fraction of $\Sigma 27$ boundaries usually increases only slightly above random values [37]. Other low-Σ CSL boundaries ($\Sigma \leq 29$) also increase just slightly above random values.

Recently, Randle has criticized the CSL model used for describing the fraction of special grain boundaries. Since a grain boundary is a planar defect, and the CSL model only relates the misorientation between grains and not the orientation of the boundary plane itself, Randle argues that the CSL framework alone is not adequate to predict special properties [37-40]. A refined approach to describing the material involves specifying the deviation from exact misorientation of the boundary and the orientation of the boundary plane. The usual method of determining the maximum allowable angular deviation ($\Delta\theta$ or v_m) is using Brandon's criterion [33]: $\Delta\theta \leq 15\ \Sigma^{-1/2}$, but a recent investigation [41] has shown that a $\Sigma^{-5/6}$ dependence may yield more useful results in relating property improvements to enhanced CSL fractions.

2.3.3 Coherent and Incoherent Twin Grain Boundaries

To determine the deviation from exact misorientation, the term v/v_m has been used, where v is the actual deviation and v_m is maximum allowable deviation [28, 38, 39]. While the CSL model does not distinguish between coherent and incoherent boundaries, it has been argued that the relative specialness of boundaries is more important than the absolute specialness [37]. A boundary which deviates by less than 8.7° from a misorientation of 60° about a 111 axis is considered a $\Sigma = 3$ misorientation

[13]. A coherent twin is one that has $v/v_m \leq 0.2$, and is considered to be a more perfect boundary and displays better properties than an incoherent boundary [28]. The reason why most studies do not specify deviations is likely due to the fact that it is technically challenging to determine this parameter [40].

There are four principal morphologies of twin boundaries as pointed out by Mahajan, et al. and shown as figure 2.3.4. In this figure, a corner twin is labeled A and its coherent twin forms MN. Twin B is thin and extends across the entire grain, while C is thicker and terminates within the grain. The trace OP of the coherent boundary of twin D is all within the grain and inclined slightly [42].

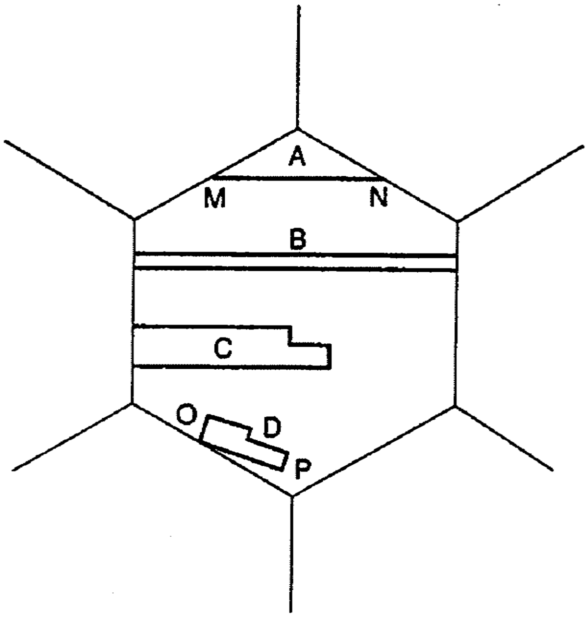

Figure 2.3.4 Schematic of different twin boundary morphologies in FCC metals [42].

2.4 Thermomechanical Processing Techniques

Thermomechanical possessing, through strain and annealing treatments, has been the common method used for decades to modify and manipulate the type and distribution of grain boundaries in materials. Interest has been focused on face centered cubic (FCC) metals with relatively low stacking fault energy (SFE) since annealing twins form readily during annealing of a strained metal. This is important since Σ3 twins account for the majority of special boundaries in processed materials.

Knowledge of the key processing parameters that govern the alteration of the resulting grain boundary character distribution, as well as their collective interactions, is still not complete. The complexity of the deformed state of metals and the subsequent changes that occur during annealing contribute to the incomplete understanding of how to effectively manipulate the type and distribution of grain boundaries. The lack of information on the basic mechanisms and the related effects of processing variables in the literature also inhibit full understanding of the basic mechanisms of the GBCD manipulation process. To further complicate the issue, the optimum GBCD and microstructural features are still not adequately defined or agreed upon by researchers.

There are two main classifications for processing schedules, each with two subsections, currently being reported in the literature as shown in figure 2.4.1.

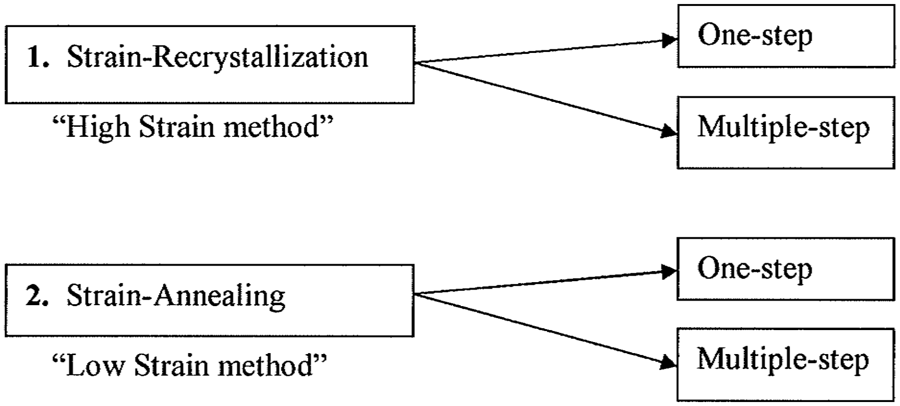

Figure 2.4.1 Classifications of thermomechanical processing routes.

These two processing routes differ significantly by the amount of deformation imposed on the material, the number of cycles, as well as the times and temperatures selected for annealing. The high-strain method (≥10% strain) is usually facilitated by cold-rolling, while the low-strain method (3-12% strain) is commonly achieved through compression forging or tensile straining. The low-strain methods usually involve moderate temperature, long time anneals to prevent recrystallization, while the high-strain method employs high temperature, and short time anneals to permit recrystallization. This is a general categorization and is not necessarily the case in all investigations, but rather a guideline for process characterization.

The two processing routes could likely be used to in conjunction with each other to exploit the beneficial effects from each, however, since they are not well understood individually, they are divided and treated separately in this report.

2.4.1 Strain-Recrystallization Technique

The multiple-step strain-recrystallization processing schedule is of specific interest, since it represents the experimental procedure used for most of the present work and is also commonly used in manufacturing processes. This procedure has been shown to be the most effective at manipulating the GBCD to increase the absolute fraction of special grain boundaries [31]. Palumbo, Aust, Lehockey, et al. and Kumar, Schwartz, King, et al. are among those having investigated this thermomechanical processing technique.

Although these two research groups employed similar processing schedules, the prime objectives differed somewhat. The main objective pursued by Palumbo, et al. was to increase the absolute fraction of special grain boundaries for property improvements, which was experimentally supported [31]. Palumbo has reported increases in the fraction of special grain boundaries to greater than 70% [31].

Kumar, et al. focused on breaking up the connectivity of the random grain boundary network by increasing the fraction of special grain boundaries to over 60% as seen in figure 2.4.2, as well as increasing the fraction of 2-CSL and 3-CSL triple junctions for property improvements. A triple junction is a point in the microstructure at which three grain boundaries meet, therefore a 2-CSL triple junction is the intersection of a random boundary with two CSL boundaries and a 3-CSL triple junction is composed entirely of CSL boundaries. The increase in 3-CSL triple junctions and the slight increase in 2-CSL triple junctions can be seen in figure 2.4.3, along with a decrease in 0-CSL triple junctions.

The evidence of the random structure being broken up in Inconel 600 through sequential strain-annealing treatments can be seen in figure 2.4.4. The connectivity is disrupted so that if a crack were to propagate, it would likely encounter a triple junction composed of 2 or 3-CSL boundaries and arrest since special boundaries are more crack resistant. Similar results were obtained with both Inconel 600 and oxygen-free electronic (OFE) copper [43]. In another recent study by Kumar et al. [44], it is pointed out that special fractions of grain boundaries are not a sufficient predictor of network topology and furthermore, that triple junction distributions give more reasonable ranking for processed materials.

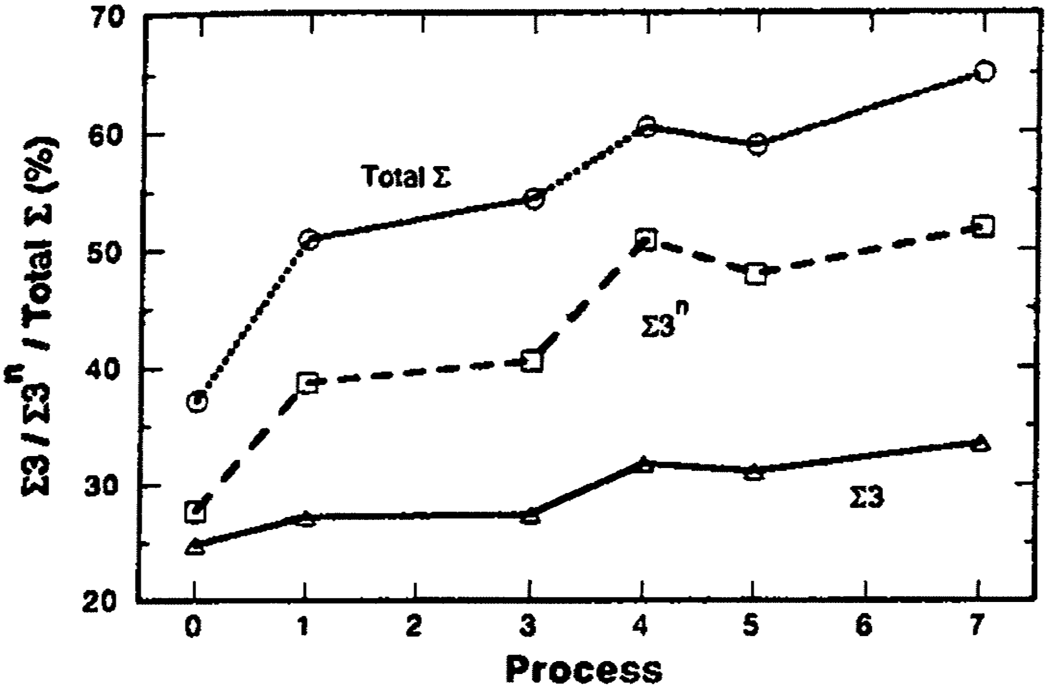

Figure 2.4.2 Grain boundary distributions showing increase in special fractions with sequentially strain-recrystallized Inconel 600 [43].

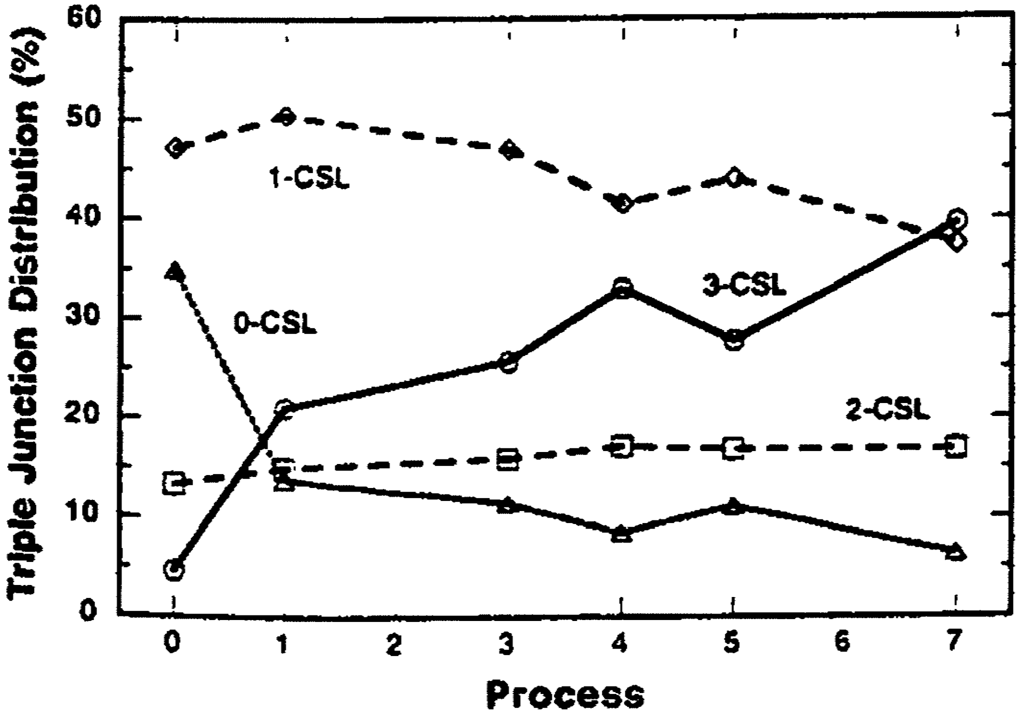

Figure 2.4.3 Distribution of triple junctions composed of various numbers of CSL boundaries in sequentially strain-recrystallized Inconel 600. Important are those with 2-CSL and 3-CSL boundaries [43].

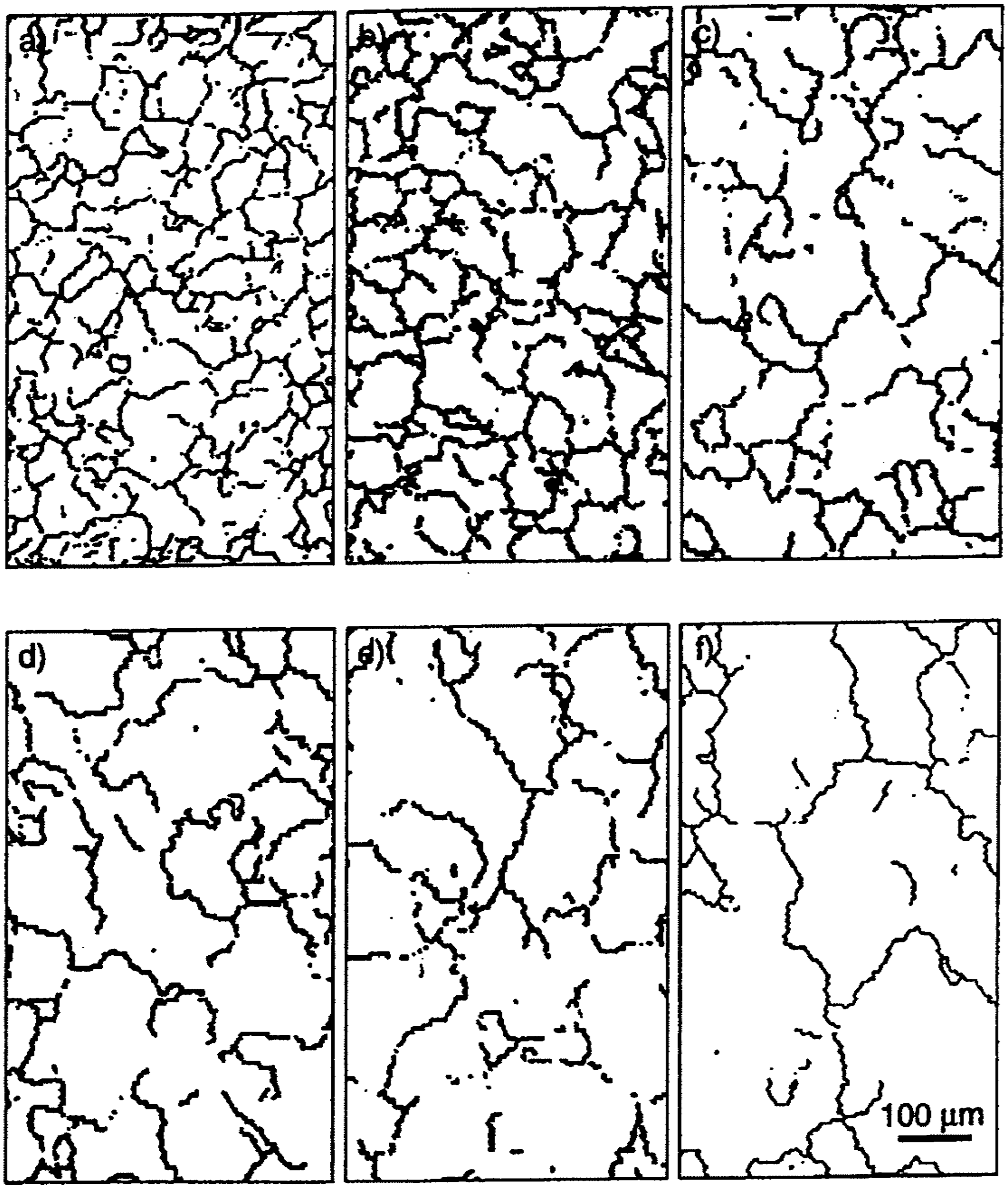

Figure 2.4.3 The break-up of the random grain boundary connectivity and reduction in path length in Inconel 600. (a) shows as received state, and after (b) one, (c) three, (d) four, (e) five, and (f) seven cycles of 20% reduction by rolling and annealing at 1000°C for 15 minutes in air followed by water quenching [43].

One-step strain-recrystallization has been used [45] to alter the GBCD, but is not used nearly as much as the multiple-step process. It is not clear why this processing technique is not being studied as extensively as other methods, but further research will likely provide answers. Comprehensive research on all methods is needed to assess the validity of processing routes for desired properties.

2.4.2 Strain-Annealing Technique

The strain annealing method has typically involved straining the material by compression, followed by lengthy anneals at moderate temperatures. Randle used this method primarily to make small adjustments or 'fine tuning' existing $\Sigma3^n$ CSL boundaries [39] to lower the deviation from exact CSL of special boundaries based on Brandon's criterion [33]. This fine tuning process is said to involve grain rotations, local lattice rotations, as well as grain boundary rotation and/or recovery during annealing [38].

Experiments with different grades of pure nickel conducted by Randle almost always involved 6% compression, followed by 24-268 hour anneals at temperatures between 500-850°C. It was found that increasing the annealing time from 24 to 168 hours had little impact on the statistical spread of CSL boundaries (GBCD) in super-pure nickel, but effectively decreased the deviation from exact CSL, v/v_m, of $\Sigma3^n$ boundaries as seen figure 2.4.4 [39]. Whether this type of thermomechanical processing results in materials with improved properties or not is unknown since there were no test results reported.

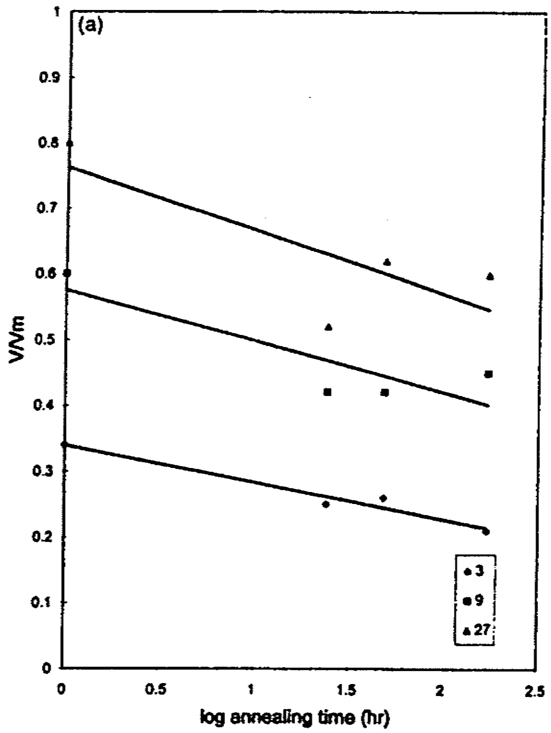

Figure 2.4.4 Normalized deviation from exact CSL of Σ3, Σ9 and Σ27 boundaries with increasing annealing time [39].

Was, et al. also used the strain annealing technique to improve the creep and intergranular cracking resistance in Inconel 600 (Ni-16Cr-9Fe) for nuclear reactor applications. Typical thermomechanical processing consisted of between 2 and 5% tensile strain, followed by annealing heat treatments at between 890 and 940°C for 1 to 20 hours [16-20].

Most of the thermomechanical processing schedules employed by Was, et al. seemed to be somewhat complex in the selection of parameters. The following is an example of such a processing schedule [16]:

1. Solution treat at 1298K for 20 min. under flowing argon, water quench.
2. 45% reduction in thickness.
3. Recrystallized at 1073K for 10 min.
4. Two cycles of 3% tensile strain, followed by heat treat at 1198K for 7.5 min.

(some samples required additional 2% tensile strain and heat treat at 1173K for 7.5 min. for comparable grain size).

From this processing history, it seems difficult to quantify the effects of any of the processing parameters or study their interactions since many are changing from cycle to cycle. This makes it difficult to understand the combined effects of processing on the grain boundary character distribution and its role in property improvements.

The fraction of special grain boundaries reported by Was et al. increased only moderately from a baseline of about 16-20% to maximum values of about 30-45% [16-20], however coherent twins were excluded from the analysis which lowers the absolute fraction values compared to other studies.

2.4.3 Special Grain Boundary Formation, Mobility, and Interaction

The mechanism by which CSL grain boundaries form and interact during annealing is complex, not well understood, and quite different for the two aforementioned processing techniques. The strain annealing technique generally does not involve recrystallization, but rather relies on local lattice rotations as well as some interaction of matrix dislocations with grain boundary dislocations by migration during annealing to adjust the boundary plane [39]. The strain recrystallization technique normally involves the formation of new grains in certain strained regions, followed by the migration and impingement of CSL and other high angle boundaries during annealing.

The final grain boundary character distribution will depend solely on how special grain boundaries form and their subsequent interaction during annealing. This process is governed by the mechanism(s) by which special grain boundaries form during annealing, and also by differences in mobility of different types of boundary which depends heavily on solute concentration and segregation at grain boundaries [46].

Since annealing twins have been the dominate special boundary type in the GBCD of grain boundary engineered materials, studies of how they form and interact are valuable. There have been several different models proposed for their formation, but they may be classified as three types, namely: 1) growth accident models, 2) grain encounter models, and 3) models involving nucleation of twins by stacking faults or fault packets [30]. A full discussion of these mechanisms is beyond the scope of this report, but regardless of the exact mechanism, at least one of two essential conditions must be met for annealing twin formation [29]:

1) A decrease in the overall interfacial energy when the energy of the boundaries between a grain's neighbors and its twin would be less that that of the boundaries between the neighbor and the grain itself. This accounts for twin formation during grain growth which is driven by the reduction in grain boundary energy.

2) Reorientation of grain boundaries so as to facilitate dislocation absorption and mobility during recrystallization.

Another study on annealing twin formation [47] has shown that the formation of twins occurs mainly during recrystallization and the destruction of those twins dominates in subsequent grain growth processes. This study was done in attempt to clarify the differences between twin formation during recrystallization and that of grain growth as proposed by Fullman and Fisher in 1951.

Pande, et al. [48] have also studied twinning in FCC metals and found that the important factors affecting twin density during grain growth are: 1) grain size D, 2) temperature T, and time t of annealing, 3) velocity of grain boundary migration, 4) grain boundary energy, and 5) twin boundary energy (or stacking fault energy).

Based on observations in a previous study [30], Pande, et al. has formulated three rules for the formation of annealing twins, namely:

1) Twins nucleate at grain boundaries during their migration steps.
2) Number of twins produced is proportional to the distance of grain boundary migration.
3) Number of twins produced is also proportional to driving force for migration.

Experimental results with nickel [30], along with these rules led an equation for the number of twin interfaces per unit length, p:

$$p = (B/D)\log(D/D_o)$$

where B is a constant, D is the grain size and D_o is the grain size at p=0. It is interesting to note that twin density depends solely on grain size in the above relationship.

Recently [29], Randle has proposed a new model for the interaction between CSL grain boundaries. This model relies on the encounter between a mobile grain boundary and a twin to increase the fraction of $\Sigma 3$s during annealing. As illustrated in figure 2.4.5, this model shows (a) two twinned grains with an arrow on the most mobile boundary. Secondly (b), the two grains impinge on each other and the boundary continues (c) until the two twin boundaries make contact (d). The Σ9 portion resulting from the two coherent Σ3 boundaries then continues (e) until in encounters the second coherent twin in the right hand grain (f). The most mobile grain boundary is now the new Σ3 with the arrow.

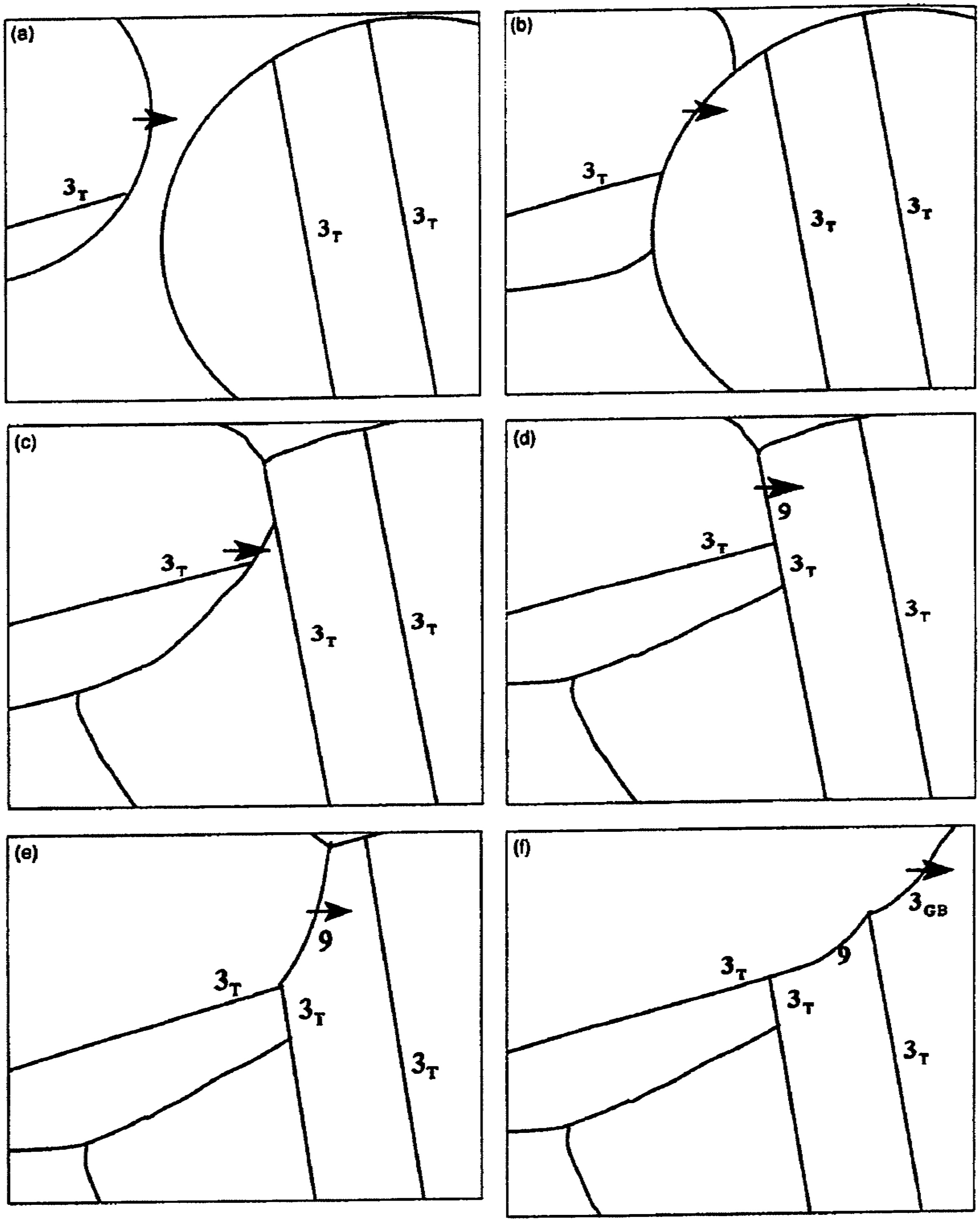

Figure 2.4.5 Model proposed by Randle for the generation of Σ3 grain boundaries from twins during and just after recrystallization. Most mobile grain boundary indicated by arrow. CSL boundaries labeled by Σ value, T subscript denotes twin [29].

2.5 Properties of Grain Boundary Modified Material

Potential properties improved by modification of grain boundary character distribution to increase the fraction of special grain boundaries include: resistance to grain boundary sliding, cavitation, and fracture; corrosion and stress-corrosion cracking; sensitization; and solute segregation [49]. Additional improvements include improved weldability, as well as enhanced fatigue and creep resistance [31], however limited data is available on these topics in the literature.

2.5.1 Strength

Improvements in mechanical strength are not the primary objective of most grain boundary engineering studies, however, some studies have reported increases in strength from 25 to 47 MPa by increasing the fraction of CSL boundaries [16]. Consideration should be given to the fact that twins contribute to hardening just as much as other boundaries since they are effective barriers to slip [29]. A study showed that the Hall-Petch relationship ($\sigma_y = \sigma_o + kD^{-1/2}$, where σ_y is yield stress, σ_o is the friction stress, k is a constant, and D is grain size) was obeyed only when twins were included in measurements of grain size [36].

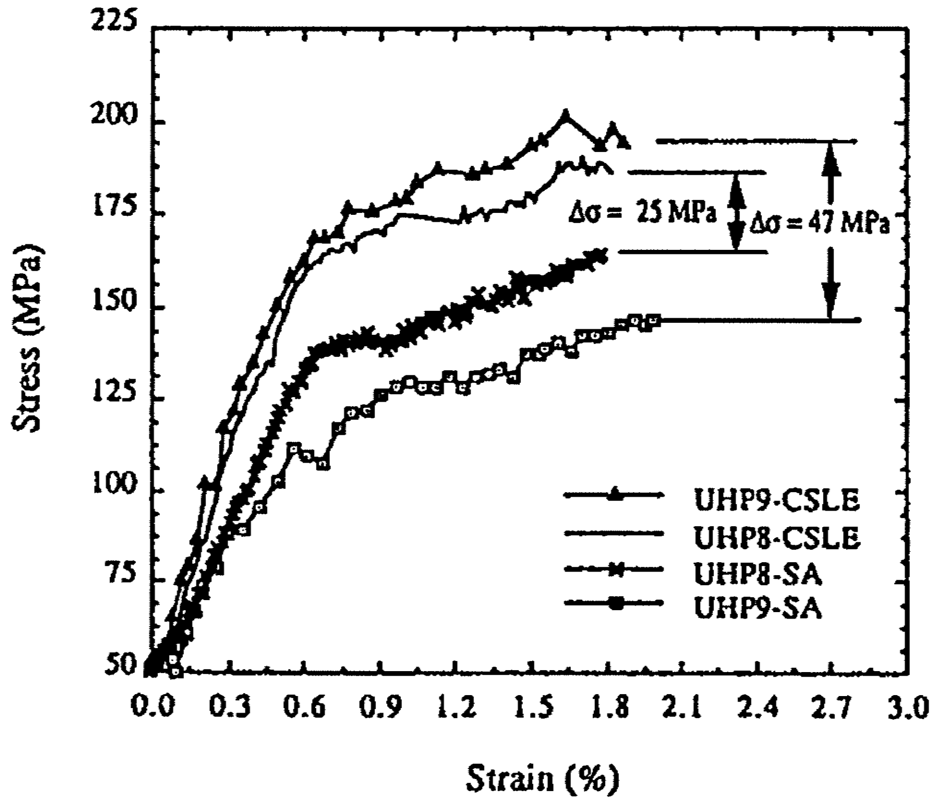

Figure 2.5.1 Stress-strain curves for two different heats of Ni-16Cr-9Fe samples. CSL enhanced samples show increased strength over solution annealed samples [16].

2.5.2 Intergranular Degradation and Corrosion

The intergranular degradation and corrosion resistance of nickel and its alloys is extremely important since they are often used in harsh environments, as experienced in gas turbine engines, as well as the petrochemical and other chemical processing industries. Traditional approaches to reducing corrosion have involved altering the material chemistry or the service environment and applying coatings, but modification of the grain boundary character distribution is proving to be a viable alternative.

By increasing the fraction of special grain boundaries to over 50 percent in nickel based superalloys 625 and V-57, it has been shown that 40 to 60 percent reductions in corrosion rates are possible [31]. It has also been suggested that it may be possible to double component service life and improve reliability of alloy 738 components by reducing pitting, sulfide spiking, and intergranular attack by 80, 30, and 50 percent respectively [31]. These improvements were accompanied by complete retention of tensile strength and ductility.

In another study [50], it was shown that the rate of intergranular corrosion of nickel based Alloy 600 decreases almost linearly with increasing fraction of special ($\Sigma \leq 29$) grain boundaries in the GBCD. The authors also demonstrated that a sensitization treatment increases the corrosion susceptibility, but is less prominent in the modified material. This can be seen in figure 2.5.2 on the following page, where it is interesting to note the convergence on a corrosion rate of zero as the fraction of special grain boundaries increases towards 100%. The resistance to intergranular attack by CSL boundaries can be seen in the optical micrograph in figure 2.5.3.

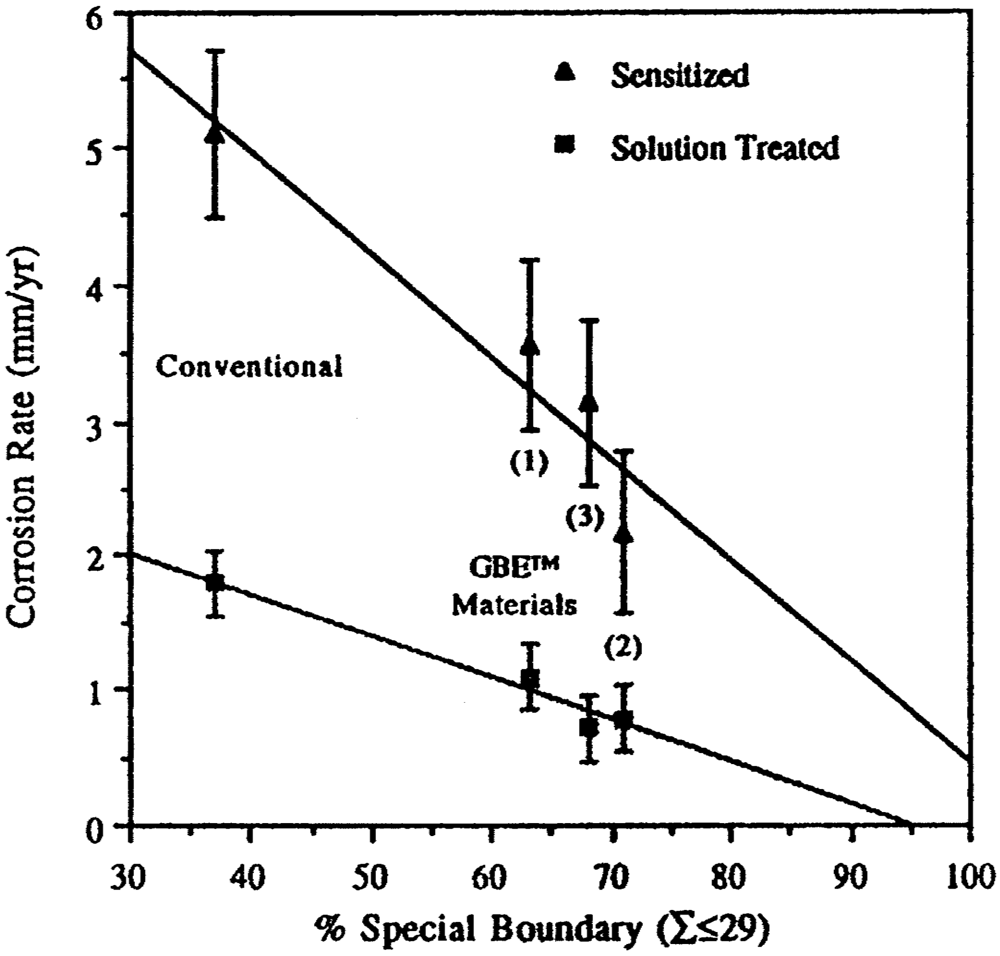

Figure 2.5.2 Intergranular attack of Alloy 600 via ASTM G-28 test as a function of % special boundaries [50].

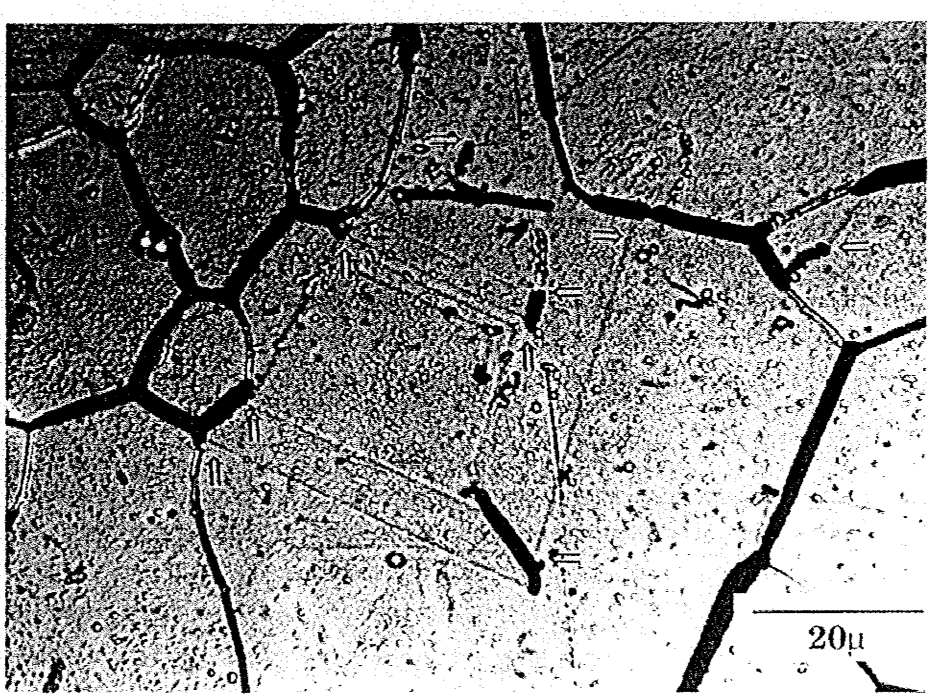

Figure 2.5.3 Optical micrograph with arrows indicating intergranular attack being resisted at twin boundaries in processed material [50].

Low angle and CSL grain boundaries have also been shown to be more resistant to cracking than general high angle boundaries, but not completely immune [18, 19]. In one study, cracked boundary fractions of CSL enhanced samples were decreased from 7-10% down to 1-8% [18].

2.5.3 Creep

Nickel-based superalloys are often used in high temperature applications where the addition of stress provides an environment for creep susceptibility. It has been recognized for more than 20 years that different types of grain boundaries behave differently in the creep regime [21]. From experimental evidence, it became clear that low energy boundaries (LABs and low-Σ boundaries) were more resistant to intergranular fracture arising from creep and that high angle random boundaries were preferential sites for crack nucleation and propagation [1], an example of which is seen in figure 2.5.4. This lead to the idea that a grain boundary modified material, with increased fractions of low energy grain boundaries, should have improved resistance to creep failure.

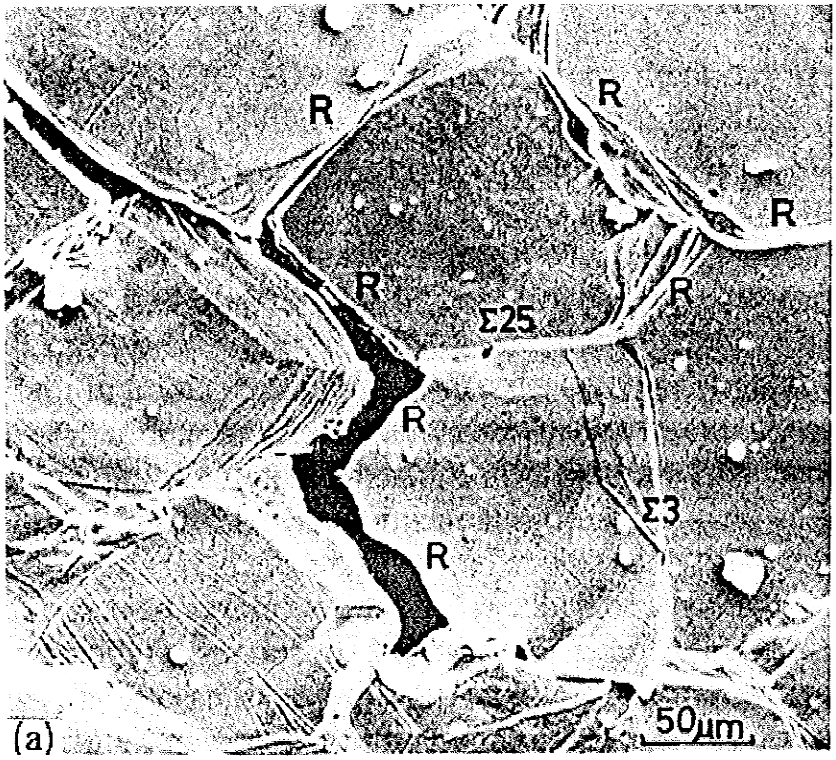

Figure 2.5.4 SEM image showing structure-dependent intergranular creep fracture in Fe-Sn alloy crept at 973K and 29.4 MPa. R denotes random boundaries [14].

Palumbo, et al. [41] have stated that a grain boundary modified material has increased structural order and reduced free volume which inhibits dislocation motion by vacancy diffusion and climb required for grain boundary sliding and void formation.

It has been reported that by increasing the fraction of special grain boundaries (F_{sp}) to over 60 percent in alloys 625 and V-57, a ten to twenty-fold reduction in steady-state creep rate with a five to ten-fold decrease in primary creep strain were obtained [31]. Reductions in total creep strain at failure for the processed material were also cited. Furthermore, reductions in grain boundary sliding of over 90 percent have been reported [31] for alloys 625 and V-57 as a result of increasing the fraction of special grain boundaries over to over 50%.

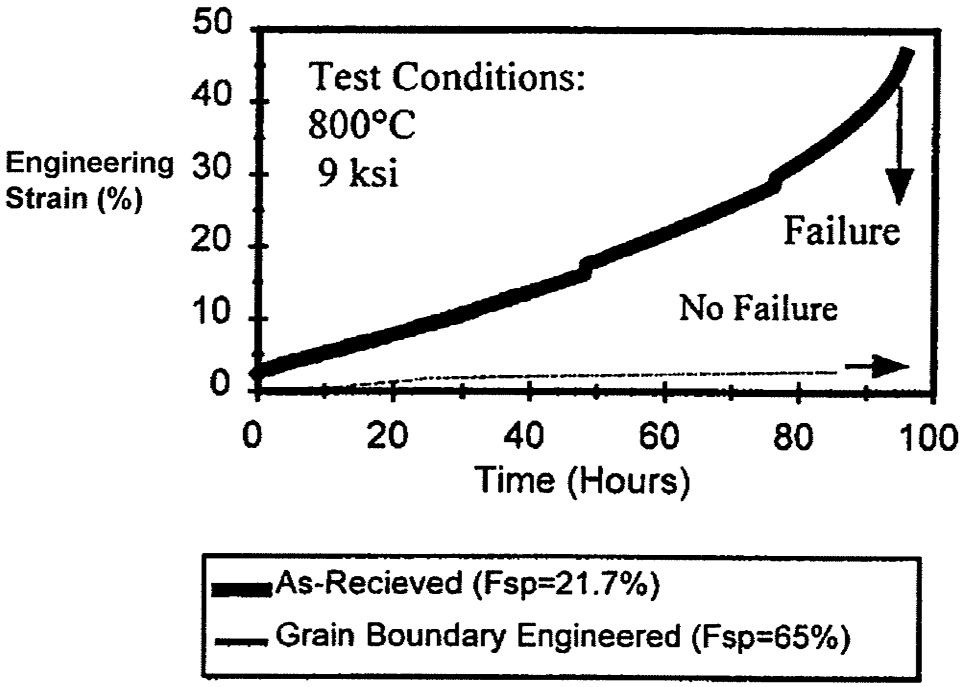

Figure 2.5.5 Creep response of alloy V-57 measured under temperature and stress conditions which grain boundary sliding mechanisms dominate [31].

Was, et al. have shown that by increasing the fraction of CSL boundaries from 16-20% to about 34-43% (excluding coherent $\Sigma3$s) in Ni-16Cr-9Fe, creep rate was reduced by a factor of 10-66 [17, 18]. It was shown that the reductions in creep rate depend non-linearly on fraction of CSL boundaries and that relatively small increases in special boundary fractions result in large reductions in creep rate.

2.5.4 Fatigue

The effect of special grain boundaries on the high-cycle fatigue resistance of alloys V-57 and 738 was evaluated by Palumbo, et al. [31]. By increasing the fraction of special boundaries, the number of cycles to failure was increased by factors of 1.5 to 3 as seen in figure 2.5.5.

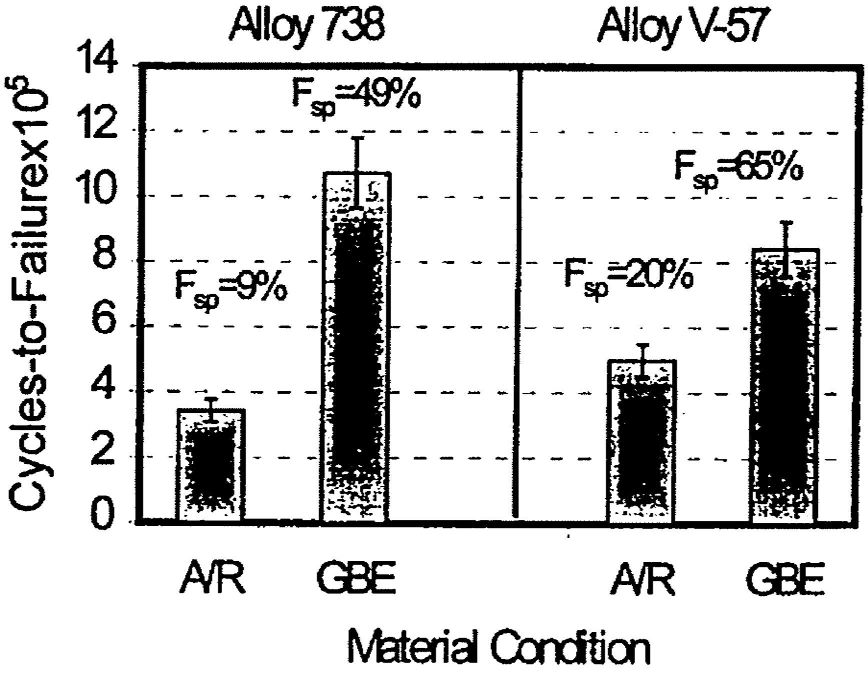

Figure 2.5.5 Room temperature fatigue resistance of as-received material vs. grain boundary modified material. Tests were conducted in uniaxial tension with a stress amplitude of 40 ksi and stress ratios between 0.068 (alloy 738) and 0.122 (alloy V-57) [31].

2.5.6 Weldability

The weldability of nickel based alloys is extremely important since repair is often favored over replacing components. Materials are now being developed with weldability in mind to facilitate high integrity welds and consequently save replacement costs.

Recently, it has been shown that minor elements such as boron preferentially segregate as interstitials at random grain boundaries, causing localized boundary liquation and contributing to microfissuring in simulated weld heat-affected zones in

Inconel 718 [51]. More importantly, special low energy boundaries, such as LABS and twins, were shown to be resistant to segregation and therefore rarely experienced the associated liquation.

Thermomechanical processing used to increase the fraction of special grain boundaries has been evaluated as a method to improve weldability [31]. The degree of post-weld heat-treatment (PWHT) cracking was observed in alloy 738 for conventional ($F_{sp} = 6\%$) and grain boundary modified material ($F_{sp} = 50\%$) after microplasma arc and TIG welding. The crack density was reduced by up to a factor of five, while the crack lengths were reduced by between three and 50-fold. These improvements in performance were directly attributed to the increase in low-CSL grain boundaries which were reinforced by demonstrating that cracks propagated exclusively along high-angle grain boundaries.

2.6 Other Engineering Applications

The manipulation of the grain boundary character distribution to increase the fraction of special grain boundaries has proven to be a versatile method of improving the properties of a wide variety of FCC metals and alloys. In addition to nickel based alloys such as 600, 625, 738, and 800, processing has been successfully applied to Monel 400 (Ni-30Cu) and iron based alloy V-57 for nuclear steam generator components to improve service performance.

In addition to high temperature service components, research is being conducted to extend the life of Pb-Ca-Sn lead-acid battery components by increasing the fraction of special boundaries in attempt to reduce the susceptibility to intergranular corrosion and creep cracking [52]. Grain boundary modified material is also of interest to the automotive industry for applications involving interstitial-free steels to improve deep drawability of autobody panels [52].

Some researchers are studying the process of optimizing the grain boundary character distribution in oxygen-free electronic (OFE) copper to improve properties [43, 53, 54]. Special fractions have been increased to about 80% in some cases by using thermomechanical processing [53].

2.7 Scope and Nature of Present Investigation

Grain boundaries can have detrimental effects on the bulk properties of polycrystalline metals, as seen in the creep regime where they provide sources for sliding and fracture. Since it has been shown repeatedly that different types of grain boundaries have different properties, the bulk material properties can be controlled by manipulating the type and distribution of grain boundaries within that material. Unfortunately, the exact GBCD and other characteristics of an 'optimum' microstructure are not well defined since many researchers place emphasis on different features.

What seems to be agreed upon, however, is that relatively high absolute fractions (>50%) of special boundaries are superior to lower fractions and that breaking up the random boundary connectivity is desirable to prevent possible crack propagation and intergranular corrosion along random boundary networks. What remains unclear is a fundamental understanding of how different thermomechanical processing schedules manipulate the GBCD and random boundary connectivity in different metals. Specifically, the manner by which processing variables interact to contribute to the final microstructural characteristics is unknown since research has not been published on this important issue.

The primary objectives of this research were to explore how different thermomechanical processing schedules altered the GBCD and random boundary connectivity in commercially pure nickel. The secondary objectives were to observe which of those processing schedules produced the highest special fractions and the most fragmented random boundary networks.

Commercially pure nickel was chosen for this study since alloying elements play important roles in the resulting strain distributions after deformation as well as the grain boundary movement during subsequent annealing. By eliminating the complexities associated with alloying elements, this study will provide a baseline for comparison to more complex superalloys, such as IN-718.

To study the interacting effects of processing on microstructural characteristics, three variables were chosen:

- Percent reduction in thickness by cold rolling
- Annealing temperature
- Number of cycles of sequential cold rolling and annealing

Several parameters were held constant, including: annealing time and atmosphere, strain rate, initial grain size and GBCD, strain method, and cooling rate.

All samples were characterized by Orientation Image Microscopy (OIM) scans to determine the GBCD. The resulting Fsp values were calculated and graphed in different groupings to determine trends in processing. This permitted observation of evolving Fsp values with increased processing, as well as comparisons between varying processing parameters such as temperature. OIM maps of the random boundary connectivity allowed qualitative observations of the degree of break-up and were useful for comparisons between samples with high or similar special fractions in attempt to determine the most effective processing schedules.

Chapter 3 EXPERIMENTAL TECHNIQUES

3.1 Material

The material selected for this study was commercially pure nickel, or nickel-200. It was received from Castle Metals as a 1/8” thick sheet measuring 4’ x 4’, and then sheared into strips to facilitate handling and further processing. The nominal composition of Ni-200 is seen in the table below.

Nickel-200 has good corrosion resistance and is often used in food handling and caustic chemical industries. Typical tensile strengths range from 414 MPa for annealed bar, to 827 MPa for hard drawn wire. Annealed strip typically has a yield strength of 138 MPa, and an ultimate strength of 483 MPa with an elongation of 40% [55]. Properties are retained at both subzero and elevated temperatures.

Nickel + Cobalt	99.5
Carbon	0.07 max (a)
Manganese	0.35 max
Iron	0.25 max
Copper	0.15 max
Sulfur	0.01 max
(a) Limited to 0.02% max	

Table 3.1.1 Nominal composition (wt.%) of Ni-200 [55].

It can be reasonably machined and formed by cold working and drawing, and is readily welded. This material is available in a variety of forms including sheet, wire, bar and strip. Commercially pure nickel has a melting point (T_{mp}) of 1440°C. The low electrical resistivity of Ni-200 makes it useful to the electronics industry for applications such as terminals and contacts. It is susceptible to corrosive attack in oxidizing or sulfurous atmospheres.

3.2 Cold rolling and annealing procedures

Cold rolling was performed at room temperature on a standard Stanat rolling mill in the fabrication and preparation laboratory. The rolls were well lubricated with oil before rolling was carried out, and re-lubricated as often as necessary. Strips of Ni-200 sheet measuring 3 inches long and 3/4 inches wide by 1/8 inch thick were used for processing. The crosshead was positioned before each pass to permit the application of prescribed amounts of deformation on the sample. Thickness measurements using a Vernier caliper were performed on all samples between passes to ensure proper crosshead positioning and the resulting sample thickness. Once rolled to the desired thickness, the lubricating oil was cleaned from the sample to prepare for annealing.

It is worth noting that sequential reductions in thickness are percentages of the new thickness values and not the original thickness. For example, 5 steps of 10% reduction per step do not result in a 50% reduction, but rather a 41% reduction from the original thickness. The thickness values were obtained by using an Excel spreadsheet to calculate percentage reduction from changing thickness values.

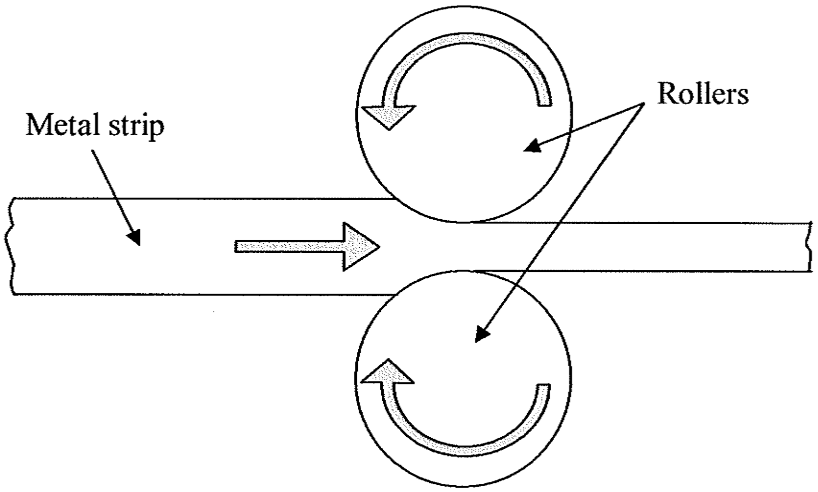

Figure 3.2.1 Cold rolling schematic.

Each rolled sample was wrapped tightly in stainless steel foil along with a thermocouple placed in the center of the sample to permit accurate temperature readings. After the thermocouple was connected to the display module, the pre-heated furnace was back-filled with flowing argon for a few seconds. The sample was then placed in the furnace at the appropriate temperature and allowed to reach the desired set point before the time was counted. The heating usually took less than 5 minutes, but was dependant on the dimensions of the sample. The argon was set to a slow flow and the time was counted to the appropriate value before the sample was removed and allowed to air cool. Once cooled back to room temperature, the foil was removed and either a small section removed for examination, or the sample was processed further.

3.3 Sample Preparation and Optical Microscopy

Small sections (approximately 3/4 x 3/4 x 1/8 inch) of rolled and annealed strip were removed by using a liquid-cooled friction saw and subsequently cleaned free of coolant and debris. Samples were mounted in black bakelite using standard mounting procedures. After grinding, they were polished to a blue colloidal silica finish (0.05 μm), and then etched by swabbing a solution of 1:1 acetic and nitric acid across the surface for about 15-20 seconds. Optical microscopy was performed using a Nikon Epiphot microscope for general observation and a Zeiss Axiovert microscope for image analysis and obtaining digital micrographs.

3.4 Microhardness Measurements

Polished samples were placed on the stage of a Leitz microhardness measuring instrument and positioned such that a series of hardness measurements could be performed at regularly spaced intervals across the thickness of the metal as schematically illustrated in figure 3.4.1. The 100-gram weight was placed on the weight holder and the site of interest was selected. The DPH indenter was released and allowed to contact the surface of the metal remaining in contact for about 10 seconds before being retracted.

After the indentation was made, its dimensions were measured and correlated to the appropriate hardness value with the use of a conversion chart. Each hardness measurement was performed at least 5 diameters away from previous measurements to minimize any residual strain effects that could alter the data. This was usually accomplished by zigzagging across the thickness of the metal, rather than the straight line depicted in the figure on the following page, to permit an increased number of measurements across the width of the sample.

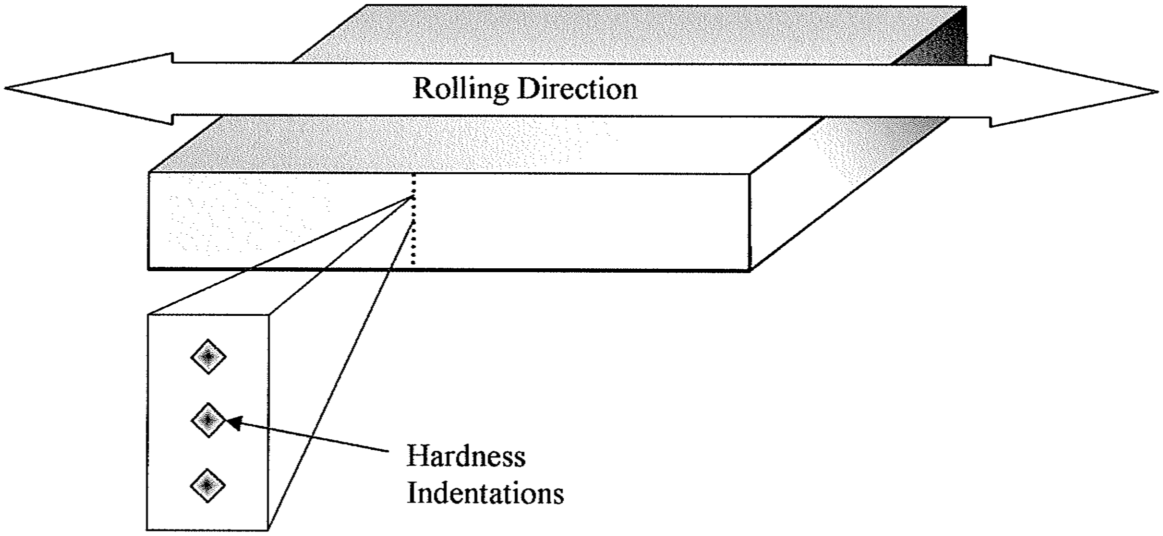

Figure 3.4.1 Schematic of microhardness measurement locations

3.5 Mechanical Testing

Mechanical testing was performed on as-received samples machined according to ASTM E8 standard rectangular tensile test specimen geometry. The sample geometry is depicted in figure 3.5.1 on the following page, where parameters used were (all in inches): L=8, B=2, A=2¼, G=2, W=0.5, R=2, C=3/4 and T=1/8. Samples were gripped and pulled to failure on an Instron screw-driven tensile testing machine using a crosshead speed of 2 mm/min. Stress-strain data was plotted using a pen plotter and graph paper. Testing parameters were used for calculating ultimate tensile strength, yield strength, and percent elongation.

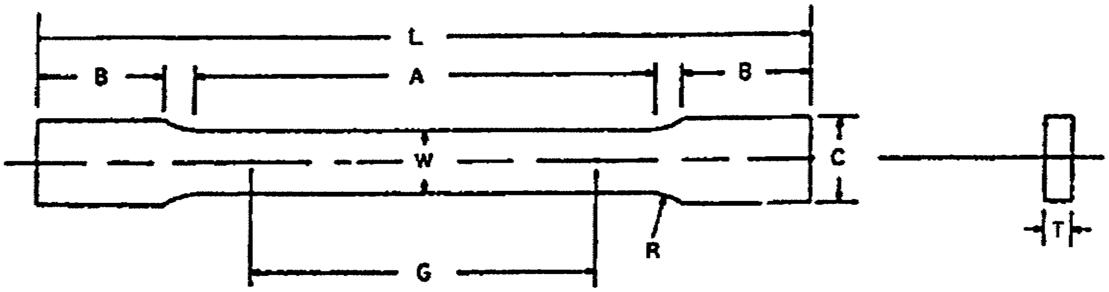

Figure 3.5.1 Sample geometry according to specification ASTM E8.

3.6 Orientation Image Microscopy (OIM)

Scanning electron microscope (SEM) based electron back-scatter diffraction (EBSD) was first developed by John A. Venables at the University of Sussex in late 1960's, and since then Dr. David Dingley and his colleagues at TexSEM Laboratories (TSL) have made several modifications to further develop the software and hardware technology. Other researchers who have worked on the development of EBSD include V. Randle, S. Wright, D. Field, A. Schwartz, B. Adams, and M. Kumar.

Orientation image microscopy, or OIM (OIM is a trademark of TexSEM Laboratories, Ltd. which is a division of EDAX, Inc.) is a microanalysis tool capable of phase identification, orientation mapping, texture determination, and many other features. It has largely replaced older diffraction techniques such as selected-area electron channeling (SAC) and Kossel x-ray diffraction since the EBSD technique does not require special sample preparation techniques and large amounts of data can be collected in relatively short periods of time due to automation. Further limitations of Kossel diffraction include limited spatial resolution and the inability to view live patterns on a phosphor screen.

When a stationary electron beam in the SEM strikes a crystalline material mounted at an incline of about 70°, the electrons disperse beneath the surface, then diffract among the crystallographic planes whenever the Bragg condition is satisfied, namely $\lambda = 2\ d \sin\theta$. This equation is Bragg's law, where λ is the wavelength, d is the lattice spacing and θ is the angle of incidence. The pattern formation is seen schematically below as figure 3.6.1, where S is the source of diffracting electrons, d_{hkl} is the lattice spacing, and 2θ is twice the Bragg angle.

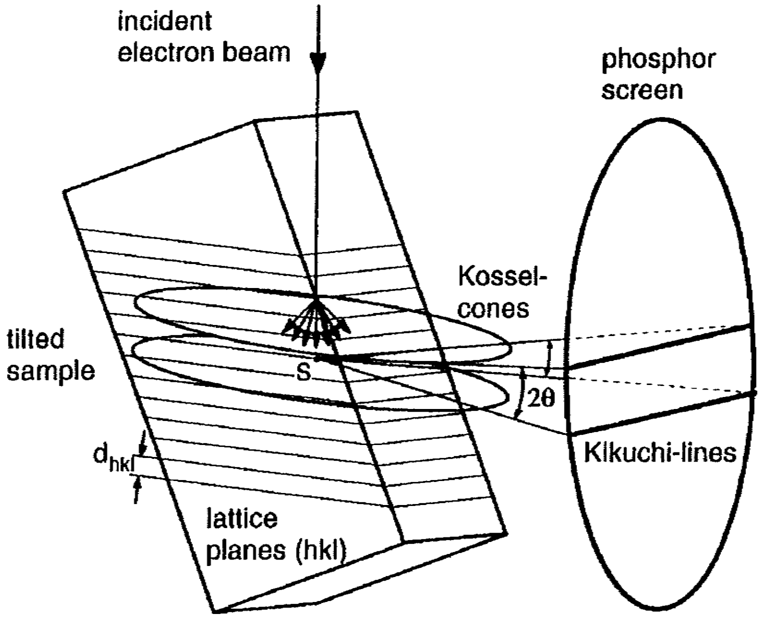

Figure 3.6.1 Electron Back-scatter Diffraction (EBSD) Pattern formation in a tilted sample [56].

The steep incline is used to minimize the fraction of electrons absorbed, and maximizes the fraction diffracted. The diffracted electrons produce a pattern consisting of intersecting bands termed electron backscatter diffraction (EBSD) patterns. These patterns are also called Kikuchi patterns since he was the first to observe them in 1928. The patterns can be detected by a special low-light camera with a phosphor screen inserted into the SEM chamber and facing the sample. The EBSD pattern that is formed is unique to the crystal lattice beneath the electron beam.

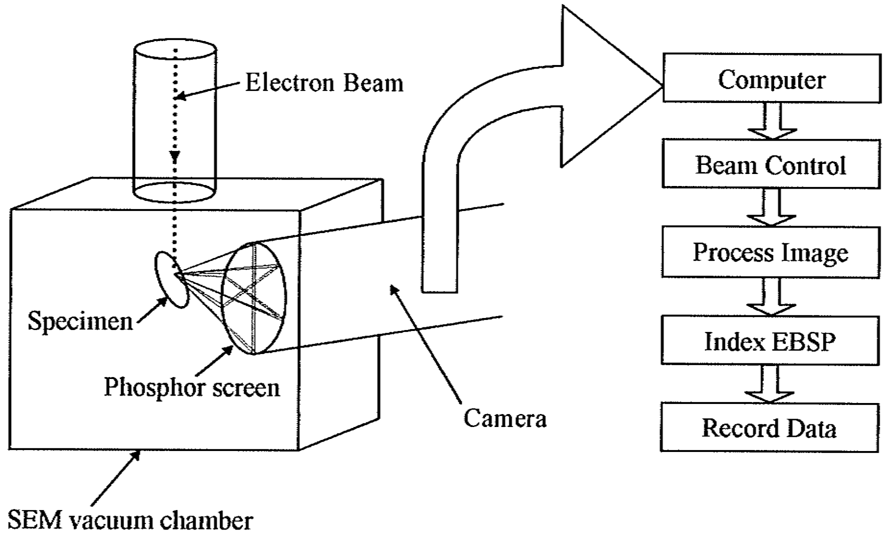

Figure 3.6.2 Sketch of SEM setup for OIM showing electron beam-sample interaction and EBSD pattern detection by phosphor screened camera. Flow chart shows operations.

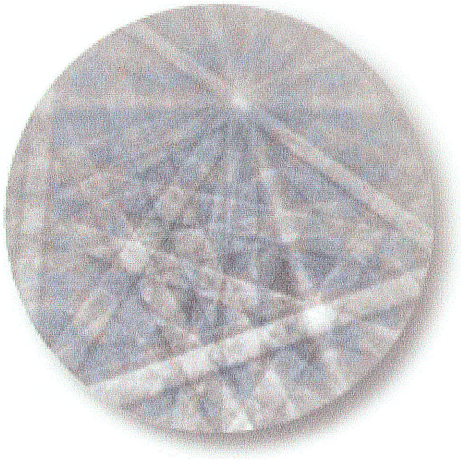

Figure 3.6.3 Example of an EBSD pattern [57].

In order to determine the orientation difference between adjacent grains, the individual orientations of each grain had to be known. This was facilitated by allowing the OIM computer software to control the focused 20kV electron beam in a JEOL JSM-5900 SEM to traverse it in steps across the surface of the sample at previously defined regularly spaced intervals. This interval spacing is called the step size and the value selected depends on the sample type and grain size.

At each point, the EBSD pattern was collected and stored in the computer. The computer software compares the pattern with a database of patterns to index the EBSD pattern and records the orientation of each individual data point. Along with the orientation, the computer assigned an Image Quality (IQ) and Confidence Index (CI) value for each data point.

Figure 3.6.4 JEOL JSM-5900 Scanning Electron Microscope [58].

The image quality is a measure of the EBSD pattern quality and is dependant on both the surface quality and the condition of the sample. If a sample has been plastically deformed or inadequately polished, the crystal lattice will be distorted and result in poor diffraction patterns and thus, low IQ values. The beam-specimen interaction depth is about 10 nm [59].

The confidence index parameter is a TSL patented voting scheme used to quantify the confidence that the pattern has been indexed correctly. The values of CI range from 0 to 1, where 0 is the lowest and 1 is the highest. TSL has reported that patterns indexed with a CI of 0.1 are correctly indexed 95% of the time, which is illustrated in figure 3.6.5 on the following page.

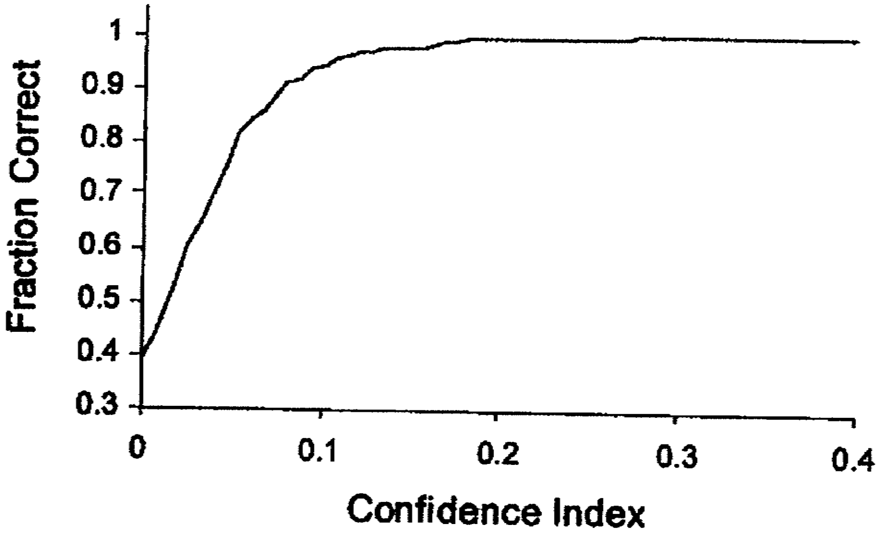

Figure 3.6.5 Correct indexing as a function of confidence index in aluminum [56].

Once the data was collected it was analyzed using the analysis software. The software was equipped with a multitude of features, however; only the grain boundary characterization was used extensively. Maps were constructed using different colors to represent different types of grain boundaries as outlined below, however Σ1 boundaries were not included in the analyses. Operating instructions for the OIM apparatus have been placed in appendix E for future reference.

Random.......................Black

Σ3........................Green

Σ9........................Orange

Σ27......................Yellow

Other 3 ≤ Σ ≤ 29....... Red

A study done on the statistical significance of GBCD data collected by OIM analysis has showed that for a CSL boundary fraction greater than 20% requires a minimum of 500 boundaries to be characterized for less than 10% fractional error [60]. A plot is provided as figure 3.6.6 where the inverse relationship between fractional error and sample size is seen. The fraction of special boundaries p was calculated by dividing the number of special boundaries by the total number of boundaries collected.

Analysis has shown that the chief source of error in the data collection procedure is associated with the correct location of the pattern center (PC) for calibration [59].

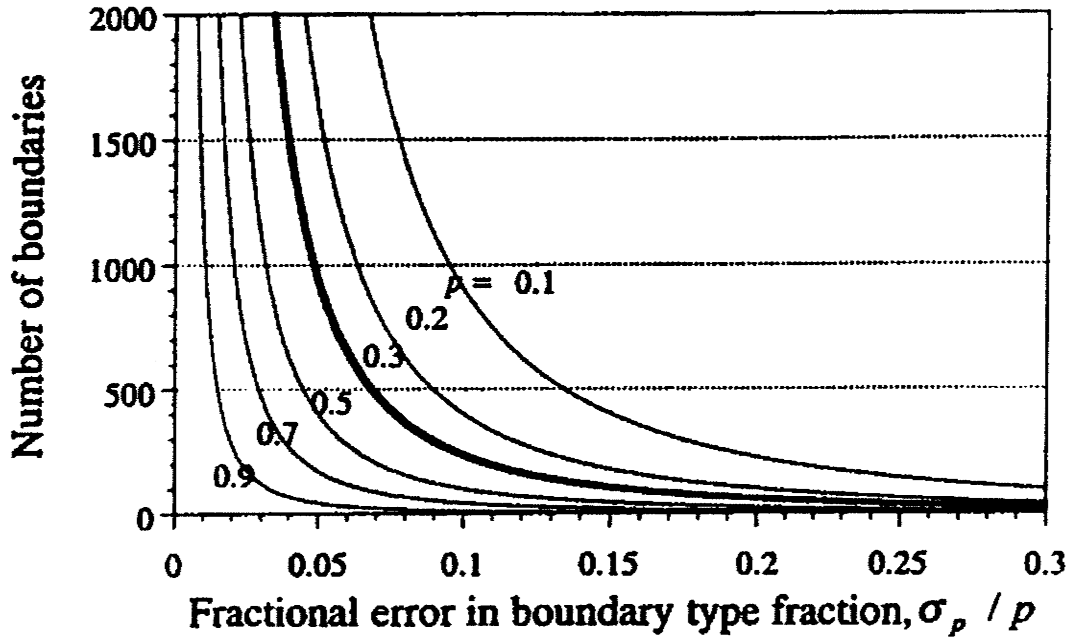

Figure 3.6.6 Fractional error as a function of sample size for different CSL boundary fractions p and σ_p is the standard deviation of p [60].

3.7 Design of Experiments

In order to design a set of experiments using the variables: (1) percent reduction in thickness by cold rolling, (2) annealing temperature, and (3) number of cycles of sequential cold rolling and annealing, the recrystallization behavior of Ni-200 had to be studied. This was facilitated by conducting a series of one-step cold rolling and annealing experiments as outlined in section 4.3. Once the recrystallization behavior was observed, values for the above parameters were assigned to design a set of experiments such that recrystallization would take place and the resulting microstructure could be characterized using OIM.

In attempting to find the optimum processing schedule to maximize the fraction of special boundaries, nine preliminary experiments were designed and conducted based on a 2^3 factorial experiment. This was done with the aid of the statistics department, however due to early errors the design was statistically flawed.

The primary objective of this study was not to maximize Fsp with the use of a factorial experiment, but to observe the effects of varying processing parameters on the GBCD and random boundary connectivity. For this reason, the author proceeded to design further experiments based on observations in the recrystallization behavior experiments and trends in GBCD of the already processed materials. This resulted in a superior set of experiments designed to observe the effects of increased number of cycles on Fsp values for a given strain per cycle and annealing temperature. These also allowed cross-comparisons between annealing temperatures and strain per cycle values as seen in the graphs in appendix D that are discussed in the following chapter.

The resulting experiments discussed in section 4.4 are largely a result of evolving knowledge of process variable interactions from continued experimentation. Several experiments were deliberately conducted beyond the expected limits of recrystallization and grain growth to observe the microstructural response of such treatments.

Chapter 4 RESULTS AND DISCUSSION

4.1 Characterization of the As-Received Material

The composition of a sample from the as-received sheet was analyzed by NSL Analytical Services, Inc. and the nickel purity was measured to be 99.7%, which is slightly higher than the nominal value of 99.5%. There were a number of trace elements detected and their respective concentrations can be seen in table 4.1.1 below. It is clear from the sorted table that the most significant contributions were made by Mn, Cu, Ti, and Fe, while only slight amounts of other elements were detected.

Nickel (Ni)	99.7
Manganese (Mn)	0.18
Copper (Cu)	0.052
Titanium (Ti)	0.023
Iron (Fe)	0.021
other	0.01343
Chromium (Cr)	0.009
Cobalt (Co)	0.0006
Tungsten (W)	0.00037
Molybdenum (Mo)	0.00036
Niobium (Nb)	0.00024

Table 4.1.1 Trace element concentrations (wt.%) in as-received Nickel-200 sheet.

A sample of the as-received material was mounted and etched for optical microscopy to determine the nature and size of the grain boundaries. A photomicrograph can be seen in figure 4.1.1 below where the equiaxed grain structure can be observed with several twin grain boundaries also observable. Manual grain size measurements using the intercept method (including twins) revealed a grain size of 31 μm.

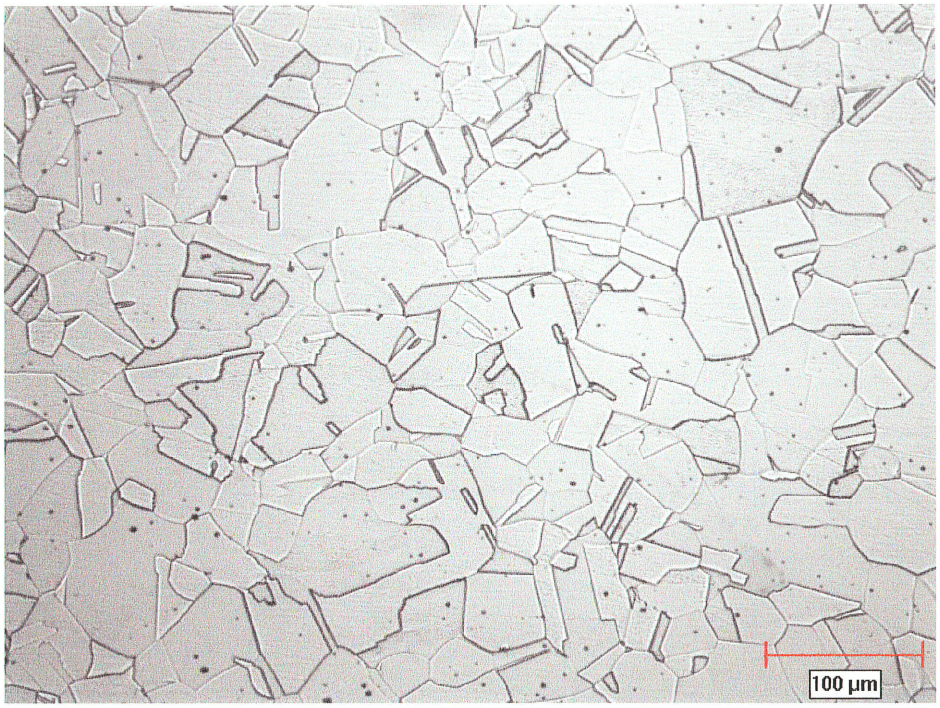

Figure 4.1.1 Optical micrograph of as-received Nickel-200.

A relatively large orientation image microscopy scan was performed on a sample of the as-received material to obtain an accurate determination of the grain boundary character distribution. This was important to serve as a baseline to permit subsequent comparisons to processed samples and also to quantify effects of processing parameters. The OIM map seen in figure 4.1.2 was generated from almost 60,000 points using a step size of 3 microns. Black lines are random boundaries, while colored lines are special boundaries according to the scheme outlined in section 3.6. The total fraction of special grain boundaries in an as-received sample was found to be 35%, of which 26% are Σ3 (green) boundaries (75% of total).

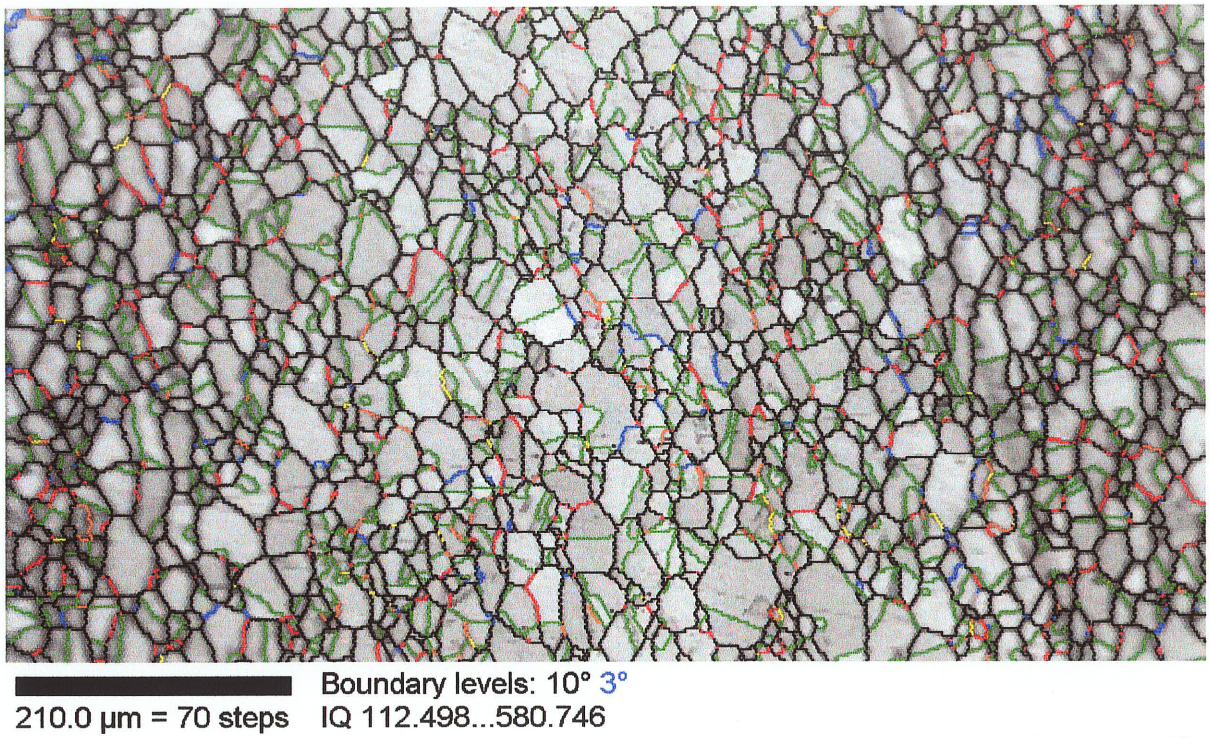

Figure 4.1.2 OIM map of as-received Ni-200 showing random and special grain boundaries (Fsp = 35%, 59,768 points, IQ_{avg} = 394.19, CI_{avg} = 0.65).

To permit observation of the random boundary network, an additional map of the same data was produced with the special boundaries (low angle and CSL) and the IQ grayscale removed. This map can be seen in figure 4.1.3 where there exists a relatively high degree of connectivity between the random boundary network, despite the 35% fraction of special boundaries.

A sample of the as-received material was mounted and etched for optical microscopy to determine the nature and size of the grain boundaries. A photomicrograph can be seen in figure 4.1.1 below where the equiaxed grain structure can be observed with several twin grain boundaries also observable. Manual grain size measurements using the intercept method (including twins) revealed a grain size of 31 μm.

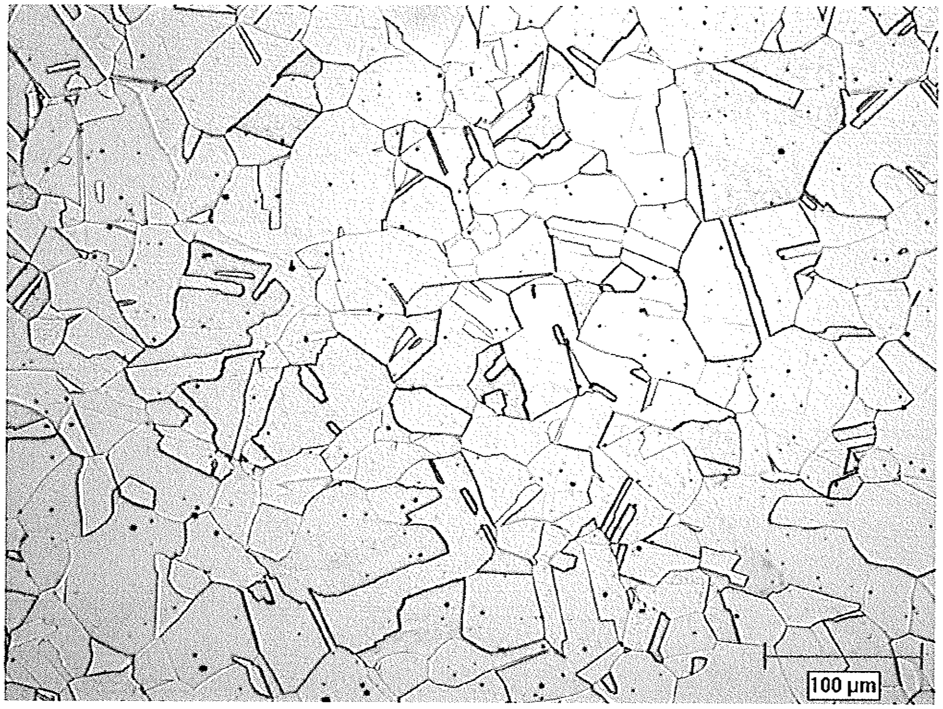

Figure 4.1.1 Optical micrograph of as-received Nickel-200.

A relatively large orientation image microscopy scan was performed on a sample of the as-received material to obtain an accurate determination of the grain boundary character distribution. This was important to serve as a baseline to permit subsequent comparisons to processed samples and also to quantify effects of processing parameters. The OIM map seen in figure 4.1.2 was generated from almost 60,000 points using a step

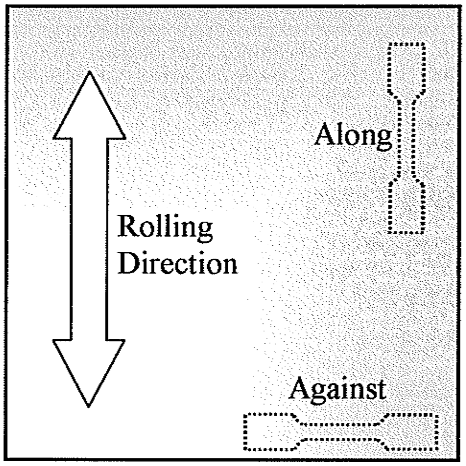

Figure 4.2.1 Schematic showing tensile samples with and against the rolling direction.

The values from the two sets of samples are displayed in table 4.2.1, where it can be seen that the samples taken along the rolling direction exhibited about 15 MPa greater strength than the samples taken against the rolling direction. Since the values were reproducible, within experimental error, and the ductility was almost identical between all samples, the mechanical properties of the as-received sheet are considered to be isotropic.

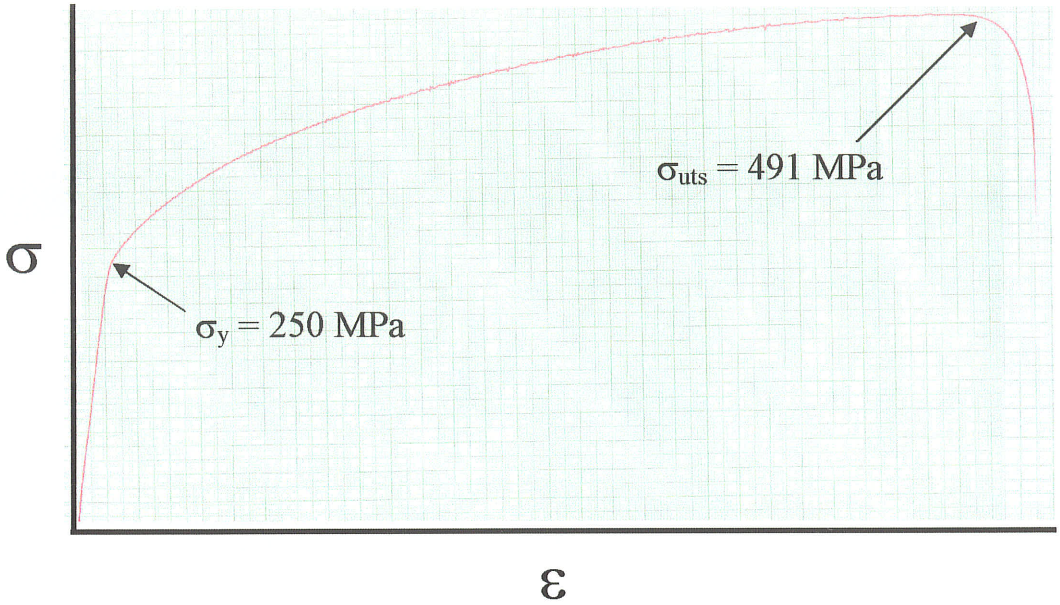

Figure 4.2.2 Stress-strain plot for as-received Ni-200 tested to failure.

Sample	Ultimate strength (MPa)	Yield strength (MPa)	Elongation (%)
with R.D. #1	504	252	59
with R.D. #2	507	261	60
against R.D. #1	491	250	60
against R.D. #2	488	246	61

Table 4.2.1 Tensile testing data from four samples tested to failure.

In addition to tensile testing, microhardness measurements were made across the thickness of a mounted as-received sample. Testing was performed on cross-sections 'perpendicular' to and 'parallel' to the original rolling direction as sketched in the hardness profile plot in figure 4.2.3. Data from each pass is shown to give an indication of scatter, with green lines representing the parallel data and orange lines represent perpendicular data. The thick lines represent average values for each distance.

It was found that the hardness profiles were not the same and that the profile for samples taken parallel to the rolling direction was more uniform. It was interesting to note the decrease in hardness near the center of the sample tested perpendicular to the rolling direction.

The data set is produced on the following page as table 4.2.2, where the three test values are shown, along with averages from both perpendicular and parallel tests. Passes labeled 1, 2 and 3 were taken parallel, while x-1, x-2, and x-3 were taken perpendicular to the rolling direction. The average of the averages for tests performed with the rolling direction was 188, while those taken against the rolling direction were 138. The source of the discrepancy is unknown, however it is not believed to be attributed to grain size variation or cold work.

Dist. from End	**Dist. (in)**	**Dist. (mm)**	**1**	**2**	**3**	**avg.**	**x-1**	**x-2**	**x-3**	**x-avg.**
0.0125	0.002	0.0508	217	217	174	**203**				
0.025	0.004	0.1016	192	192	193	**192**	172	172	173	**173**
0.050	0.008	0.2032	147	191	181	**173**	147	157	166	**157**
0.100	0.016	0.4064	169	178	169	**172**	161	161	151	**158**
0.150	0.024	0.6096	168	171	183	**174**	159	142	138	**146**
0.200	0.032	0.8128	215	178	188	**193**	126	145	126	**132**
0.250	0.040	1.016	198	195	188	**194**	150	136	126	**137**
0.300	0.048	1.2192	216	202	192	**203**	125	123	123	**124**
0.350	0.056	1.4224	191	178	173	**181**	112	124	120	**119**
0.400	0.064	1.6256	199	169	198	**189**	104	106	108	**106**
0.450	0.072	1.8288	195	151	188	**178**	112	108	105	**108**
0.500	0.080	2.032	206	167	207	**194**	120	122	125	**122**
0.550	0.088	2.2352	224	179	189	**197**	135	137	128	**133**
0.600	0.096	2.4384	192	172	197	**187**	139	146	136	**141**
0.650	0.104	2.6416	189	158	193	**180**	140	146	148	**145**
0.700	0.112	2.8448	191	160	168	**173**	171	130	170	**157**
0.750	0.120	3.048	221	194	201	**205**	143	119	164	**142**

Table 4.2.2 Hardness data for as-received material.

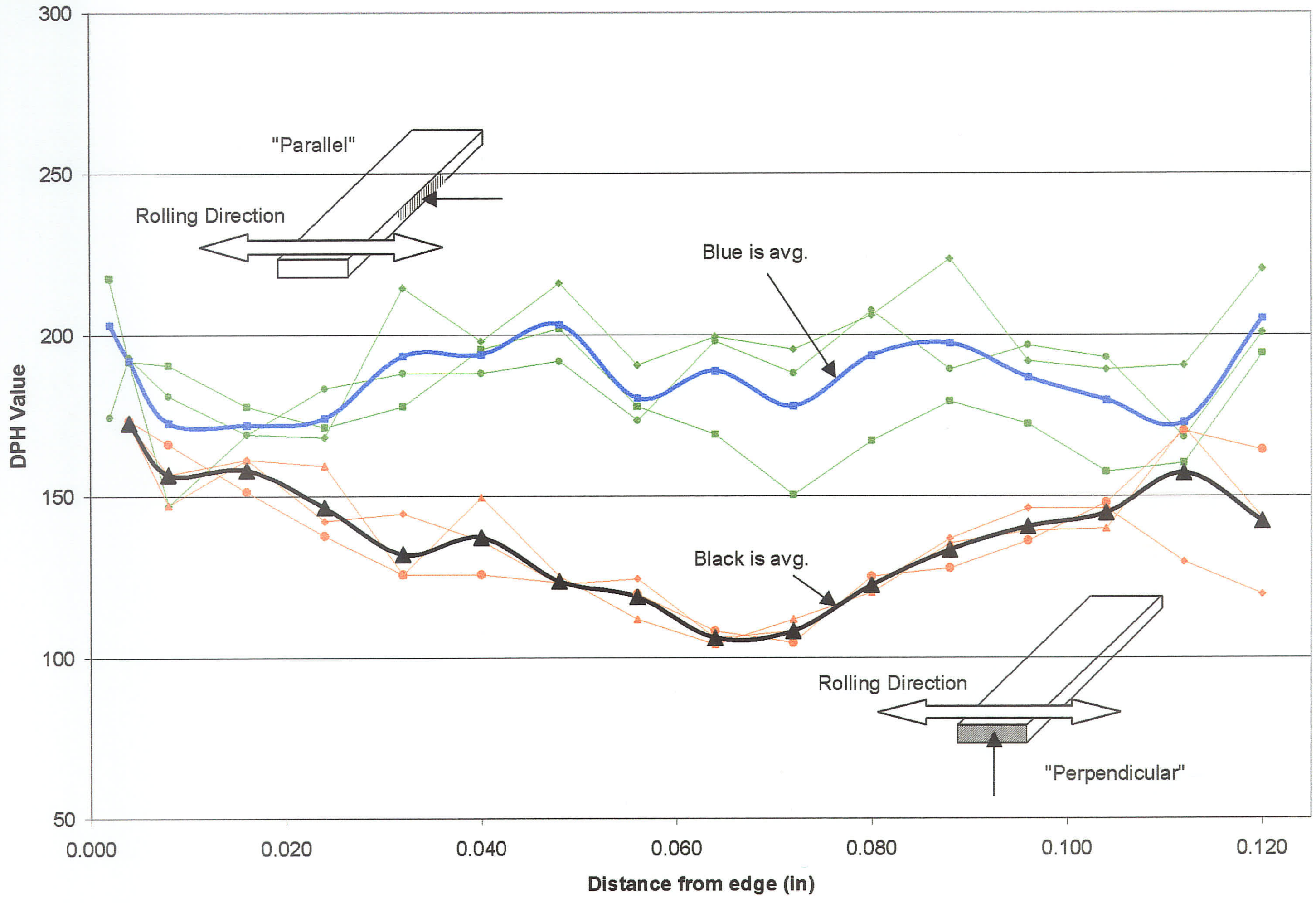

Figure 4.2.3 As-received material hardness profiles for tests performed with and against the rolling direction as shown.

4.3 Recrystallization Behavior Experiments

The recrystallization process is controlled by several interacting factors, therefore a careful and systematic set of experiments were performed to observe the role of each variable for this material. The amount of deformation and the annealing temperature were chosen as variables, while the strain rate, initial grain size, annealing time, and the annealing atmosphere were held constant.

Strips of 3/4 inch wide and 1/8 inch thick commercially pure nickel sheet were cold rolled to reductions in thickness of 10, 20, 40, 60, and 90 percent. Small samples of each were cut off, wrapped in stainless steel foil and annealed in flowing argon at 400, 500, 600, 700, 800, and 900°C for 7 minutes.

Samples were mounted and polished using standard metallographic procedures to colloidal silica, then etched with a 1:1 mixture of nitric and acetic acid. Optical micrographs of all samples were taken to qualitatively determine the transition points from deformed to recrystallized structure. These have been grouped by increasing cold rolled percentages and placed in appendix B for reference purposes.

Micro-hardness tests were performed on all samples to determine the transition from cold-worked to recrystallized, then subsequently to grain growth. Hardness testing was performed at regularly spaced intervals across the thickness of the sample to study the uniformity. Three data sets were collected from each sample to improve the accuracy.

Hardness profiles for each individual sample were plotted with either sample annealed at the same temperature (constant strain lines) or samples cold rolled the same amount (constant temperature lines) and have placed in appendix A. This was found to be useful since it allowed comparison by different grouping methods. Since the graphs with those samples annealed at the same temperature contain data from samples of different thicknesses, the distances from the edge have been divided by the total thickness of the sample to facilitate comparison. This was labeled 'normalized distance from edge', where 50 represents the center of the sample.

It was initially assumed that the strain distribution across the thickness of the cold rolled material would not be uniform, but rather hardness would increase towards the edges as a result of cold rolling. This behavior was not observed in any of the samples from the planned set of experiments, including the lowest strained sample (10%). To verify strain uniformity, an additional sample was prepared by cold rolling only 5% reduction in thickness and hardness testing was performed. As seen in a plot of the cold rolled material hardness as figure 4.3.1, the hardness profiles are all essentially horizontal, including the 5% cold rolled sample. This led to the conclusion that the strain distribution was relatively uniform in all of the samples.

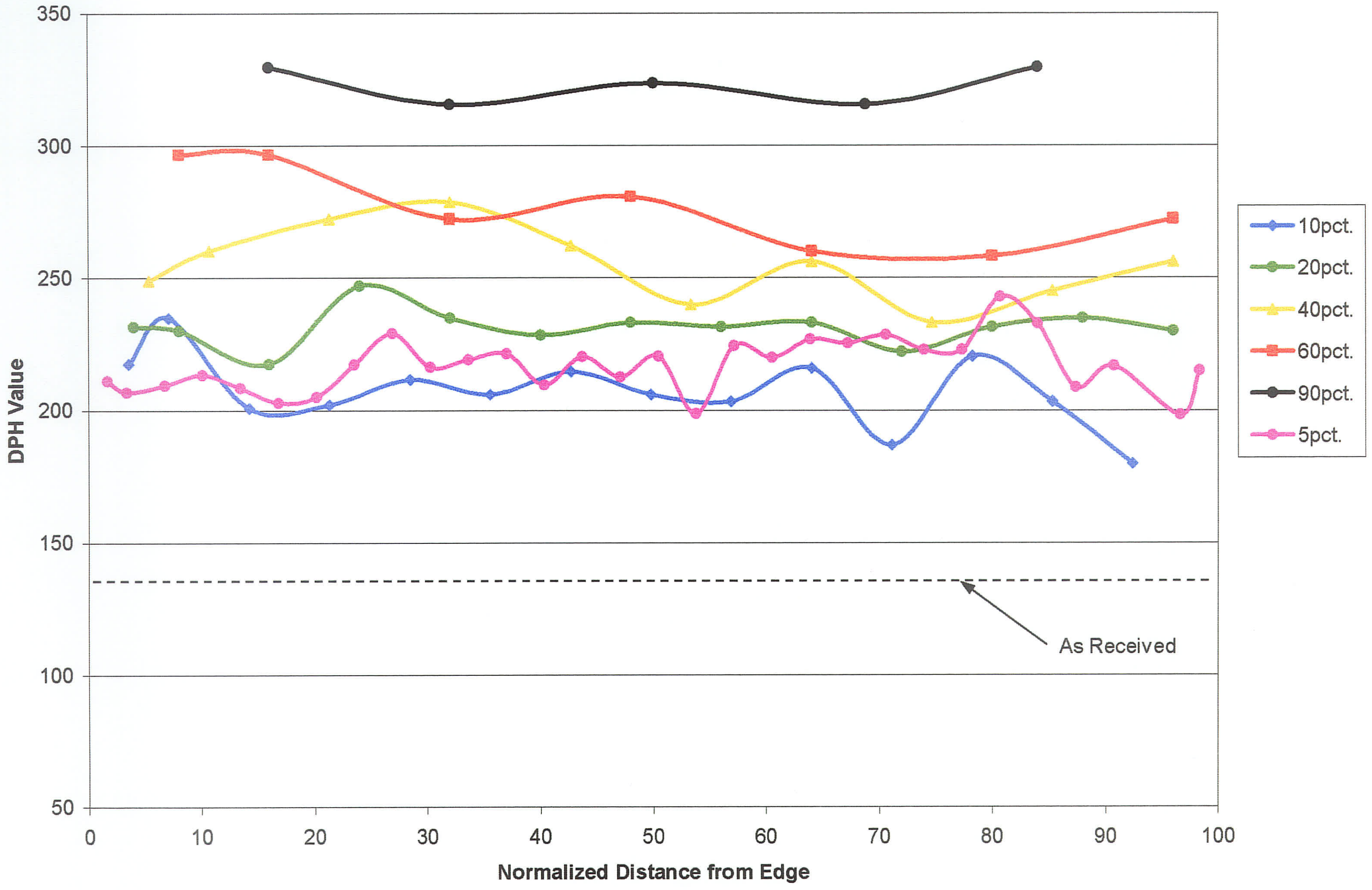

Figure 4.3.1 Cold rolled material hardness profiles across thickness showing relatively uniform strain distributions.

The hardness values for the samples cold rolled between 10 and 90% and annealed at 400°C have been plotted in figure 4.3.2 along with a dotted line to represent the average hardness of the as-received material. The trend of increasing hardness with increased strain can be seen from the stacking sequence of lines. Decreases in hardness at the edges of some samples could be attributed to sampling error since the metal near the edge has the ability to move outwards, or "mushroom" out into the relatively soft mounting compound.

As temperature was increased to 600°C, the samples cold rolled more than 40% experienced softening as seen in figure 4.3.3. It is assumed that the softening is a direct result of recrystallization having taken place. When the temperature was increased to 900°C, all of the samples softened as seen in figure 4.3.4, which can be attributed to recrystallization and subsequent grain growth.

Figure 4.3.5 shows a summary of almost all of the collected data. Each data point was calculated by averaging the values across the thickness of that sample, which is a good indication of hardness since the profiles were relatively uniform.

10% Samples							
Dist. from edge	no anneal	**400C**	**500C**	**600C**	**700C**	**800C**	**900C**
0.002		207	188	138	152	111	114
0.004	217	203	203	136	160	114	118
0.008	235	209	186	150	151	112	108
0.016	201	212	183	156	157	111	115
0.024	202	192	195	145	164	109	115
0.032	212	198	187	145	155	135	119
0.040	206	201	177	157	149	138	120
0.048	215	195	191	131	142	154	131
0.056	206	181	180	143	150	138	146
0.064	203	188	207	149	152	146	140
0.072	216	183	192	149	144	143	142
0.080	187	183	180	142	154	140	132
0.088	221	188	202	151	153	141	127
0.096	203	194	202	138	153	142	113
0.104	180	201	187	134	148	126	112
Average	207	196	191	144	153	131	124

Table 4.2.3 Hardness data for 10% cold rolled and annealed (7 min.) Ni-200.

20% Samples							
Dist. from edge	no anneal	**400C**	**500C**	**600C**	**700C**	**800C**	**900C**
0.002		233	205	173	103	102	110
0.004	232	221	201	197	120	113	121
0.008	230	232	213	195	128	119	131
0.016	217	206	203	182	147	123	135
0.024	247	232	195	187	155	124	138
0.032	235	228	185	163	126	138	139
0.040	228	195	212	176	139	130	138
0.048	233	201	209	163	130	110	144
0.056	232	193	203	172	134	129	123
0.064	233	225	205	154	121	146	124
0.072	222	194	209	167	162	139	133
0.080	232	210	186	159	159	130	118
0.088	235	233	202	174	148	128	123
0.096	230	222	216	162	141	115	123
Average	231	216	203	173	137	125	129

Table 4.2.4 Hardness data for 20% cold rolled and annealed (7 min.) Ni-200.

40% Samples							
Dist. from edge	no anneal	**400C**	**500C**	**600C**	**700C**	**800C**	**900C**
0.002		234	211	172	132	148	122
0.004	249	236	223	205	124	155	113
0.008	260	240	217	204	125	153	110
0.016	272	224	201	201	119	127	117
0.024	279	209	215	184	139	145	119
0.032	262	206	187	195	141	130	122
0.040	240	228	210	187	144	121	123
0.048	256	218	205	195	141	119	110
0.056	233	224	199	200	142	133	126
0.064	245	222	217	212	133	132	123
0.072	256	256	199	198	130	133	123
Average	255	227	208	196	134	136	119

Table 4.2.5 Hardness data for 40% cold rolled and annealed (7 min.) Ni-200.

60% Samples							
Dist. from edge	no anneal	**400C**	**500C**	**600C**	**700C**	**800C**	**900C**
0.002		248	219	143	146	138	124
0.004	297	237	232	130	131	151	117
0.008	297	243	218	143	142	158	127
0.016	272	247	216	157	142	152	122
0.024	281	237	240	157	149	116	142
0.032	260	266	246	141	153	147	136
0.040	258	249	249	148	145	118	130
0.048	272	251	237	146	159	106	116
Average	277	247	232	146	146	136	127

Table 4.2.6 Hardness data for 60% cold rolled and annealed (7 min.) Ni-200.

90% Samples							
Dist. from edge	no anneal	**400C**	**500C**	**600C**	**700C**	**800C**	**900C**
0.0020	329	287	262	111	97	100	93
0.0040	316	303	237	119	109	100	99
0.0063	324	288	278	116	107	105	96
0.0086	316	303	237	119	109	100	99
0.0105	329	287	262	111	97	100	93
Average	323	293	255	115	103	101	96

Table 4.2.7 Hardness data for 90% cold rolled and annealed (7 min.) Ni-200.

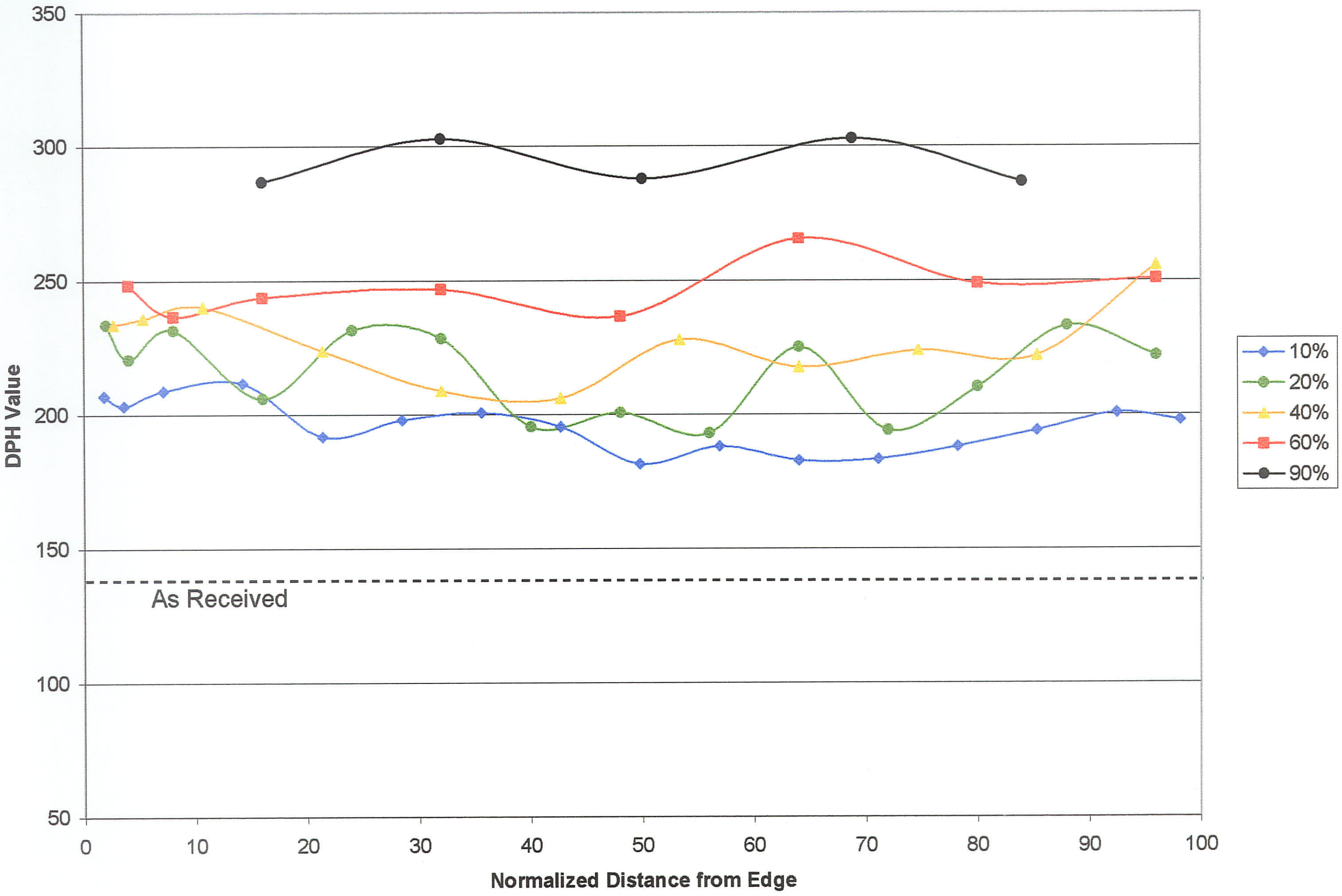

Figure 4.3.2 Hardness profiles for samples cold rolled and annealed at 400°C.

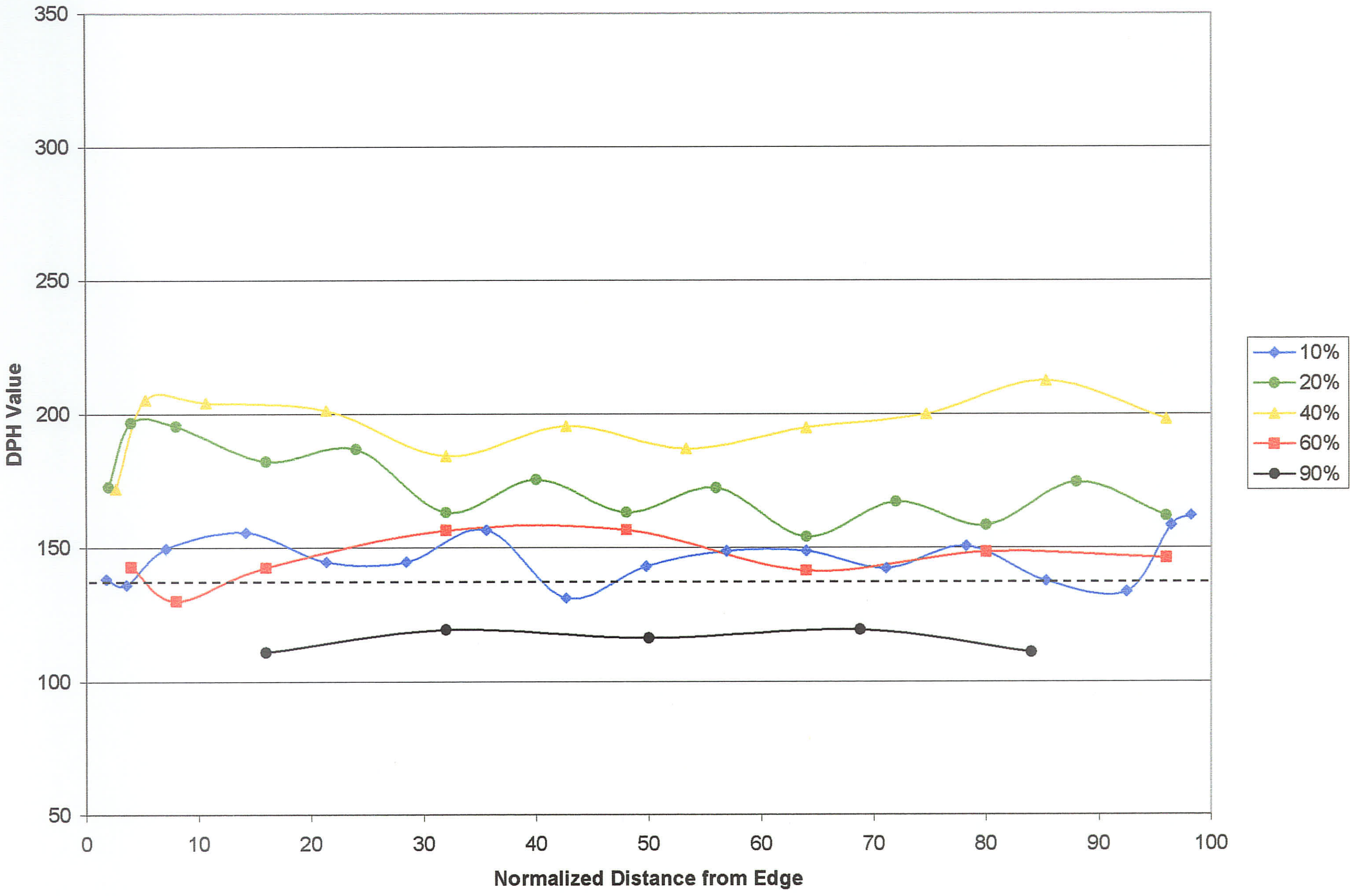

Figure 4.3.3 Hardness profiles for samples cold rolled and annealed at 600°C.

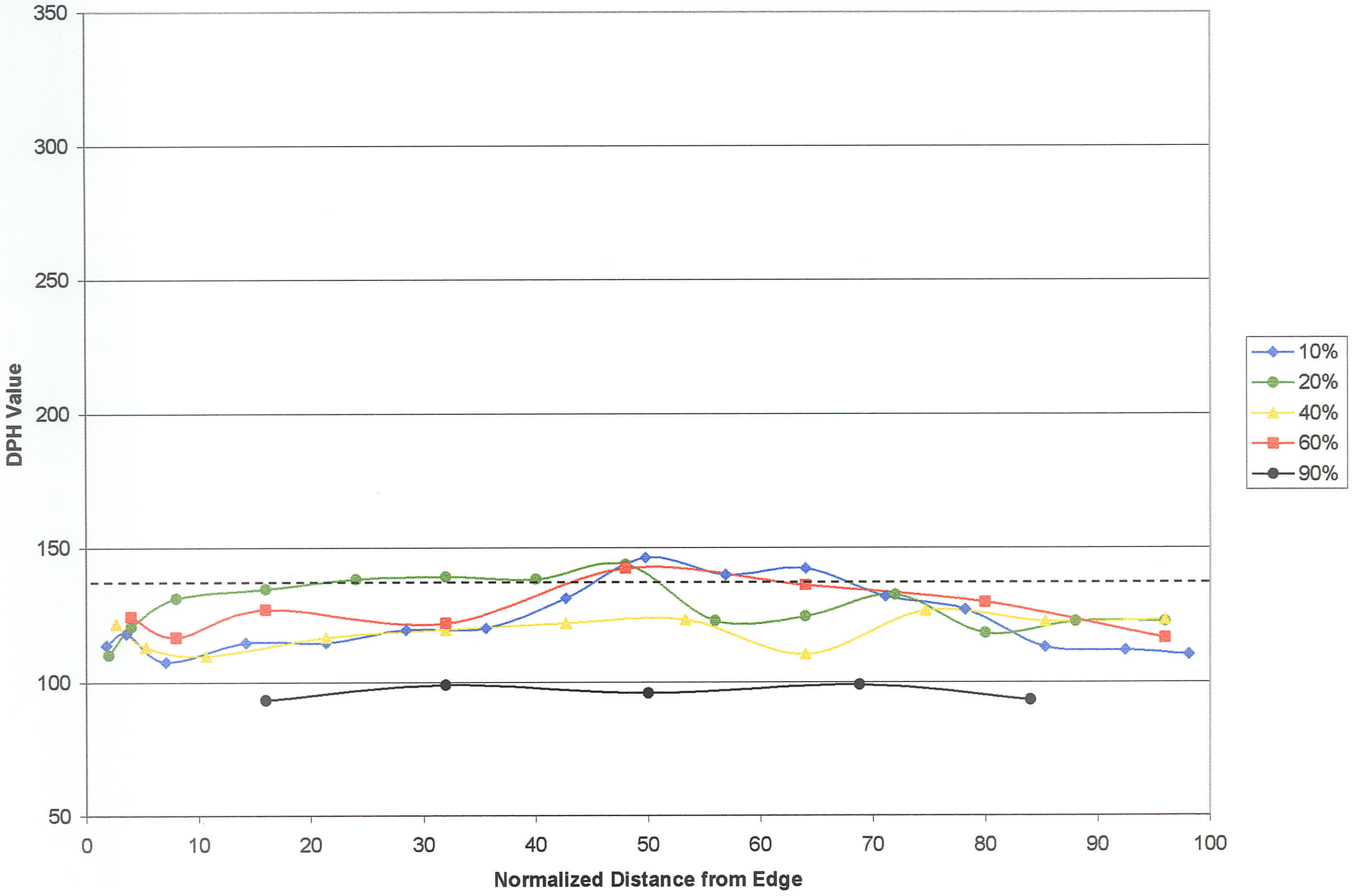

Figure 4.3.4 Hardness profiles for samples cold rolled and annealed at 900°C.

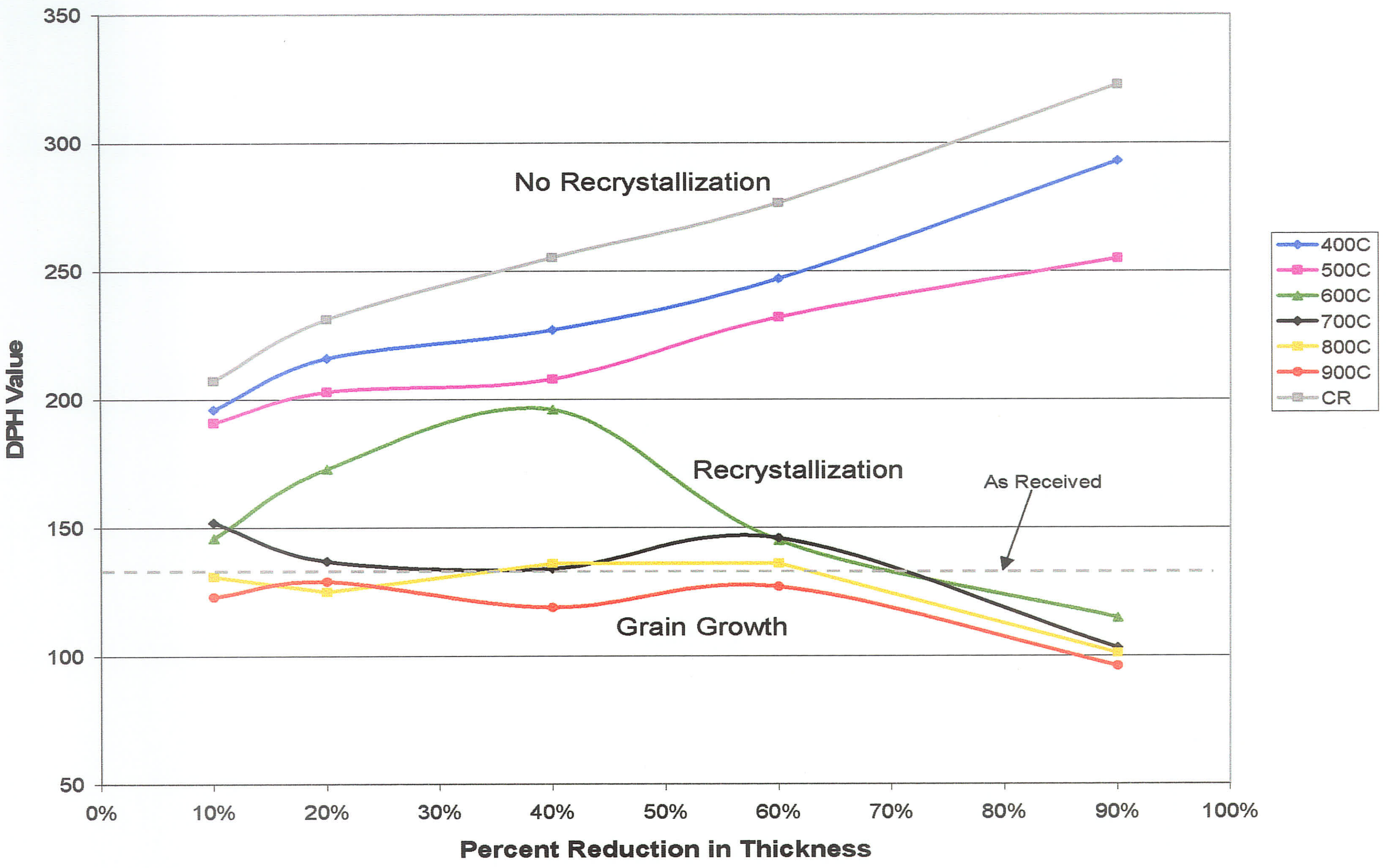

Figure 4.3.5 Microhardness test results showing transitions from cold worked to recrystallized then grain growth.

From the summary plot in figure 4.3.5 on the previous page, it can be seen that the hardness of the cold rolled samples that had not been annealed increase almost linearly along with those samples annealed at 400°C and 500°C. This behavior, along with the observed microstructures, implies recrystallization has not occurred at any deformation level. An example of a sample that has not recrystallized is seen in figure 4.3.6 where the grains are elongated in the rolling direction. The black portion on the left is the mounting compound, since the micrograph was taken at the edge to observe any possible microstructural differences near the edges.

For the samples annealed at 600°C however, there is a critical point between 40% and 60% percent reduction in thickness at which enough energy has been stored from the cold rolling and recrystallization occurs. This behavior was also observed in the microstructures as seen in figure 4.3.7 where the deformed grain structure from 40% cold rolled becomes equiaxed for the 60% cold rolled sample due to recrystallization. It is important to note that almost all of the samples annealed at 700°C, 800°C, and 900°C have softened and do not appear to have any residual strain remaining.

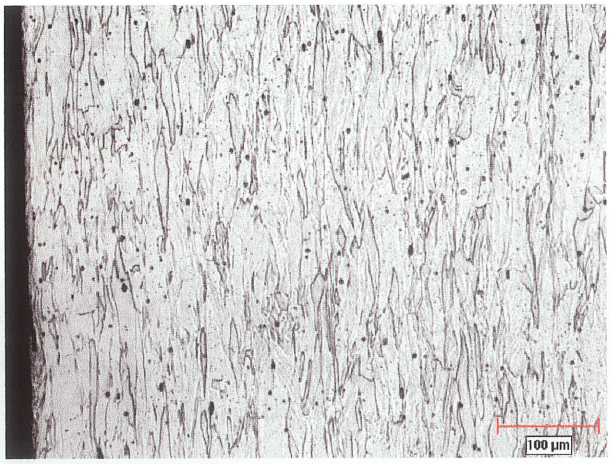

Figure 4.3.6 Optical micrograph of 60% cold rolled and annealed at 400°C Ni-200.

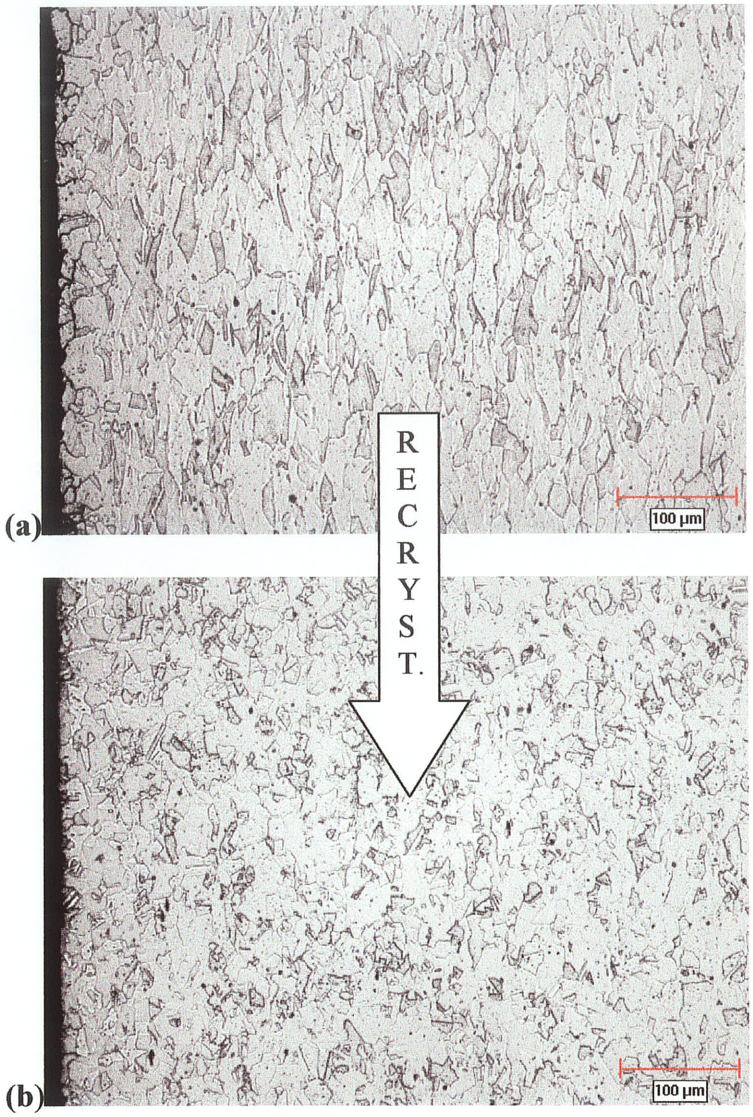

Figure 4.3.7 Optical micrographs of samples cold rolled (a) 40% and (b) 60% and annealed at 600°C.

The sample cold rolled 10% and annealed at 700°C appears to have increased in hardness somewhat, but it is possible that it can be attributed to statistical variance and has little or no significance. All of the samples cold rolled 90% have softened substantially as seen by the downward-sloped lines at the right hand portion of the graph that accompany evidence of grain growth through optical microscopy. This is due to appreciable grain growth resulting from the large amount of cold work and relatively high temperatures used for annealing.

4.4 Characterization of Processed Samples

OIM scans were performed on all processed samples and accompanying OIM grain boundary and connectivity maps have been placed in appendix C to maintain the flow of this report. The trends in the changing GBCDs with processing and the qualitative break-up of the random boundary connectivity are the prime interest to this study and therefore account for the majority of the discussion to follow, however samples with high Fsp values and highly fragmented random boundary networks are given special attention.

Table 4.4.1 shows all of the data collected from the processed samples, where fractions of individual boundary types are listed along with total fraction of special boundaries (Fsp), fraction of random boundaries (Frdm), number of grains scanned (No. Gs), the average IQ and CI values, and number of points used for the scan (# Pts.). Processing has been listed by number of cycles of a given strain and annealing temperature, for example 3x10%, 600C represents the sample processed 3 cycles of 10% cold rolled and annealed at 600°C each cycle.

Figure 4.4.1 shows the corresponding GBCD histogram for this data. The data has been arranged from left to right firstly by increasing temperature, secondly by increasing strain per cycle, and finally by increasing number of cycles.

Processing	Σ3	**Σ9**	**Σ27**	**other**	**Fsp**	**Frdm**	**No. Gs**	**IQ$_{avg}$**	**CI$_{avg}$**	**# Pts.**
As Received	26.2	2.1	0.6	6.0	**34.9**	65.1	1951	394.19	0.65	59,768
3x10%, 600C	2.2	0.2	0.2	2.1	**4.7**	95.3	124	216.17	0.55	21,411
15x10%, 600C	2.4	0.7	0.1	2.8	**6.0**	94.0	1044	139.85	0.27	21,411
1x25%, 600C	2.4	0.3	0.0	2.1	**4.8**	95.2	499	224.22	0.59	20,801
6x25%, 600C	2.9	0.7	0.2	2.2	**6.0**	94.0	548	147.20	0.35	12,491
3x10%, 700C	5.6	0.3	0.1	2.2	**8.2**	91.8	356	185.79	0.46	31,232
7x10%, 700C	22.4	1.6	0.3	3.5	**27.8**	72.2	245	430.25	0.76	33,733
15x10%, 700C	15.3	1.1	0.4	2.6	**19.4**	80.6	205	458.94	0.72	23,450
1x25%, 700C	11.2	1.0	0.3	3.2	**15.7**	84.3	725	211.87	0.55	29,963
6x25%, 700C	19.8	0.9	0.2	2.3	**23.2**	76.8	208	509.43	0.75	19,951
1x5%, 750C	36.1	4.0	1.6	4.3	**46.0**	54.0	598	607.52	0.46	48,312
5x5%, 750C	24.9	1.9	0.2	1.8	**28.8**	71.2	321	436.97	0.72	47,932
2x18%, 750C	34.2	3.1	0.8	3.5	**41.6**	58.4	365	561.82	0.72	38,141
4x18%, 750C	39.1	3.5	0.5	2.6	**45.7**	54.3	299	423.89	0.65	35,670
1x20%, 750C	36.4	4.4	0.1	5.7	**46.6**	53.4	507	500.41	0.74	38,279
5x20%, 750C	45.3	3.3	0.9	4.0	**53.5**	46.5	292	535.66	0.75	44,982
10 min @ 800C	29.5	2.0	0.7	5.5	**37.7**	62.3	622	489.94	0.70	34,884
1x10%, 800C	47.4	4.8	0.7	3.9	**56.8**	43.2	361	506.04	0.75	42,424
2x10%, 800C	44.2	6.8	2.3	2.2	**55.5**	44.5	175	403.56	0.76	44,195
3x10%, 800C	53.8	3.7	0.9	4.6	**63.0**	37.0	218	516.20	0.79	45,743
4x10%, 800C	25.1	1.6	0.5	0.6	**27.8**	72.2	62	399.87	0.75	42,625
6x10%, 800C	18.3	0.8	0.2	2.0	**21.3**	78.7	154	351.13	0.65	32,690
11x10%, 800C	36.7	2.3	0.7	2.6	**42.3**	57.7	204	561.46	0.73	10,301

Table 4.4.1 OIM Data for all processed samples (continued on next page).

1x18%, 800C	46.6	5.1	1.0	4.8	**57.5**	42.5	489	477.91	0.74	59,293
2x18%, 800C	37.1	3.1	1.1	3.6	**44.9**	55.1	351	421.47	0.73	46,494
3x18%, 800C	46.8	2.8	0.9	3.8	**54.3**	45.7	223	463.32	0.77	40,663
4x18%, 800C	43.0	3.5	0.4	3.6	**50.5**	49.5	213	547.72	0.77	46,665
4x18%, 800C	39.5	3.6	1.0	3.4	**47.5**	52.5	322	420.65	0.72	46,898
4x18%, 800C	36.5	3.4	0.5	3.1	**43.5**	56.5	218	519.39	0.72	44,375
6x18%, 800C	32.1	2.3	0.6	2.6	**37.6**	62.4	156	457.13	0.77	19,602
1x25%, 800C	24.7	2.0	0.6	2.2	**29.5**	70.5	284	387.74	0.68	21,821
3x25%, 800C	33.3	1.7	0.3	3.9	**39.2**	60.8	267	449.16	0.71	25,063
6x25%, 800C	15.0	0.5	0.0	2.3	**17.8**	82.2	192	425.82	0.67	15,971
3x12.5%, 825C	26.1	2.9	1.4	1.0	**31.4**	68.6	196	546.02	0.74	56,795
10 min @ 900C	24.8	1.9	0.8	1.9	**29.4**	70.6	351	361.56	0.68	41,527
1x2.5%, 900C	37.4	5.6	0.8	2.5	**46.3**	53.7	399	585.34	0.70	58,479
1x5%, 900C	50.2	8.1	3.0	3.8	**65.0**	35.0	580	494.15	0.72	74,844
2x5%, 900C	55.0	5.0	2.4	1.2	**63.6**	36.4	233	549.77	0.74	48,074
3x5%, 900C	38.9	2.9	0.8	0.7	**43.3**	56.7	185	500.86	0.62	28,087
5x5%, 900C	17.5	1.0	0.2	1.2	**19.8**	80.2	111	445.03	0.65	18,149
1x10%, 900C	38.0	5.2	0.9	2.5	**46.6**	53.4	397	476.81	0.73	63,175
3x10%, 900C	25.4	2.2	0.7	2.4	**30.7**	69.3	163	374.25	0.77	21,882
15x10%, 900C	11.2	1.8	0.8	2.3	**16.0**	84.0	19	228.83	0.74	9,555
1x20%, 900C	31.3	1.7	0.6	7.3	**40.9**	59.1	444	593.93	0.73	46,284
5x20%, 900C	17.0	1.2	0.7	2.7	**21.5**	78.5	262	553.37	0.35	13,098
1x25%, 900C	9.5	0.3	0.2	1.8	**11.7**	88.3	280	468.89	0.81	24,453
6x25%, 900C	10.8	0.3	0.2	1.9	**13.1**	86.9	118	358.50	0.74	16,271

Table 4.4.1 OIM Data for all processed samples (continued from previous page).

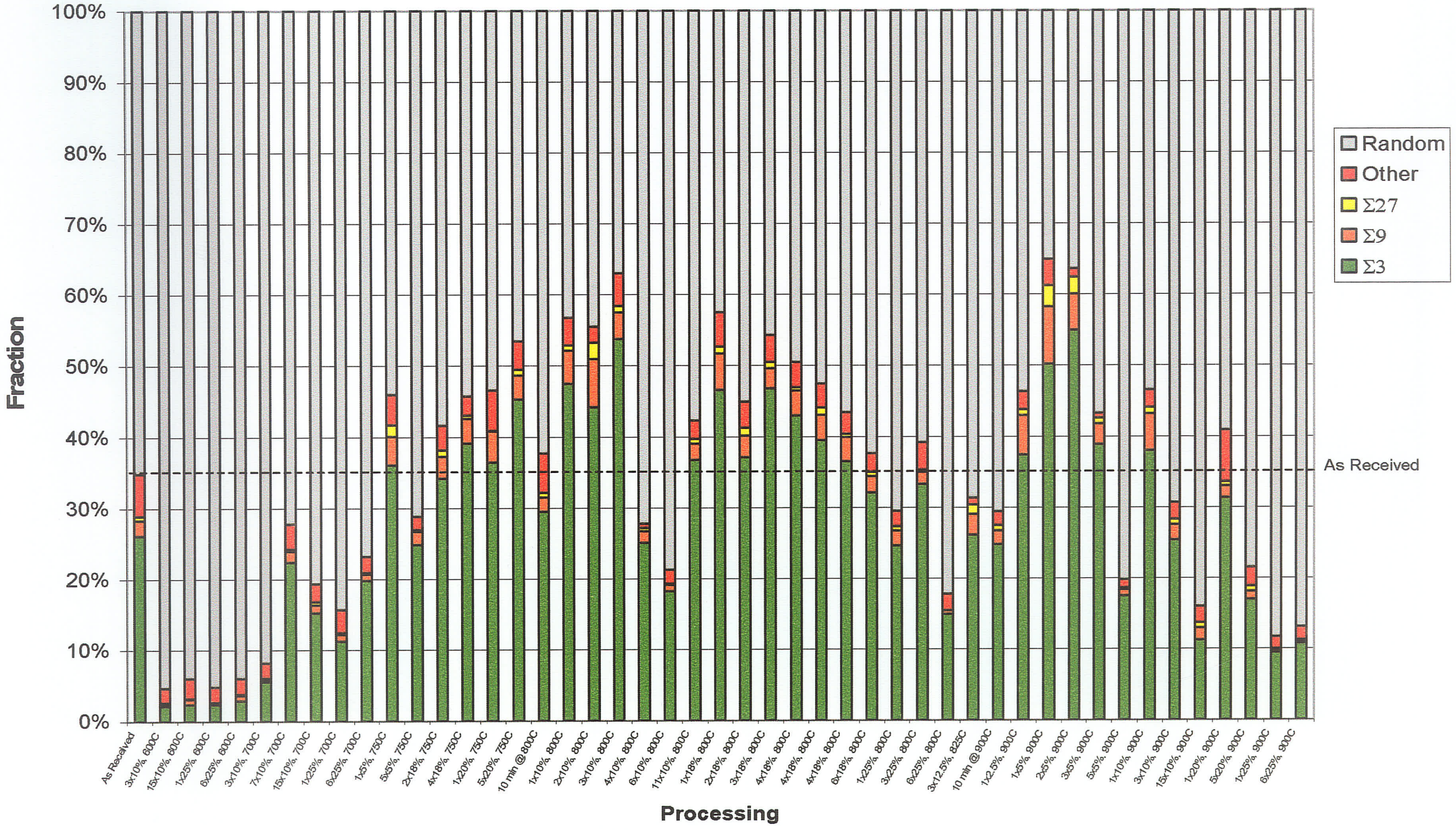

Figure 4.4.1 Grain Boundary Character Distribution for all samples.

To observe the relative contributions from each type of special boundary, a pie chart was plotted using average values from all of the processed samples. From the chart seen below, it immediately becomes clear that the most significant contribution of 80% was made by Σ3 boundaries, while all other types combined to account for only 20% of the total fraction.

Randle has reported [61] that in a grain boundary engineering material, the Σ3 fraction is high, the Σ9 fraction is about 1/5 that of the Σ3 fraction, and the Σ27 fraction is only slightly higher than for random distributions. From the observed distribution below, it is clear that Σ9s account for less than 1/10 of the Σ3 fraction. Since it remains unclear which CSL is most special, or which relative fraction of each type is optimal for property improvements, the fractions will be discussed in terms of total special fractions (Fsp) and individual CSL boundary fractions will not be discussed in detail.

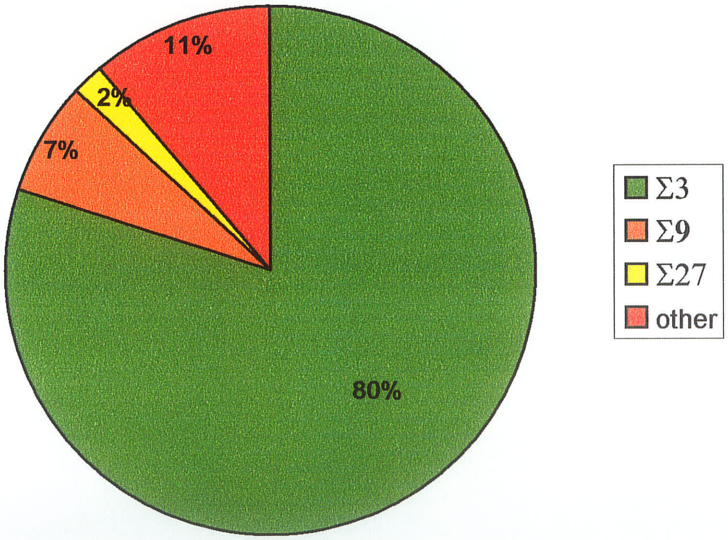

Figure 4.4.2 Pie chart showing average contributions of CSL boundaries from all processed samples.

4.4.1 600°C Samples

This relatively low temperature was initially chosen since samples cold rolled over 40% experienced recrystallization at 600°C as reported in section 4.3. A set of four experiments were planned to observe the effect on the GBCD, namely: 3 x 10%, 15 x 10%, 1 x 25%, and 6 x 25%. These parameters were selected since the total strain from the pairs 3 x 10% and 1 x 25%, and also 15 x 10% and 6 x 25% were approximately the same. It was expected that the higher strained samples would undergo recrystallization.

Upon scanning all of the samples with OIM, it was found that none of the samples had increased special boundaries fractions over the as-received fraction. In fact, the fractions of special boundaries for these four samples were all between 4 and 6%, which was a drastic reduction from the initial 35%. Distorted and elongated grains, along with very low IQ values collected by OIM scans, were evidence of large amounts of strain that remained in all of these samples. From studying this behavior, it became clear that moderate to high levels of strain combined with relatively low temperature anneals without recrystallization occurring were not effective at increasing the fraction of special boundaries, regardless of the number of cycles used.

4.4.2 700°C Samples

Since 600°C was inadequate to activate recrystallization for the strain levels used, the same strain treatments were applied using 700°C in attempt to invoke recrystallization. Results of OIM scans showed that all of the samples contained special fractions of between 8 and 28%, which was still lower than the as-received fraction of 35%. From relatively low IQ values, it appeared that the lower strained samples contained residual deformation, while the higher strained samples appeared to be strain-free with evidence of recrystallization. In addition, there existed a relatively high degree of random boundary connectivity in all of the samples processed, for example, as seen in the OIM map from the sample cold rolled 25% and annealed at 700°C for 10 minutes shown in figure 4.4.3 (b).

These results combined to lead to the conclusion that 700°C was a high enough temperature to cause recrystallization, but still inadequate to effectively increase Fsp or fragment the random boundary network for this particular material.

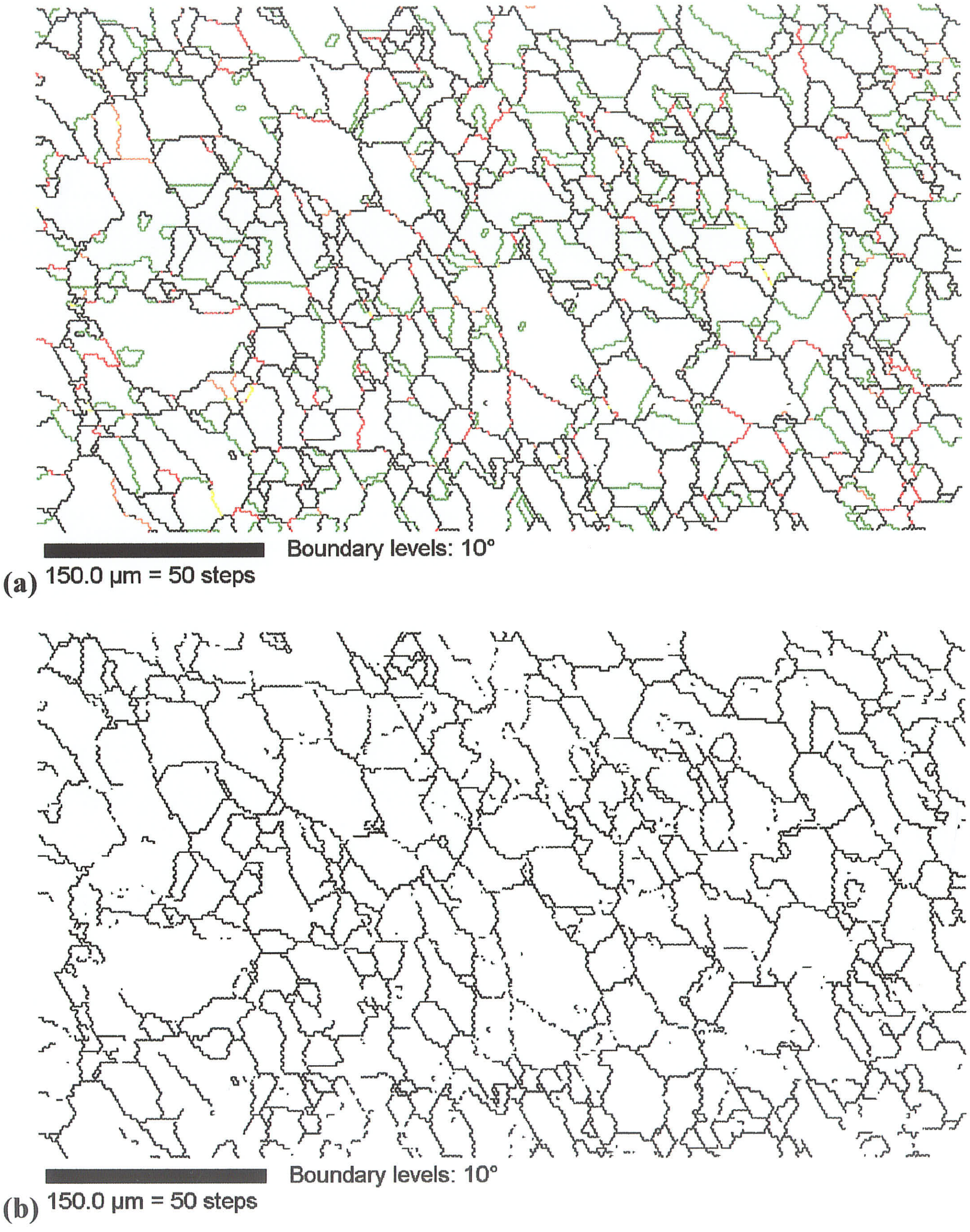

Figure 4.4.3 (a)-(b) OIM maps of sample 1 cycle of 25% and 700°C. (a) shows both special and random boundaries, while (b) shows only random boundaries. Note relatively high degree of connectivity in (b). Fsp = 16%.

4.4.3 750°C Samples

OIM revealed that special fractions for the six samples processed using 750°C for an annealing temperature ranged from 29 to 54%, with only one sample having a decreased special fraction from the as-received value of 35% as seen in figure 4.4.5.

While samples cold rolled 1 x 20% and 1 x 5% and annealed contained almost equal special fractions of about 46%, the sample strained only 5% appeared to have disrupted the random boundary network connectivity slightly more effectively than the 20% strained sample. It is worth noting the similar grain sizes of these two samples, namely the 5% strained sample was measured manually to be 40μm, while that of the 25% strained sample was 37 μm. According to ASTM specification E112, these grain size measurements are accurate within ± 15% since approximately 200 intercepts were counted for each sample.

The sample processed 5 cycles of 5% strain and annealed had the lowest special fraction of the samples annealed at 750°C (Fsp = 29%) and showed some grain growth, but effectively broke up much of the random boundary connectivity as seen in figure 4.4.4(b). This was unexpected since the Fsp value was lower than the as-received fraction of 35%. The higher strained samples, cold rolled 18-20%, showed increases in their special fractions to over 50%, but failed to disrupt the connectivity of random boundaries to any appreciable extent.

These results proved that Fsp fractions alone are not adequate predictors of random boundary network connectivity and that accurate characterization of the microstructure requires careful examination of both features.

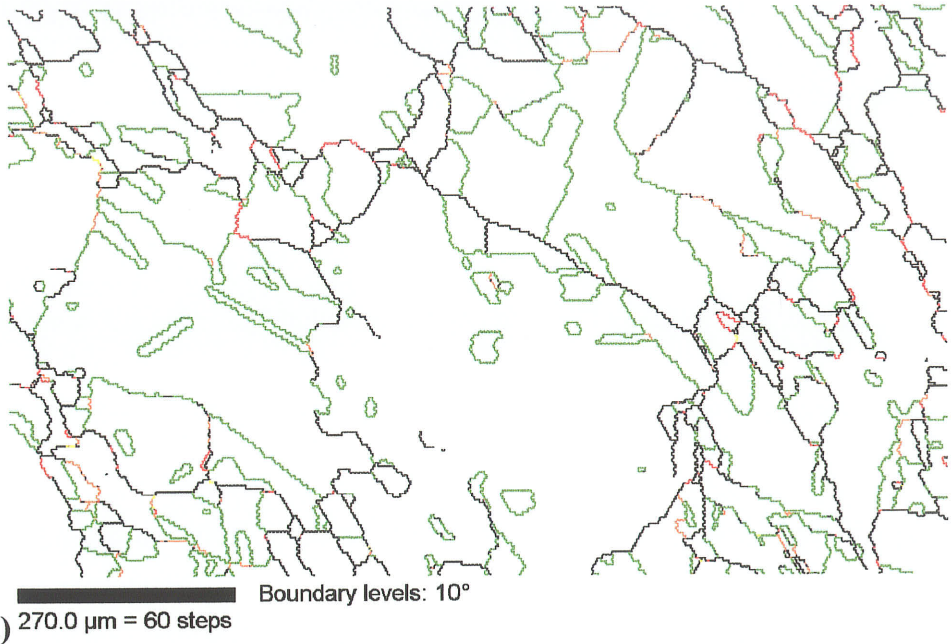

(a)

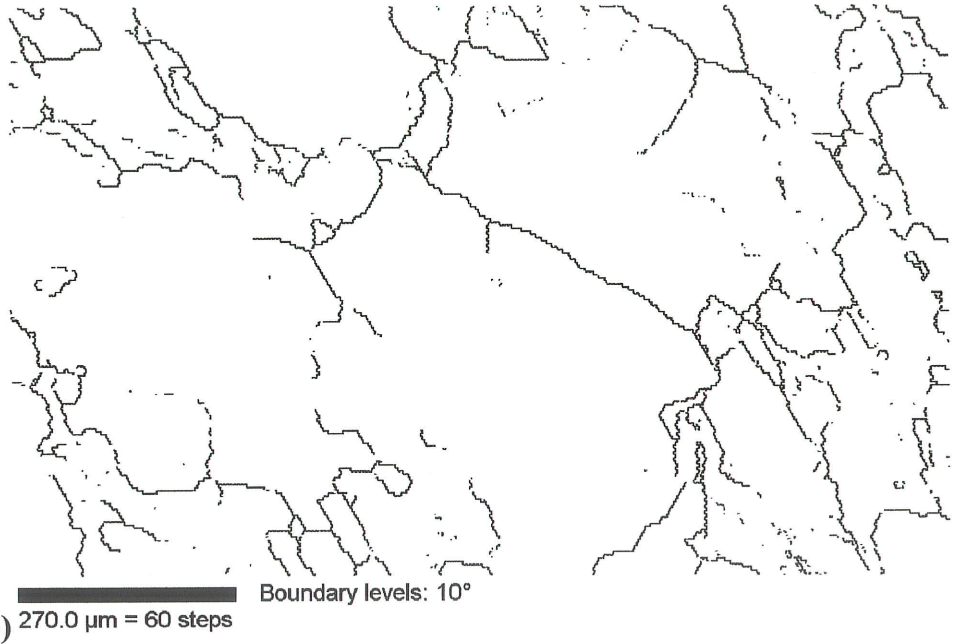

(b)

Figure 4.4.4 OIM maps of sample processed 5 cycles of 5% and annealed at 750°C showing (a) All grain boundaries (b) Random boundaries only. Fsp = 29%.

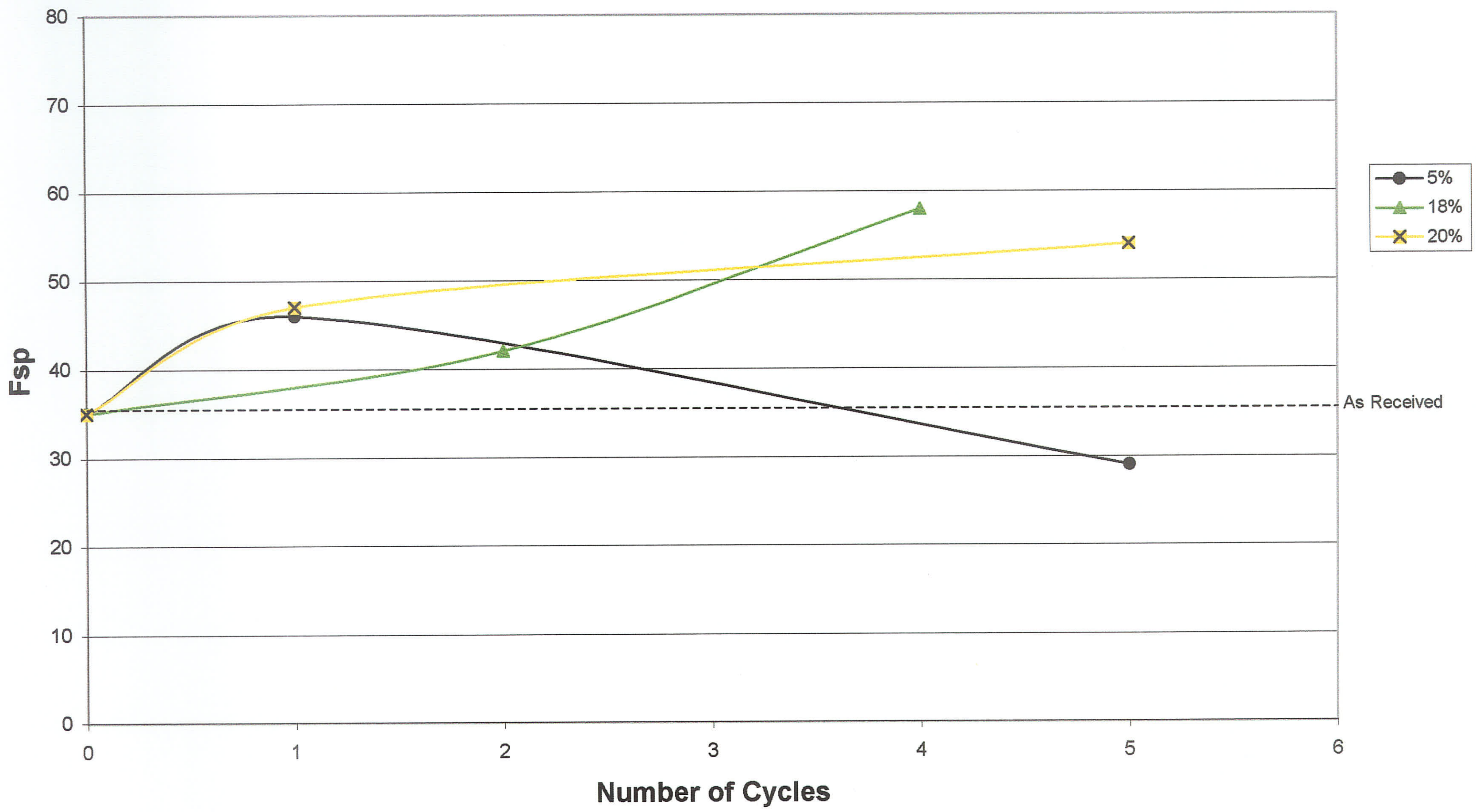

Figure 4.4.5 Fsp Profiles for samples cold rolled various amounts and annealed at 750°C for 10 minutes

4.4.4 800°C Samples

Using 10% strain per cycle, samples were processed 1, 2, 3, 4, 6 and 11 cycles and annealed at 800°C between straining. The samples processed between 1 and 3 cycles of 10% strain and annealed showed increases in special fractions between 57 to 63% from the initial fraction of 35%, while the others had decreased fractions, likely owing to excessive grain growth. This behavior is seen as the blue line in figure 4.4.6 on the following page. It is important to note that the 10% line extends to 11 cycles since it involves relatively low reductions in thickness per step, while the 18 and 25% lines are terminated at 6 cycles since the material has already been thinned considerably at that point.

Figure 4.4.7 (a)-(l) shows OIM maps of the 10% strained and annealed samples, with both the random and special grain boundaries shown on the left-hand side and only the random boundaries on the right-hand portion. Maps (a) and (b) show the sample processed 1 cycle, (c) and (d) show the sample processed 2 cycles, (e) and (f) show 3 cycles, (g) and (h) show 4 cycles, (i) and (j) show 6 cycles, and (k) and (l) show 11 cycles. The special fractions of these samples were found to be 57, 56, 63, 28, 21, and 42%, respectively.

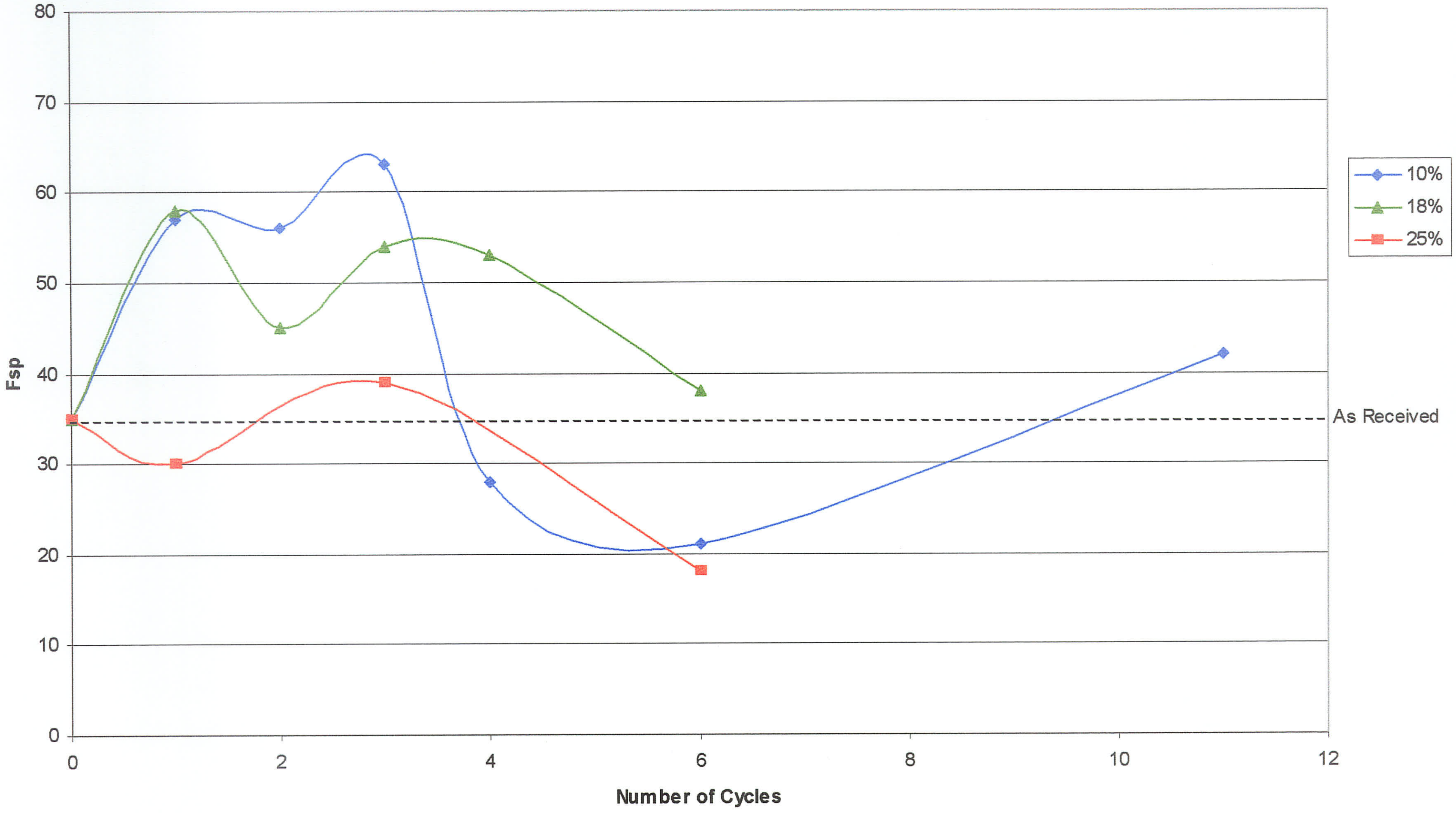

Figure 4.4.6 Profiles showing changing Fsp with increasing number of cycles of 10% strained and annealed at 800°C.

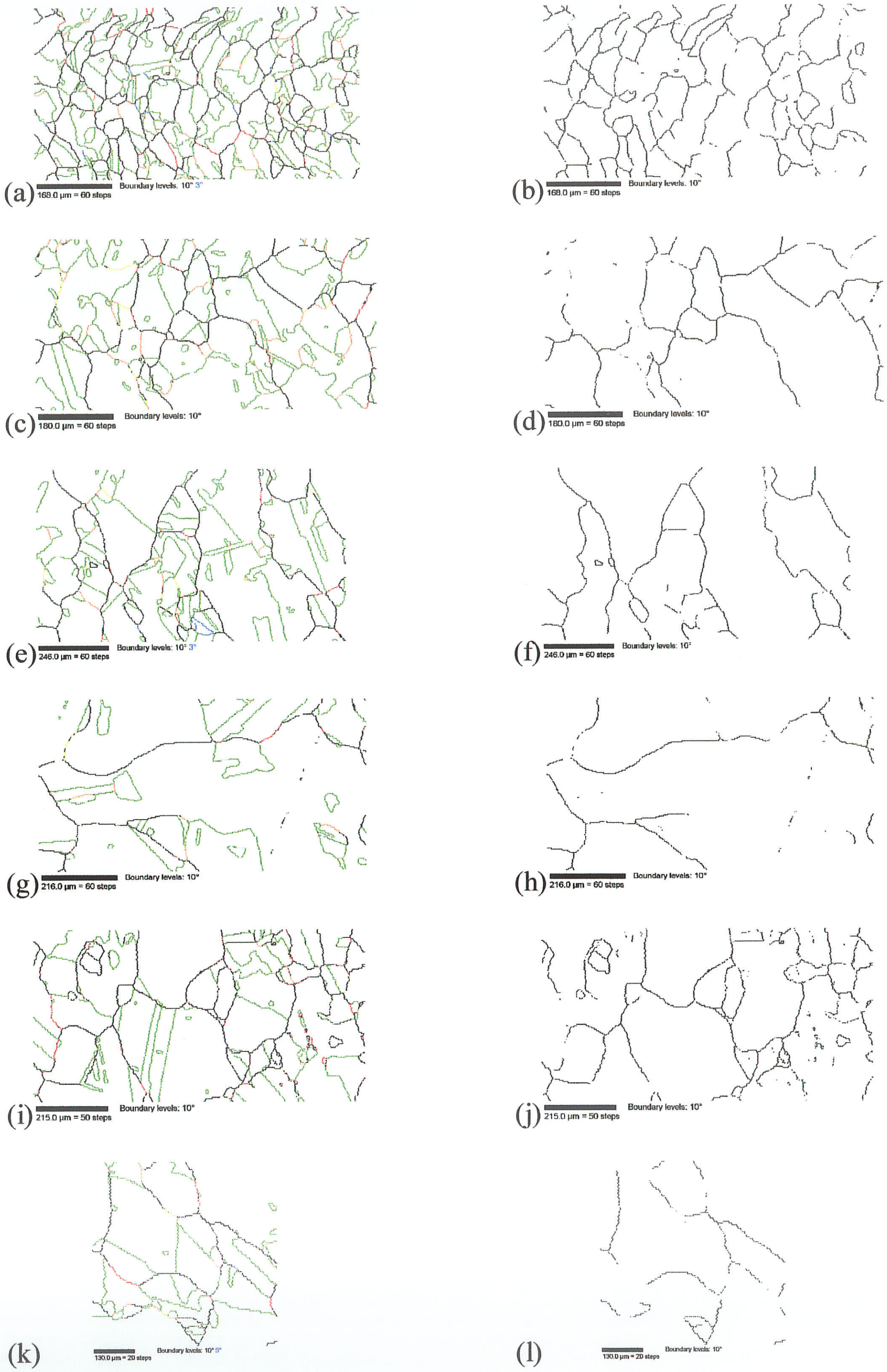

Figure 4.4.7 (a)-(l) OIM maps of samples processed 1 (a,b), 2 (c,d) , 3 (e,f), 4 (g,h), 6 (i,j), and 11 (k,l) cycles of 10% strain per cycle and annealed at 800°C each step.

It is interesting to note that the grains grew with increased number of cycles, until the 6-cycle sample where they are smaller than the 4-cycle sample, which could be attributed to recrystallization. The sharp increase in grain size from 1 to 2 cycles is interesting to note, as well as the unchanged grain size from 2 to 3 cycles which is observed in the figure below.

Perhaps the most important feature of figure 4.4.8 is the sharp decrease in Fsp which corresponds directly with another sharp increase in grain size between 3 and 4 cycles. This suggests a limiting behavior, whereby some grain growth is desirable for increasing Fsp, but beyond some point, excessive grain growth destroys special grain boundaries.

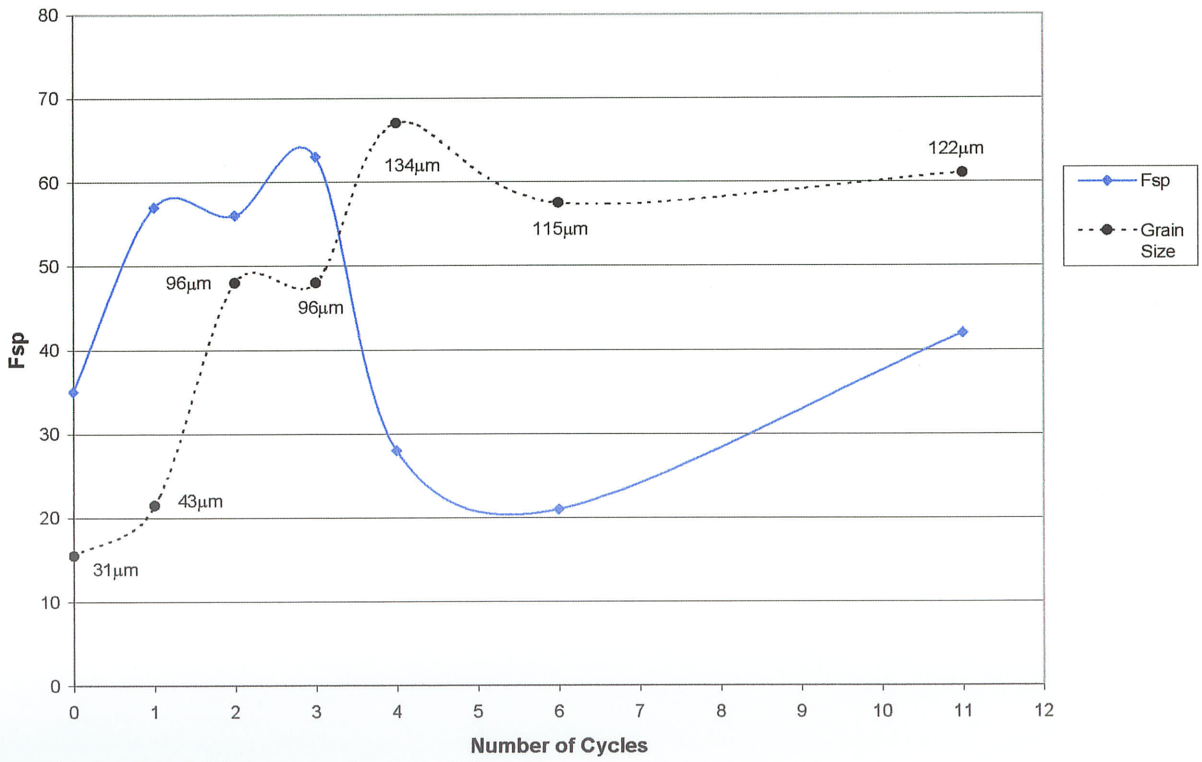

Figure 4.4.8 Grain size variation with increasing number of cycles for 10% strained and annealed at 800°C Ni-200.

Although the sample processed 11 cycles of 10% strain per cycle showed an increase in special fraction to 42%, there was insufficient data to warrant extensive study of this sample (<100 grains). Since the sample was physically very thin, several scans were performed from edge to edge of the width of the sample and the data was averaged, but still limited data was collected compared to other samples.

Observing the random boundary networks on the right had portion of figure 4.4.7 it seems as though it is being broken up somewhat as number of cycles increased from 1 to 3. Beyond three cycles, grain growth was over active and it becomes difficult to draw conclusions on the boundary structure.

The samples cold rolled 18% per cycle and annealed at 800°C contained special fractions between 38 and 58%, which are all above the as-received fraction of 35%. The changing Fsp values with increased processing is represented by the green line in figure 4.4.6, where the fraction of special boundaries increases above the as-received fraction, but then begins to decrease at 6 cycles.

OIM maps for these 18% strained and annealed samples are seen in figure 4.4.9 (a)-(j), where (a) and (b) show 1 cycle, (c) and (d) show 2 cycles, (e) and (f) show 3 cycles, (g) and (h) show 4 cycles, and (i) and (j) show 6 cycles of 18% strain and annealed at 800°C for 10 minutes. Again, the maps on the left hand side show both the random and special boundaries, while those on the right show only the random boundaries.

It is important to note that the samples processed between one and four cycles of 18% strain and 800°C anneals are all very similar. Not only are the absolute Fsp values similar, but also the random boundary networks all appear relatively undisturbed and grain sizes were all similar, measuring 42, 49, 64, and 65 μm, respectively.

Increasing the strain per cycle to 25% and using between 1 and 6 cycles did not increase the fraction of special boundaries or break up the random boundary connectivity to any appreciable extent. For this reason, they are acknowledged, but not discussed further.

In attempt to quantify the effects of strain in thermomechanical processing, a sample was annealed at 800°C for 10 minutes without prior deformation and scanned using OIM. The results showed that the fraction of special boundaries and the GBCD remained almost identical to that of the as-received state. This proved that the strain played a crucial role in manipulating the GBCD during annealing and thus the total fraction of special boundaries at 800°C.

To observe the reproducibility of GBCD from processing, three samples were independently processed 4 cycles of 18% and annealed at 800°C and scanned using OIM with the same scan dimensions. The resulting GBCDs showed that the distributions were all very similar and the Fsp values were found to be 51, 48, and 44%. This showed that results of Fsp values were reproducible within 10%.

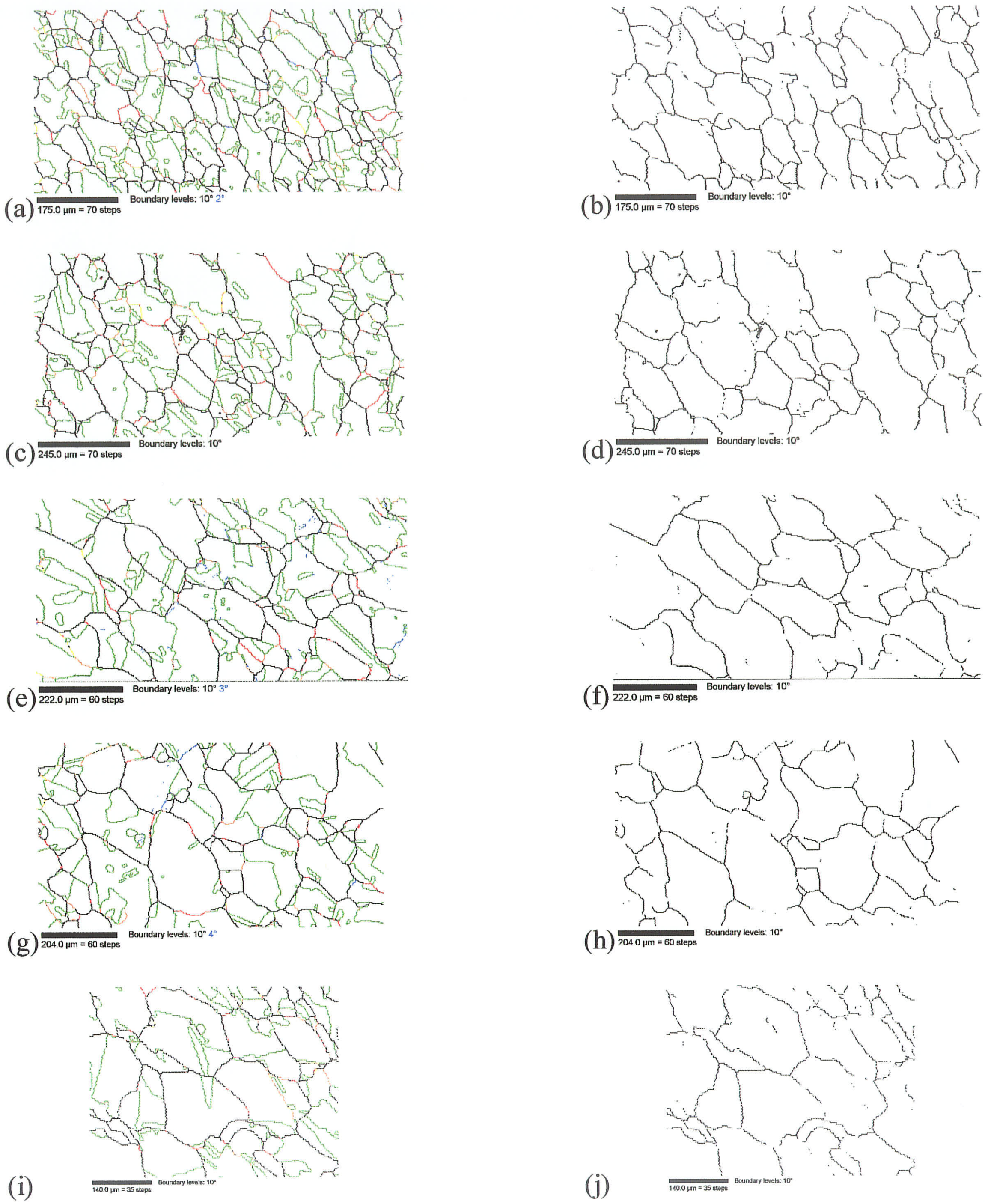

Figure 4.4.9 (a)-(j) OIM maps of samples processed 1 (a,b), 2 (c,d), 3 (e,f), 4 (g,h), and 6 (i,j) cycles of 18% strain and annealed at 800°C each step. Fsp = 58, 45, 54, 47, and 38%, respectively.

4.4.5 900°C Samples

The fraction of special boundaries for samples processed using 900°C for the annealing temperature ranged more than any other group, from 12 to 65%. Generally, the samples processed using high strain (≥20%) or high number of cycles of low strain (≤10%) resulted in low Fsp values, but those processed using low strain and low number of cycles produced some of the highest Fsp values of all experiments conducted in this research.

Considering only absolute special fractions, the samples processed 1 and 2 cycles of 5% strain and annealed at 900°C resulted in the highest Fsp values recorded of 65 and 64% special boundaries, respectively. When processing was continued further to 3 cycles, that value decreased to 43%, while 5 cycles resulted in a further decrease to 20%. This profile, along with grain sizes, was plotted and is seen as figure 4.4.11. Although Fsp values were not as high as reported by Palumbo, et al. [31] or King, et al. [53] of 70-80%, several important characteristics were observed.

It is important to note that the grain size increases with increasing Fsp, but there exists a sharp decrease in Fsp between 2 and 3 cycles, which corresponds directly with a sharp increase in grain size. This reinforces the notion that some grain growth is tolerable while increasing Fsp, as discovered with the 10%-800°C samples, but excessive amounts should be suppressed to maximize the fraction of special boundaries. The exact amounts of grain growth desired for maximum Fsp values and the mechanisms responsible for the reduction in Fsp are unclear.

To observe the effect of continued processing on the random boundary connectivity, the OIM maps have been arranged for comparison in figure 4.4.10 (a)-(h), but scale bars on the images should be noted to facilitate relative grain size comparisons. It can be seen that even the one-step processing was extremely effective at breaking up the random boundary networks through the introduction of large special boundary networks among the random boundaries.

The most impressive break-up of random boundaries in this study was seen in the sample processed 2 cycles of 5% and annealed at 900°C for 10 minutes, seen in figure 4.4.10 (c) and (d). Almost the entire left-hand portion of this map is composed of special boundaries, while the remainder contains a few fragmented random boundaries as well as many additional special boundaries.

Increasing the strain per cycle to 10% effectively increased Fsp to almost 50% in just one cycle, but further processing beyond 3 cycles decreased that value to below the as-received value of 35%. This behavior was the same for the 20% strained samples, where the fraction increased slightly to just over 40% with one cycle, but further processing decreased Fsp. The highest strain used was 25%, but both the samples processed 1 cycle and 6 cycles experienced sharp decreases in Fsp to less than 15%. None of these processing schedules that used relatively high strain were effective at breaking up the connectivity of the random boundary network either, despite some modest increases in Fsp.

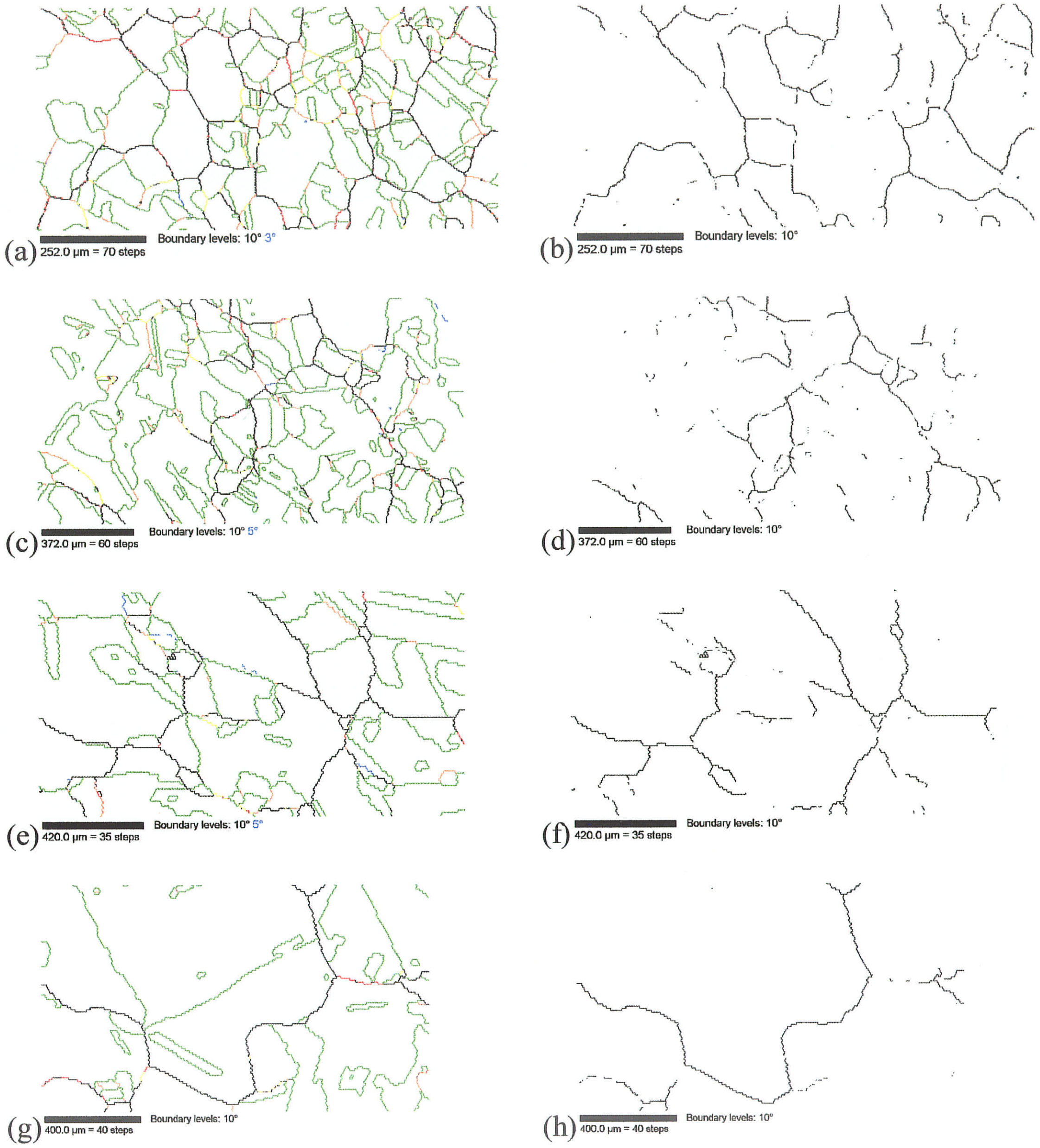

Figure 4.4.10 (a)-(h) OIM maps of samples processed 1, 2, 3, and 5 cycles of 5% strain and annealed at 900°C each step.

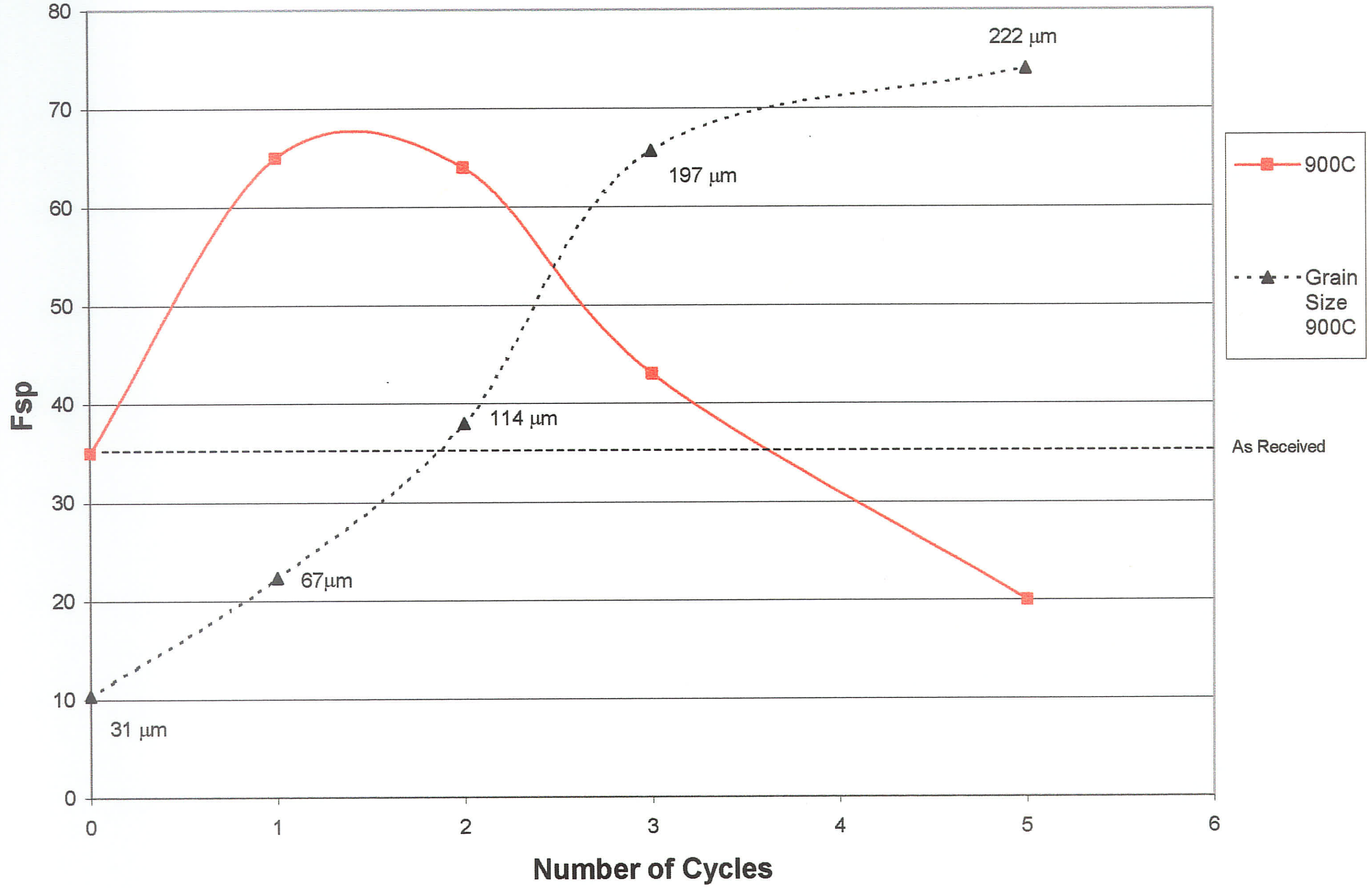

Figure 4.4.11 Fsp and grain size profiles for 5% cold rolled and annealed Ni-200.

Upon analyzing the data from the 1-cycle samples strained and annealed at 900°C, it became clear that the sample processed 1 cycle of 5% strain and annealed contained higher fraction of special boundaries than any of the other samples processed in this study. It was also seen that 1 cycle of 10% only produced an Fsp of 47%. To put this in perspective, two more samples were processed, namely 1 cycle of 2.5% and annealed at 900°C, and one annealed at 900°C with no prior strain. The OIM scans showed that the annealed only sample had a slightly lower Fsp of 30%, whereas the sample strained 2.5% had an increased Fsp of 46%, which is shown in figure 4.4.12.

Since the Fsp values were almost equal for the 2.5% and the 10% strain sample, a look at their connectivity maps revealed that the lower strain treatment was more effective at breaking up the random boundary networks than the higher strained sample. The 5% strained sample with the highest Fsp had the most fragmented random boundary network, suggesting it was the best of the one-step processed samples.

These results are quite different than those reported in the literature, especially by Palumbo, et al. who have stressed the importance of a minimum of 3 cycles, and in some cases, using even higher temperatures (up to 1050°C) and strain per cycle up to 30%. It is believed that the discrepancies are mainly due to the fact that Palumbo had used superalloys and not pure nickel. As mentioned in chapter 2, precipitates and alloying elements play important roles in the resulting strain distributions after deformation and grain boundary movement during annealing. It is possible that there are other differences, such as experimental procedures that account for the lack of agreement but further study needs to be done to provide definitive answers.

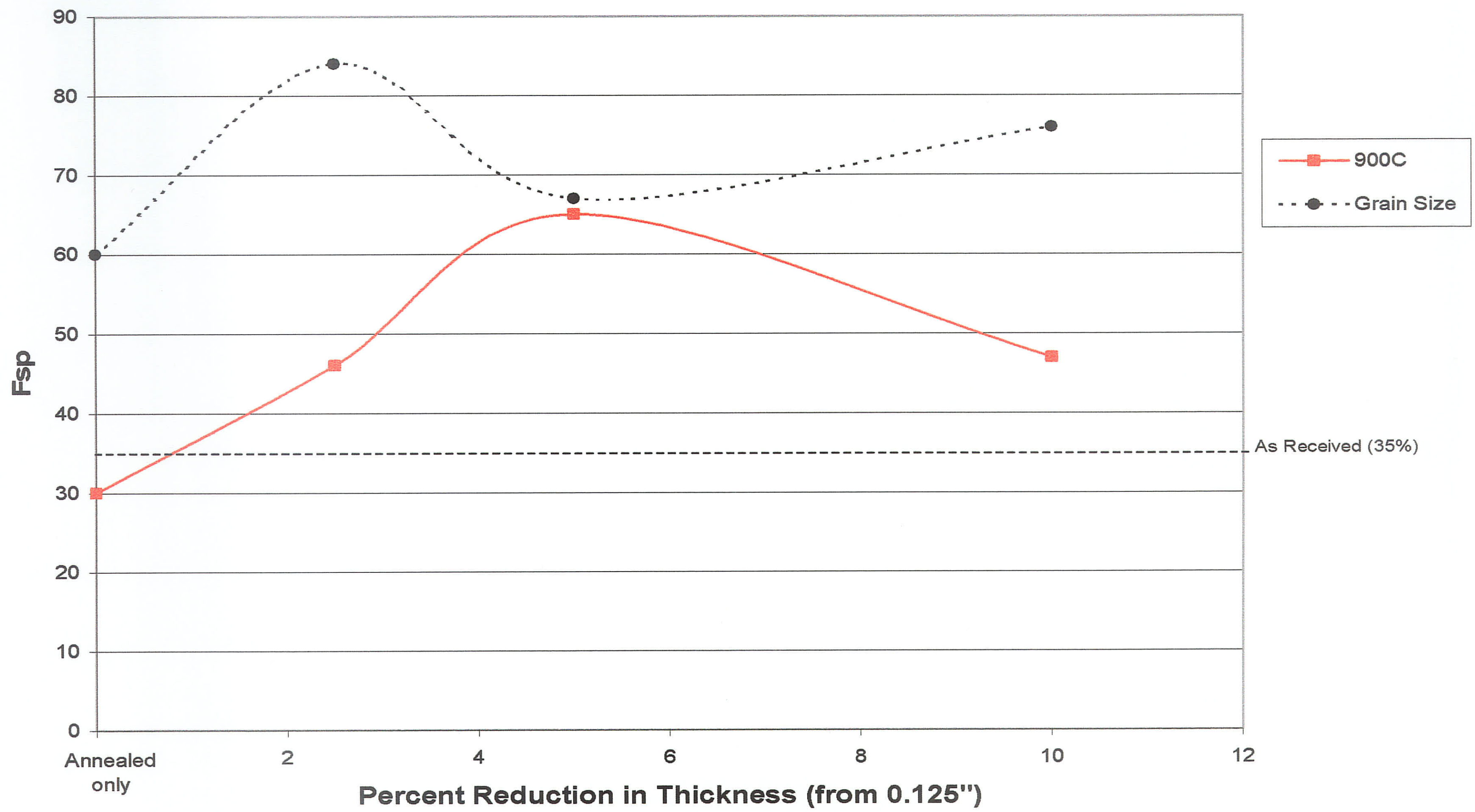

Figure 4.4.12 Fsp and grain size profiles for one-step cold rolled and annealed Ni-200.

4.4.6 Statistical Analysis of Select Experiments

The results of a subset of experiments were analyzed with the assistance of Dr. Ken Mount in the department of statistics. These nine experiments were included in section 4.4, but are extracted and repeated here to clarify the discussion (based on a 2^3 factorial design):

1) 1 x 5%+750°C Fsp = 46%
2) 5x 5%+750°C Fsp = 29%
3) 1 x 20%+750°C Fsp = 47%
4) 5 x 20%+750°C Fsp = 54%
CP) 3 x 12.5%+825°C Fsp = 31%
5) 1 x 5%+900°C Fsp = 65%
6) 5 x 5%+900°C Fsp = 20%
7) 1 x 20%+900°C Fsp = 41%
8) 5 x 20%+900°C Fsp = 22%

The objectives of the analyses were to prove that there were interactions between variables and to develop an equation to relate Fsp to the three process variables: strain, annealing temperature, and number of cycles. The figures on the following page show individual plots to show the main effects of the process variables. To determine if there were interactions among variables, plots were made with pairs of variables to observe the effects of low and high values as seen in figure 4.4.14.

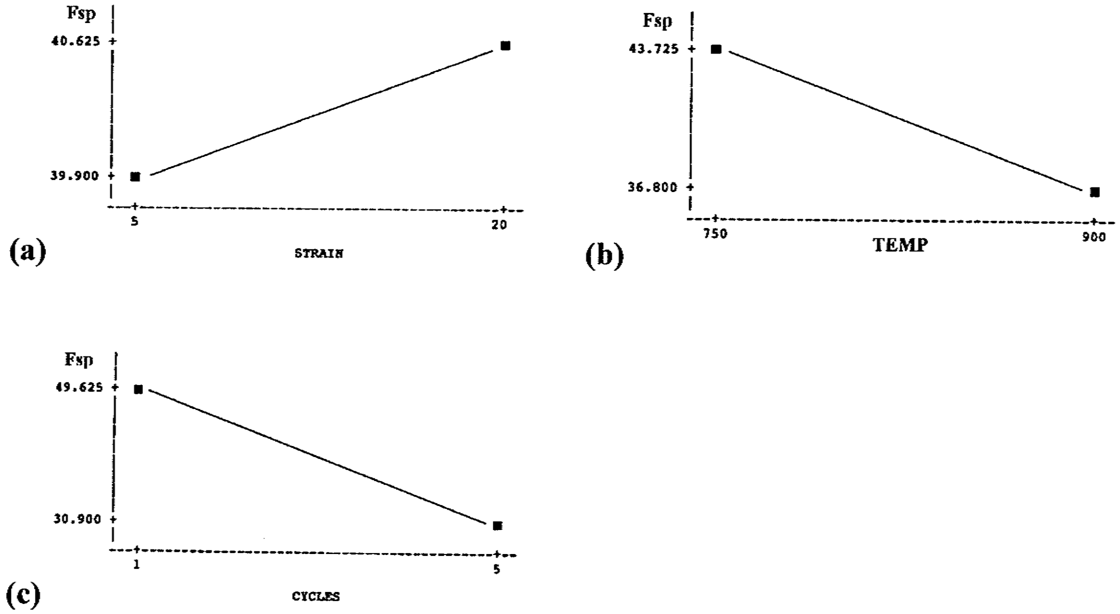

Figure 4.4.13 (a)-(c) Main effect plots for (a) strain, (b) temperature and (c) number of cycles.

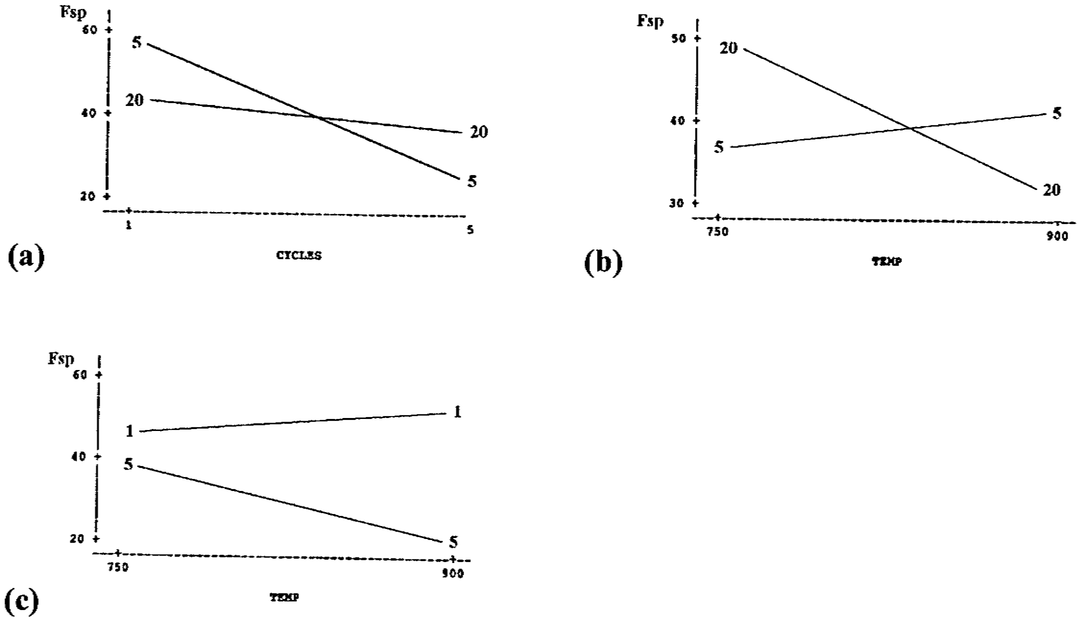

Figure 4.4.14 (a)-(c) Variable effect combinations (a) strain per cycle and number of cycles, (b) temperature and strain per cycle, and (c) number of cycles and temperature.

The main effect plots displayed in figures 4.4.13 (a)-(c) showed that relative strain had a minimal effect on Fsp, while temperature and number of cycles had a negative effect on Fsp. Since the plots in figure 4.4.14 (a)-(c) show that the lines are not parallel, there were interactions among the three variables and thus a logistical regression analysis was necessary.

Preliminary analysis of the nine experiments showed that the center point was producing data that could not be fit properly to a model and therefore, it was removed to facilitate analysis. An equation was developed to relate Fsp to the three variables without the center point:

$$\ln [Fsp/(1-Fsp)] = -6.8775 + 0.3099\varepsilon + 0.0093T + 1.2681C - 0.0004\varepsilon T - 0.0021TC + 0.0175\varepsilon C$$

Where Fsp is the fraction of special boundaries, ε is the strain per cycle, T is the annealing temperature, and C is the number of cycles. The logarithm was used to ensure the value for Fsp is between 0 and 1 since it must be a fraction. The table on the following page compares values calculated from this equation with actual values determined experimentally.

PROCESSING				
Cycles	Strain (%)	Temp. (°C)	Actual Fsp	Calc. Fsp
1	5	750	46%	48%
5	5	750	29%	28%
1	20	750	47%	58%
5	20	750	54%	63%
1	5	900	65%	67%
5	5	900	20%	19%
1	20	900	41%	55%
5	20	900	22%	30%

Table 4.4.2 Actual and calculated Fsp values.

The actual data was plotted against the calculated data for the 8 data points used for analysis as shown in figure 4.4.15 below. A linear trendline was added with the intercept set at zero and the equation was found to be:

$$(\text{Fsp actual}) = 0.8744(\text{Fsp calculated}) \qquad \text{and} \qquad r = 0.95$$

Since the correlation coefficient r is greater than 0.8, a strong correlation is present between actual and calculated values.

To determine the applicability of this equation to a wide range of processing variables, it was applied to all experiments conduced in this research. As seen in figure 4.4.16, there is a large degree of scatter and the correlation is poor between actual and calculated values. This implies that this model is limited to application in processing ranges from which it was derived.

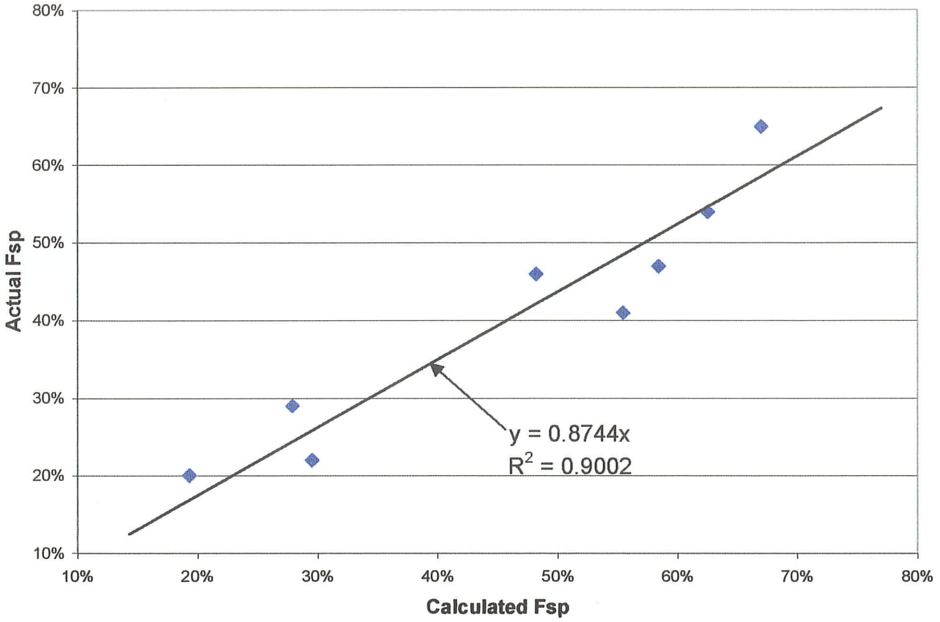

Figure 4.4.15 Plot of actual Fsp vs. calculated Fsp for 8 experiments used in analysis.

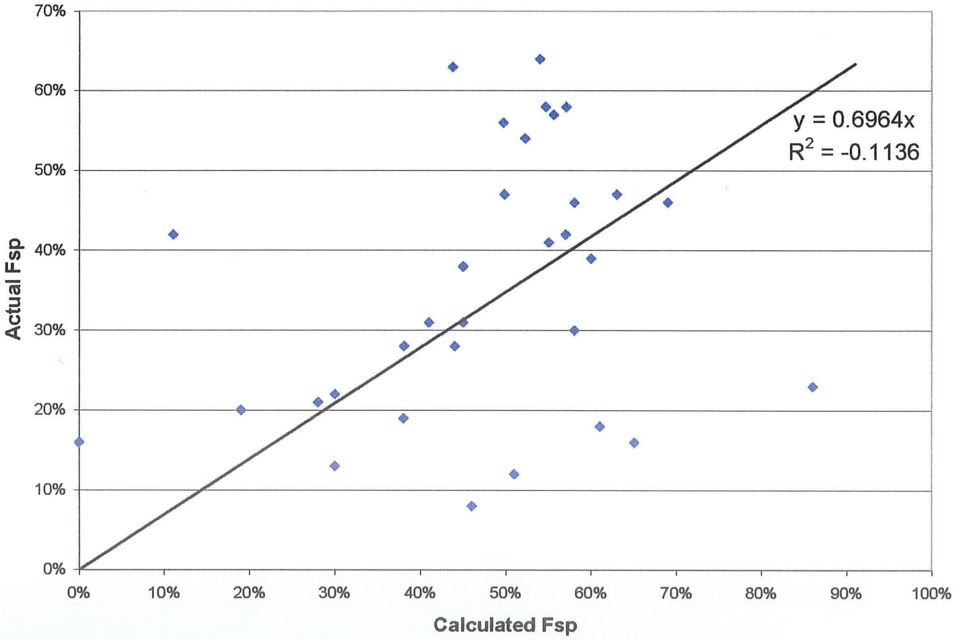

Figure 4.4.16 Plot of actual Fsp vs. calculated Fsp for all experiments.

Chapter 5 CONCLUSIONS

This study has shown that thermomechanical processing parameters must be chosen carefully to obtain desired microstructural features since they all interact with each other to complicate a fundamental understanding of the grain boundary manipulation process. By exploring a wide range of values for the three selected processing parameters, this research has shown which combinations are most effective to increase the fraction of special boundaries and fragment the random boundary connectivity in commercially pure nickel.

The most significant conclusions made in this study were as follows:

1) Recrystallization was necessary, but excessive grain growth was undesirable. It was shown that deforming the microstructure without permitting recrystallization was not an effective method of increasing the fraction of special boundaries. By increasing the annealing temperature to invoke recrystallization, effective manipulation of the GBCD was possible depending on processing variables chosen. Large increases in Fsp were usually accompanied by some grain growth, but high strain combined with high temperatures or large number of cycles always resulted in excessive grain growth and very low Fsp values.

2) Optimum processing conditions for increasing Fsp and breaking up the random boundary connectivity were:

- 2 to 20% reduction in thickness by cold rolling
- Anneal at between 750 and 900°C (for 10 minutes)
- Process between 1 and 3 cycles of sequential cold rolling and annealing

Samples with the highest Fsp in the above process ranges include: one and two cycles of 5% cold rolled and annealed at 900°C produced the highest Fsp fractions of 65 and 64% respectively, while 3 cycles of 10% cold rolled and annealed at 800°C produced an Fsp of 63% and 1 cycle of 18% and 800°C resulted in an Fsp of 58%.

3) Inverse relationship exists between strain and temperature for maximum Fsp. It was found that to produce the highest special fractions, relatively low strain levels and high temperature anneals were the most effective, but high Fsp values were also obtained by using slightly lower temperatures and higher strain levels. This implies that there exists an inverse relationship between strain per cycle and annealing temperature for maximizing Fsp. The effect of number of cycles was less profound in all of the processed samples, except for at high values (>4 cycles) where excessive grain growth usually dominated and low Fsp values were expected.

4) Fsp values were not accurate predictors of random boundary connectivity. Generally, samples with high Fsp values (>50%) contained the most severely fragmented random boundary networks, but as seen in section 4.4.3, Fsp values alone are not adequate predictors of this microstructural feature. It was found that using 5 cycles of 5% strain and annealing at 750°C resulted in an Fsp of only 29%, which was a reduction from the original 35%, but effectively broke up some of the random boundary connectivity.

5) Low strain, high temperature processing was most effective for fragmenting random boundary connectivity. The samples with the most severely disrupted random boundary connectivity were 1 and 2 cycles of 5% strain and annealed at 900°C. It is important to note, however, that by using higher strain per cycle and lower temperatures was not as effective at breaking up the random boundary connectivity, despite large increases in Fsp up to 63%.

6) Process variable contributions and interactions are complex. From the wide optimum ranges for the process variables reported in this study, it is clear that several combinations are possible to result in a large number of unique processing schedules. Many of these are capable of producing similar GBCDs and absolute Fsp values, which complicates an understanding of individual process variable contributions. This also suggests the possibility of different mechanisms of grain boundary interaction are operative during annealing of a highly strained sample at low temperatures and a low strained sample at high temperatures since similar GBCDs result. There are likely several 'optimum' process schedules, depending on the desired GBCD, grain size, and other microstructural characteristics. This shows that the process variable interactions are complex, even for the simplified study of a pure metal with only three variables.

7) Results do not agree with literature. Many processing schedules reported by Palumbo, et al. involved much higher strain and annealing temperatures, along with an increased number of cycles, while resulting in a metal with a fine grained microstructure and Fsp values over 70%. It is believed that the lack of agreement was a result of the markedly different materials being used by Palumbo, et al., which included more complex alloys such as alloys 625, and V-57. Since the processing of pure metals for grain boundary design was found to be quite complex in this study, contrasting results from alloys is futile. A controlled study of pure metals and alloys together is required for a meaningful analysis and discussion.

8) An equation for Fsp as a function of the three variables was developed:

$$\ln [Fsp/(1-Fsp)] = -6.8775 + 0.3099\varepsilon + 0.0093T + 1.2681C$$

$$- 0.0004\varepsilon T - 0.0021TC + 0.0175\varepsilon C$$

Where Fsp is the fraction of special boundaries, ε is the strain per cycle by cold rolling (%), T is the annealing temperature (°C), and C is the number of cycles. It was found that this equation could reasonably predict the Fsp for the data from which it was derived, however the error became extremely large when applied to many other experiments conducted in this research.

It is believed that the ranges of variables used in the analysis were too large for accurate modeling since it is possible that different metallurgical mechanisms were operative under different processing conditions. Upper and lower bounds should also be placed on the ranges of variables in the above equation since it does not account for excessive grain growth or non-recrystallized samples which both result in abnormally low Fsp values.

Chapter 6 SUGGESTIONS FOR FUTURE WORK

It was the aim of this research on nickel to serve as a baseline for future work on more complex alloys, such as Inconel 718. Future studies could benefit from this work by studying the effects of alloying and precipitates on final microstructural characteristics.

The large number of interacting material and processing variables combines to create an extremely complex experiment. The three variables studied in this research were chosen since they were some of the most influential on the final microstructure. It is known that the initial microstructure and composition of the material, as well as the straining and the annealing conditions all play important roles in the final GBCD and microstructure.

The effect of the initial material composition should be studied to determine the effects of precipitate and solute concentrations and distributions. The initial grain size could play an important role in the recrystallization behavior and should be considered. These factors contribute to the resulting strain distributions and the grain boundary migration behavior during annealing.

The straining conditions can also have large impacts on the microstructural characteristics of processed materials. The strain method, rate, and temperature should be examined to observe effects of strain distribution on final GBCD. This study looked only at cold rolling, however compression or tension could also be used. Altering the cold rolling parameters, such as the roller friction or roller speed would likely have an effect on results as well.

Annealing variables, such as heating rate, temperature, time, cooling rate, and atmosphere should be considered. Depending on the material composition, an initial solution heat treat would likely play an important role in the solute and precipitate distribution and resulting grain boundary movement and interaction during annealing.

Property testing should be performed on materials with different fractions of special boundaries to quantify the effects of GBCD and random boundary connectivity. Corrosion, creep and fatigue testing would provide valuable information on which microstructural features are most important for property improvements.

REFERENCES

1. WATANABE, TADAO
"An Approach to Grain Boundary Design for Strong and Ductile Polycrystals"
Res Mechanica, Vol. 11, pp. 47-84, 1984

2. DIETER, G.E.
"Mechanical Metallurgy" 2nd Edition
McGraw-Hill, 1976

3. HAASEN, PETER
"Physical Metallurgy" 2nd Edition
Cambridge University Press, 1986

4. DOHERTY, R.D., HUGHES, D.A., HUMPHREYS, F.J., JONAS, J.J., JUUL JENSEN, D., KASSNER, M.E., KING, W.E., McNELLEY, T.R., McQUEEN, H.J., and ROLLETT, A.D.
"Current Issues in Recrystallization: A Review"
Materials Science and Engineering, A238, pp. 219-274, 1997

5. Metals Handbook, **"Recrystallization"**, pp.259-268, ASM, Metals Park, Ohio, 1948.

6. BUCHANAN, P.J., RANDLE, V., and FLEWITT, P.E.J.
"A Simple Procedure for the Assessment of Plastic Strain in Electron Back-Scatter Diffraction Patterns"
Scripta Materialia, Vol. 37, No. 10, pp. 1511-1518, 1997

7. AVRAMI, M.
Journal of Physical Chemistry, Vol. 7, p. 1103, 1939

8. DOHERTY, R.D., KASHYAP, K, and PANCHANADEESWARAN, S.
"Direct Observation of the Development of Recrystallization Texture in Commercial Purity Aluminum"
Acta Metallurgica et Materialia, Vol. 41, No. 10, pp. 3029-3053, Oct. 1993

9. RADHAKRISHNAN, B., SARMA, G.B., and ZACHARIA, T.
"Modeling the Kinetics and Microstructural Evolution During Static Recrystallization"
Acta Materialia, Vol. 46, No. 12, pp. 4415-4433, July 1998

10. CLINCH, M.R., HARRIS, S.J., HEPPLES, W., HOLROYD, N.J.H., and WOOD, J.V.
"The Effect of Small Particles During Recrystallization of Cold Worked AA6061 and AA7032 Aluminum Alloys"
Materials Science Forum, Vol. 331-337, pp. 861-866, 2000

11. PALUMBO, G. and AUST, K.T.
"Solute Effects in Grain Boundary Engineering"
Canadian Metallurgical Quarterly, Vol. 34, No. 3, pp. 165-173, 1995

12. AUST, K.T., and RUTTER, J.W.
"Grain Boundary Migration in High-Purity Lead and Dilute Lead-Tin Alloys"
Transactions of the Metallurgical Society of AIME, Vol. 215, pp. 119-127, Feb. 1959

13. HORTON D., THOMSON, C.B, and RANDLE, V.
"Aspects of Twinning and Grain Growth in High Purity and Commercially Pure Nickel"
Materials Science and Engineering, A203, pp. 408-414, 1995

14. WATANABE, TADAO
"Grain Boundary Design and Control for High Temperature Materials"
Materials Science and Engineering, A166, pp. 11-28, 1993

15. RANDLE, V. and HORTON, D.
"Grain Growth Phenomena in Nickel"
Scripta Metallurgica et Materialia, Vol. 31, No. 7, pp. 891-895, 1994

16. THAVEEPRUNGSRIPORN, V. and WAS, G.S.
"Grain Boundary Properties of Ni-16Cr-9Fe at 360°C"
Scripa Materialia, Vol. 35, No. 1, pp. 1-8, 1996

17. WAS, G.S., THAVEEPRUNGSRIPORN, V., and CRAWFORD, D.C.
"Grain Boundary Misorientation Effects on Creep and Cracking in Ni-Based Alloys"
JOM, pp.44-49, Feb. 1998

18. THAVEEPRUNGSRIPORN, V. and WAS, G.S.
"The Role of Coincidence-Site-Lattice Boundaries in Creep of Ni-16Cr-9Fe at 360°C"
Metallurgical and Materials Transactions A, Vol. 28A, pp. 2101-2112, Oct. 1997

19. CRAWFORD, D.C. and WAS, G.S.
"The Role of Grain Boundary Misorientation in Intergranular Cracking of Ni-16Cr-9Fe in 360°C Argon and High-Purity Water"
Metallurgical Transactions A, Vol. 23A, pp. 1195-1205, April 1992

20. ALEXANDREANU, BOGDAN, CAPELL, BRENT, AND WAS, GARY S.
"Combined effect of special grain boundaries and grain boundary carbides on IGSCC of Ni-16Cr-9Fe-xC alloys"
Materials Science and Engineering, A300, pp. 94-104, 2001

21. WATANABE, TADAO
"Grain Boundary Sliding and Stress Concentration During Creep"
Metallurgical Transactions A, Vol. 14A, pp. 531-545, April 1983

22. WATANABE, TADAO
"The Potential for Grain Boundary Design in Materials Development"
Materials Forum, Vol. 11, pp. 284-303, 1988

23. WATANABE, TADAO
"Grain Boundary Design for Desirable Mechanical Properties"
Journal de Physique, Vol. 49, Symposium C5, pp. 507-516, Oct. 1988

24. LIM, L.C., and WATANABE, TADAO
"Fracture Toughness and Brittle-Ductile Transition Controlled by Grain Boundary Character Distribution (GBCD) in Polycrystals"
Acta Metallurgica et Materialia, Vol. 38, No. 12, pp. 2507-2516, 1990

25. WATANABE, TADAO
"The Importance of Grain Boundary Character Distribution (GBCD) to Recrystallization, Grain Growth and Texture"
Scripta Metallurgica et Materialia, Vol. 27, pp. 149-1502, 1992

26. WATANABE, TADAO
"The Impact of Grain Boundary Character Distribution on Fracture in Polycrystals"
Materials Science and Engineering, A176, pp. 39-49, 1994

27. WATANABE, TADAO, and TSUREKAWA, SADAHIRO
"The Control of Brittleness and Development of Desirable Mechanical Properties in Polycrystalline Systems by Grain Boundary Engineering"
Acta Materialia, Vol. 47, No. 15, pp. 4171-4185, 1999

28. THOMSON, C.B., and RANDLE, V.
"A Study of Twinning in Nickel"
Scripta Materialia, Vol. 35, No. 3, pp. 385-390, 1996

29. RANDLE, V.
"Mechanism of Twinning-Induced Grain Boundary Engineering in Low Stacking-Fault Energy Materials"
Acta Materialia, Vol. 47, No. 15, pp. 4187-4196, 1999

30. PANDE, C.S., IMAM, M.A., and RATH, B.B.
"Study of Annealing Twins in FCC Metals and Alloys"
Metallurgical Transactions A, Vol. 21A, pp. 2891-2896, Nov. 1990

31. LEHOCKEY, E.M., PALUMBO, G., and LIN, P.
"Improving the Weldability and Service Performance of Nickel- and Iron-Based Superalloys by Grain Boundary Engineering"
Metallurgical and Materials Transactions A, Vol. 29A, pp. 3069-3079, Dec. 1998

32. **"Recrystallization, Grain Growth and Textures"**
Papers presented at a Seminar of the American Society for Metals, October 16 and 17, 1965.

33. BRANDON, D.G.
"The Structure of High-Angle Grain Boundaries"
Acta Metallurgica, Vol. 14, pp. 1479-1484, Nov. 1966

34. WARRINGTON, D.H., and BOON, M.
"Ordered Structures in Random Grain Boundaries; Some Geometrical Probabilities"
Acta Metallurgica, Vol. 23, pp. 599-607, May 1975

35. KRONBERG, M.L., and WILSON, F.H.
"Secondary Recrystallization in Copper"
Metals Transactions, Vol. 185, pp. 501-514, Aug. 1949

36. MEYERS, M.A., and CHAWLA, K.K.
"Mechanical Metallurgy: Principles and Applications"
Prentice Hall, New Jersey, 1984

37. RANDLE, V.
"The Effects of Thermomechanical Processing on Interfacial Crystallography in Metals"
Materials Science Forum, Vol. 294-296, pp.51-58, 1999

38. RANDLE, V.
"Refined Approaches to the Use of the Coincidence Site Lattice"
JOM, pp.56-59, Feb. 1998

39. THOMSON, C.B., and RANDLE, V.
"Fine Tuning at $\Sigma 3^n$ Boundaries in Nickel"
Acta Materialia, Vol. 45, No.12, pp. 4909-4916, 1997

40. RANDLE, V.
"A Methodology for Grain Boundary Plane Assessment by Single-Section Trace Analysis"
Scripta Materialia, Vol. 44, pp. 2789-2794, 2001

41. PALUMBO, G., AUST, K.T., LEHOCKEY, E.M., ERB, U., and LIN, P.
"On a More Restrictive Geometric Criterion for "Special" CSL Grain Boundaries"
Scripta Materialia, Vol. 38, No. 11, pp. 1685-1690, 1998

42. MAHAJAN, S., PANDE, C.S., IMAM, M.A., and RATH, B.B.
"Formation of Annealing Twins in f.c.c. Crystals"
Acta Materialia, Vol. 45, No. 6, pp.2633-2638, 1997

43. KUMAR, MUKUL, KING, WAYNE E., and SCHWARTZ, ADAM J.
"Modifications to the Microstructural Topology in F.C.C. Materials Through Thermomechanical Processing"
Acta Materialia, Vol. 48, pp. 2081-2091, 2000

44. SCHUH, CHRISTOPHER A., KUMAR, MUKUL, and KING, WAYNE, E.
"Analysis of Grain Boundary Networks and Their Evolution During Grain Boundary Engineering"
Acta Materialia, Vol. 51, pp.687-700, 2003

45. ROMERO, R.J. and MURR, L.E.
"Torque-related Lamellar Carbide Growth Associated with Annealing Twins in 304 Stainless Steel"
Acta Metallurgica et Materialia, Vol. 43, No.2, pp. 461-469, 1995

46. PALUMBO, G. and AUST, K.T.
"Solute Effects in Grain Boundary Engineering"
Canadian Metallurgical Quarterly, Vol. 34, No. 3, pp. 165-173, 1995

47. GINDRAUX, G., and FORM, W.
"New Concepts of Annealing-Twin Formation in Face-Centered Cubic Metals"
Journal of the Institute of Metals, Vol. 101, pp. 85-93, 1973

48. AUST, K.T., and PALUMBO, G.
"Interface Control in Metals"
Structure and Property Relationship for Interfaces, J.L.W. Wallis, et. al (eds)
ASM 1991, p.3

49. PALUMBO, G., LEHOCKEY, E.M., and LIN, P.
"Applications for Grain Boundary Engineered Materials"
JOM, pp. 40-43, Feb. 1998

50. LIN, P., PALUMBO, G., ERB, U., and AUST, K.T.
"Influence of Grain Boundary Character Distribution on Sensitization and Intergranular Corrosion of Alloy 600"
Scripta Metallurgica et Materialia, Vol. 33, No. 9, pp. 1387-1392, 1995

51. GUO, H., CHATURVEDI, M.C., RICHARDS, N.L., and McMAHON, G.S.
"Interdependence of Character of Grain Boundaries, Intergranular Segregation of Boron and Grain Boundary Liquation in Simulated Weld Heat-Affected Zone in Inconel 718"
Scripta Materialia, Vol. 40, No. 3, pp. 383-388, 1999

52. PALUMBO, G., LEHOCKEY, E.M., and LIN, P.
"Applications for Grain Boundary Engineered Materials"
JOM, pp. 40-43, Feb. 1998

53. KING, WAYNE E., and SCHWARTZ, ADAM J.
"Toward Optimization of the Grain Boundary Character Distribution in OFE Copper"
Scripta Materialia, Vol. 38, No. 3, pp. 449-455, 1998

54. SCHWARTZ, ADAM J. and KING, WAYNE E.
"The Potential Engineering of Grain Boundaries Though Thermomechanical Processing"
JOM, pp.50-55, Feb. 1998

55. ASM International, **"Alloy Digest"**, downloaded from www.asminternational.com

56. SCHWARTZ, A.J., KUMAR, M., and ADAMS, B., Editors
"Electron Backscatter Diffraction in Materials Science"
Kluwer Academic/Plenum Publishers, 2000

57. TSL website: **www.tsl-oim.com**

58. Japan Electron Optics Laboratory Ltd. (JEOL) website: **www.JEOL.com**

59. DINGLEY, D.J. and RANDLE, V.
Review: "Microtexture Determination by Electron Back-Scatter Diffraction"
Journal of Materials Science, Vol. 27, pp. 4545-4566, 1992

60. ALEXANDREANU, BOGDAN, and WAS, GARY S.
"A priori determination of the sampling size for grain-boundary character distribution and grain-boundary degradation analysis"
Philosophical Magazine A, Vol. 81, No. 8, pp. 1951-1965, 2001

61. KUMAR, MUKUL, SCHWARTZ, ADAM J., and KING, WAYNE E.
"Microstructural Evolution During Grain Boundary Engineering of Low to Medium Stacking Fault Energy Materials"
Acta Materialia, Vol. 50, pp. 2599-2612, 2002

APPENDIX A

DPH Microhardness Plots

Figure A1 - DPH Microhardness of Cold Rolled and Annealed Ni-200 (Constant Temperature Lines)

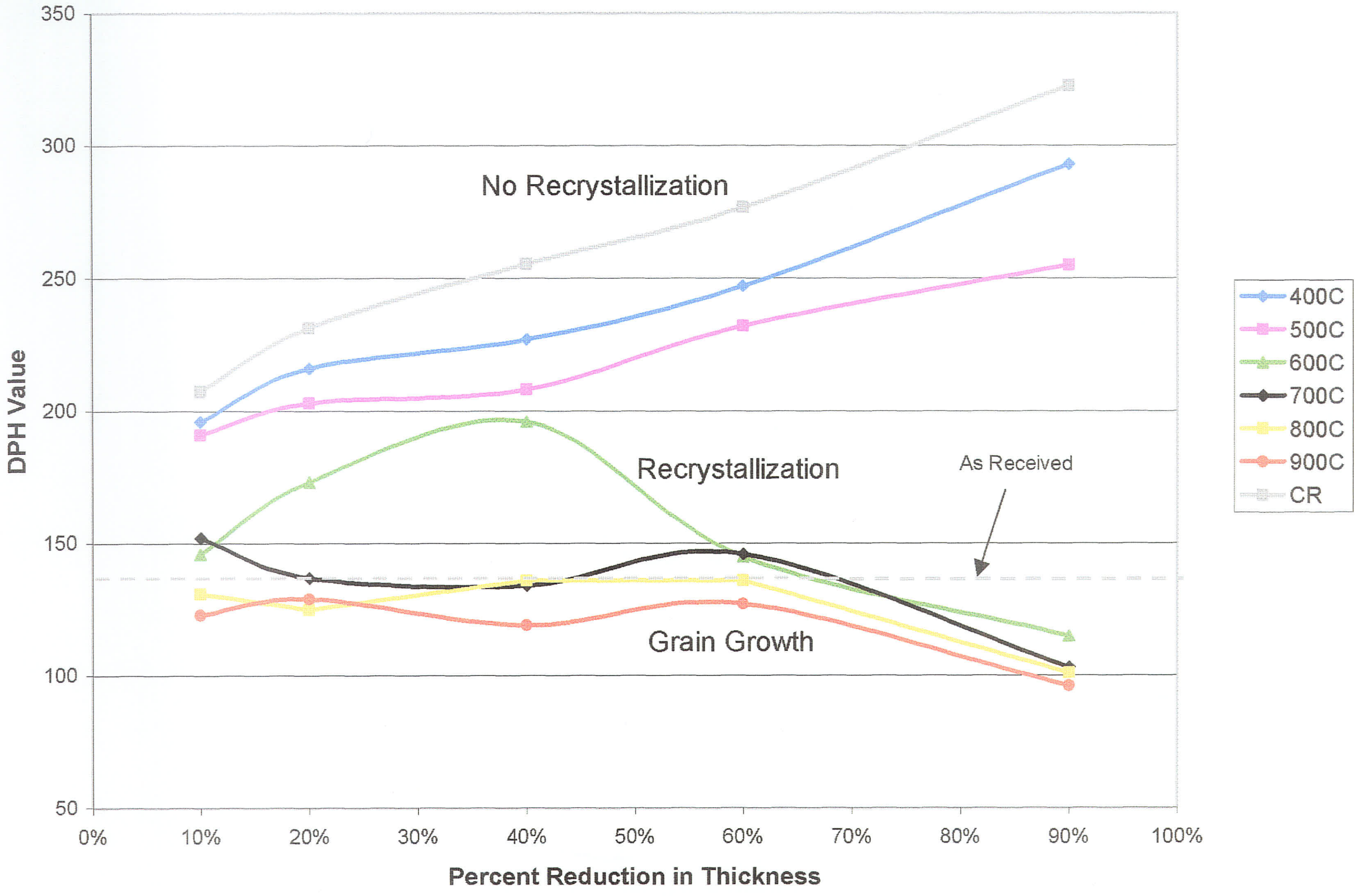

Figure A2 - DPH Microhardness of Cold Rolled and Annealed Ni-200 (Constant Strain Lines)

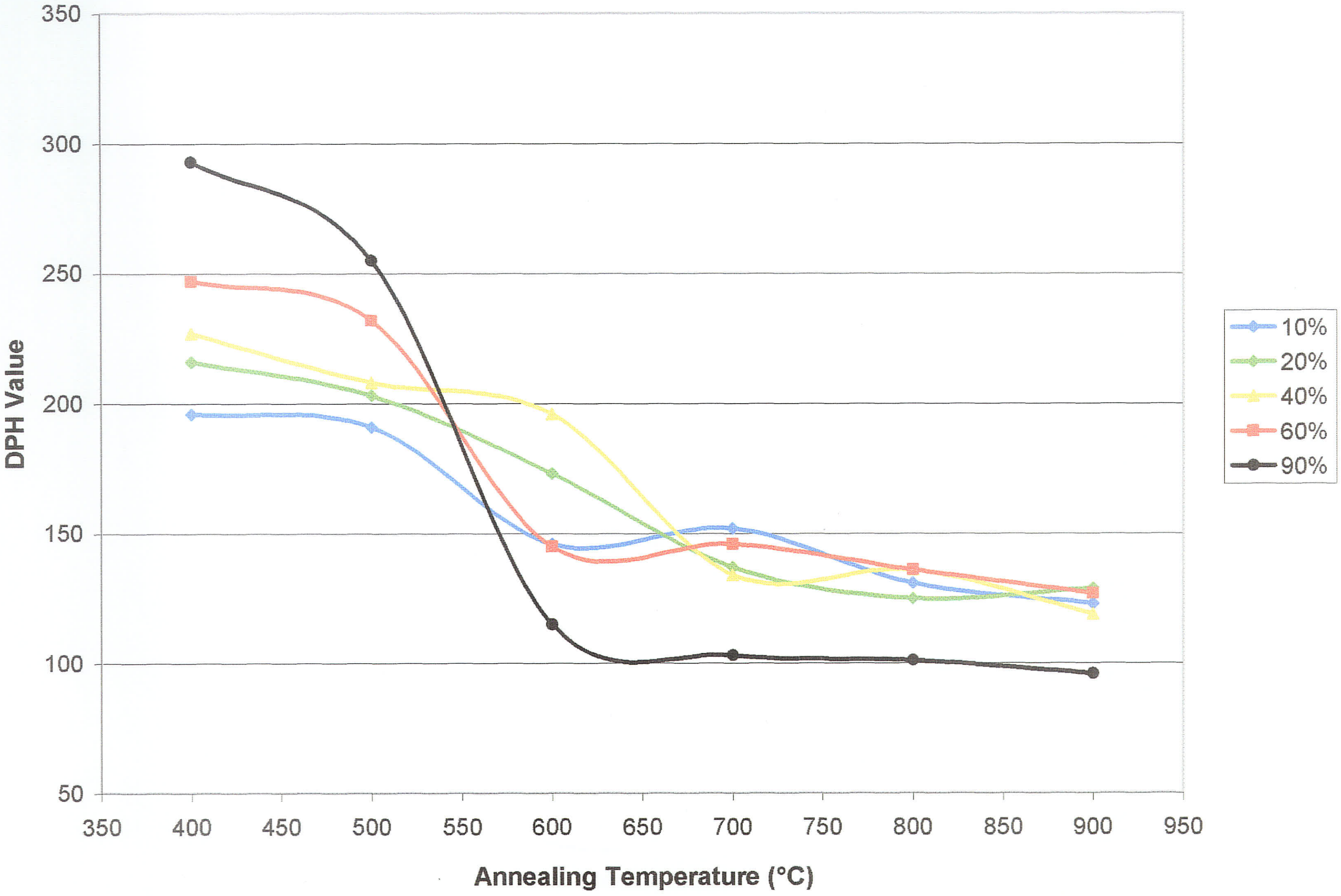

Figure A3 - DPH Microhardness Profiles for Cold Rolled Ni-200

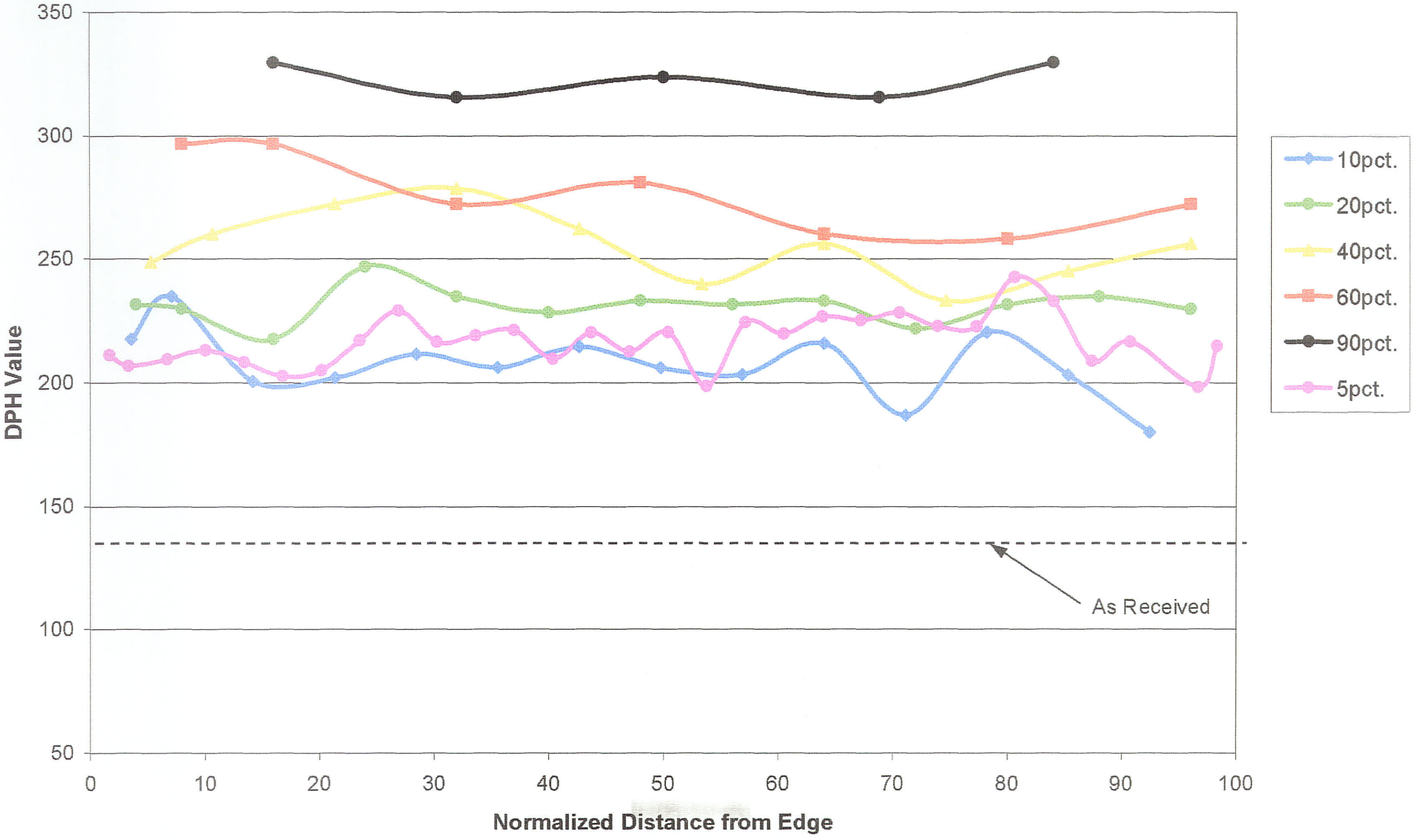

Figure A4 - Cold Rolled Hardness as a Function of Increasing Reduction in Thickness of Ni-200

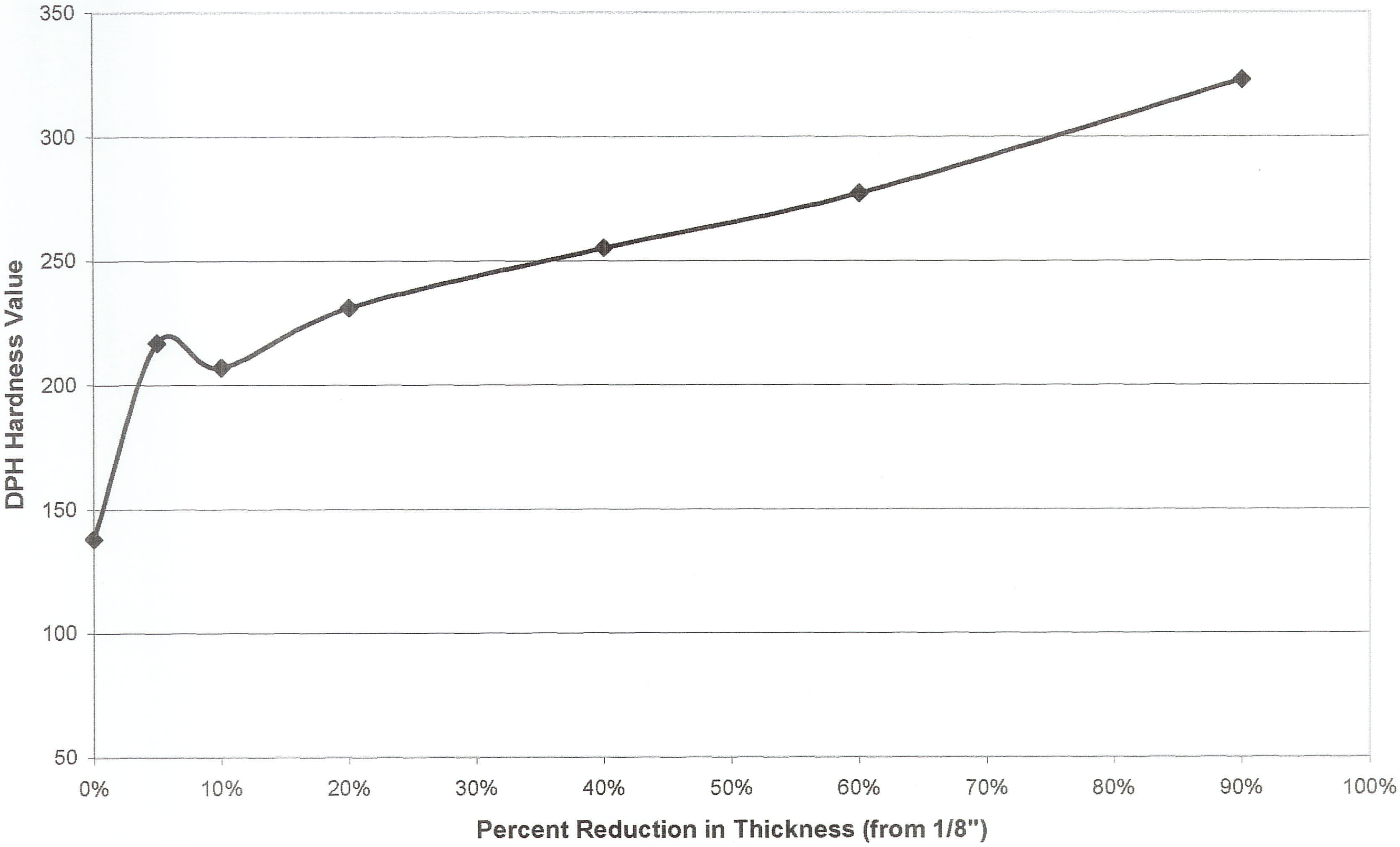

Figure A5 - DPH Microhardness of 10% Cold Rolled and Annealed Ni-200

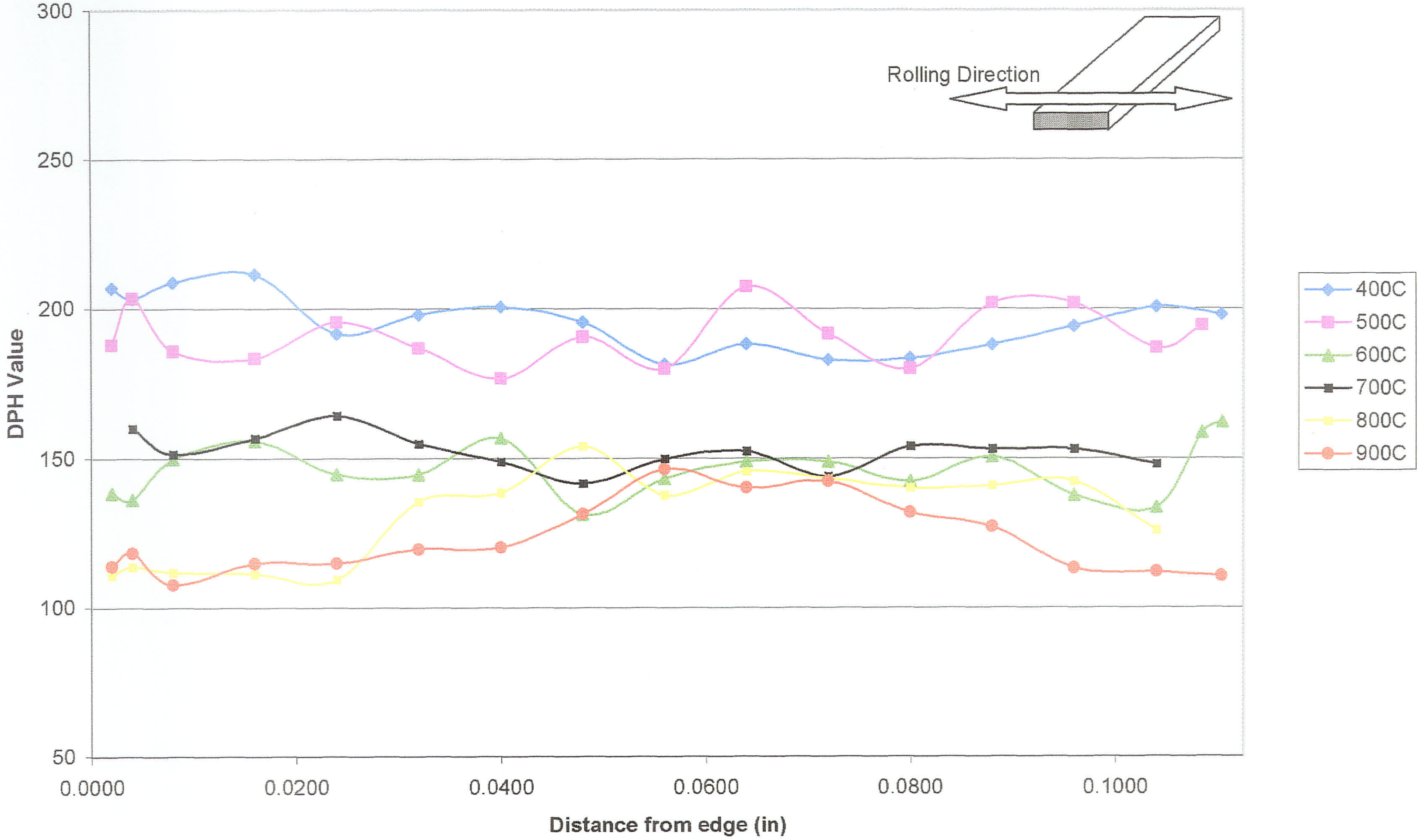

Figure A6 - DPH Microhardness of 20% Cold Rolled and Annealed Ni-200

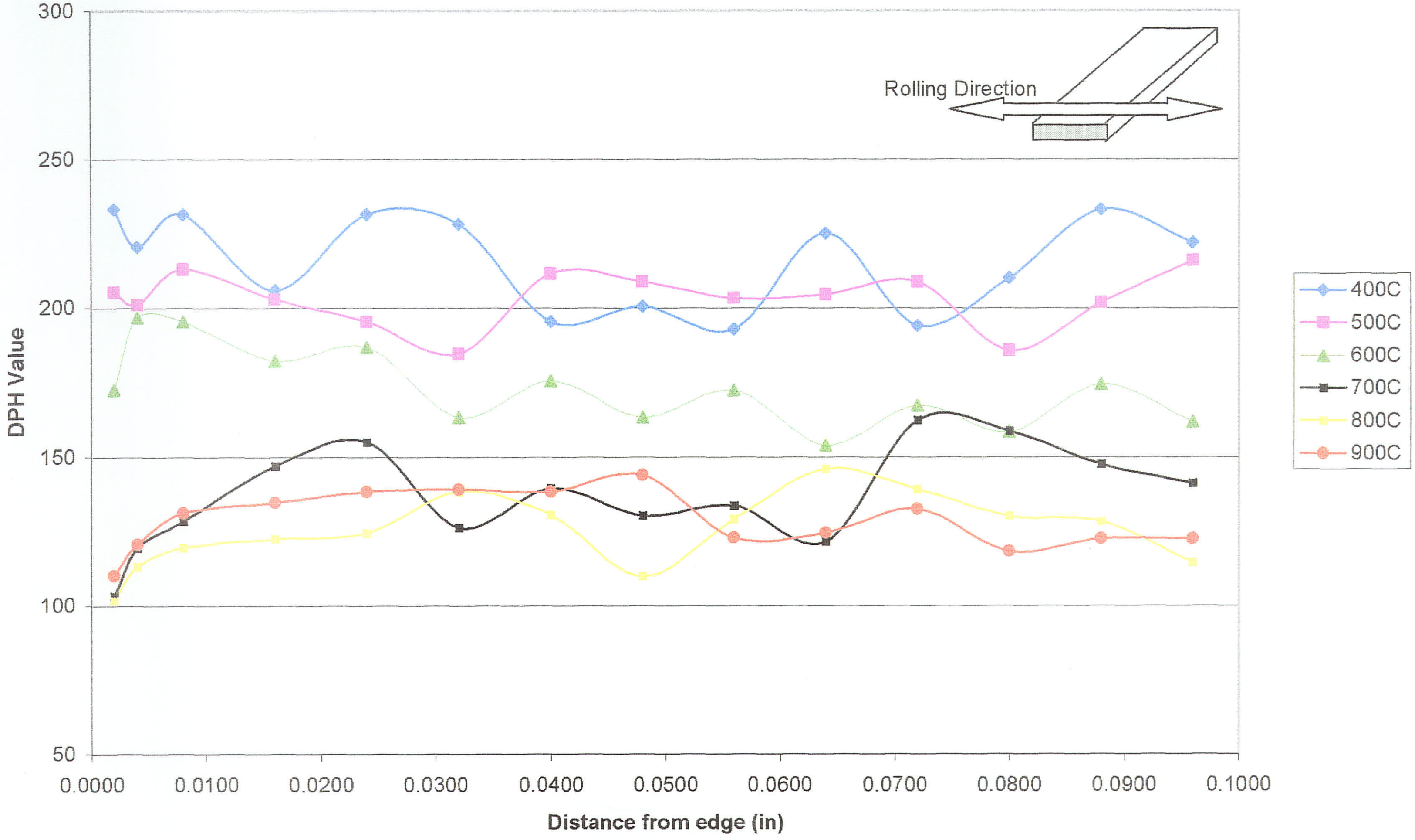

Figure A7 - DPH Microhardness of 40% Cold Rolled and Annealed Ni-200

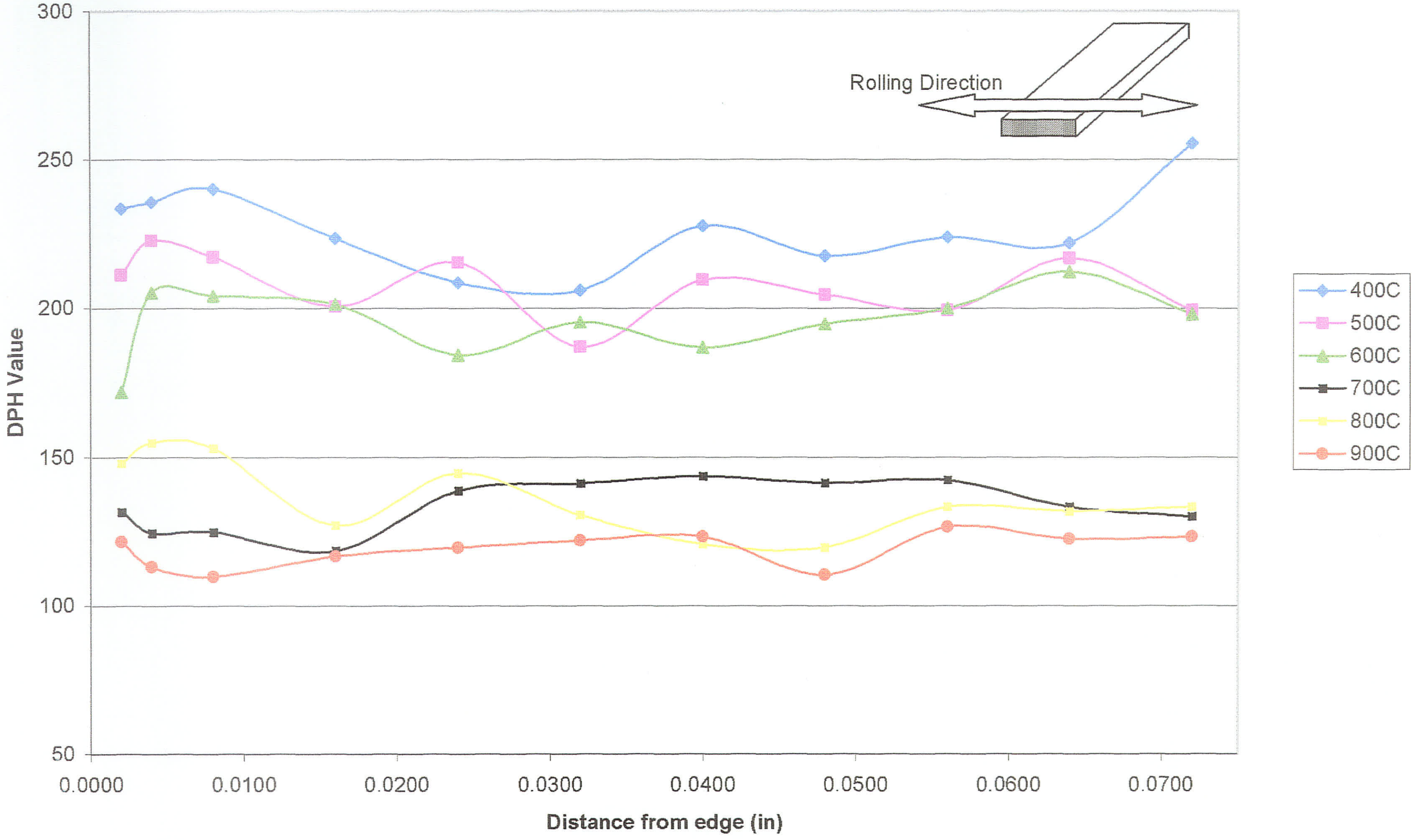

Figure A8 - DPH Microhardness of 60% Cold Rolled and Annealed Ni-200

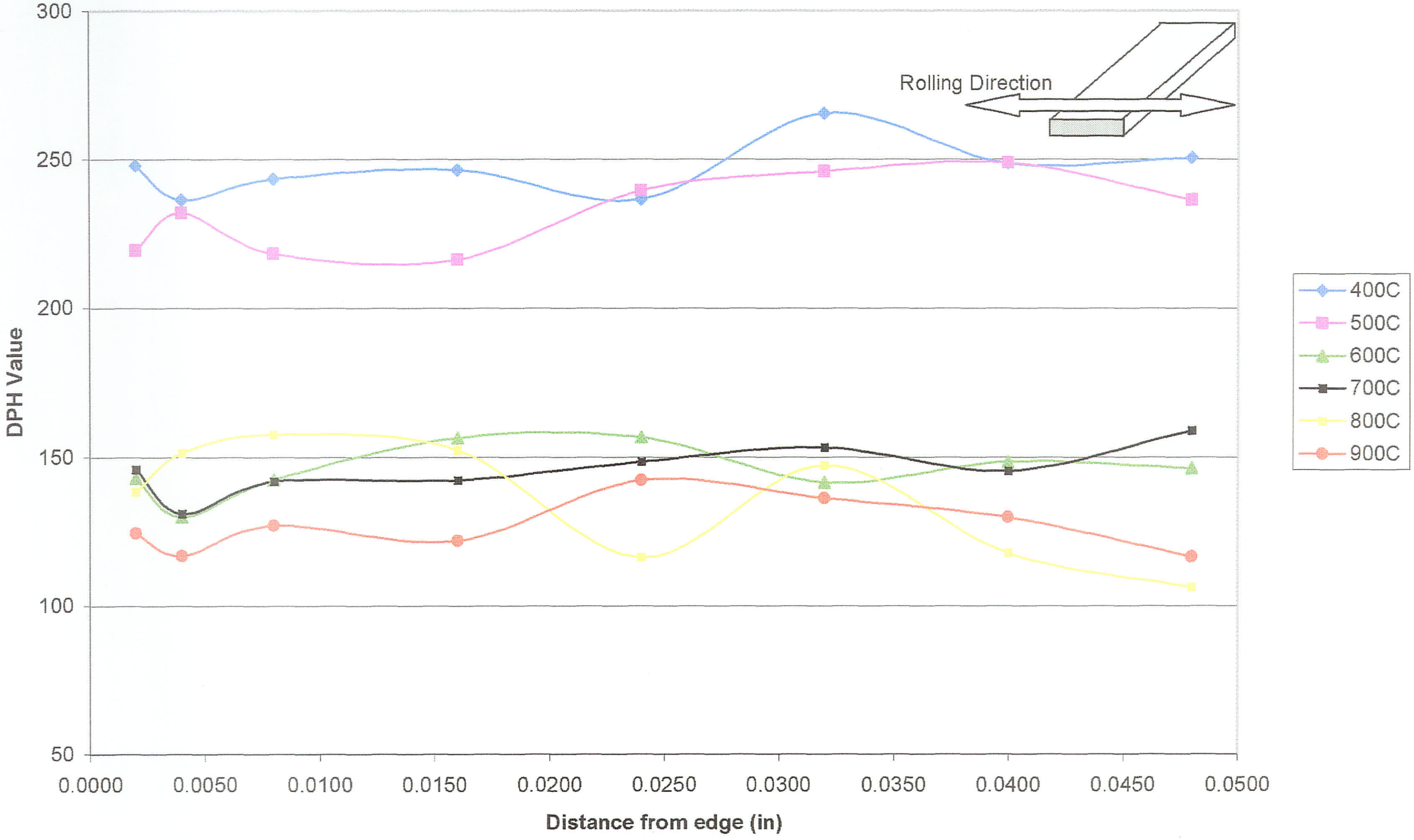

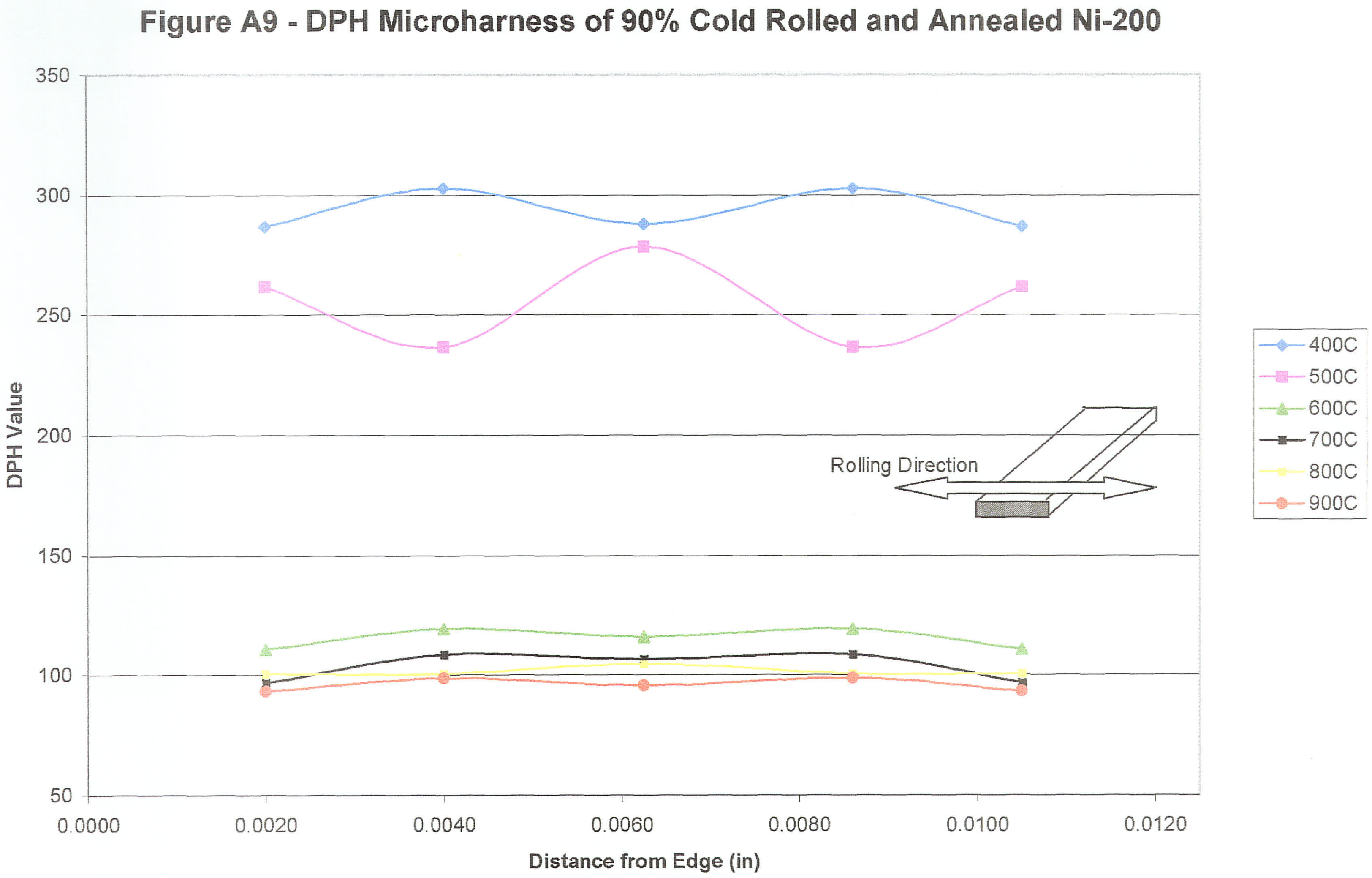
Figure A9 - DPH Microharness of 90% Cold Rolled and Annealed Ni-200
DPH Value
350
300
250
200
150
100
50
0.0000
0.0020
0.0040
0.0060
0.0080
0.0100
0.0120
Distance from Edge (in)
400C
500C
600C
700C
800C
900C
Rolling Direction

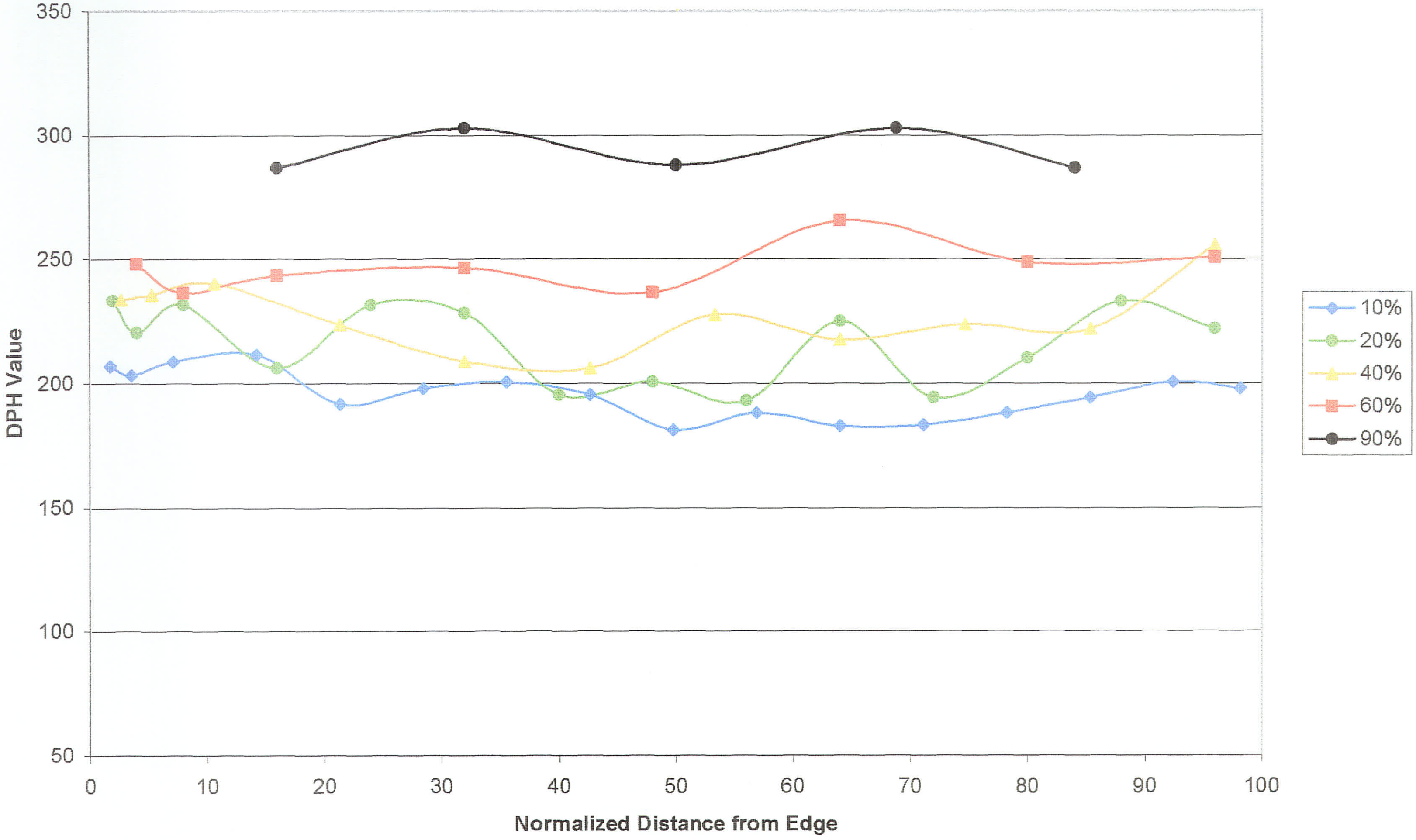

Figure A10 - Cold Rolled and Annealed at 400°C Ni-200

Figure A11 - Cold Rolled and Annealed at 500°C Ni-200

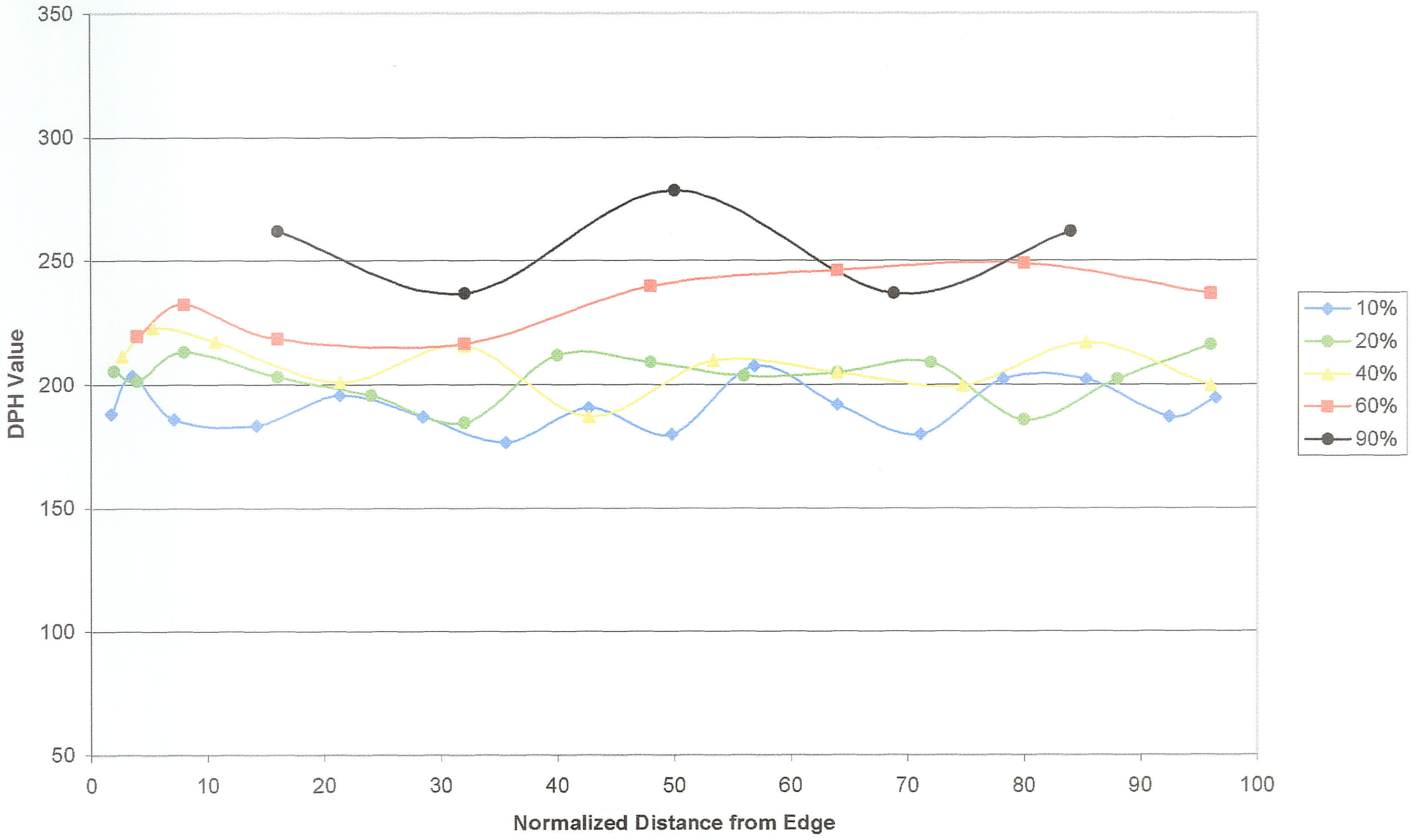

Figure A12 - Cold Rolled and Annealed at 600°C Ni-200

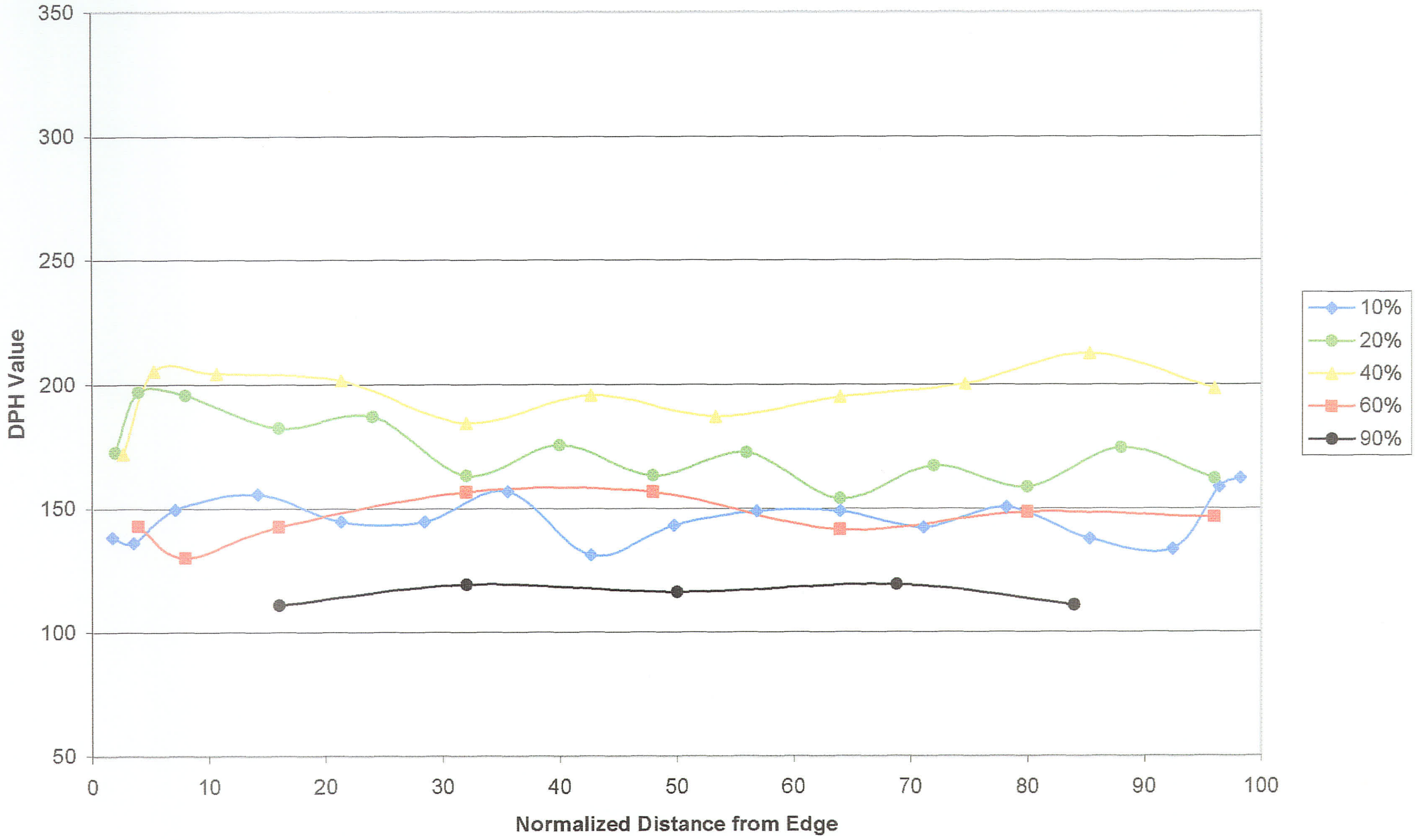

Figure A13 - Cold Rolled and Annealed at 700°C Ni-200

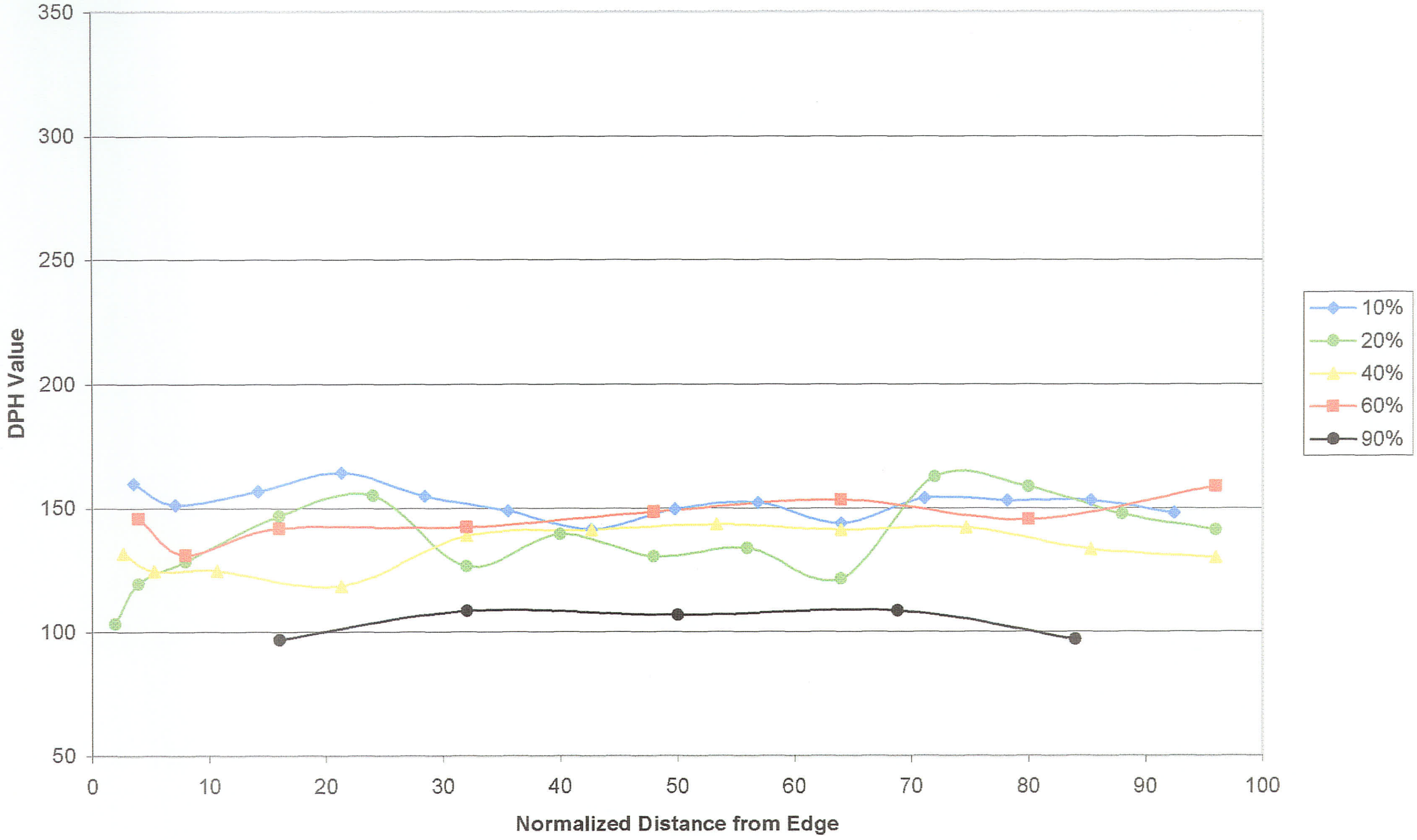

Figure A14 - Cold Rolled and Annealed at 800°C Ni-200

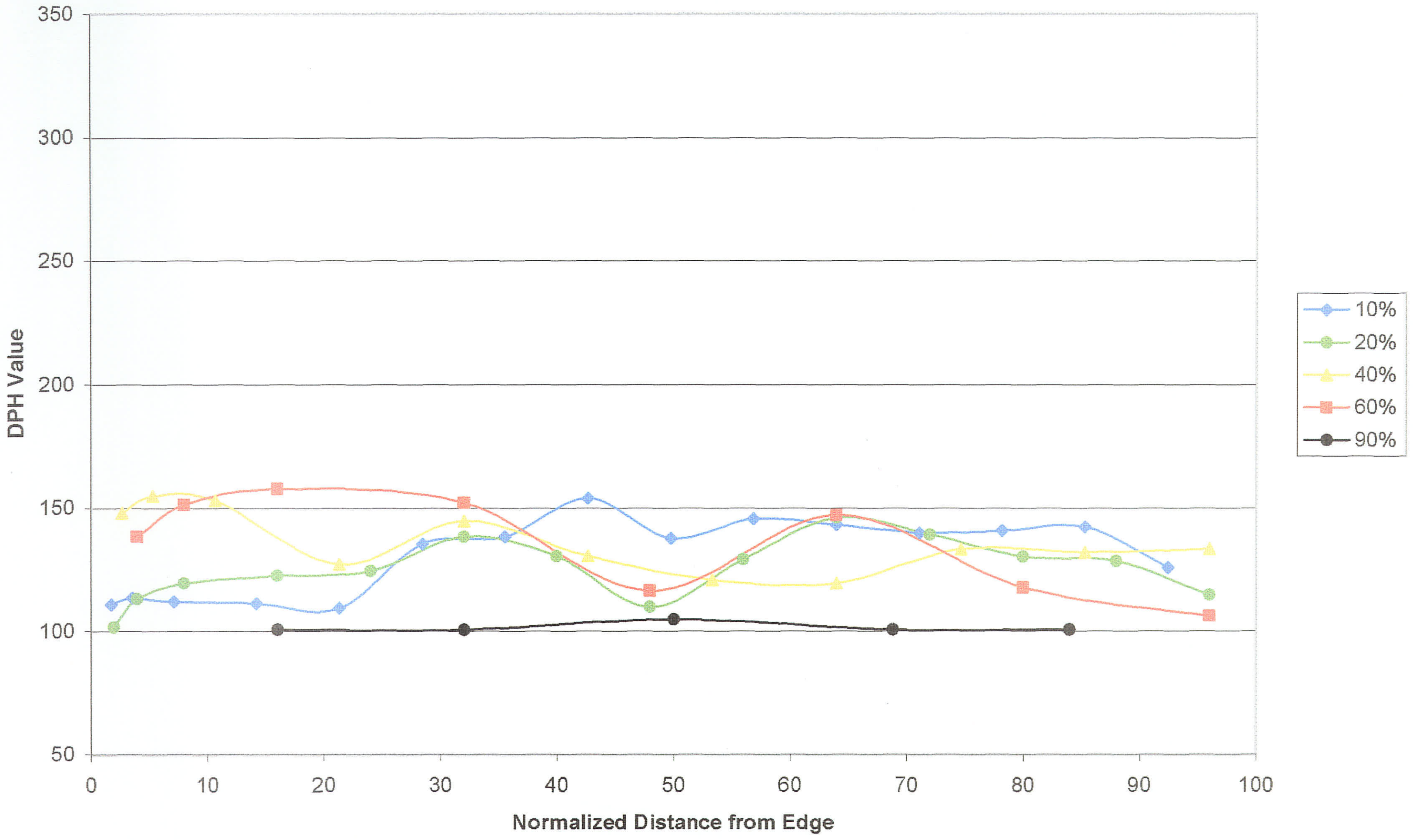

Figure A15 - Cold Rolled and Annealed at 900°C Ni-200

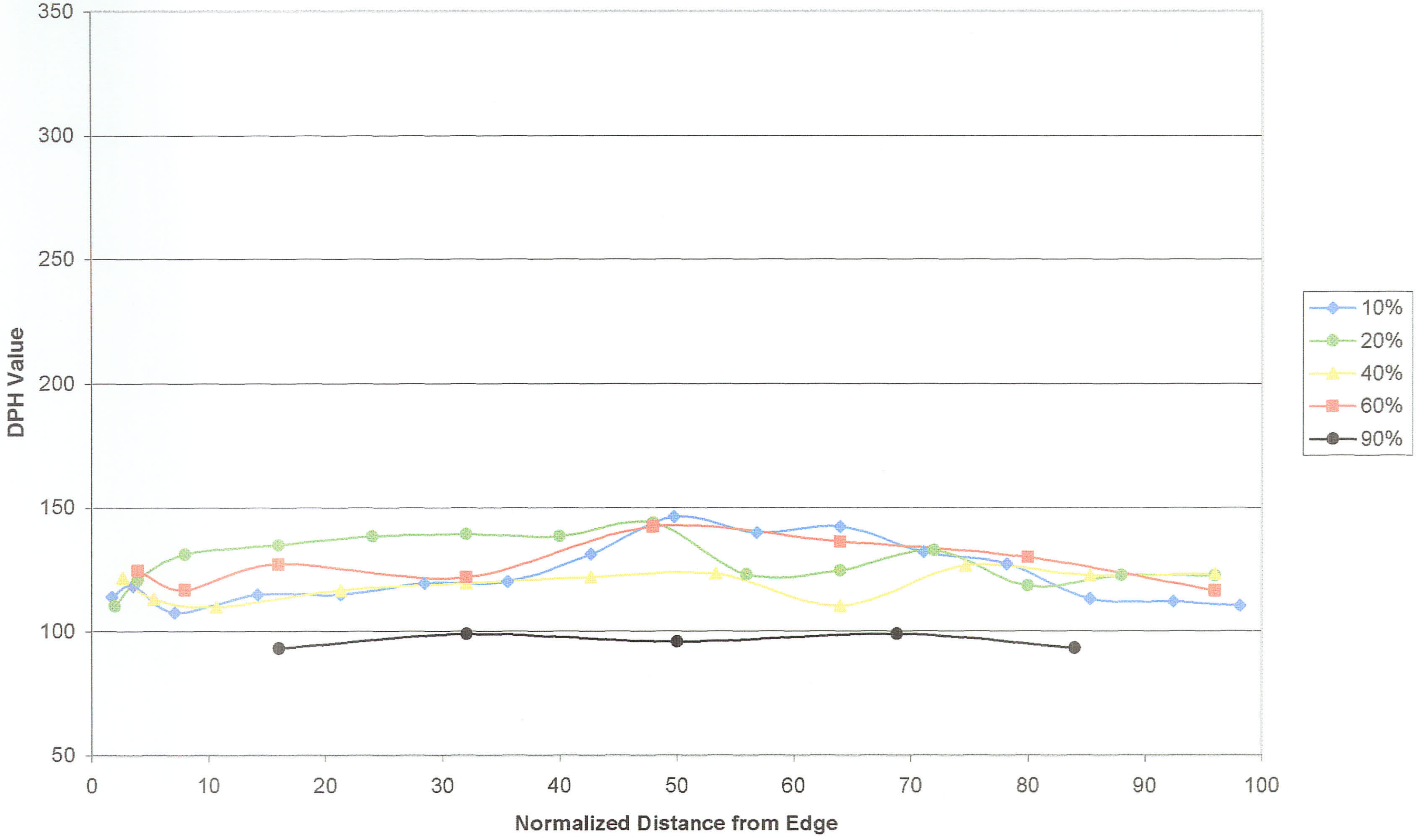

APPENDIX B

Selected Optical Micrographs

Fig. B1 - 10% Cold Rolled

Fig. B2 - 20% Cold Rolled

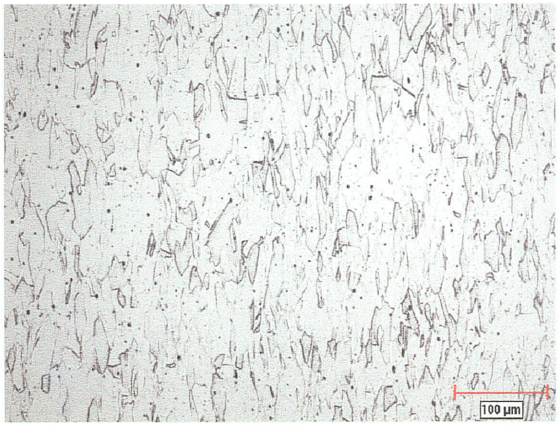

Fig. B3 - 40% Cold Rolled

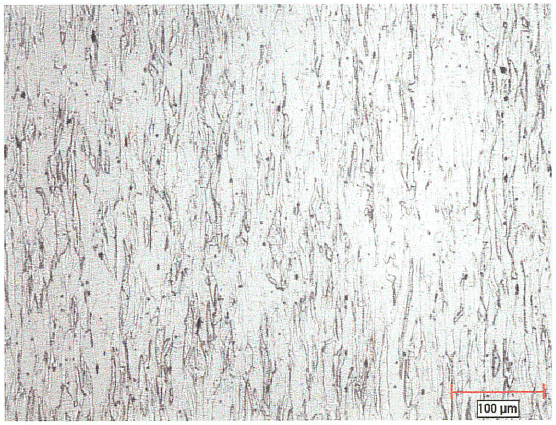

Fig. B4 - 60% Cold Rolled

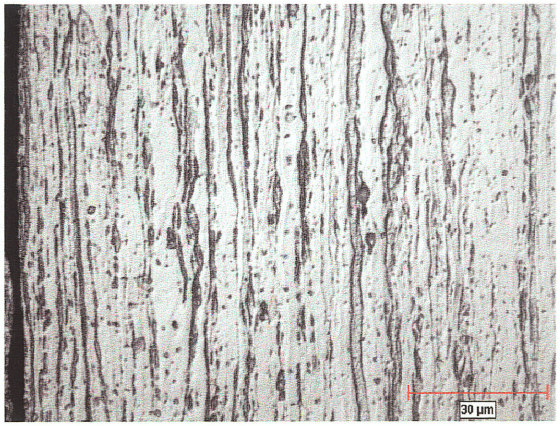

Fig. B5 - 90% Cold Rolled

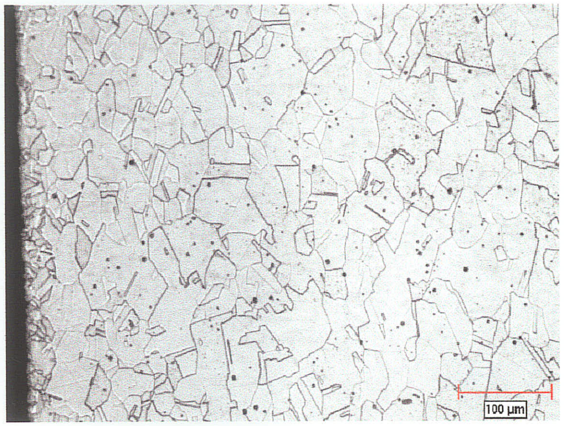

Fig. B6 – C/R 10% - 400°C

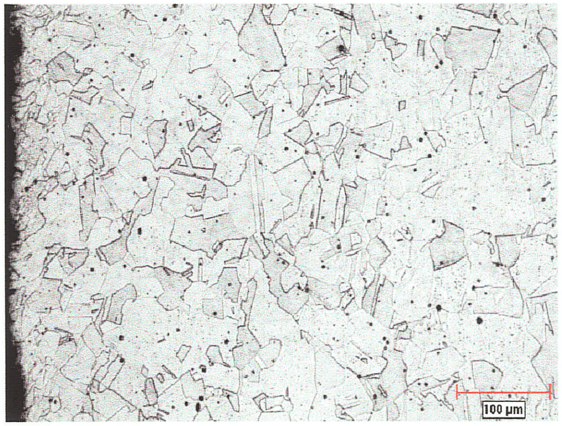

Fig. B7 - C/R 10% - 500°C

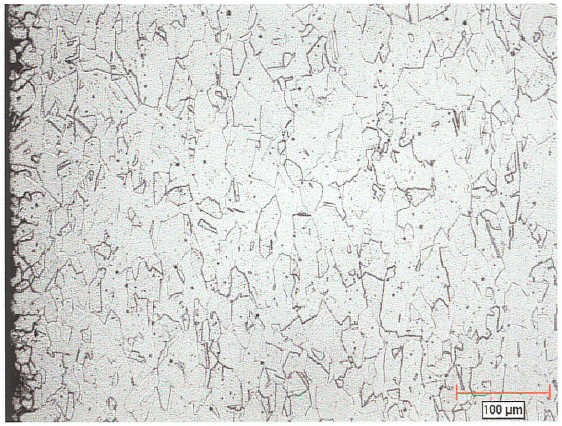

Fig. B8 - C/R 10% - 600°C

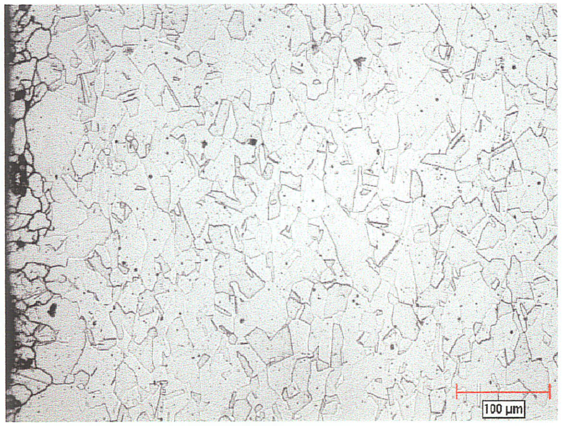

Fig. B9 - C/R 10% - 700°C

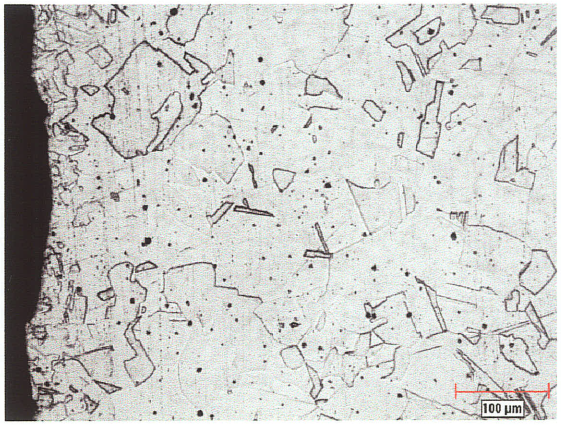

Fig. B10 - C/R 10% - 800°C

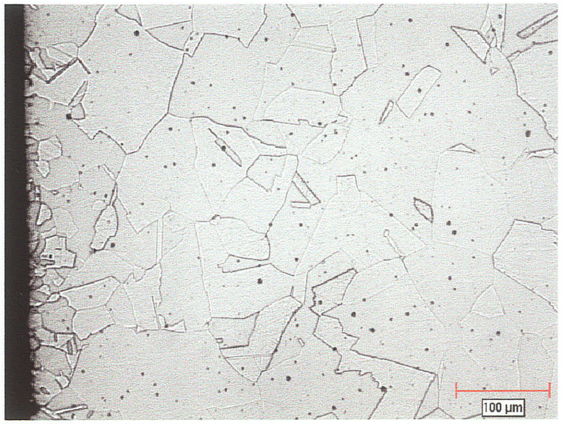

Fig. B11 - C/R 10% - 900°C

Fig. B12 - C/R 20% - 400°C

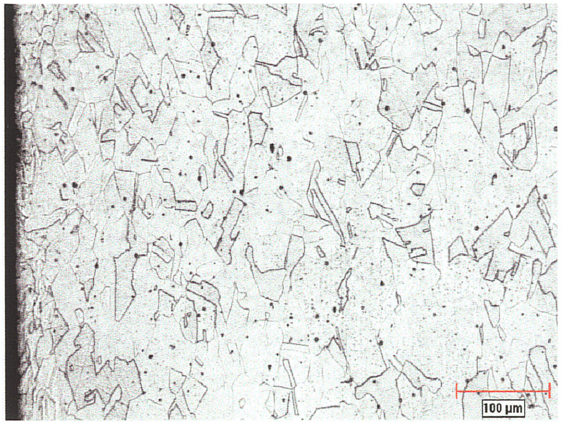

Fig. B13 - C/R 20% - 500°C

Fig. B14 - C/R 20% - 600°C

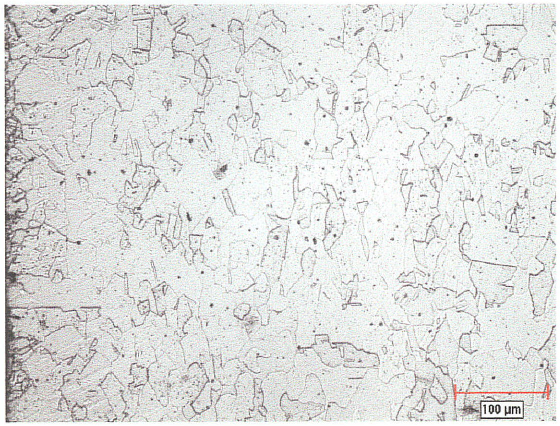

Fig. B15 - C/R 20% - 700°C

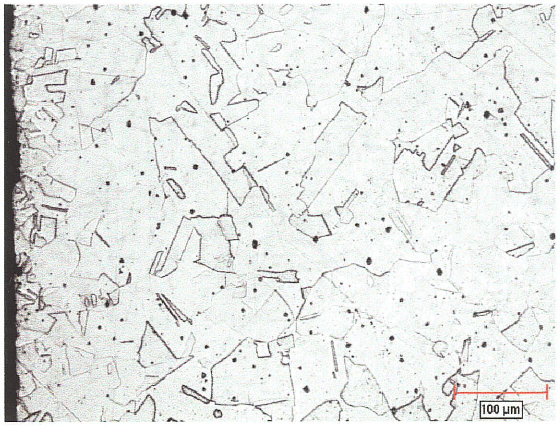

Fig. B16 - C/R 20% - 800°C

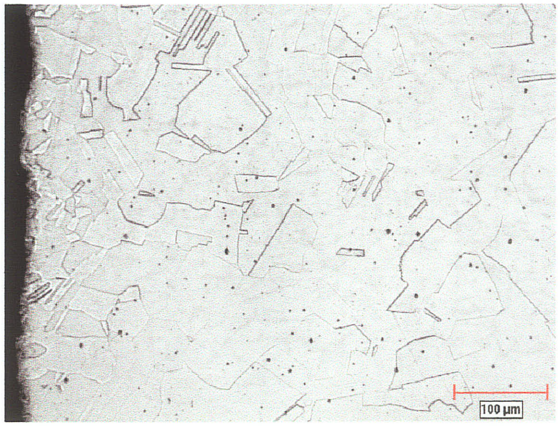

Fig. B17 - C/R 20% - 900°C

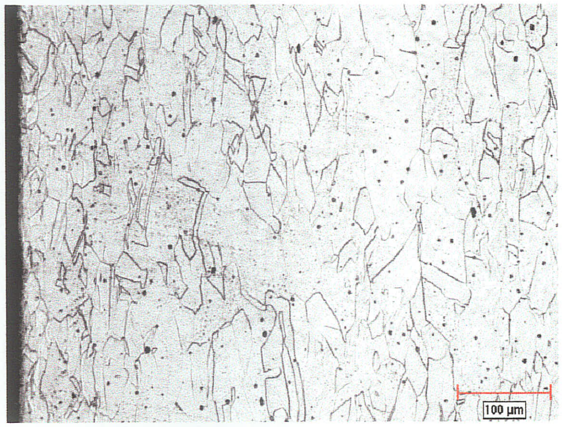

Fig. B18 - C/R 40% - 400°C

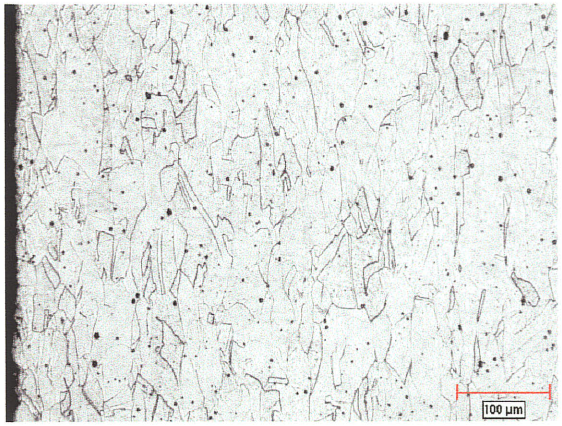

Fig. B19 - C/R 40% - 500°C

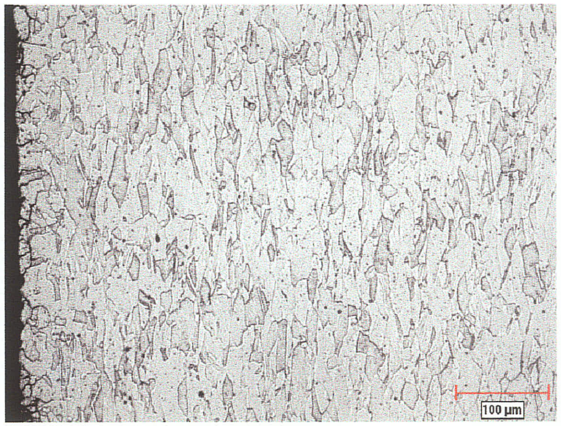

Fig. B20 - C/R 40% - 600°C

Fig. B21 - C/R 40% - 700°C

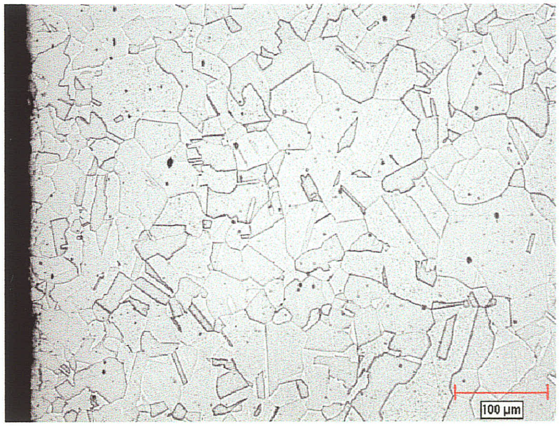

Fig. B22 - C/R 40% - 800°C

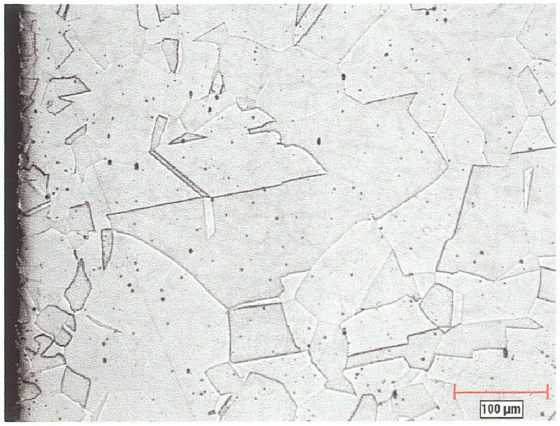

Fig. B23 - C/R 40% - 900°C

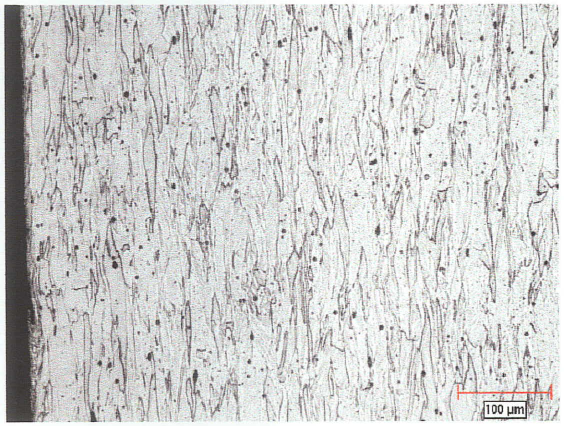

Fig. B24 - C/R 60% - 400°C

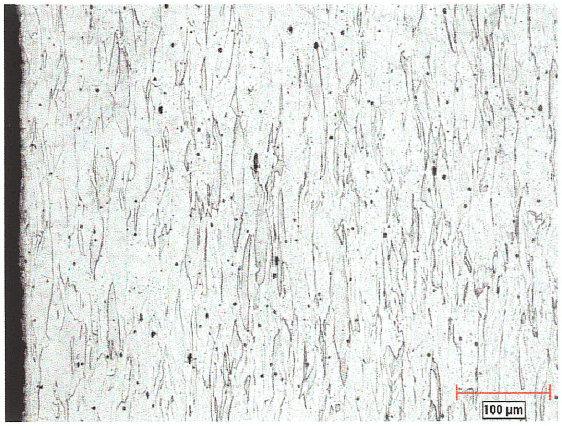

Fig. B25 - C/R 60% - 500°C

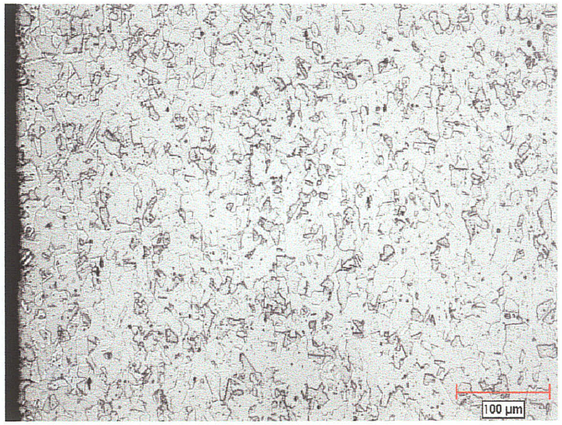

Fig. B26 - C/R 60% - 600°C

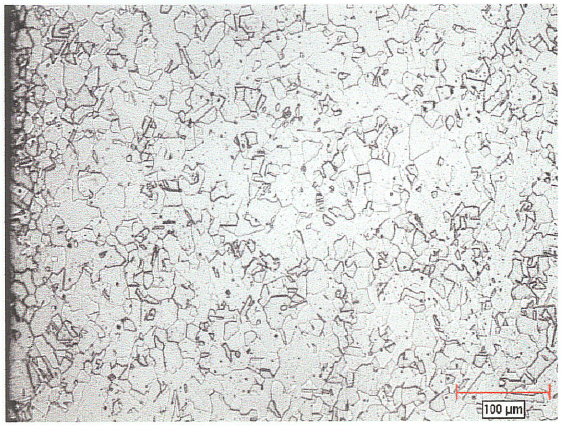

Fig. B27 - C/R 60% - 700°C

Fig. B28 - C/R 60% - 800°C

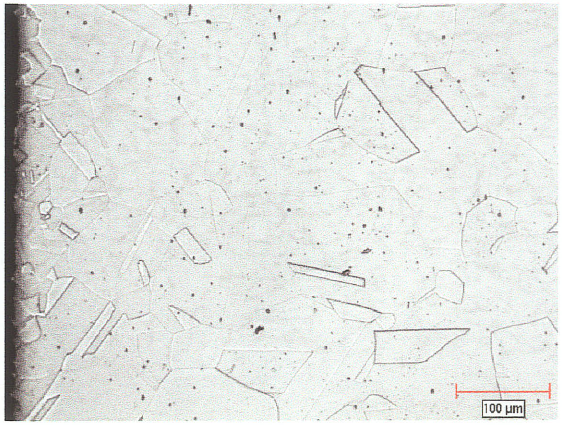

Fig. B29 - C/R 60% - 900°C

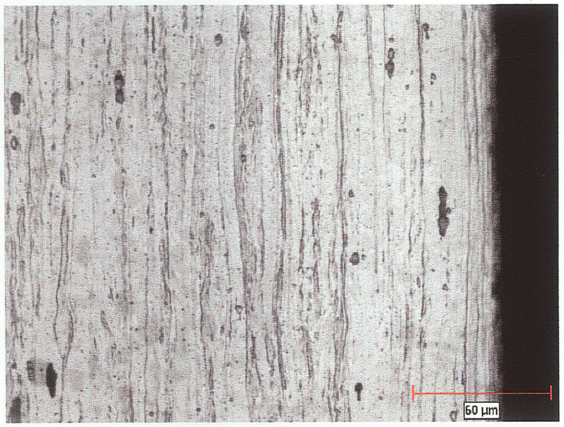

Fig. B30 - C/R 90% - 400°C

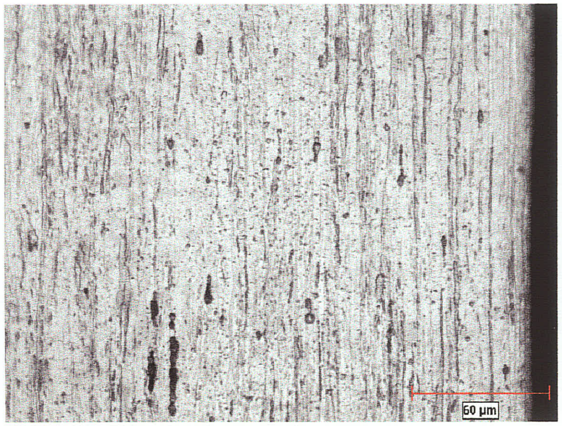

Fig. B31 - C/R 90% - 500°C

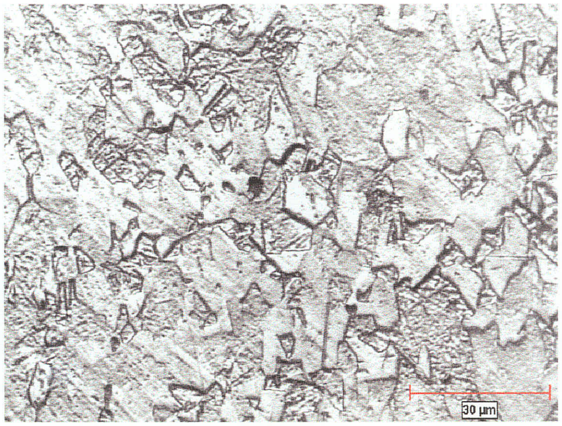

Fig. B32 - C/R 90% - 600°C

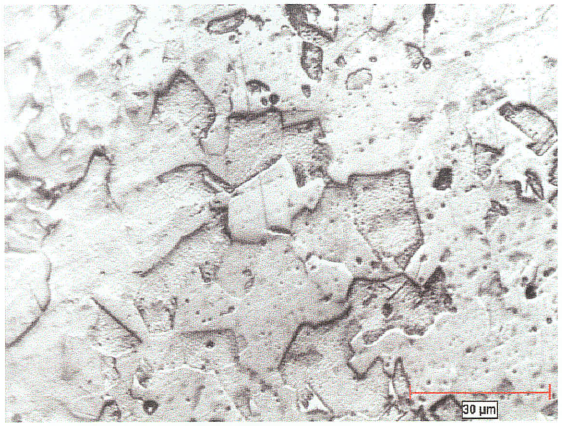

Fig. B33 - C/R 90% - 700°C

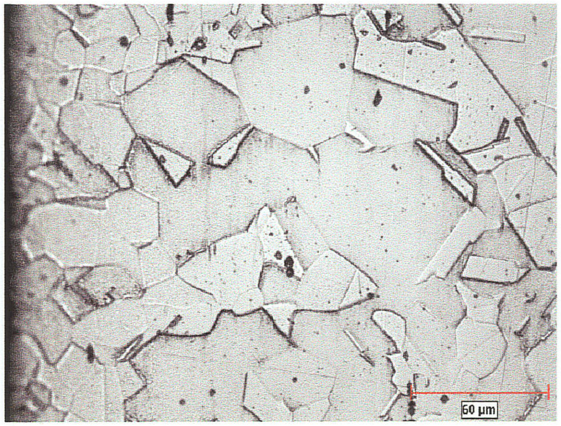

Fig. B34 - C/R 90% - 800°C

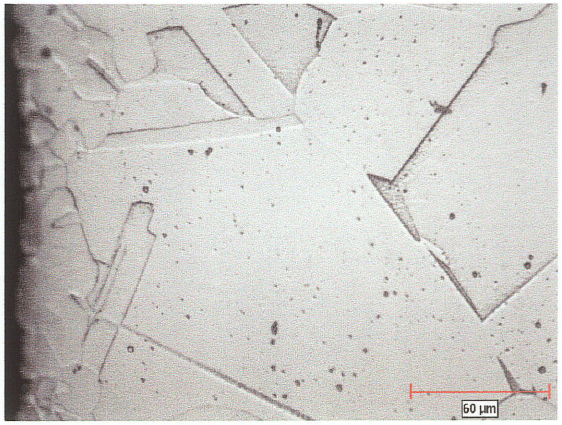

Fig. B35 - C/R 90% - 900°C

APPENDIX C

OIM Grain Boundary and Connectivity Maps of Processed Materials

Fig. C1 - 3x10%-600°C

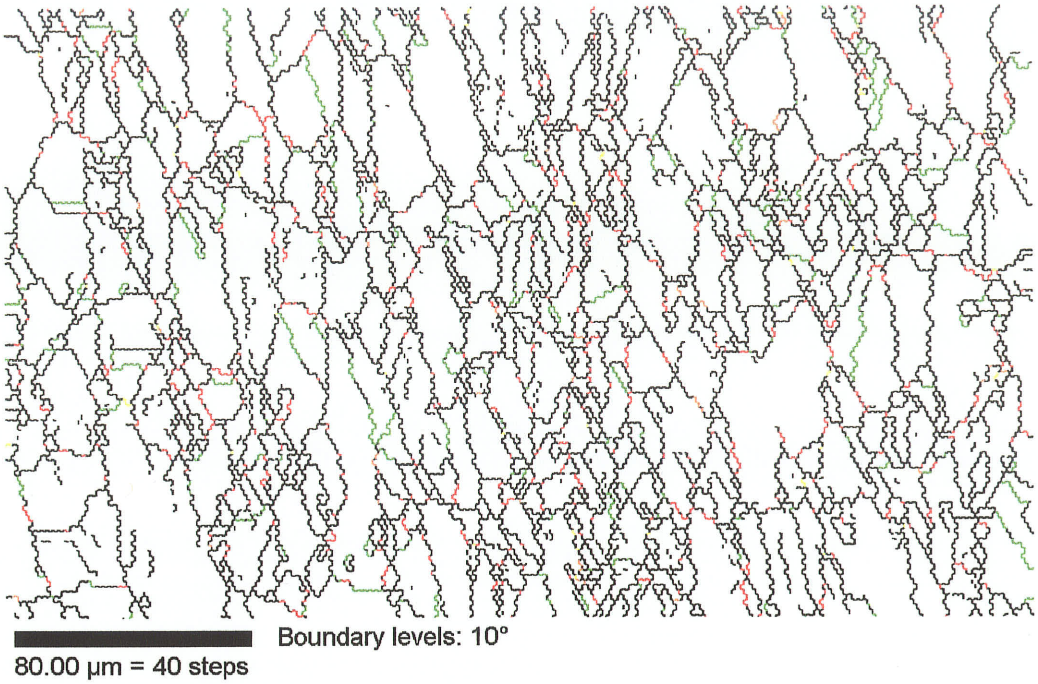

Fig. C2 - 15x10%-600°C

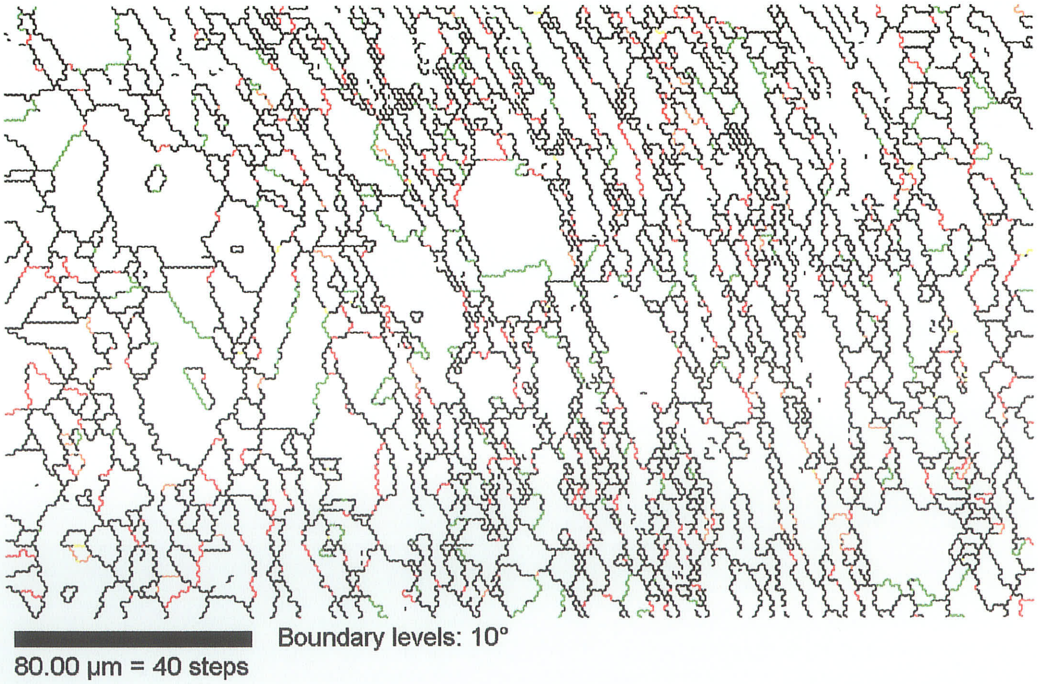

Fig. C3 - 1x25%-600°C

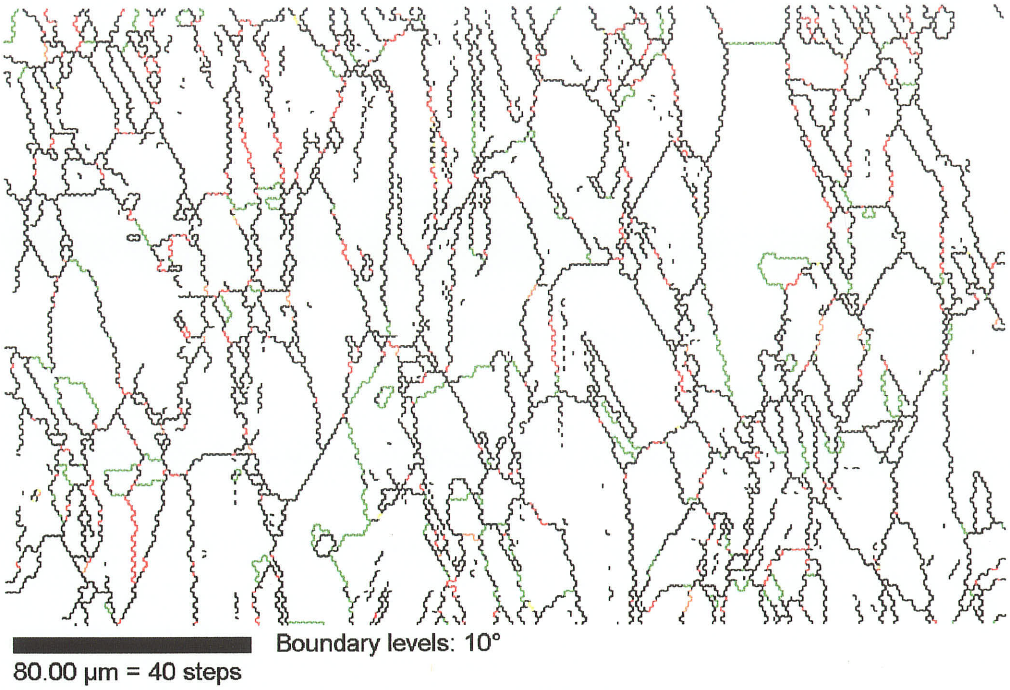

Fig. C4 - 6x25%-600°C

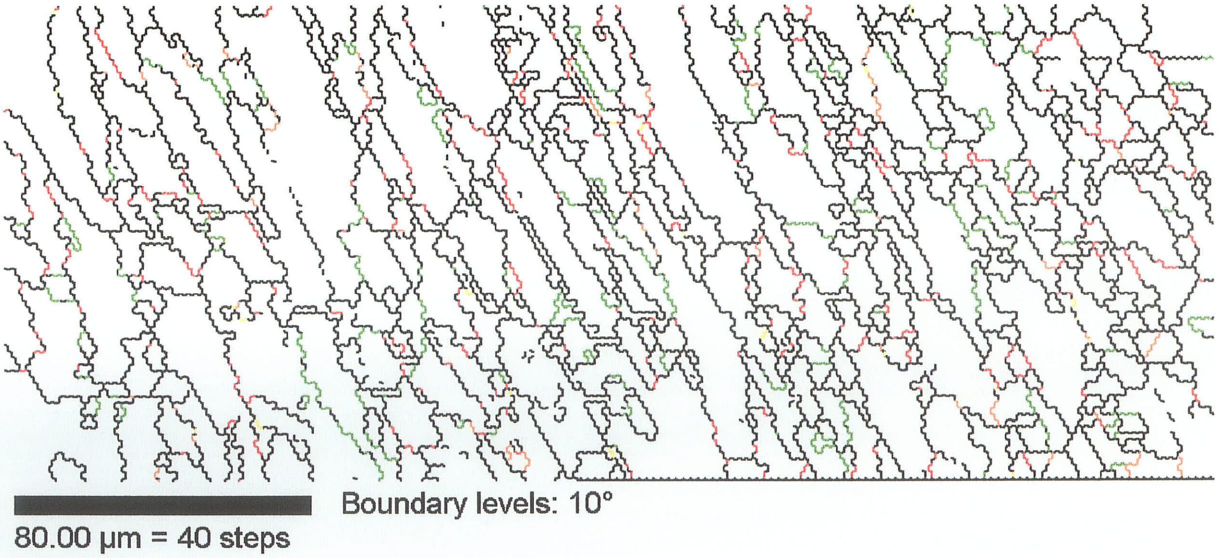

Fig. C5 (a)-(b) - 3x10%-700°C

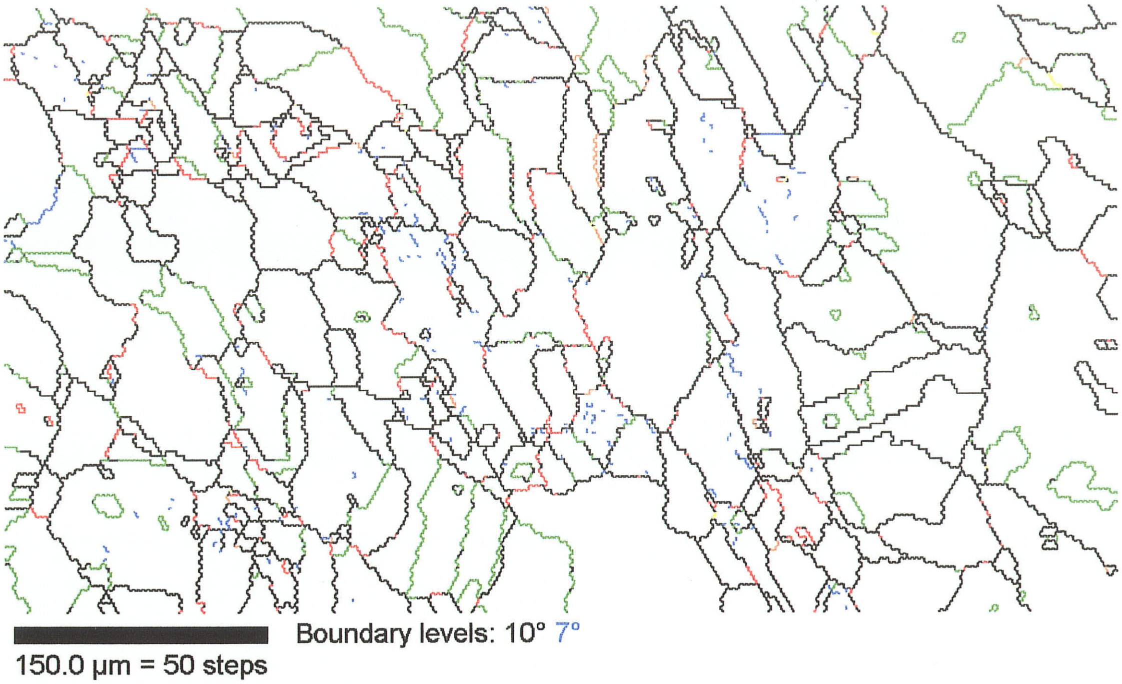

(a)

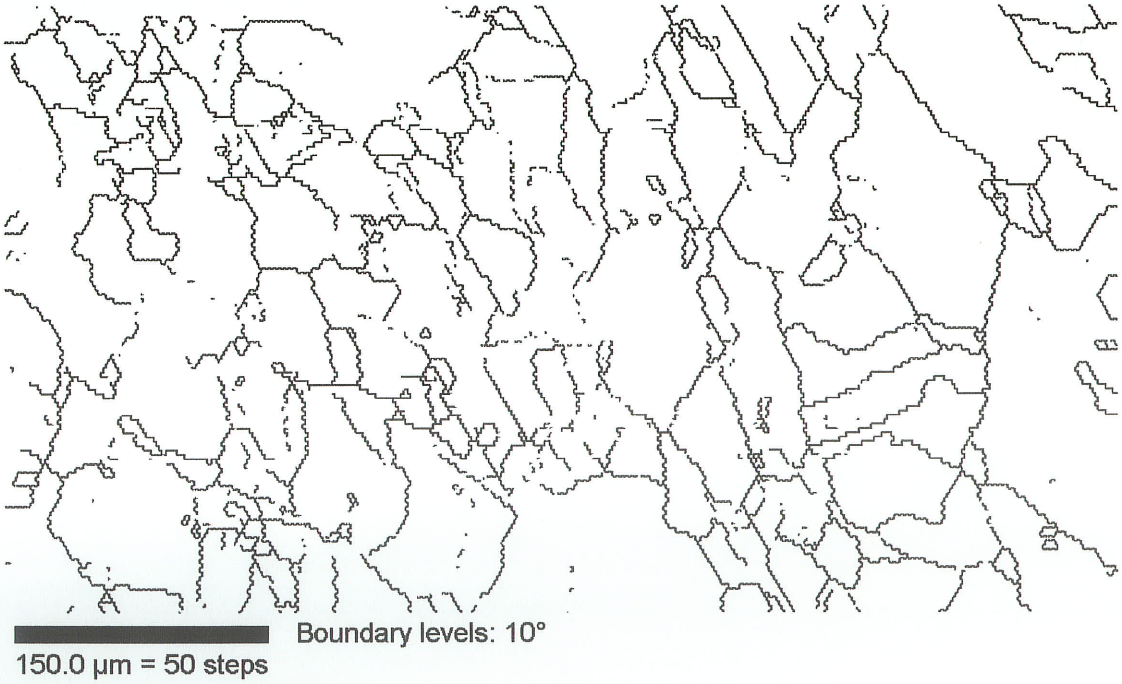

(b)

Fig. C6 (a)-(b) - 7x10%-700°C

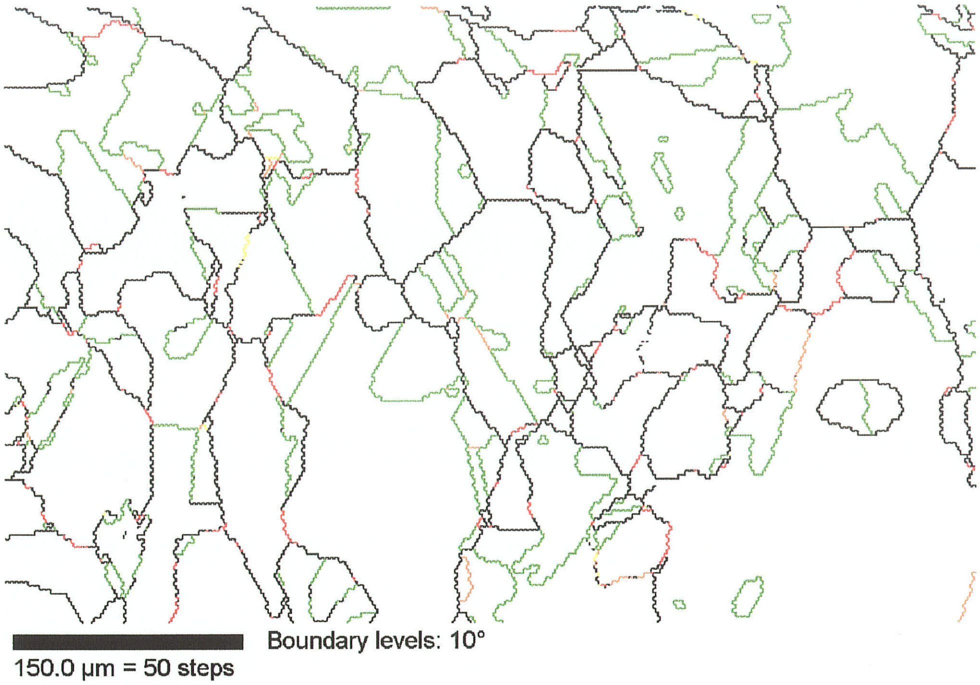

(a)

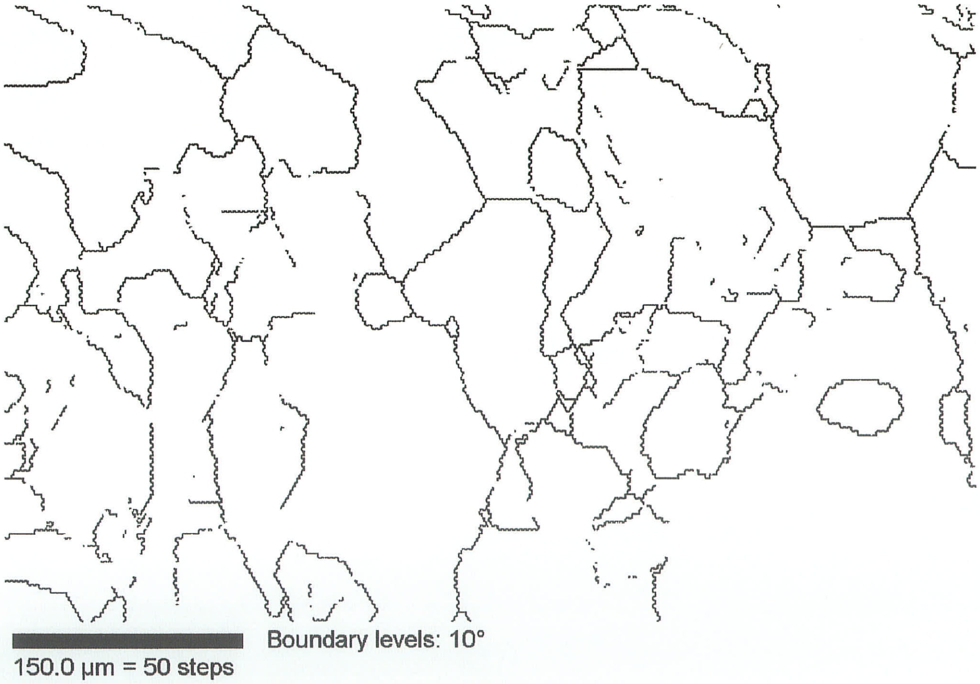

(b)

Fig. C7 (a)-(b) - 15x10%-700°C

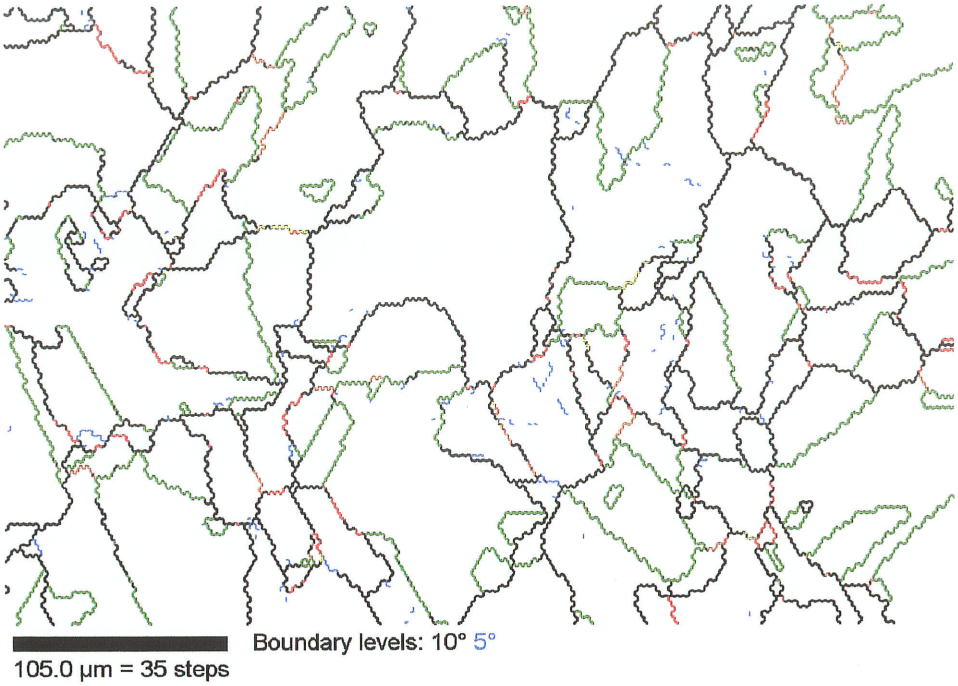

(a)

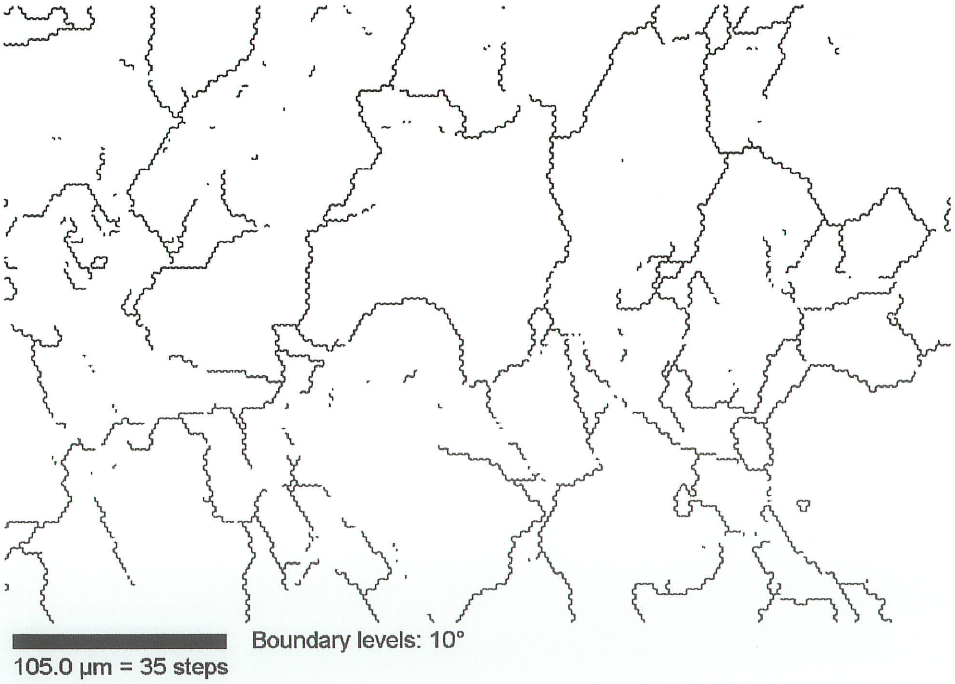

(b)

Fig. C8 (a)-(b) - 1x25%-700°C

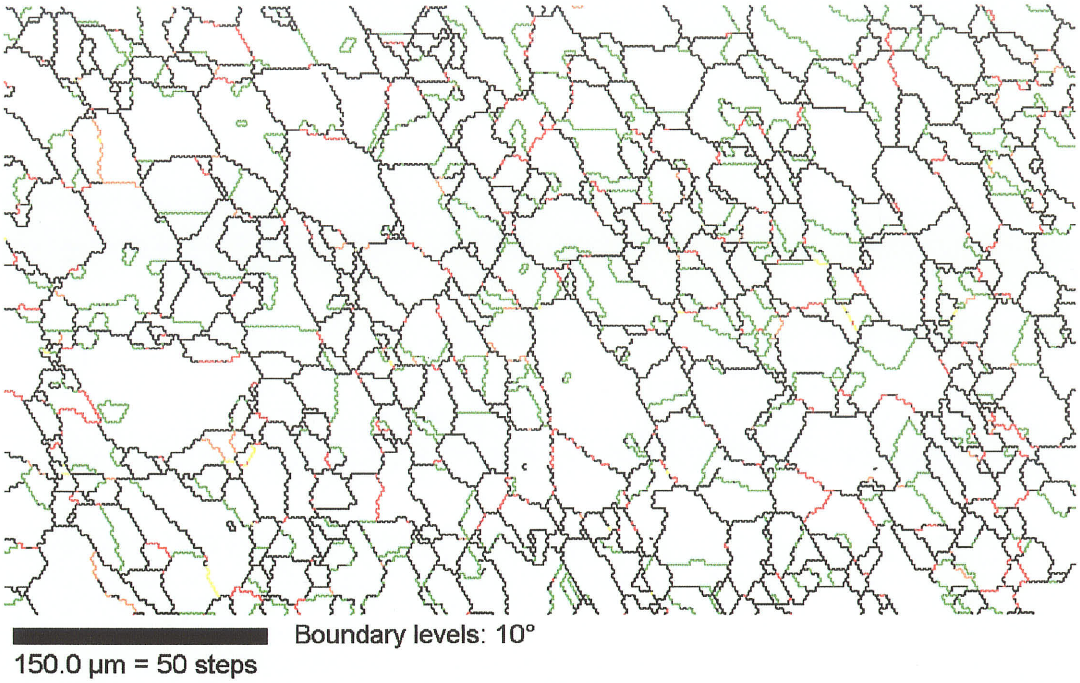

(a)

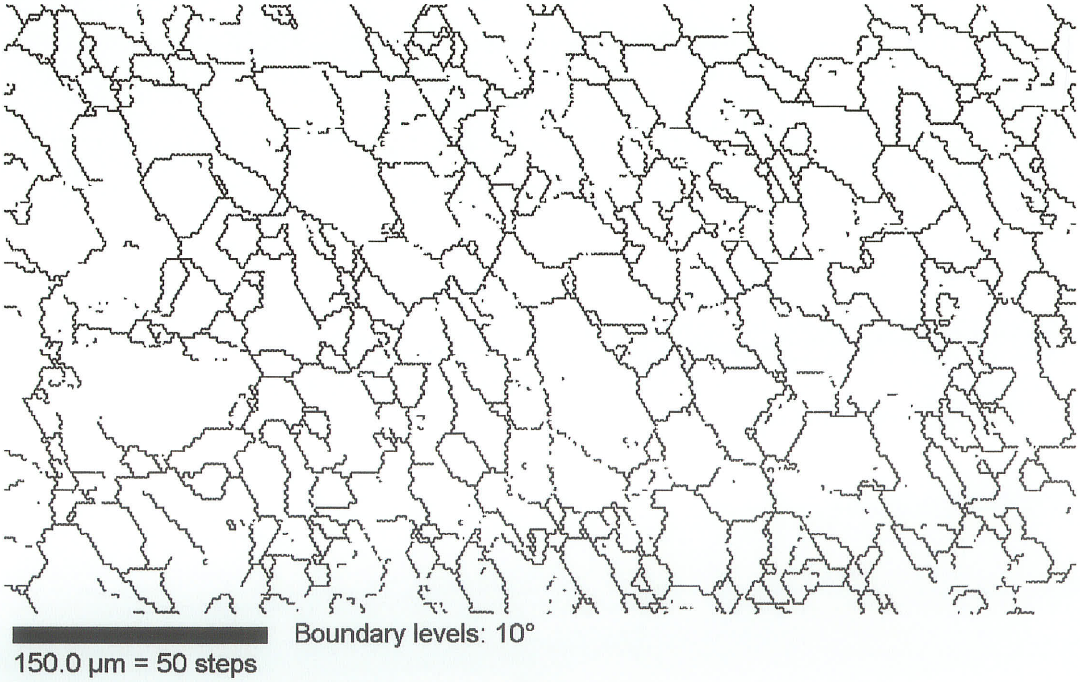

(b)

Fig. C9 (a)-(b) - 6x25%-700°C

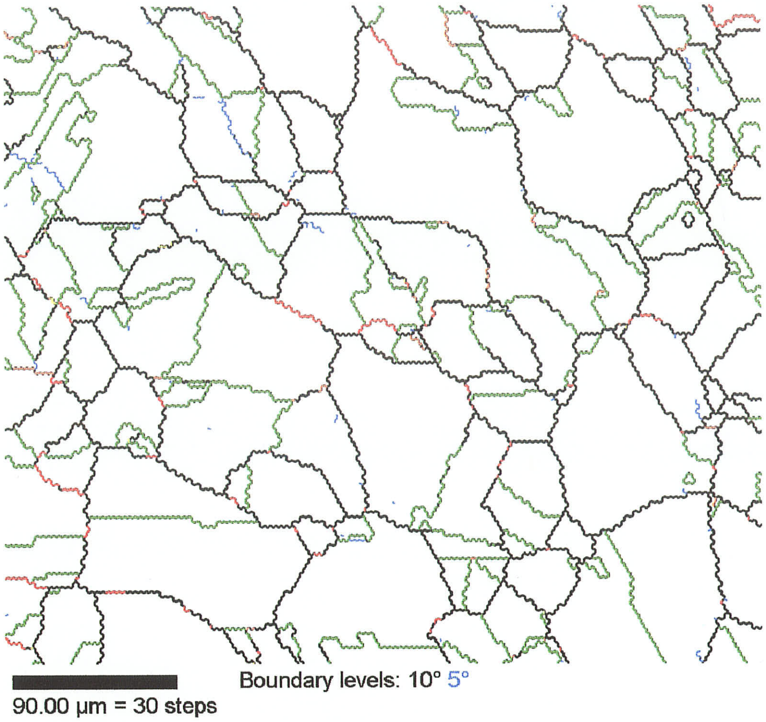

(a)

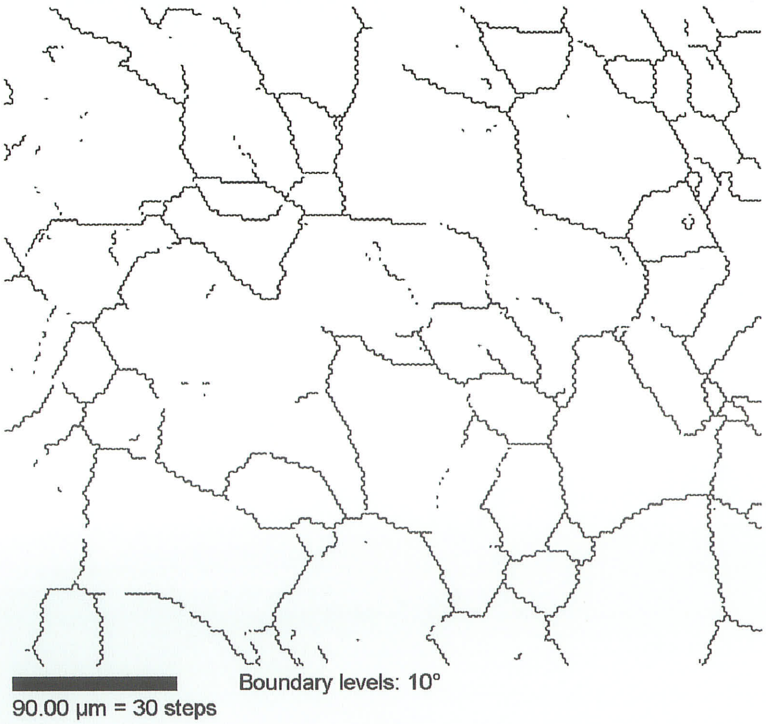

(b)

Fig. C10 (a)-(b) -1x5%-750°C

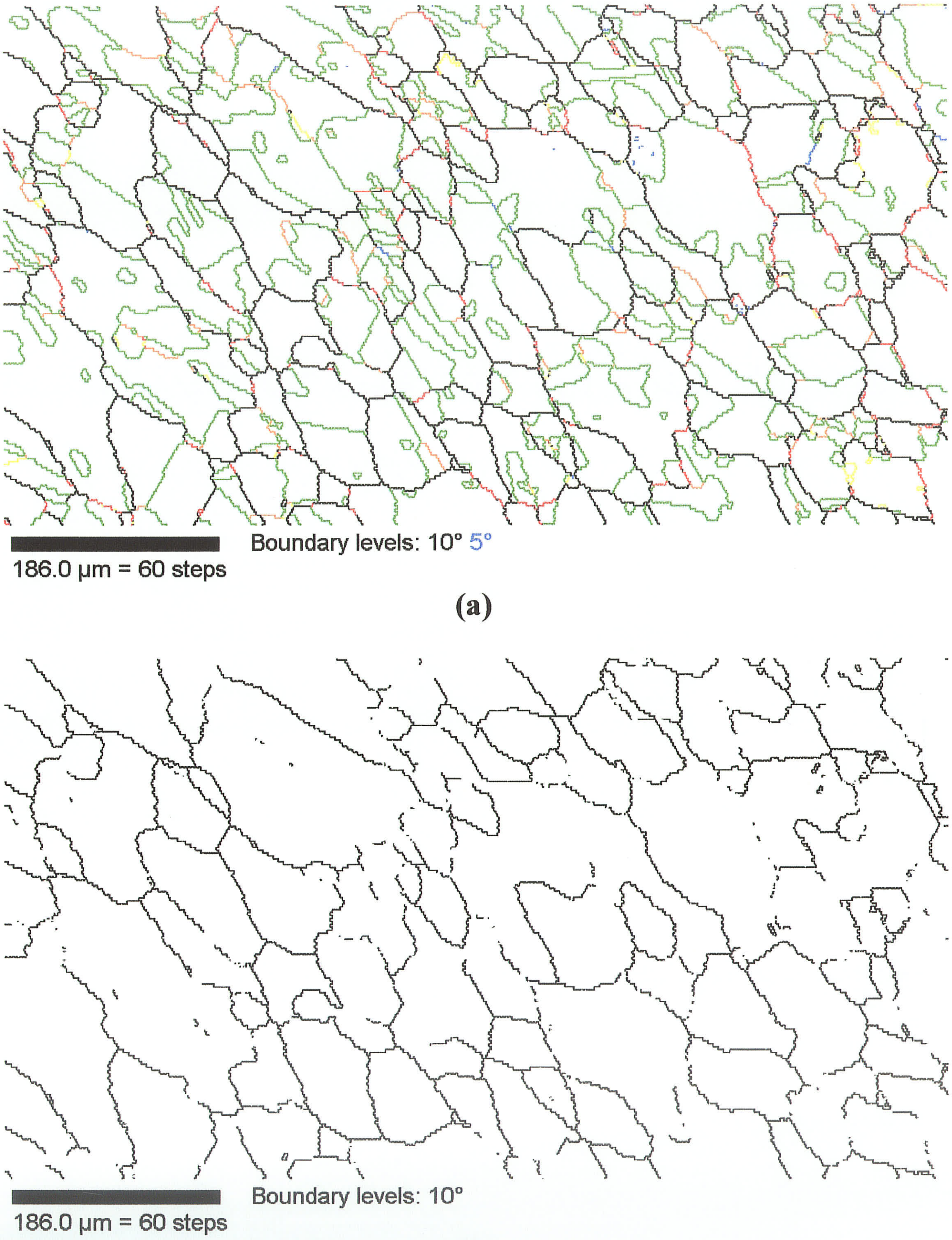

(a)

(b)

Fig. C11 (a)-(b) -5x5%-750°C

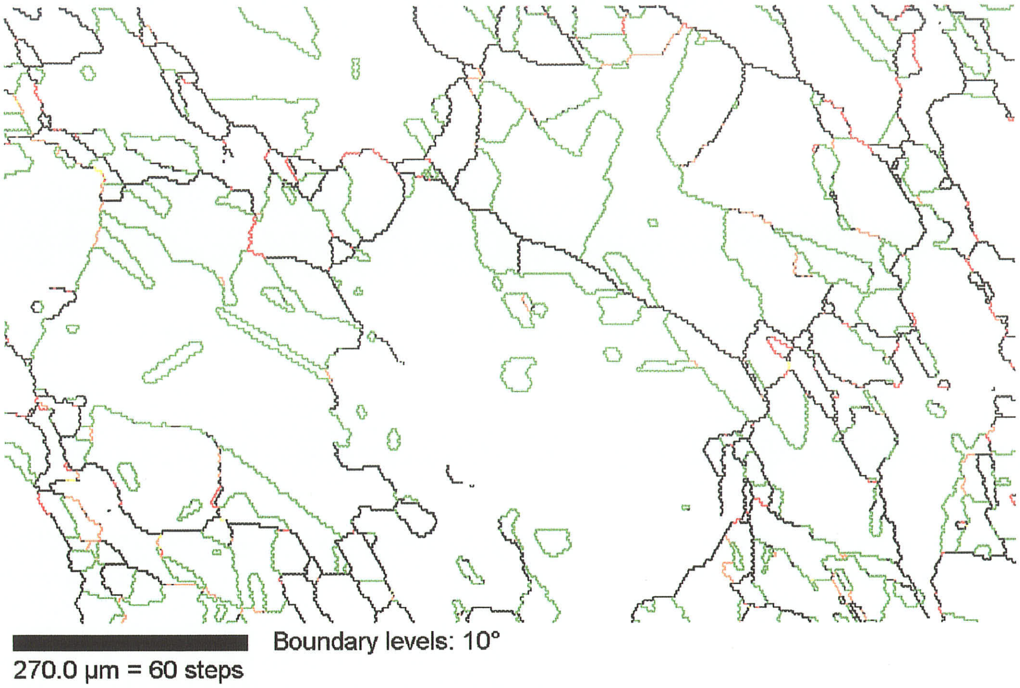

(a)

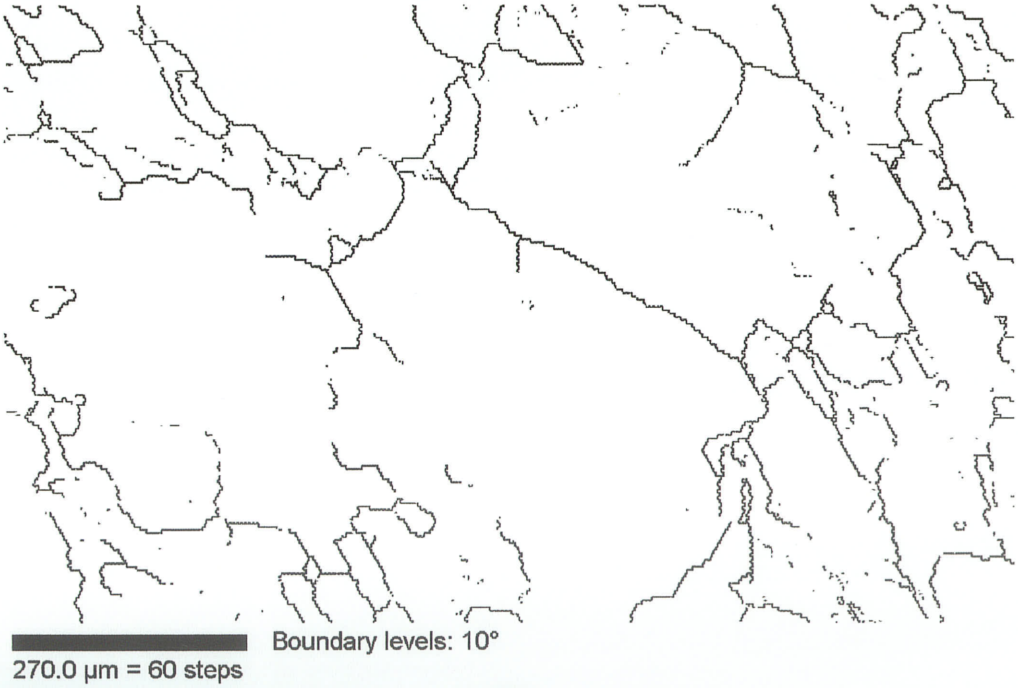

(b)

Fig. C12 (a)-(b) -2x18%-750°C

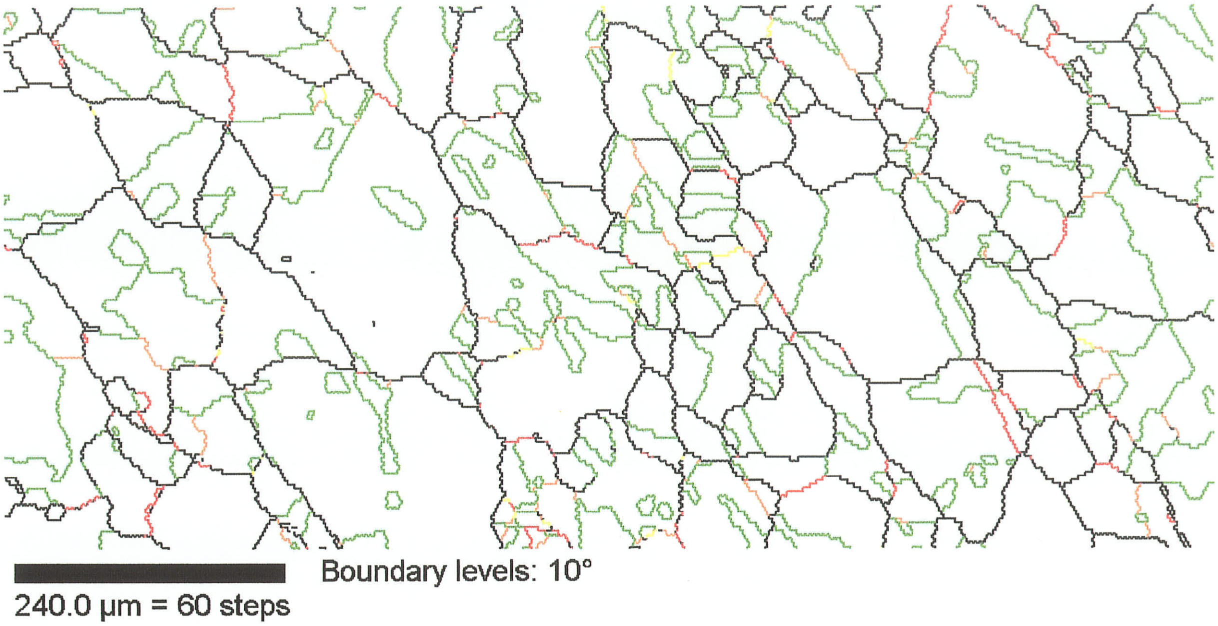

(a)

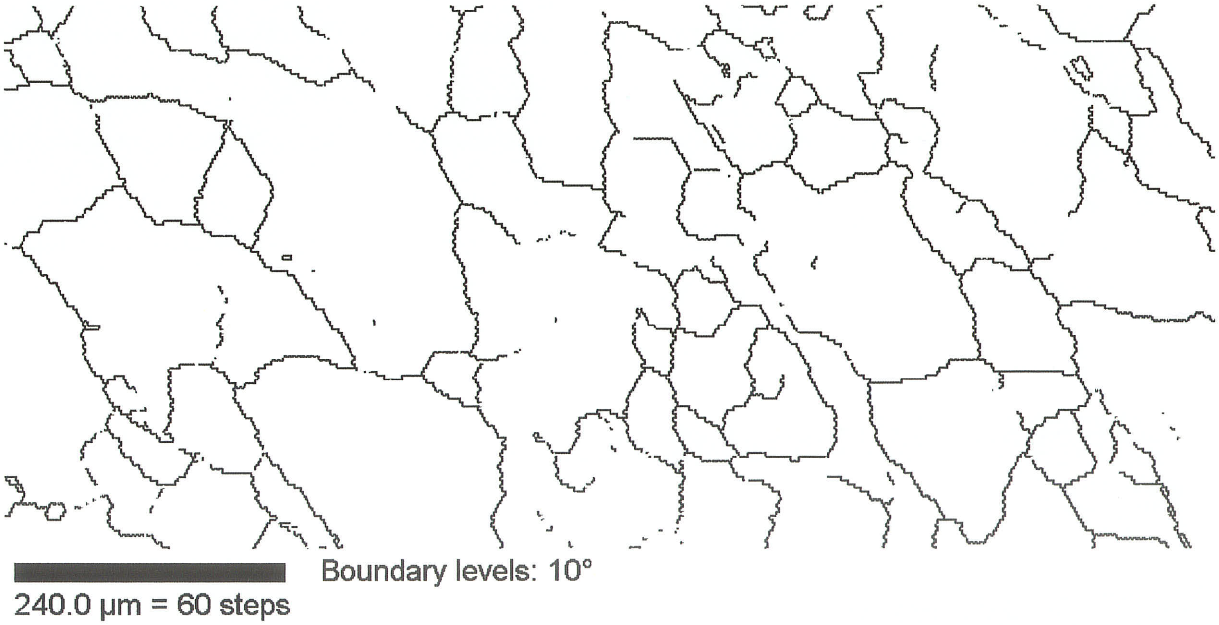

(b)

Fig. C13 (a)-(b) -4x18%-750°C

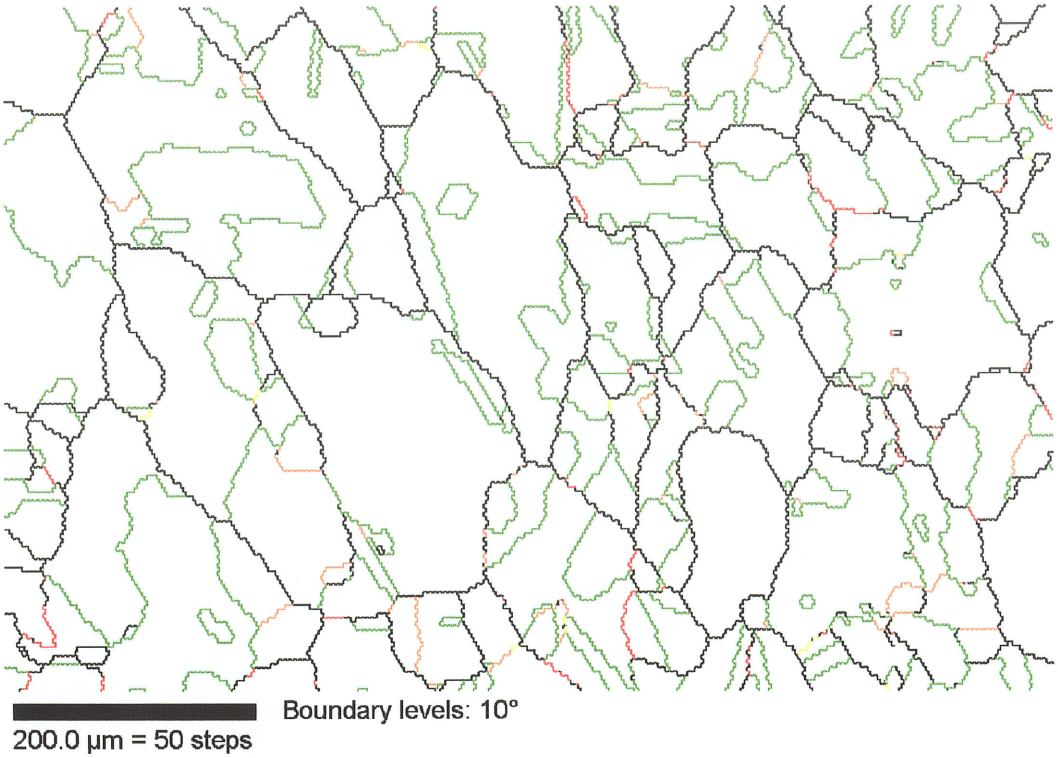

(a)

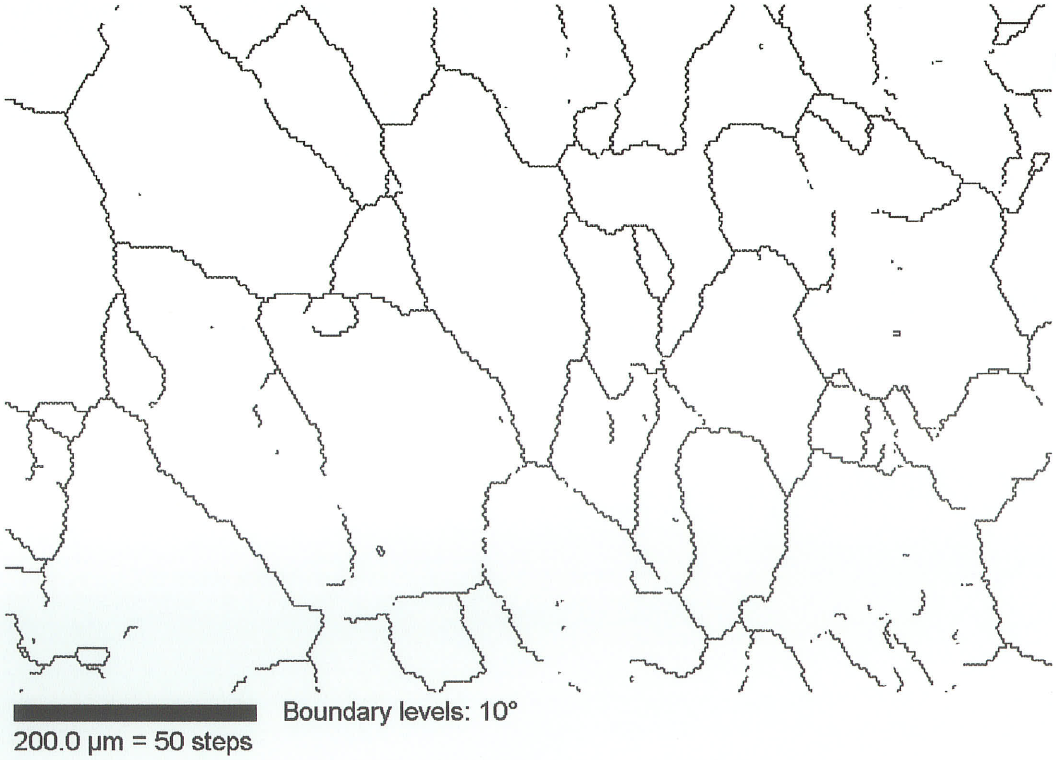

(b)

Fig. C14 (a)-(b) -1x20%-750°C

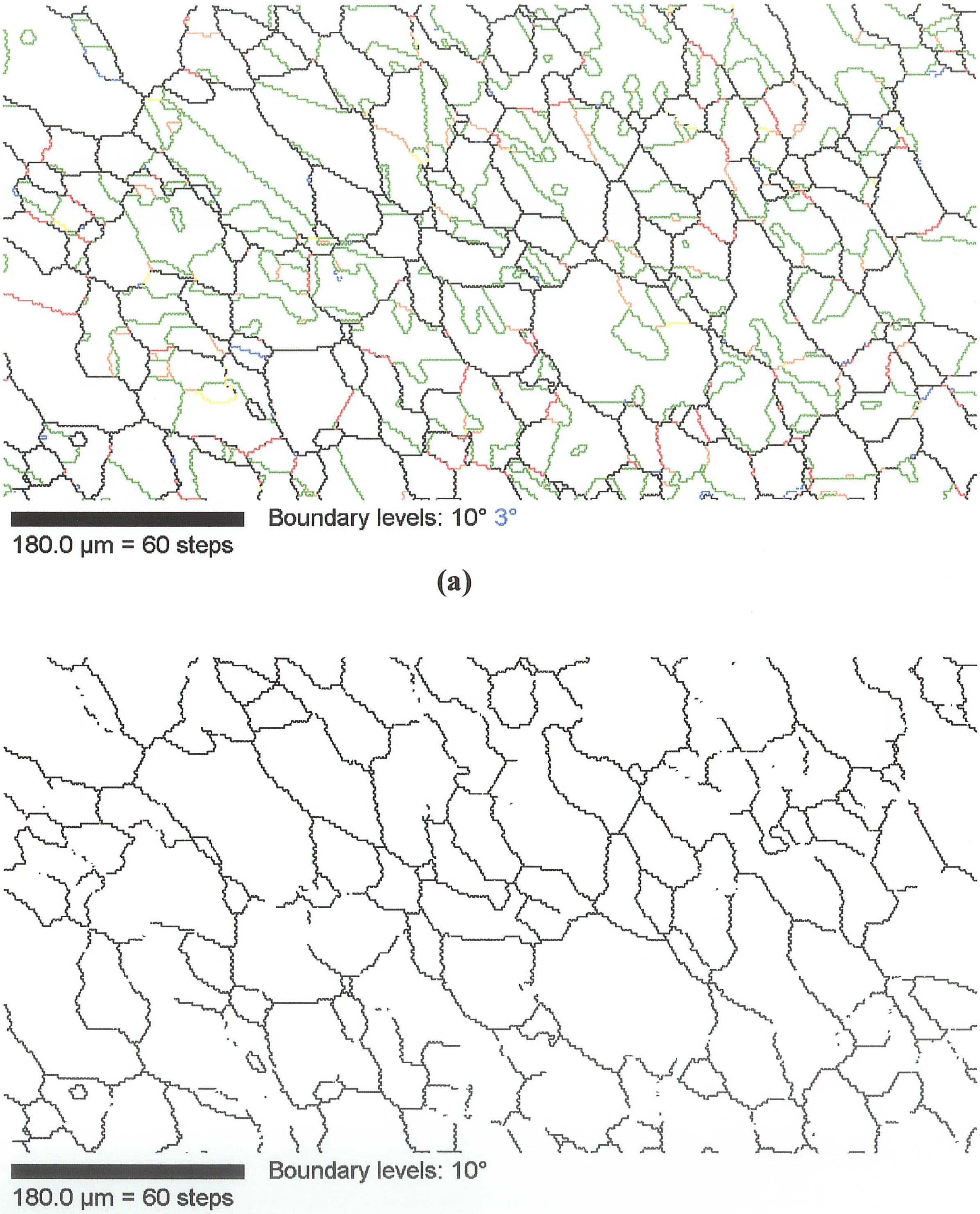

(a)

(b)

Fig. C15 (a)-(b) - 5x20%-750°C

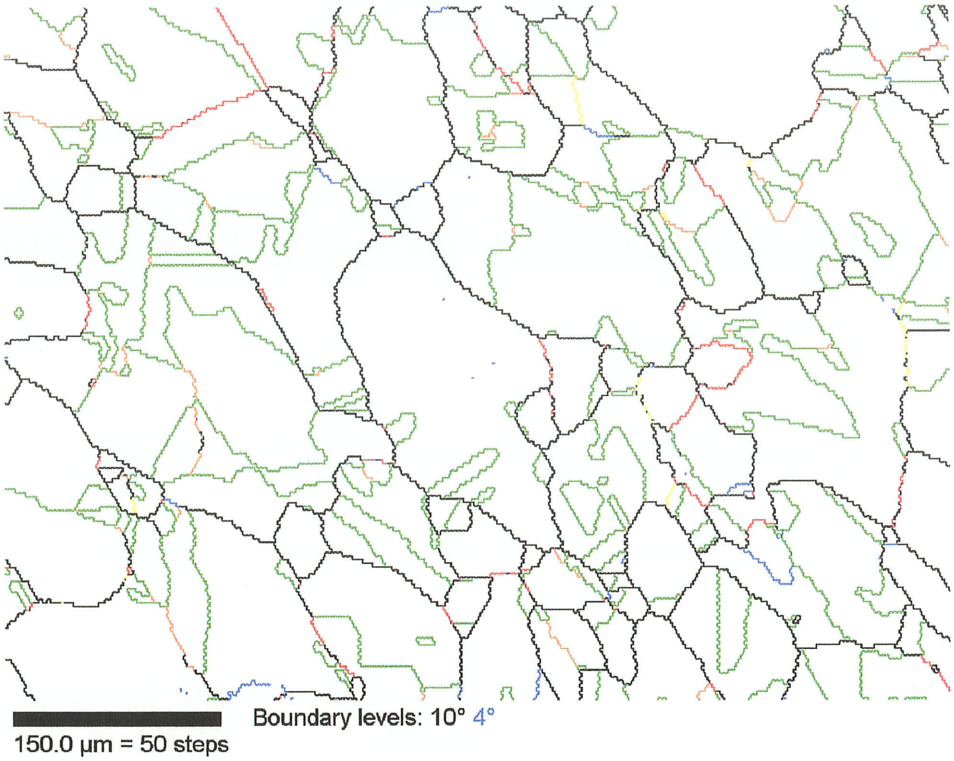

(a)

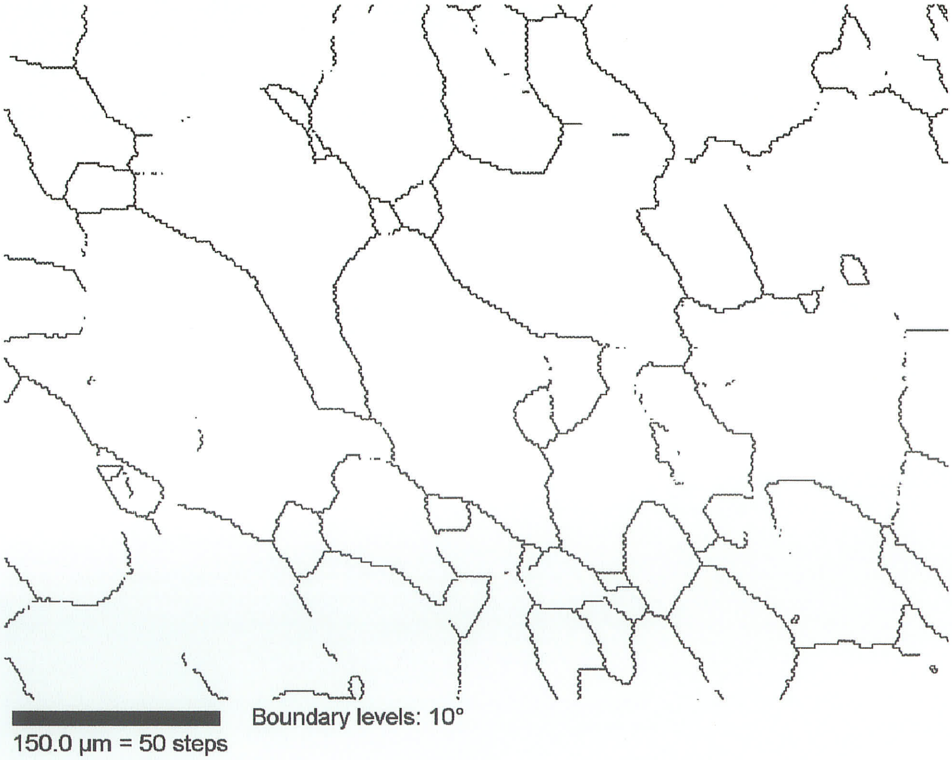

(b)

Fig. C16 (a)-(b) -Annealed only @ 800°C

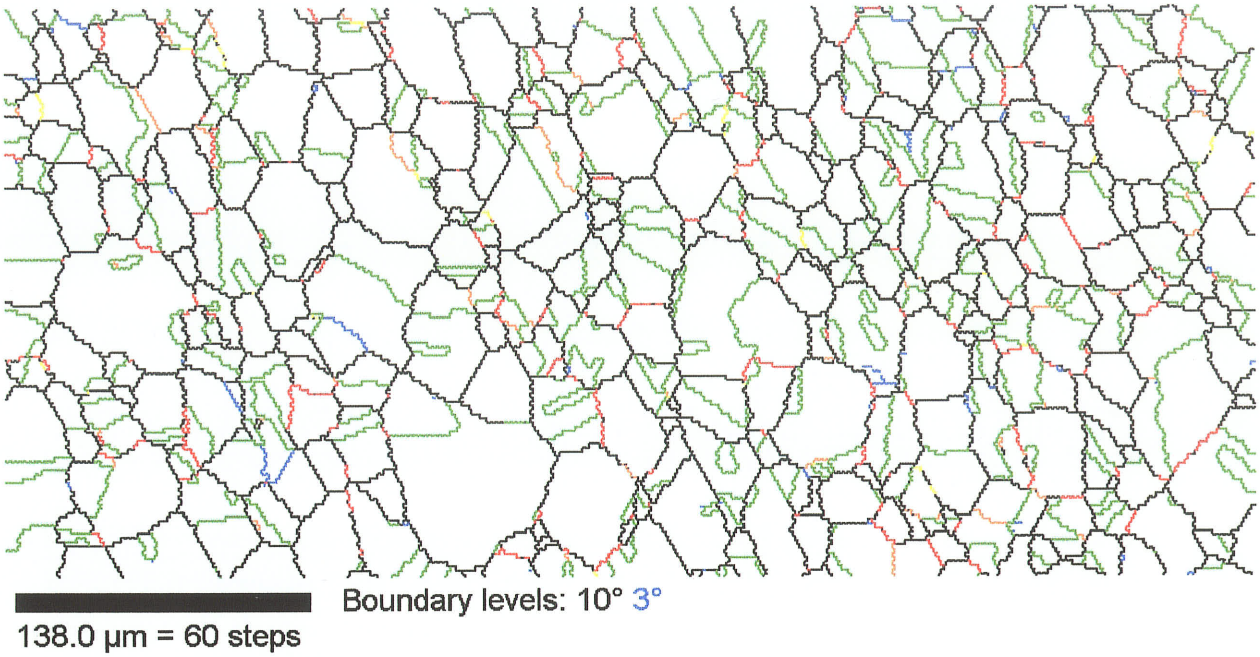

(a)

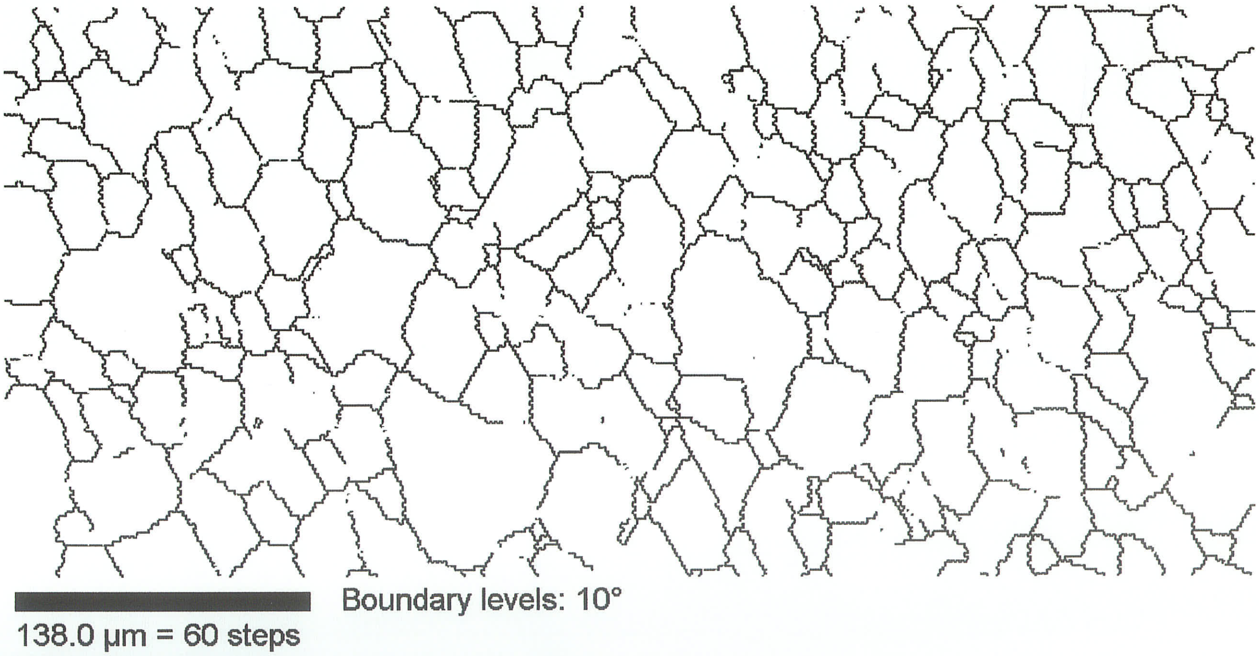

(b)

Fig. C17 (a)-(b) -1x10%-800°C

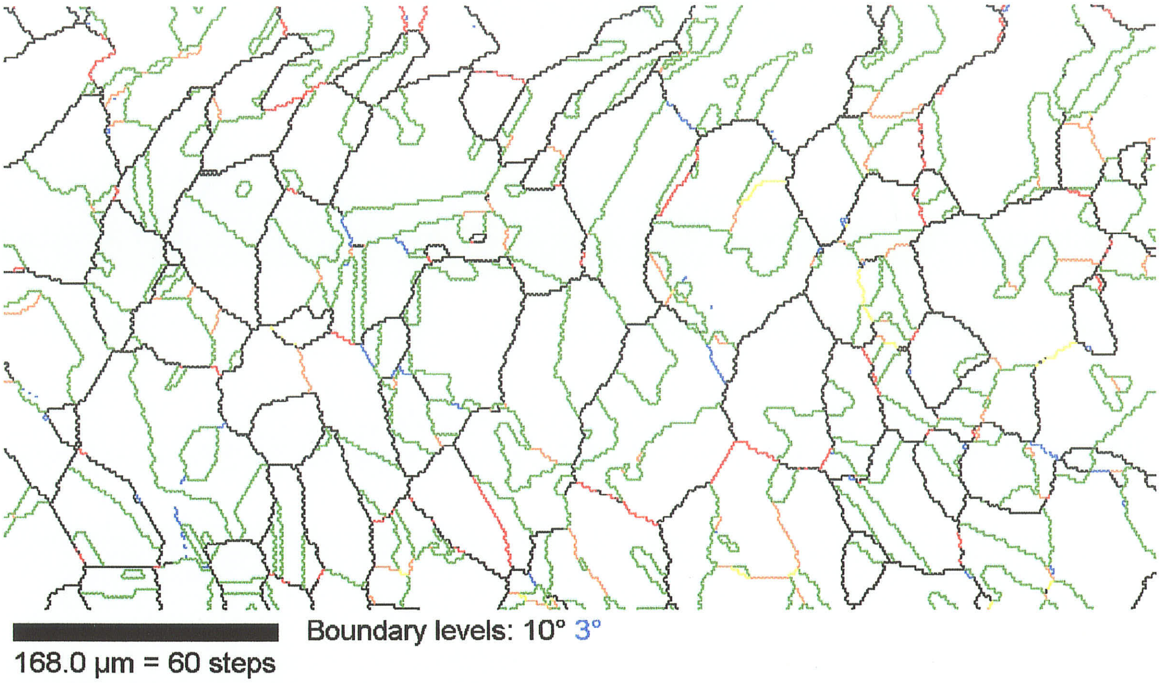

(a)

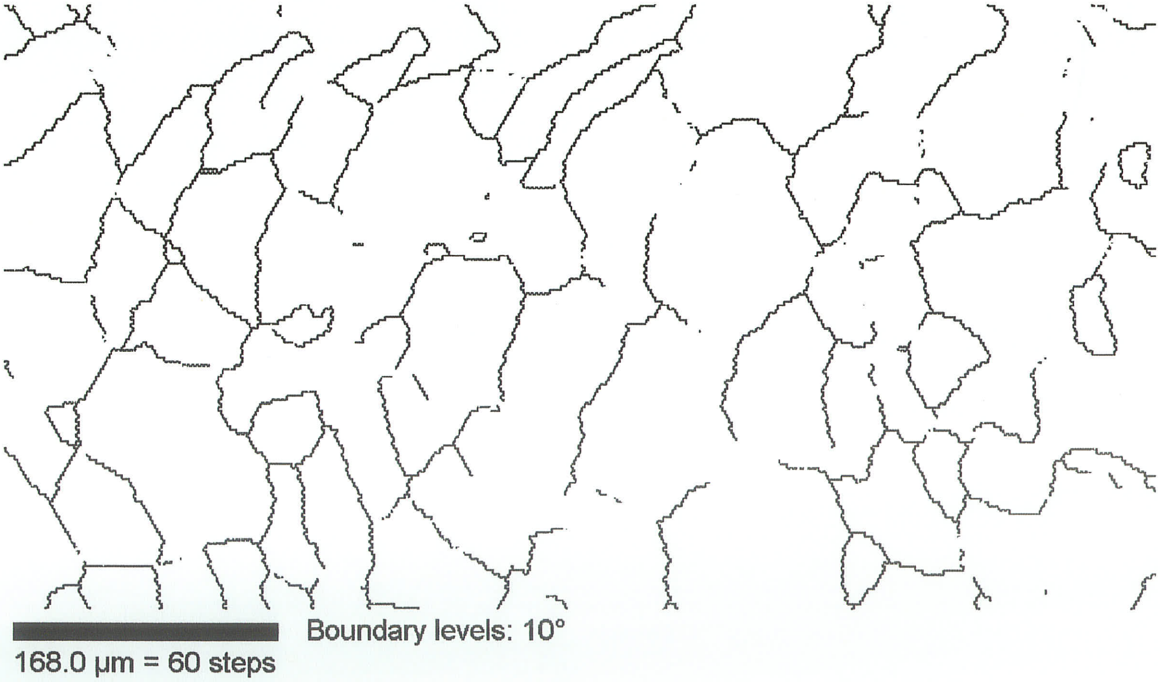

(b)

Fig. C18 (a)-(b) - 2x10%-800°C

(a)

(b)

Fig. C19 (a)-(b) - 3x10%-800°C

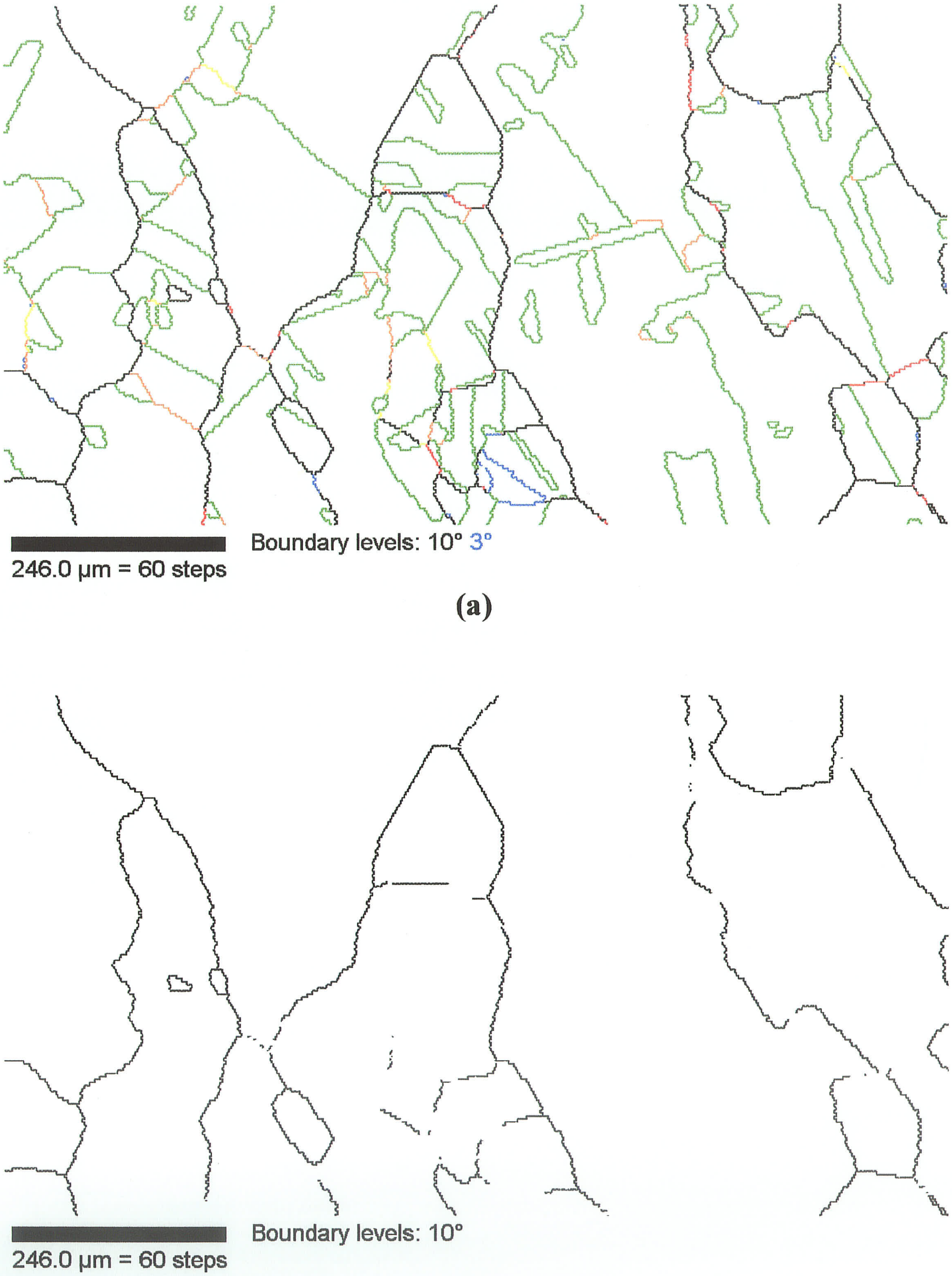

(a)

(b)

Fig. C20 (a)-(b) - 4x10%-800°C

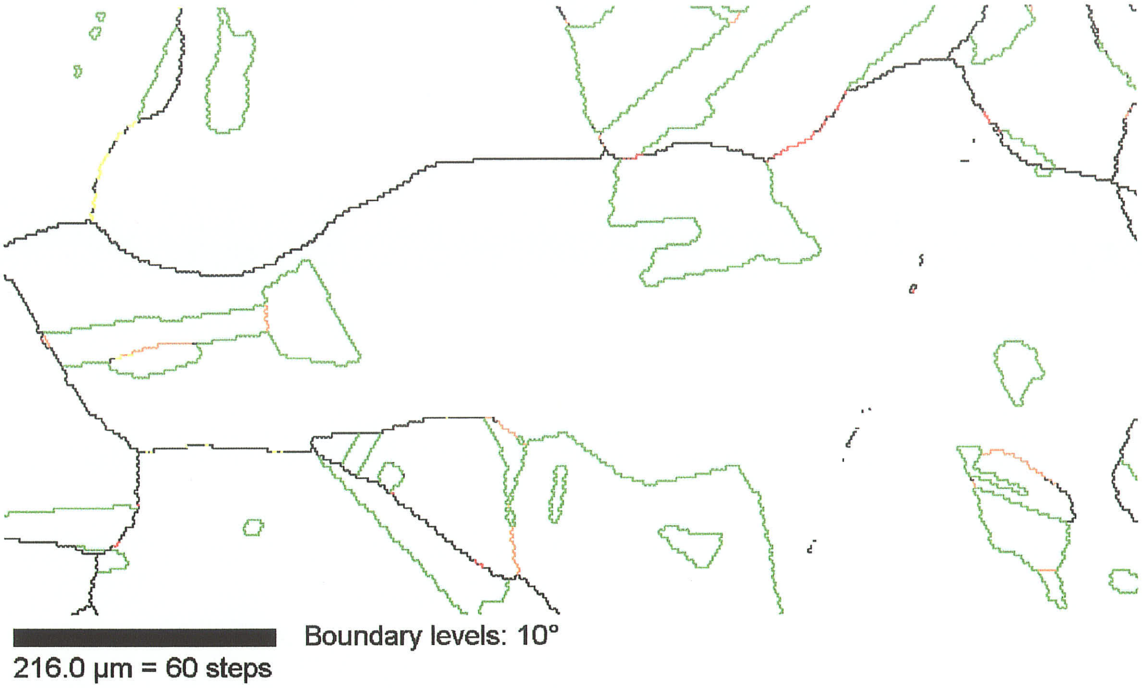

(a)

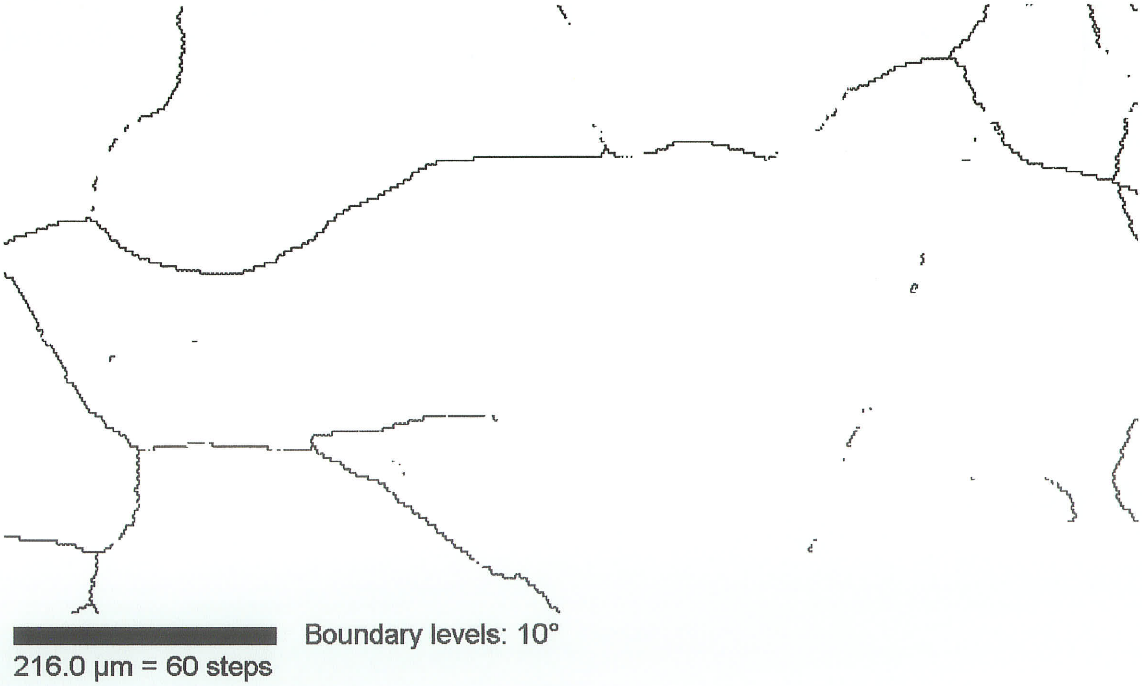

(b)

Fig. C21 (a)-(b) - 6x10%-800°C

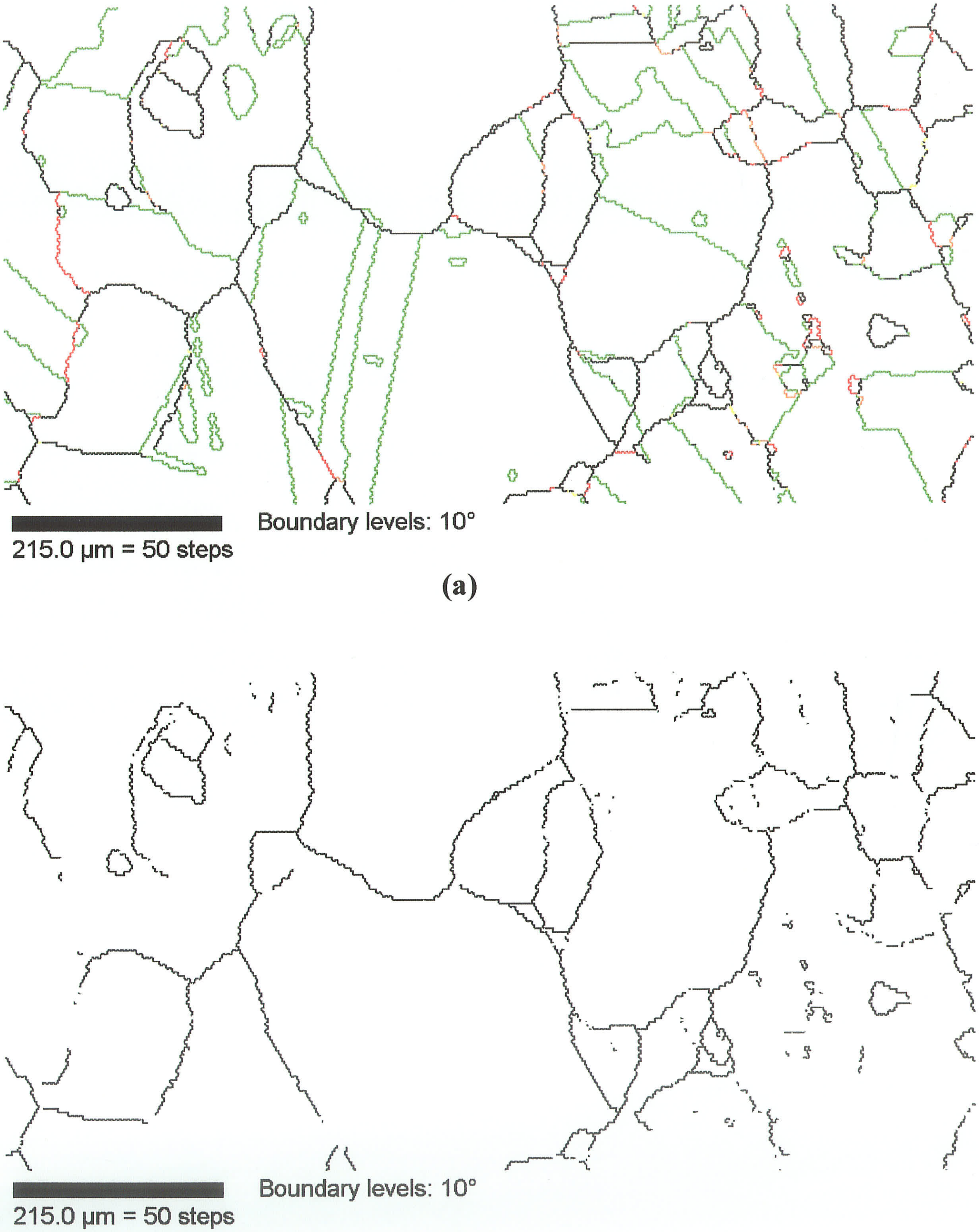

(a)

(b)

Fig. C22 (a)-(b) - 11x10%-800°C

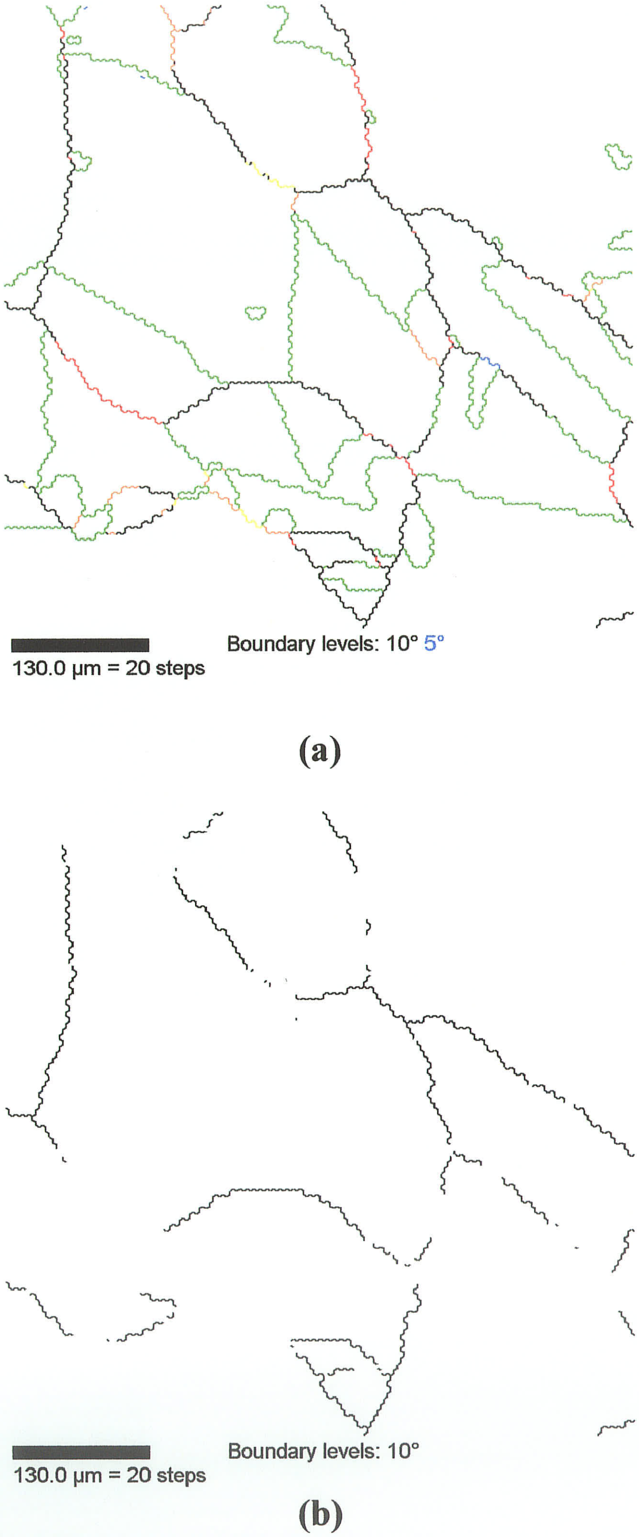

Fig. C23 (a)-(b) - 1x18%-800°C

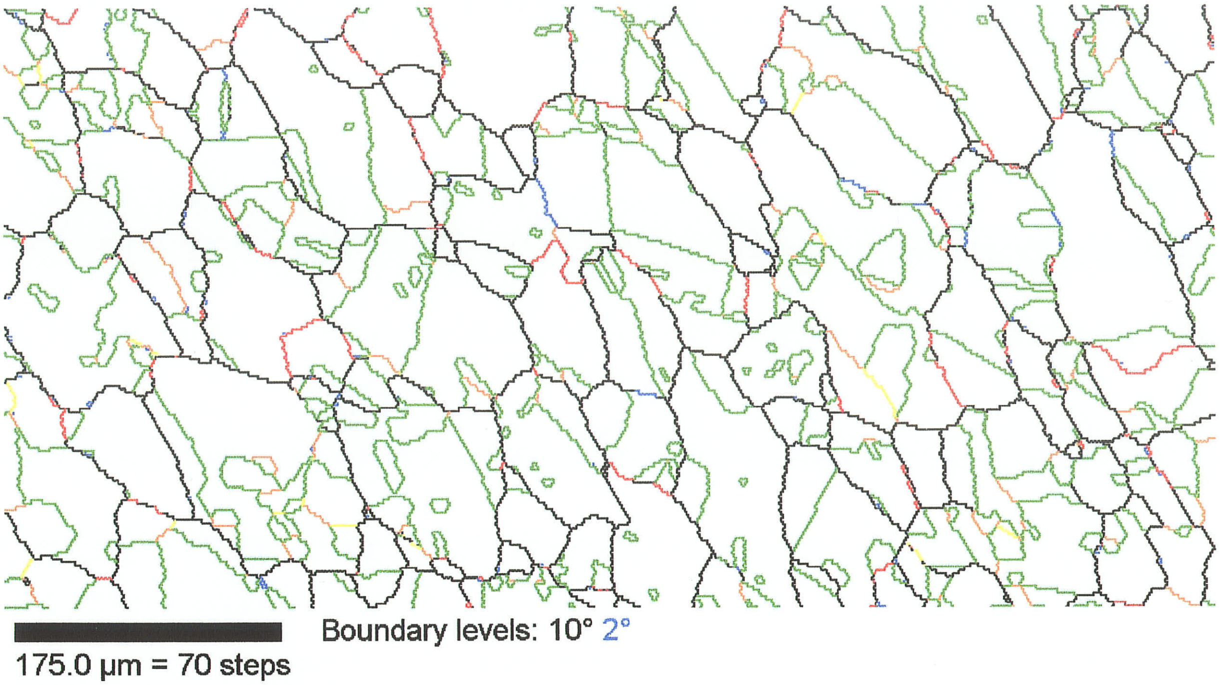

(a)

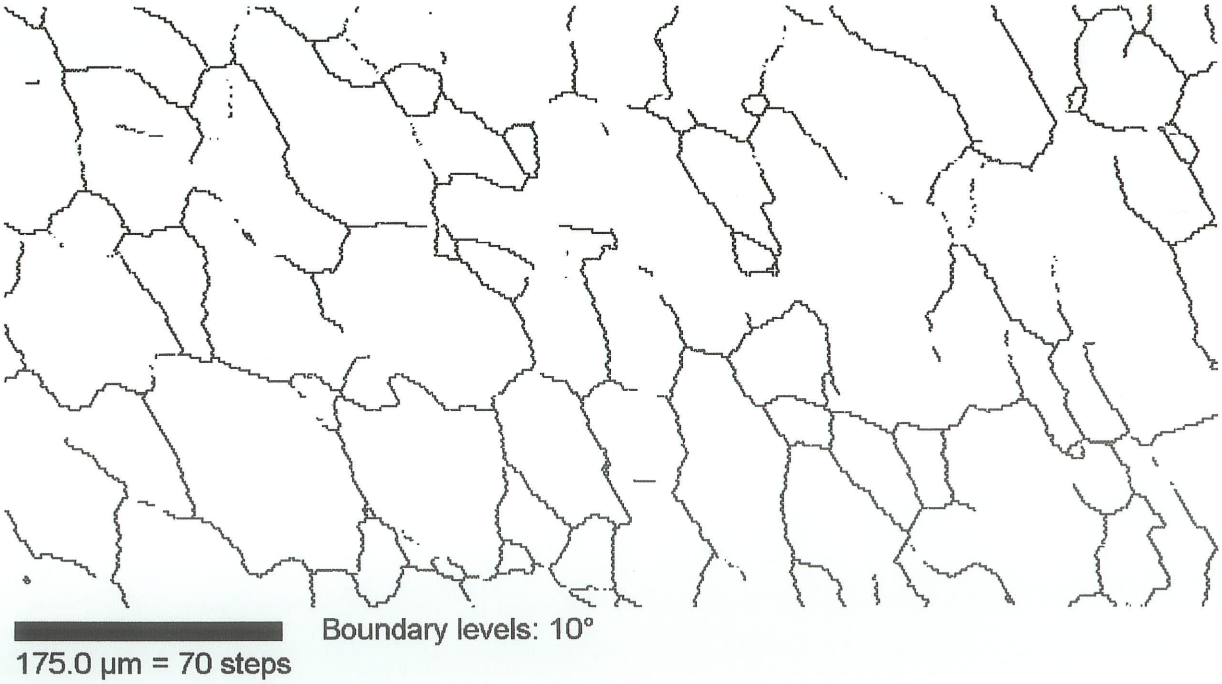

(b)

Fig. C24 (a)-(b) - 2x18%-800°C

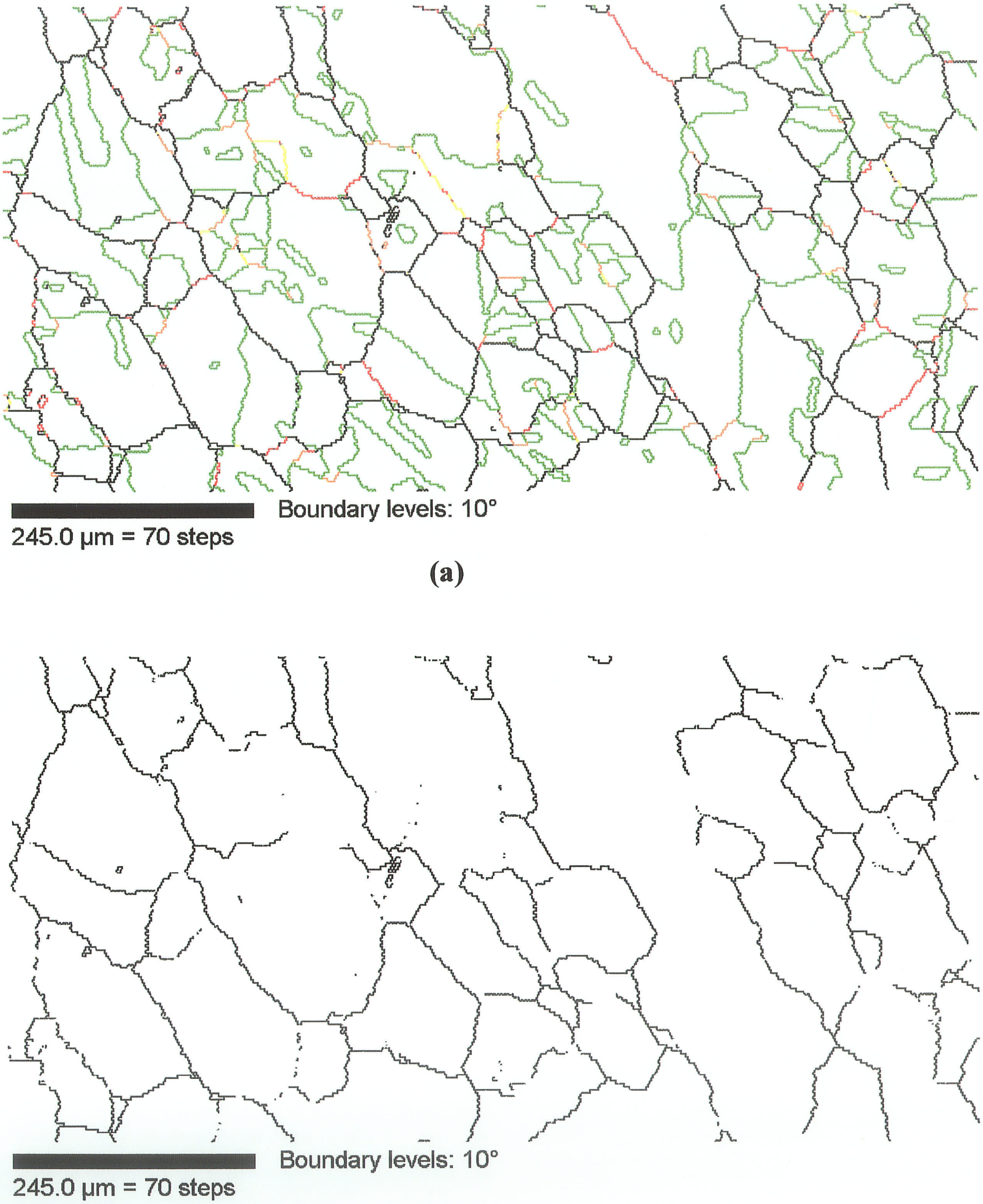

(a)

(b)

Fig. C25 (a)-(b) - 3x18%-800°C

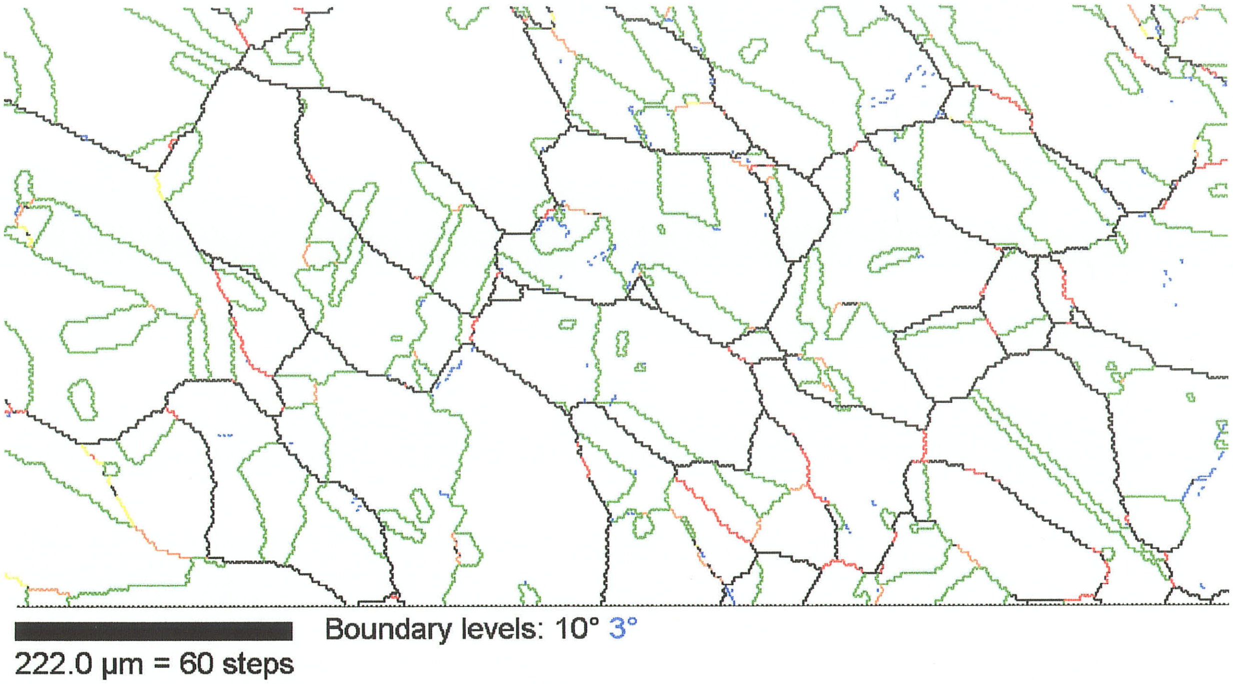

(a)

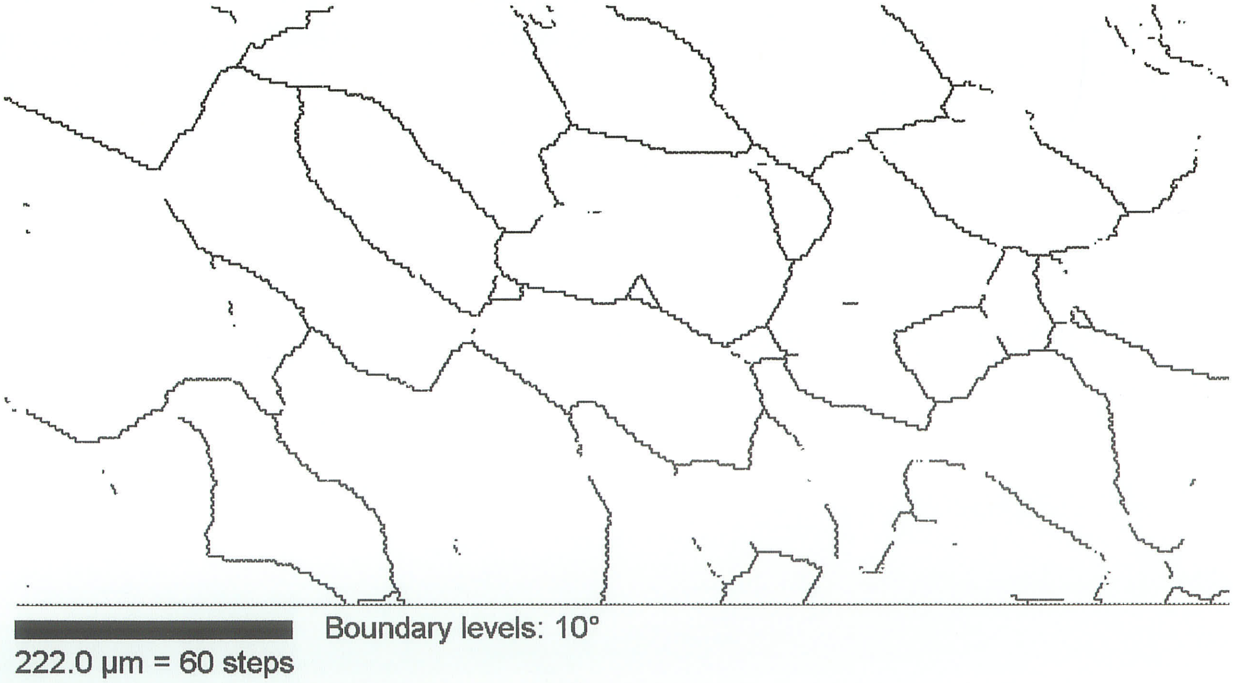

(b)

Fig. C26 (a)-(b) - 4x18%-800°C

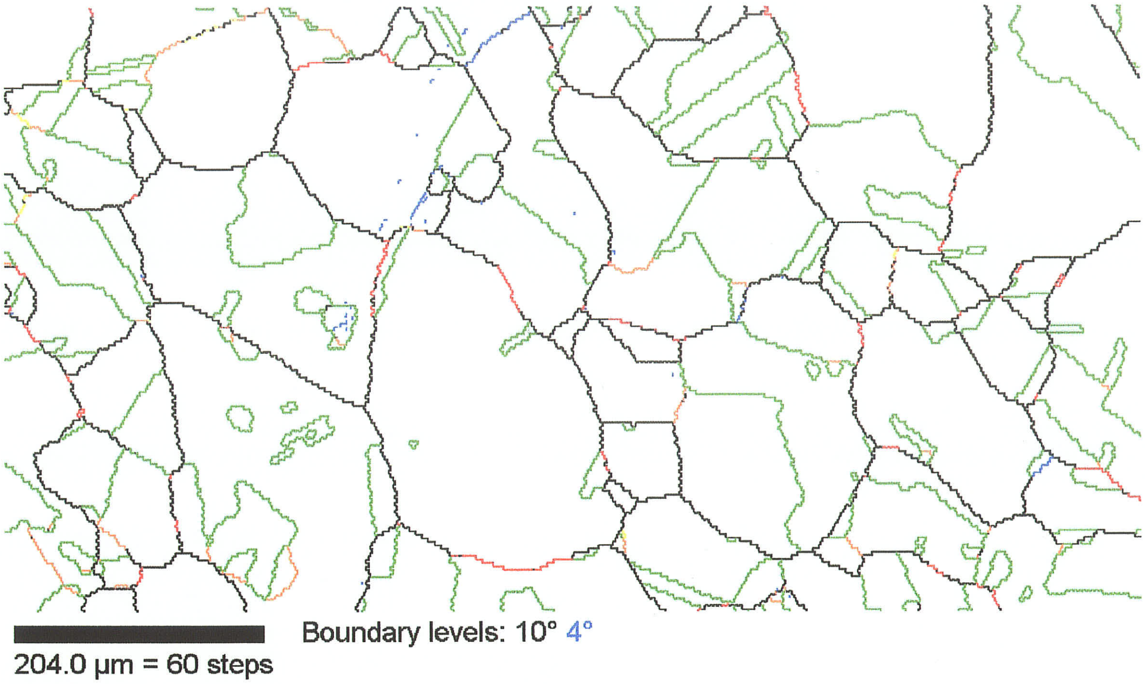

(a)

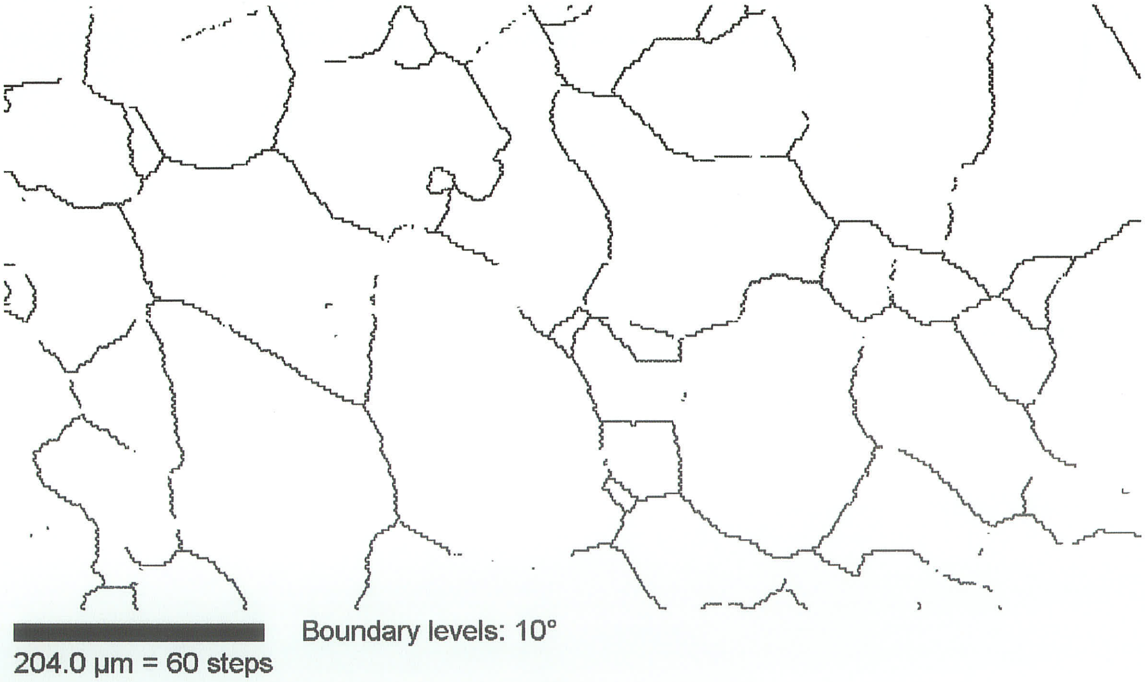

(b)

Fig. C27 (a)-(b) - 6x18%-800°C

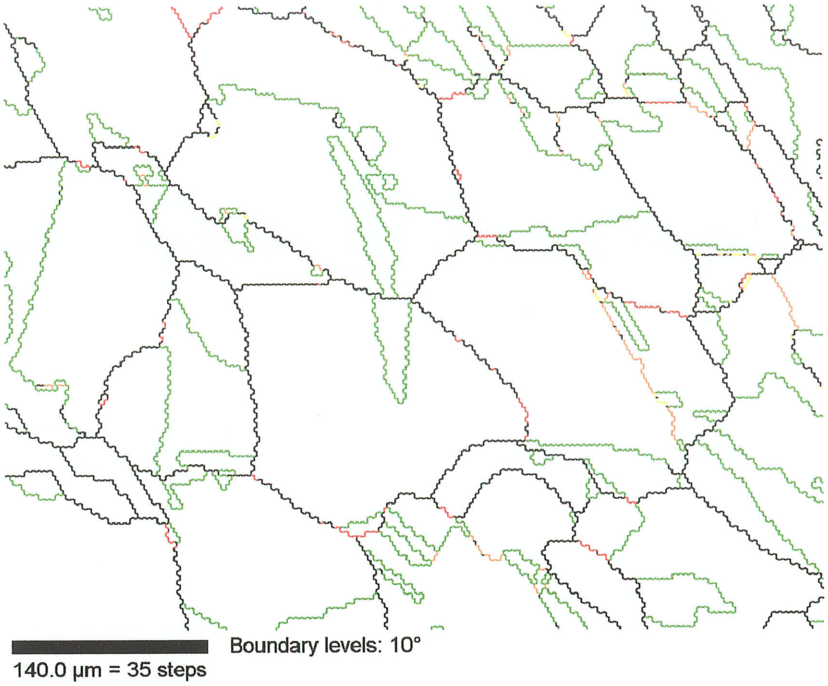

(a)

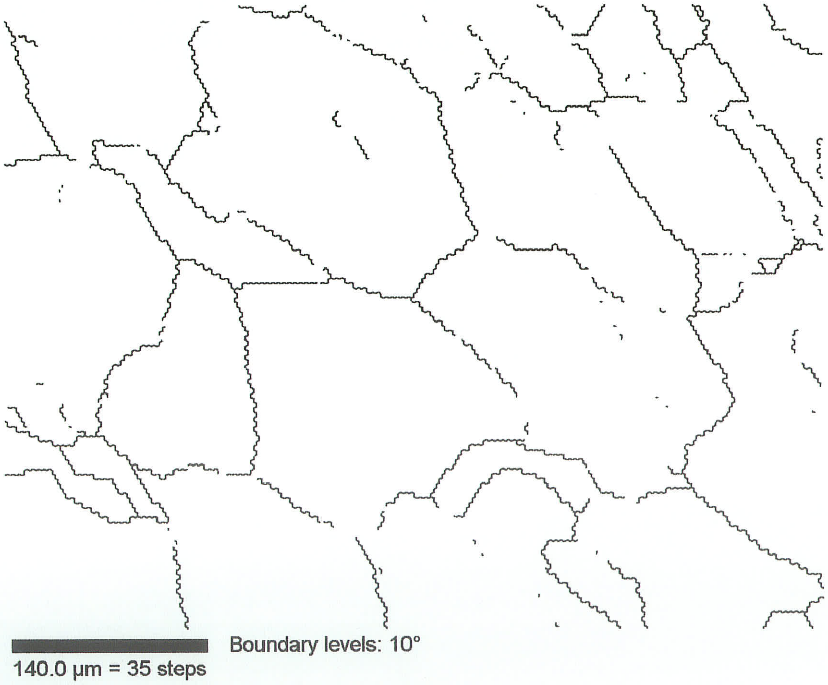

(b)

Fig. C28 (a)-(b) - 1x25%-800°C

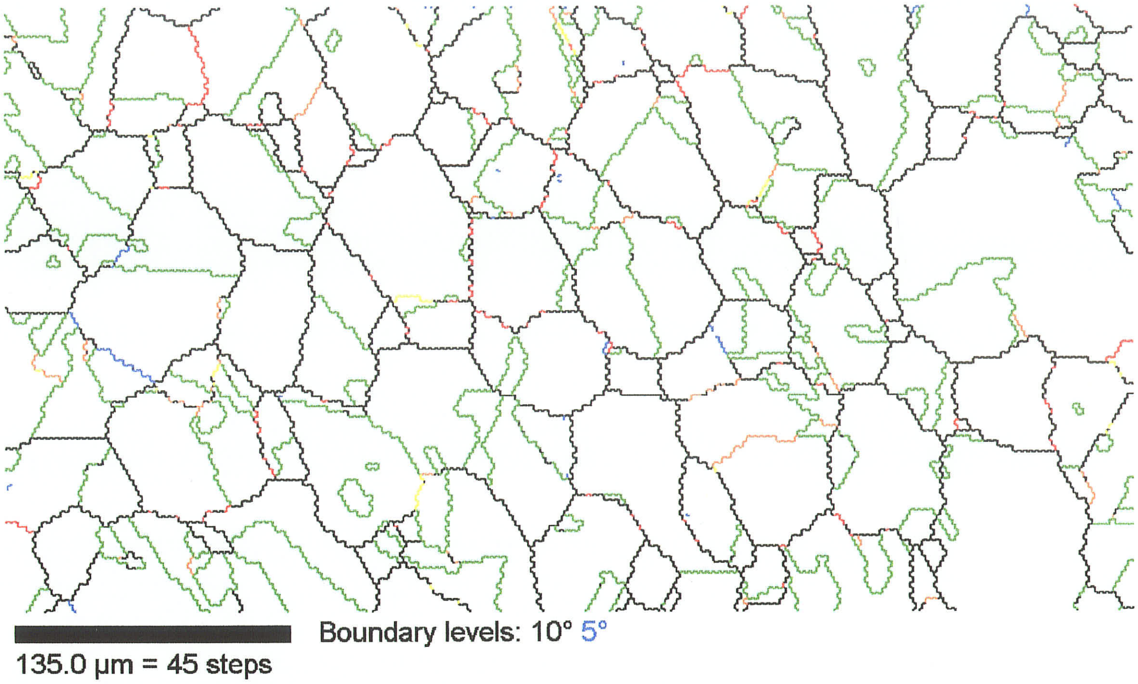

(a)

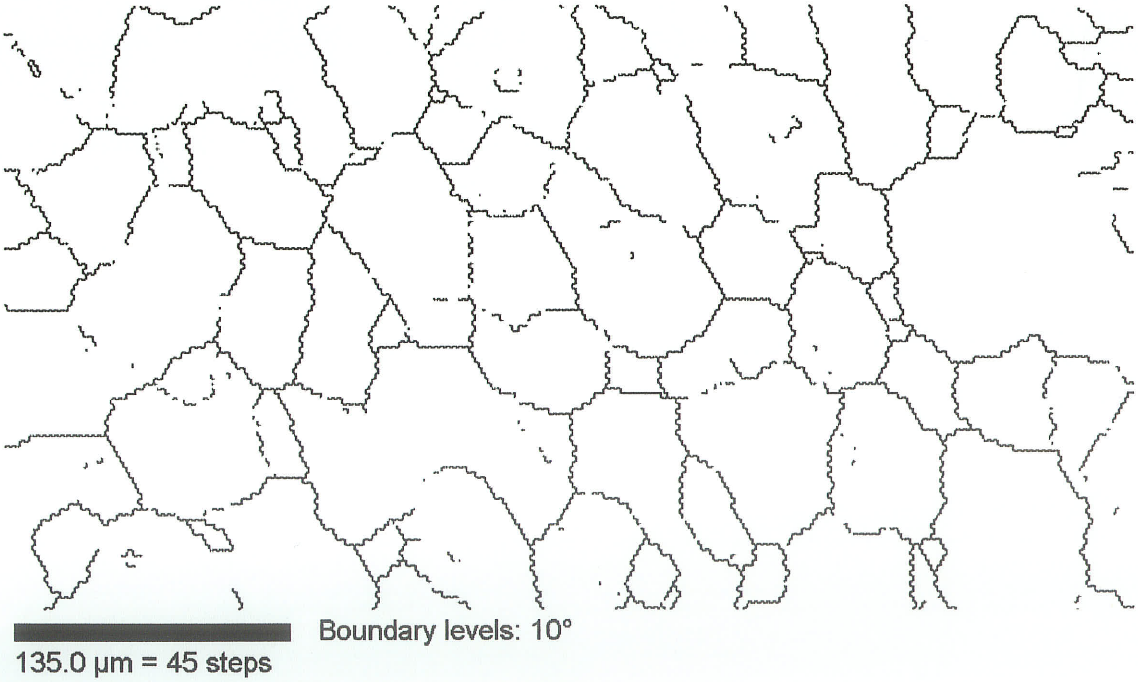

(b)

Fig. C29 (a)-(b) - 3x25%-800°C

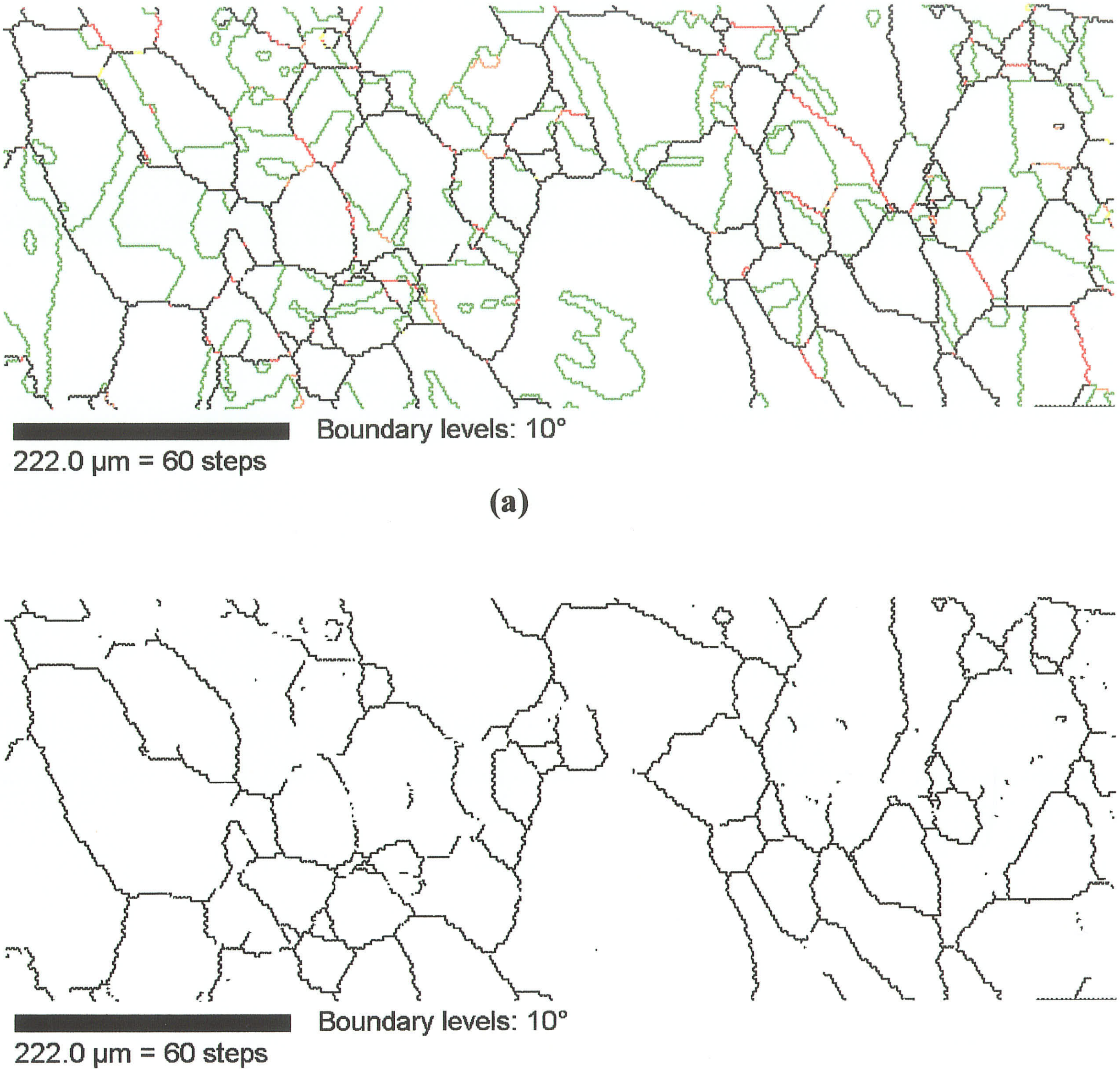

(a)

(b)

Fig. C30 (a)-(b) - 6x25%-800°C

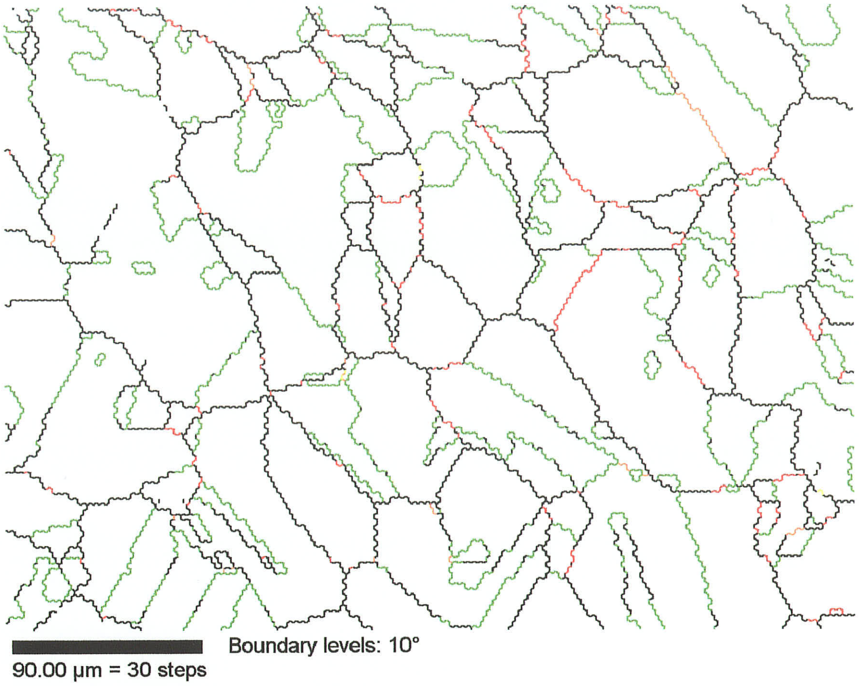

(a)

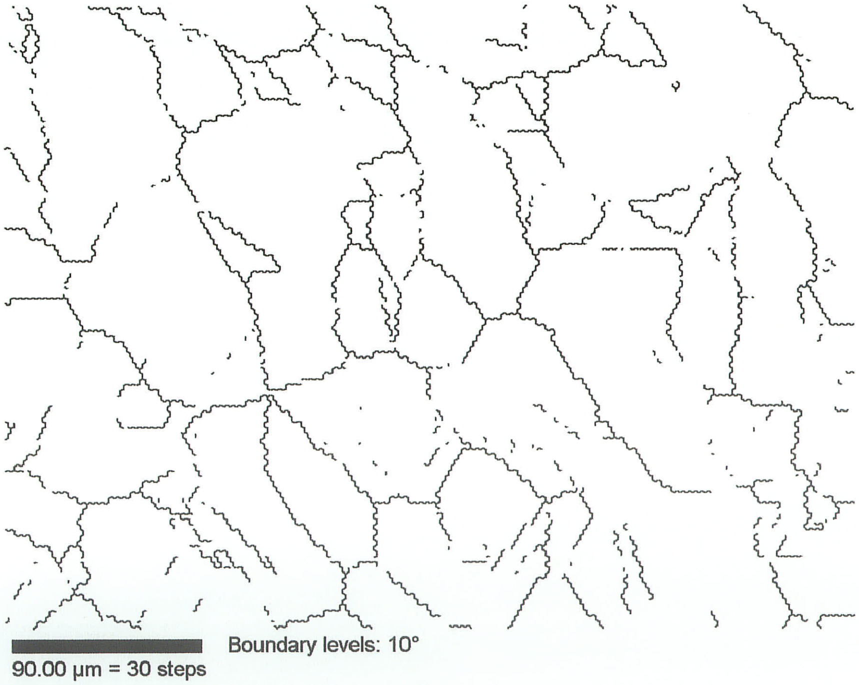

(b)

Fig. C31 (a)-(b) - 3x12.5%-825°C

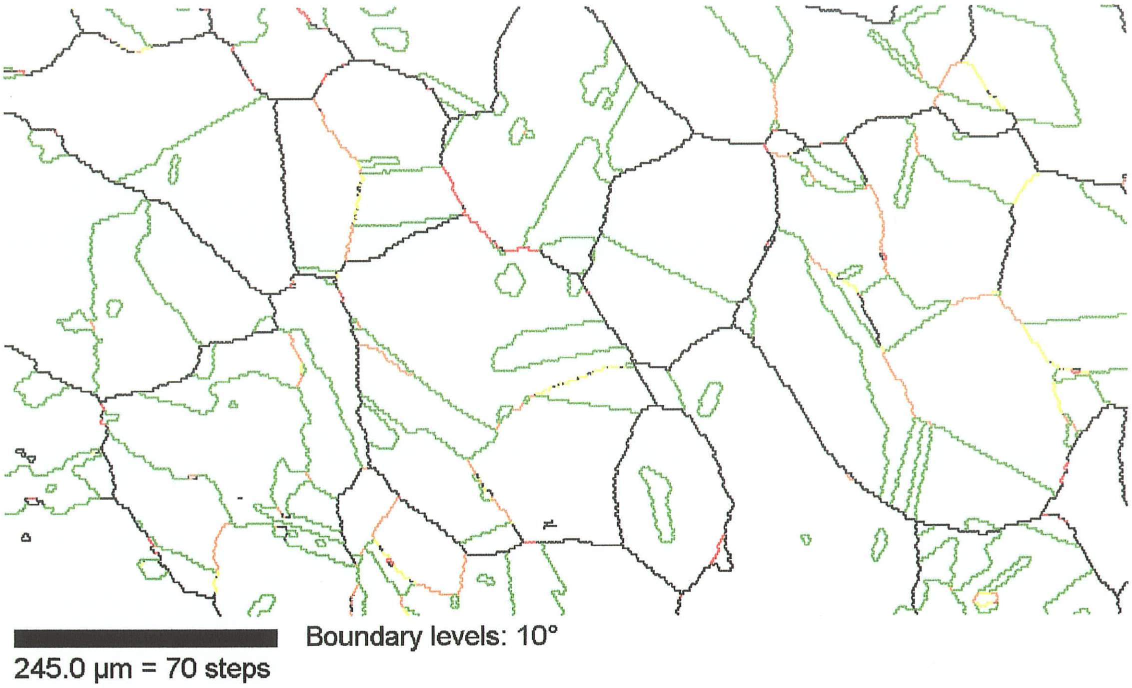

(a)

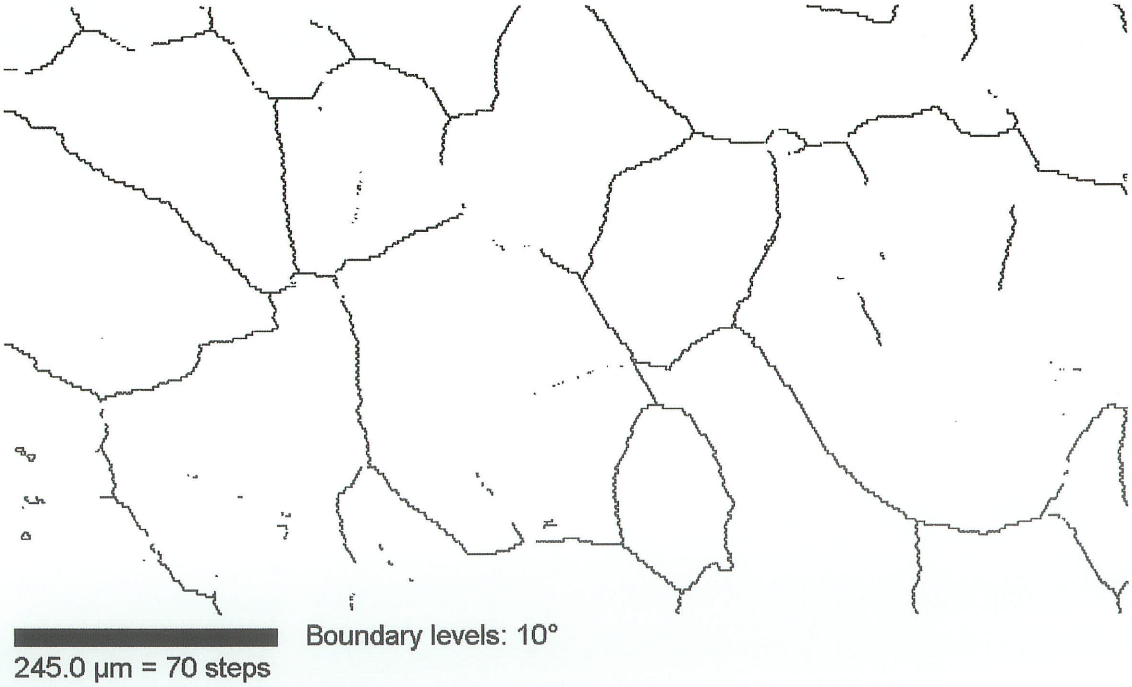

(b)

Fig. C32 (a)-(b) -Annealed only @ 900°C

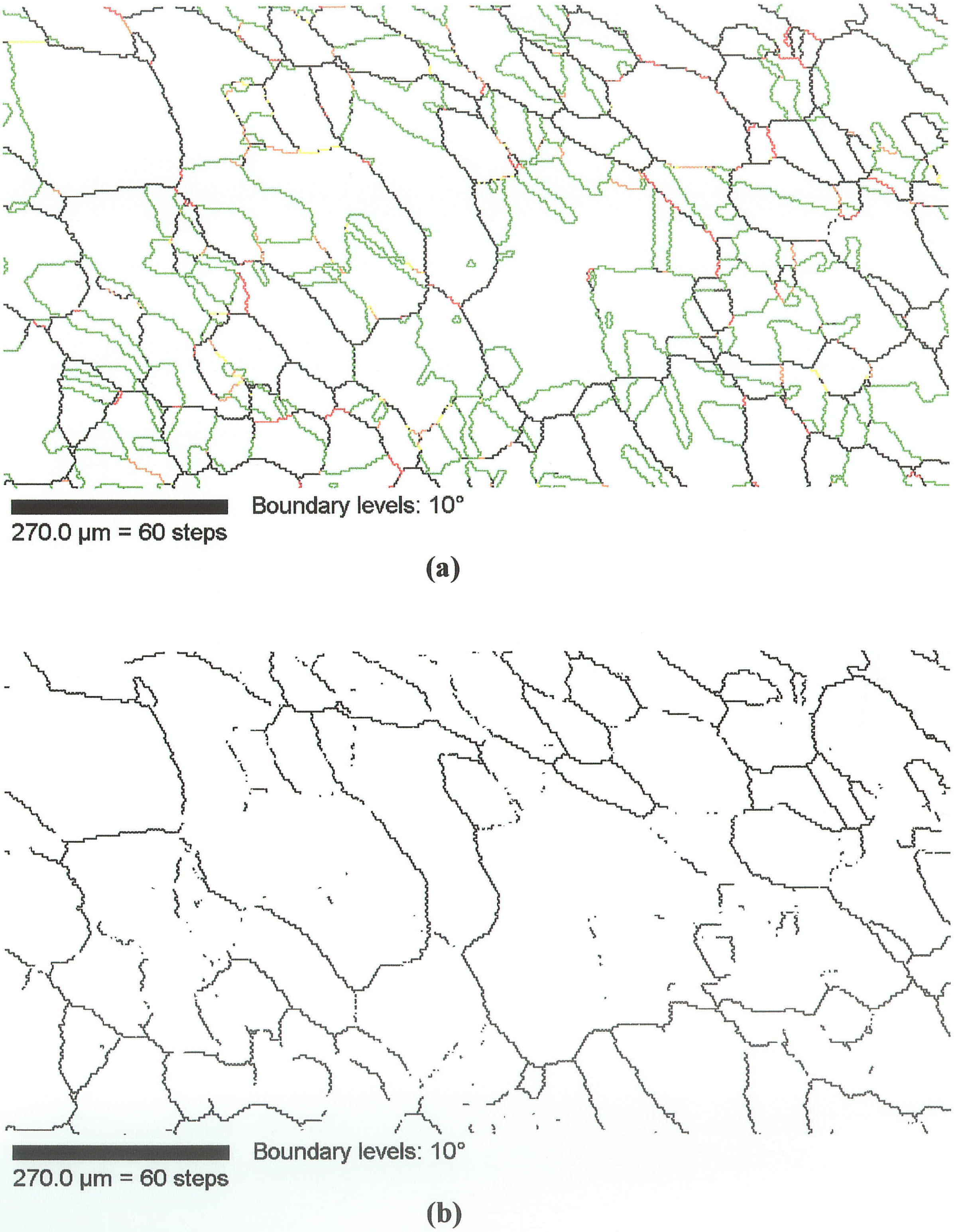

Fig. C33 (a)-(b) -1x2.5%-900°C

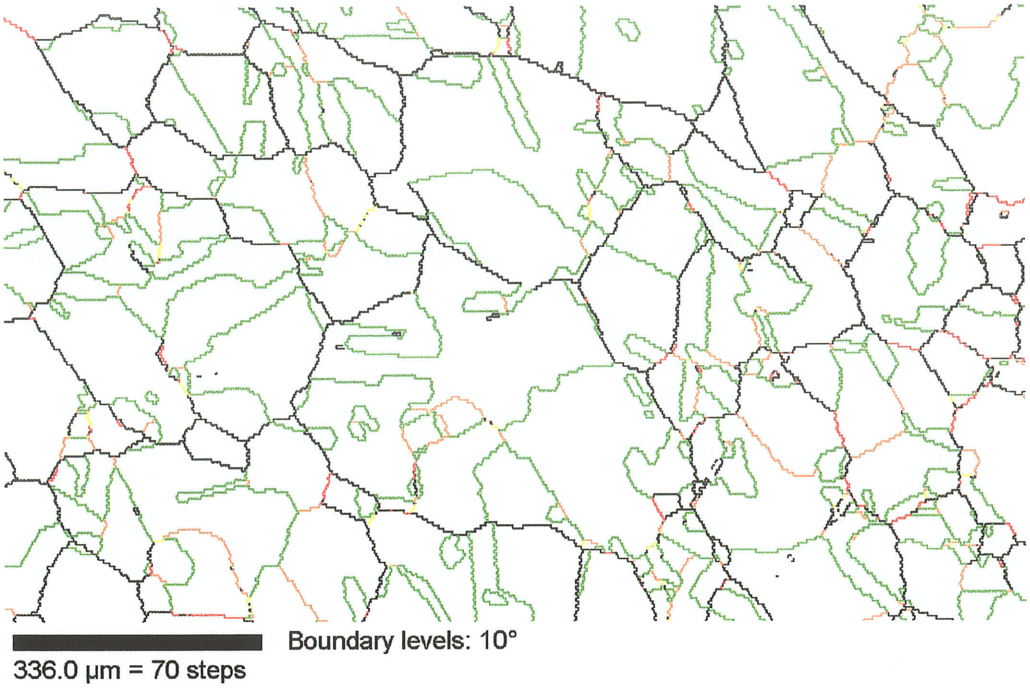

(a)

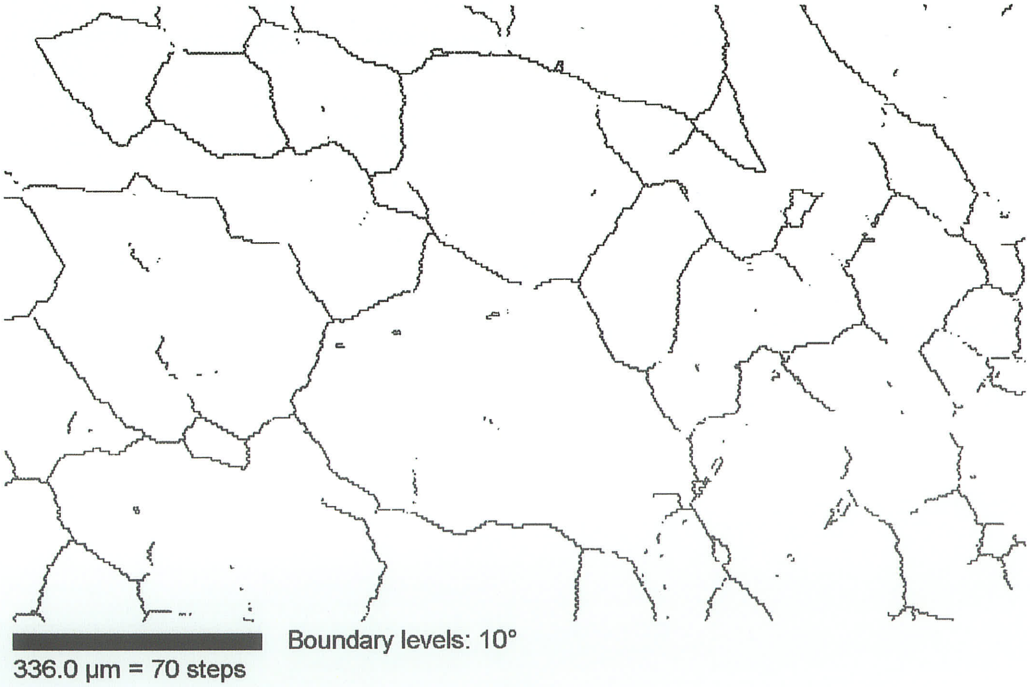

(b)

Fig. C34 (a)-(b) -1x5%-900°C

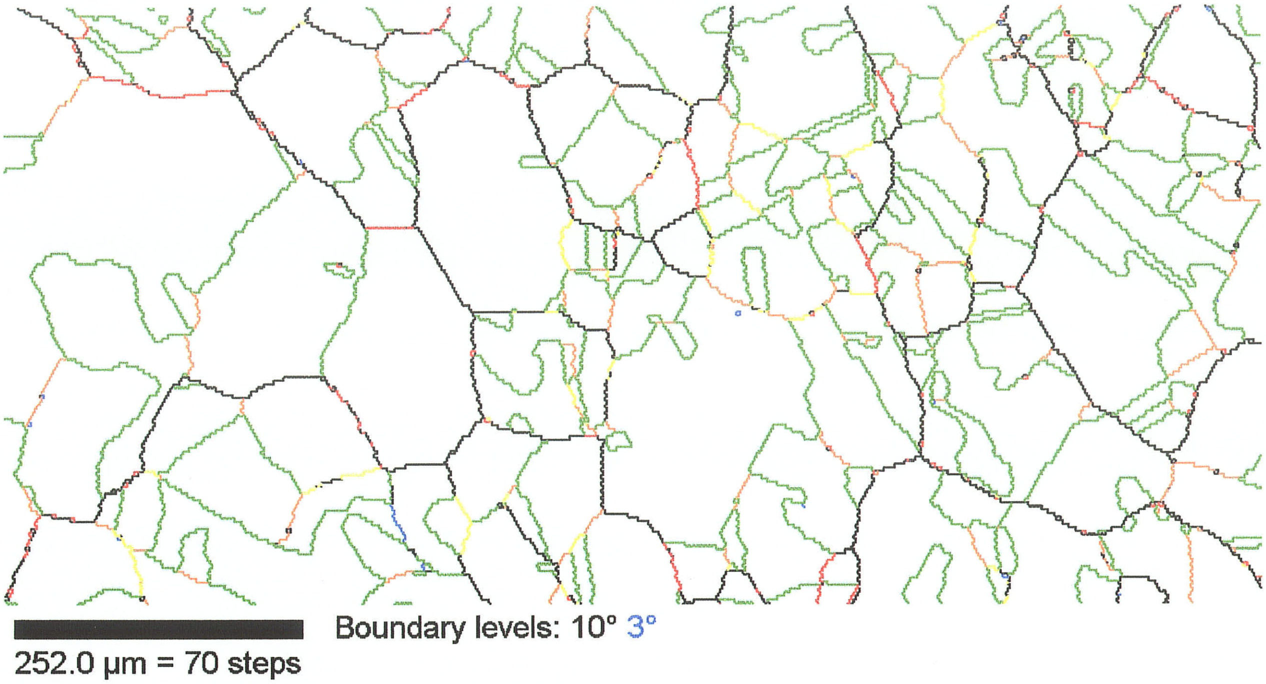

(a)

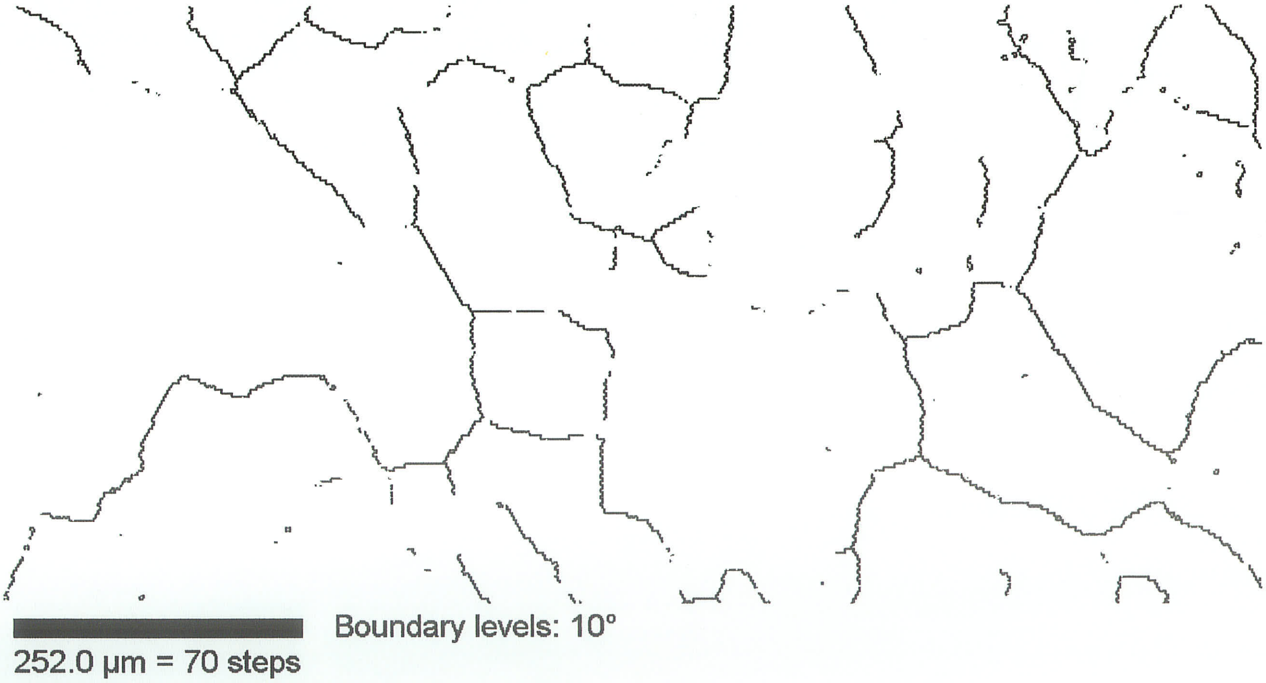

(b)

Fig. C35 (a)-(b) -2x5%-900°C

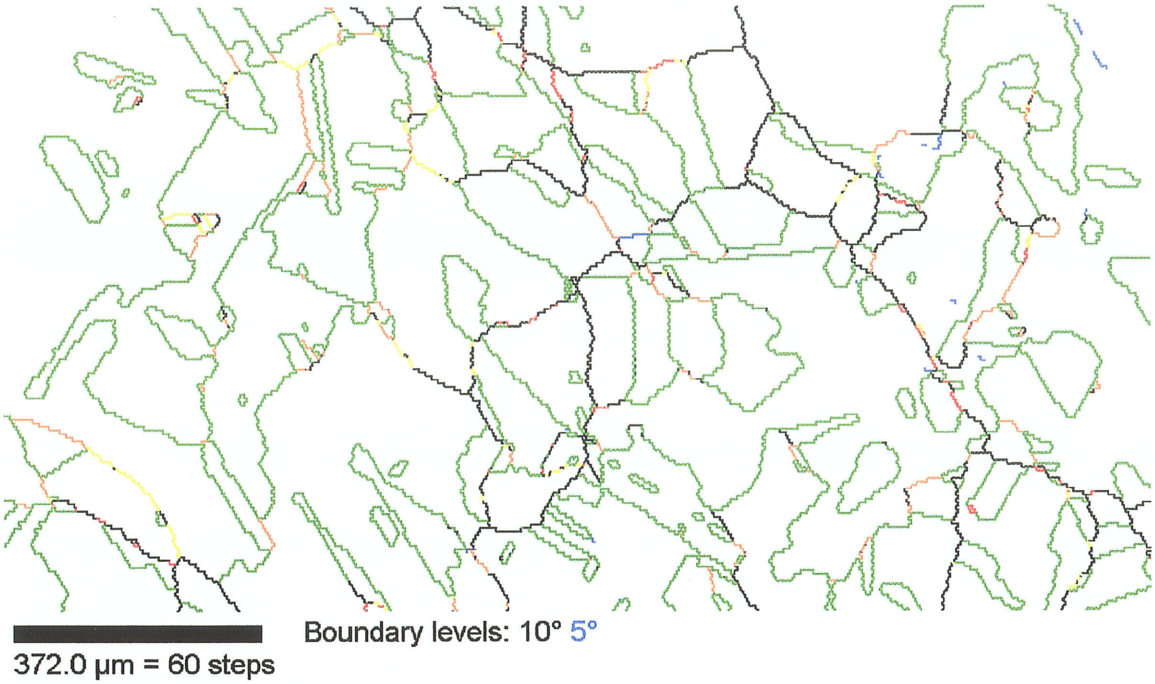

(a)

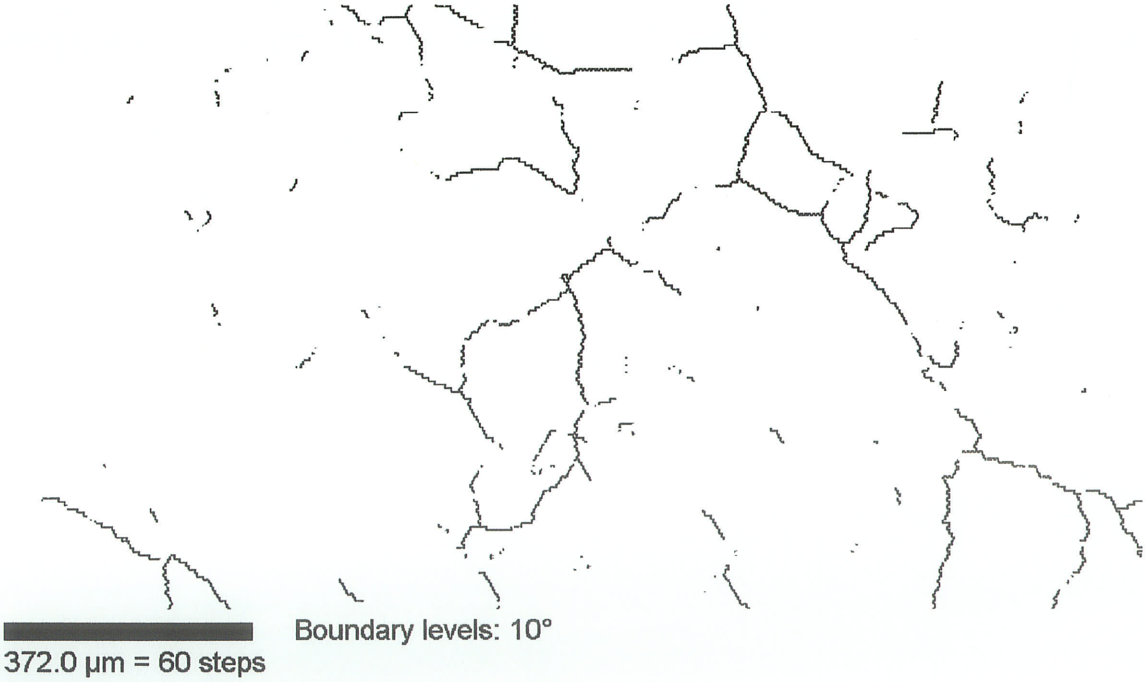

(b)

Fig. C36 (a)-(b) -3x5%-900°C

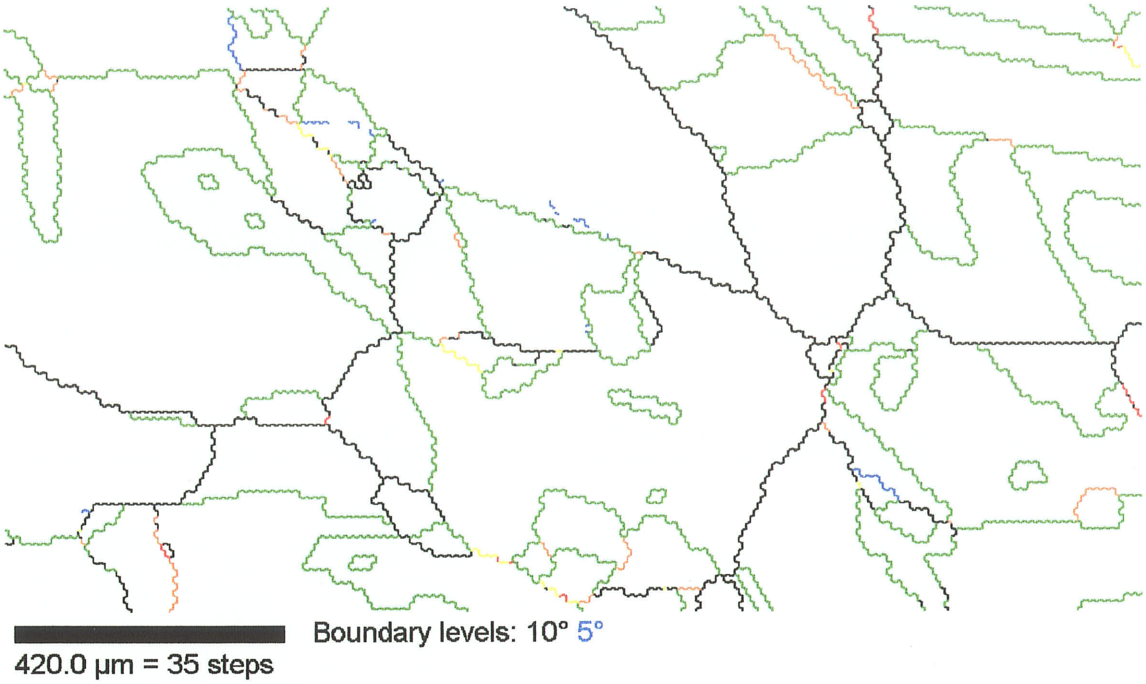

(a)

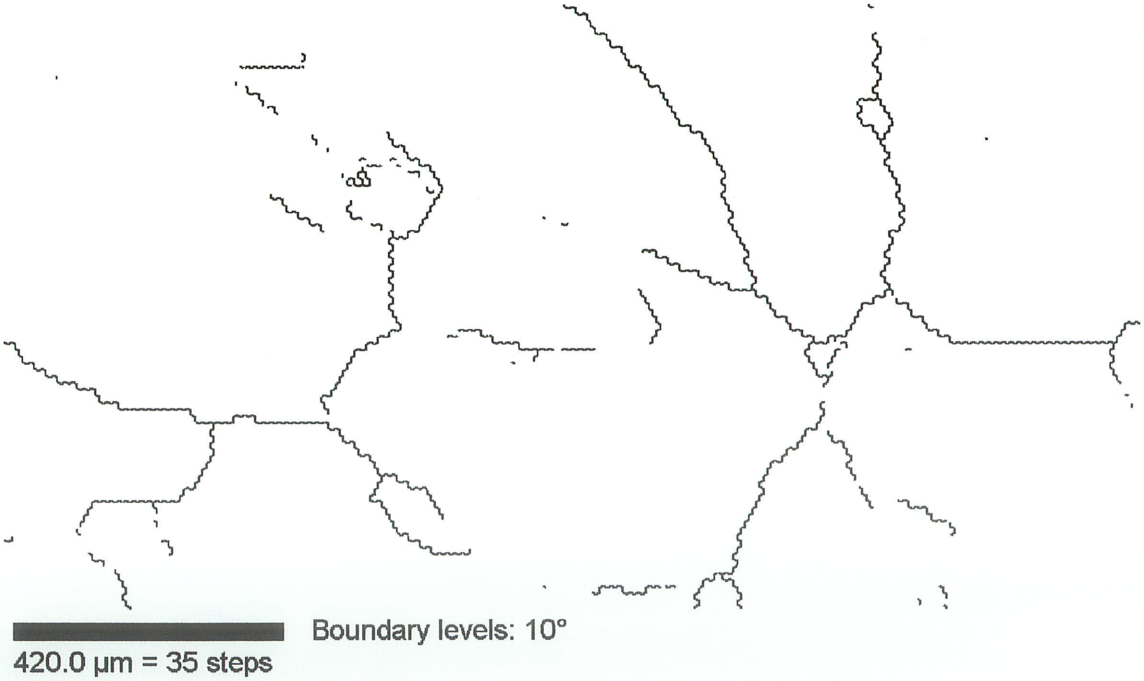

(b)

Fig. C37 (a)-(b) - 5x5%-900°C

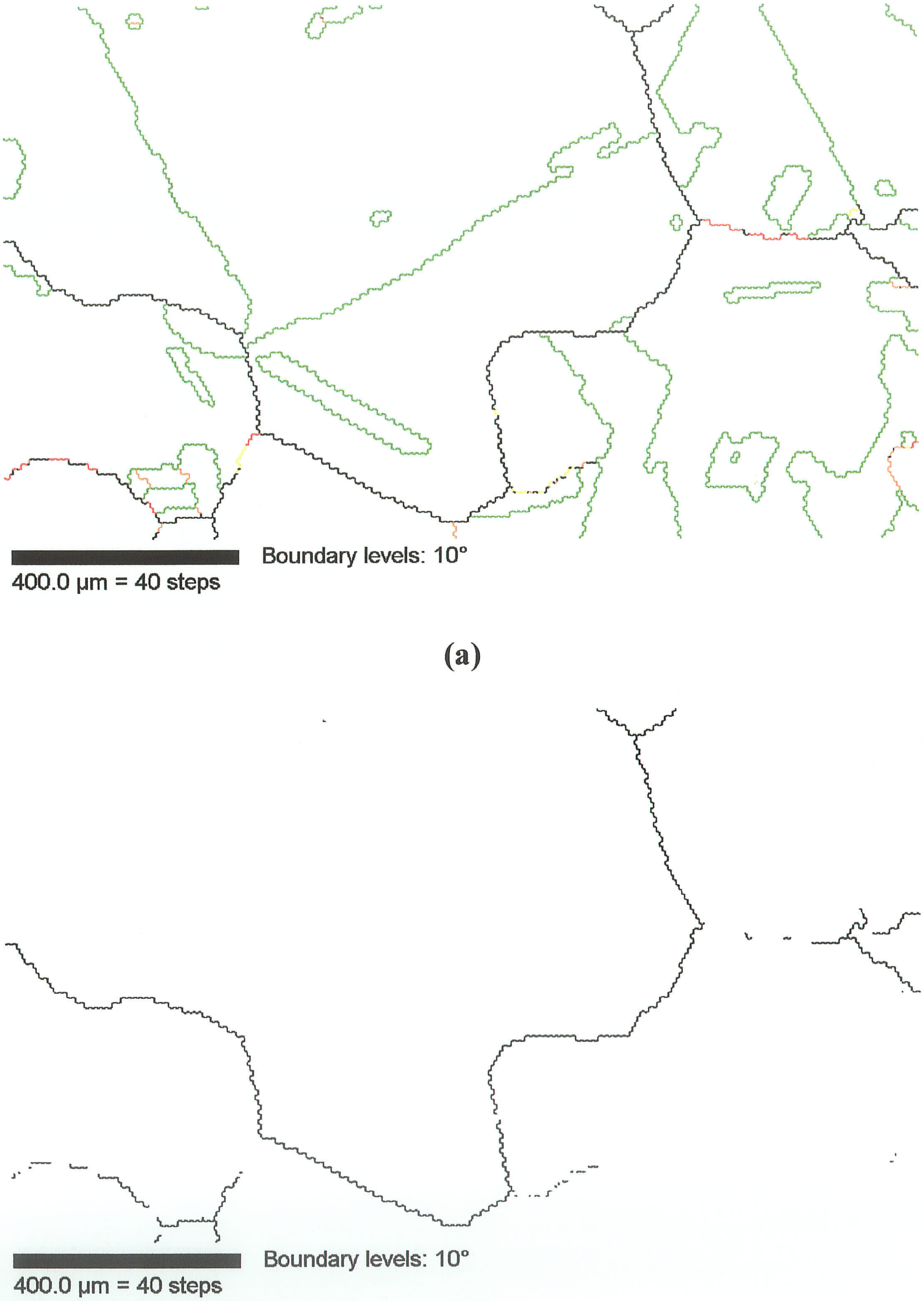

(a)

(b)

Fig. C38 (a)-(b) -1x10%-900°C

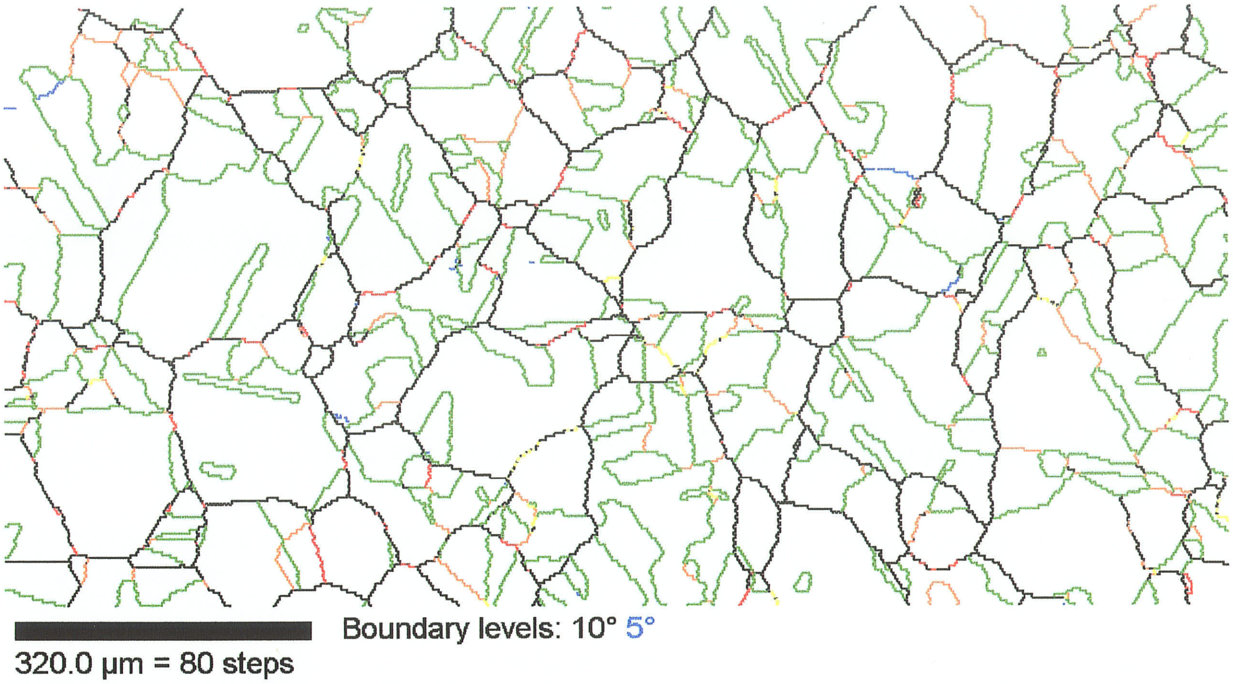

(a)

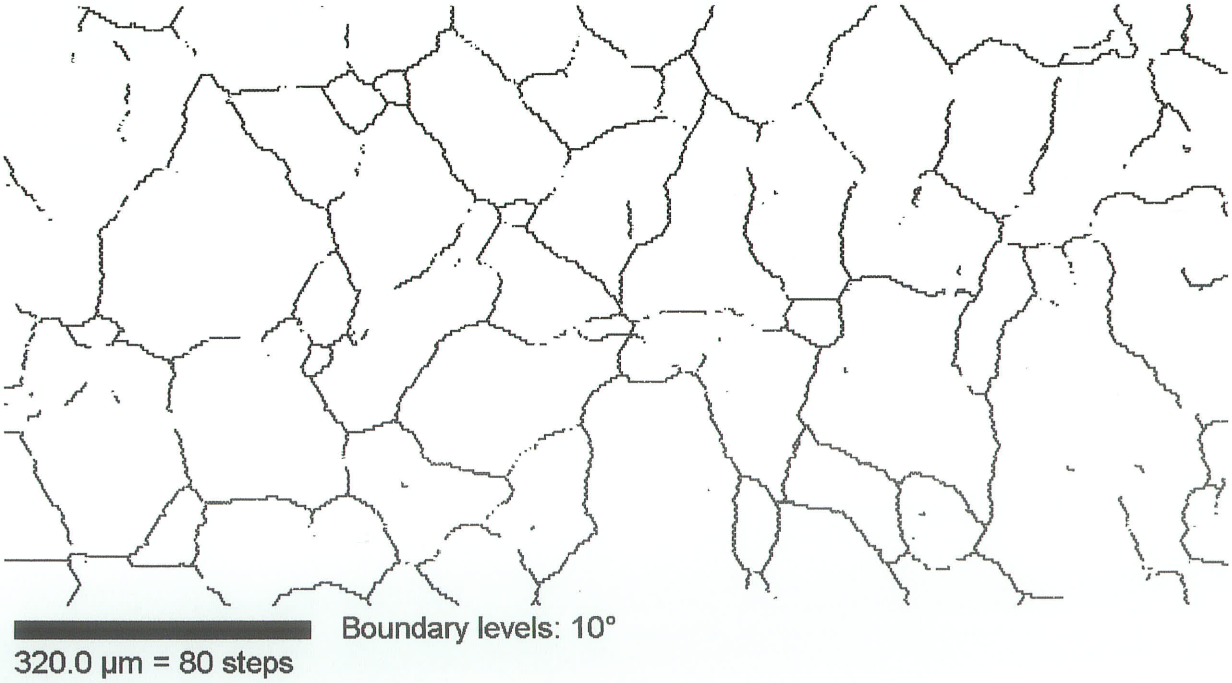

(b)

Fig. C40 (a)-(b) - 15x10%-900°C

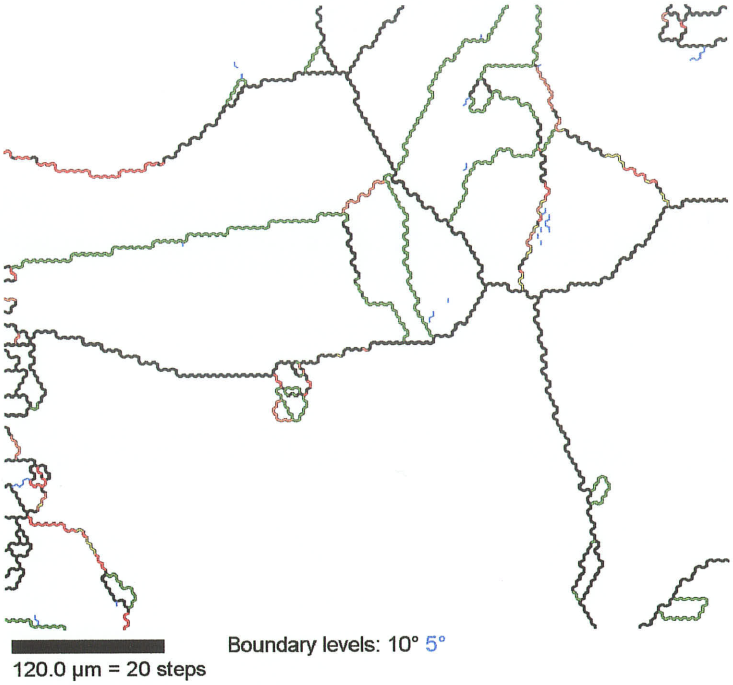

(a)

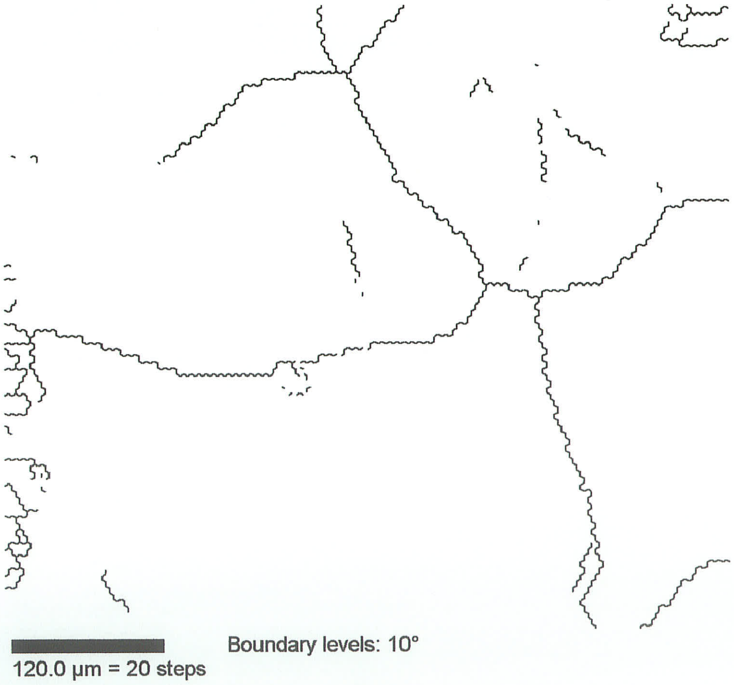

(b)

Fig. C41 (a)-(b) - 1x20%-900°C

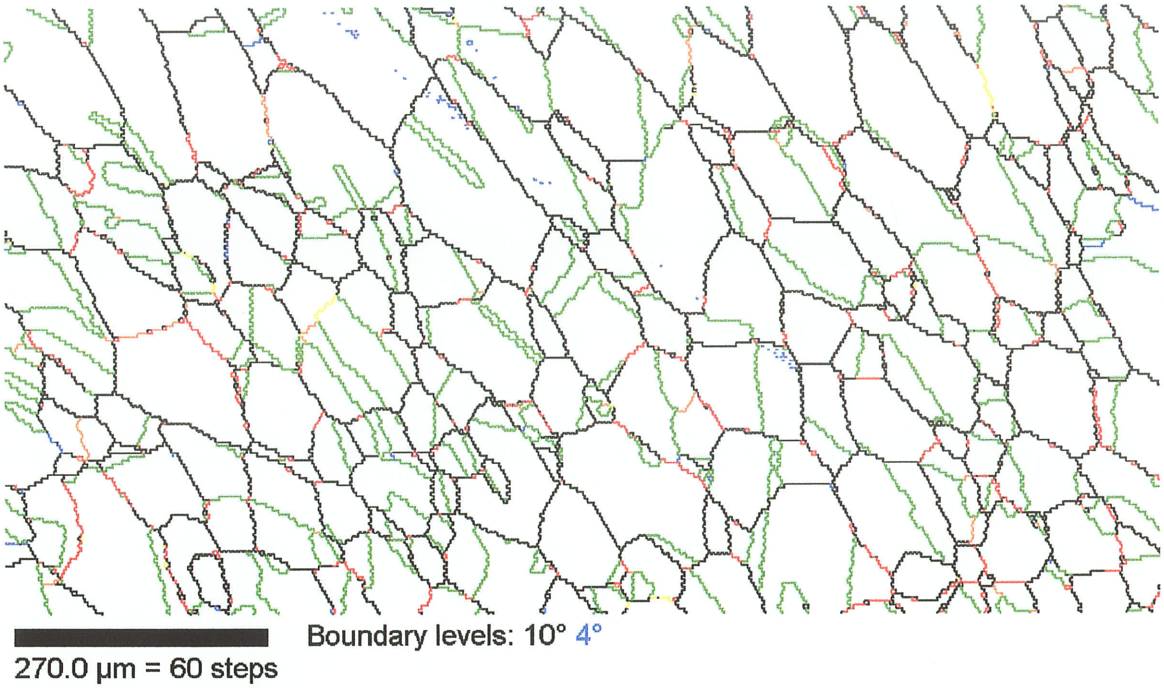

(a)

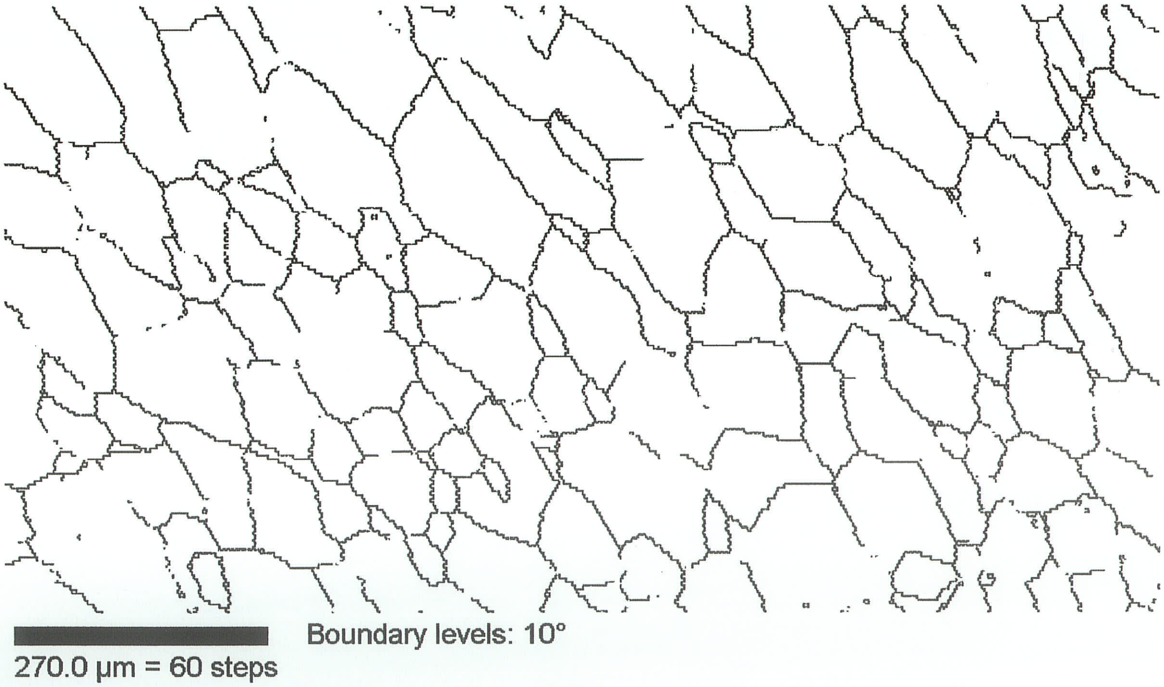

(b)

Fig. C42 (a)-(b) - 5x20%-900°C

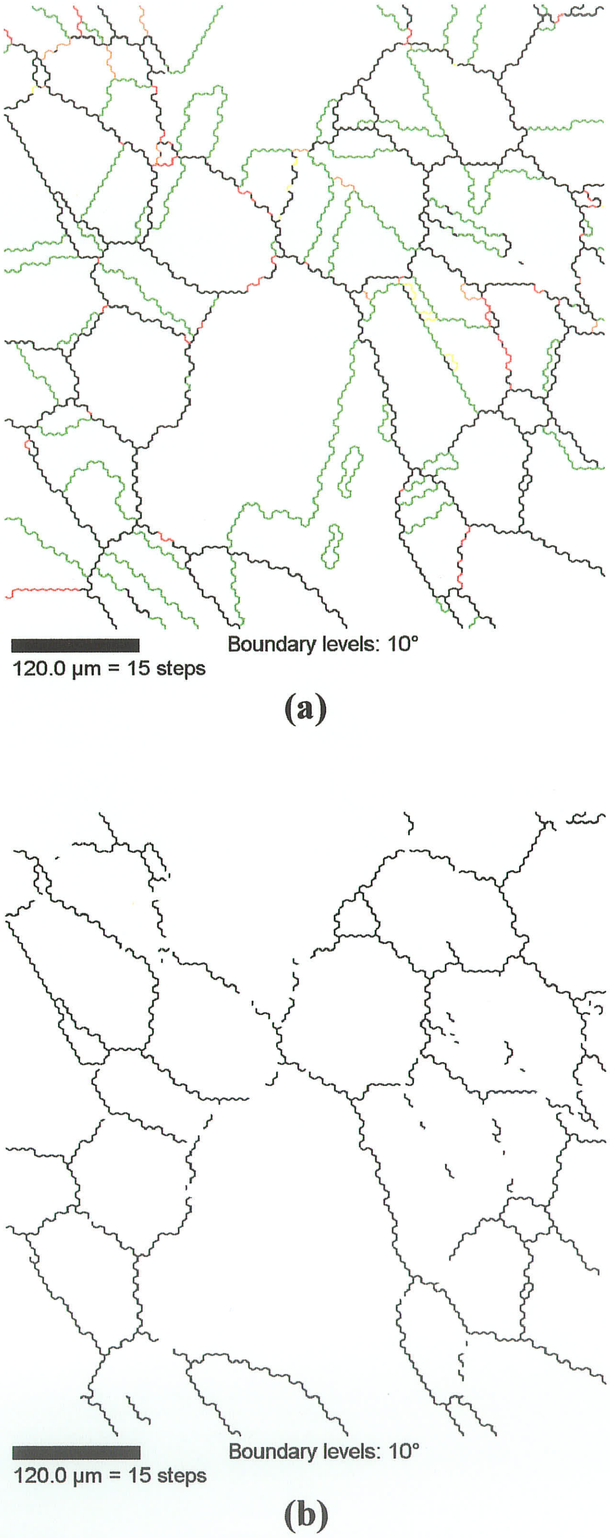

(a)

(b)

Fig. C39 (a)-(b) - 3x10%-900°C

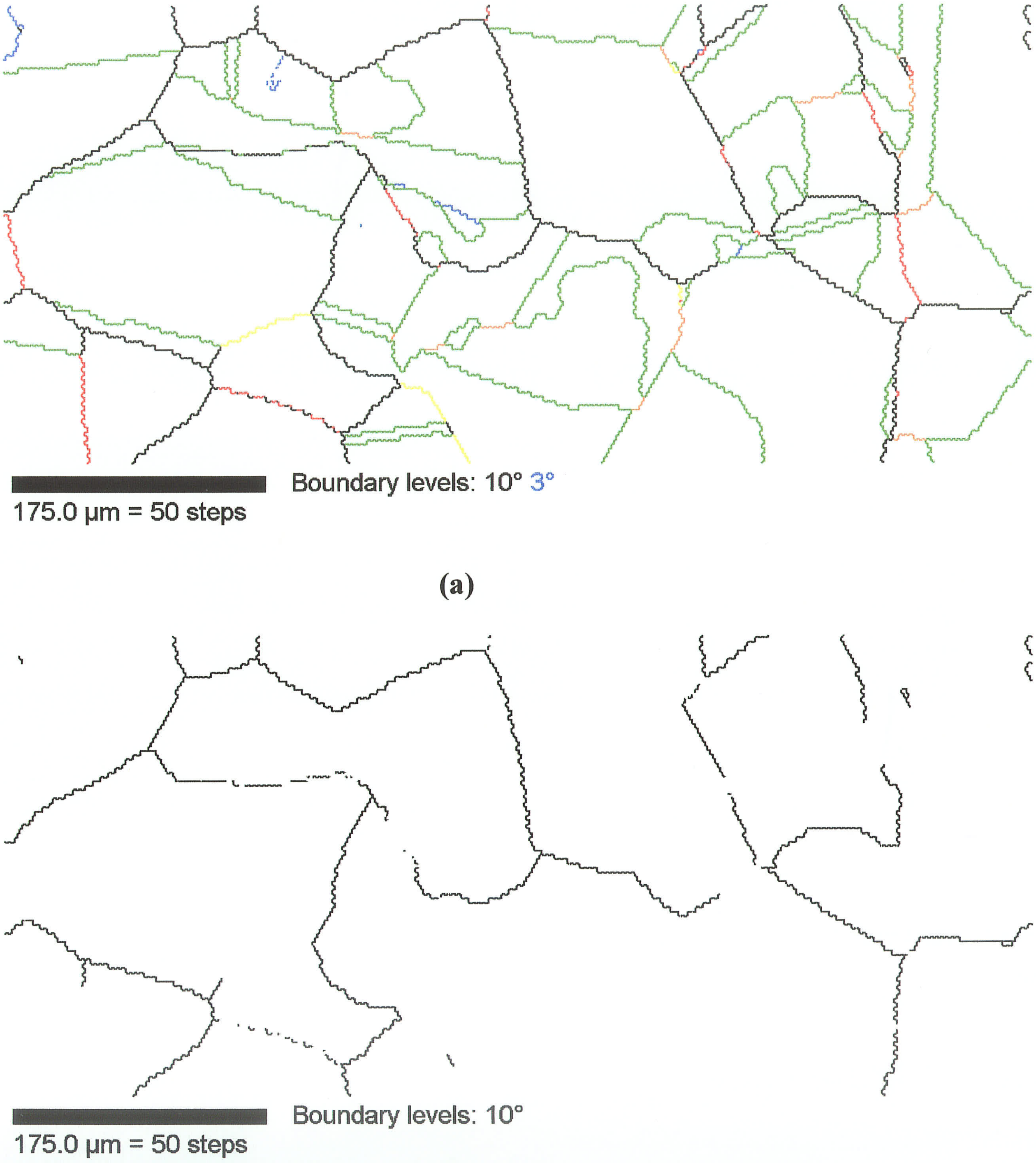

(a)

(b)

Fig. C43 (a)-(b) - 1x25%-900°C

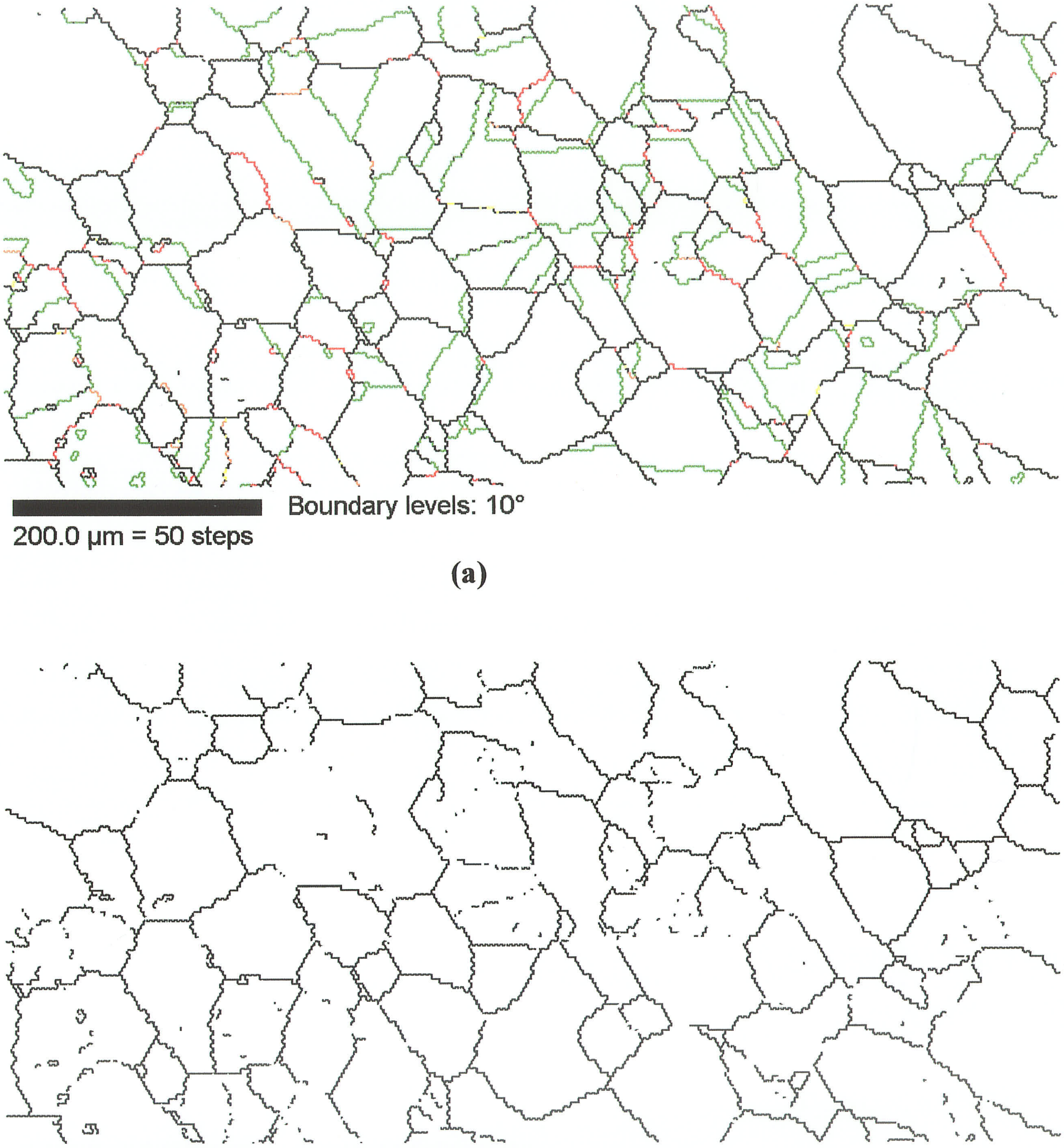

(a)

(b)

Fig. C44 (a)-(b) - 6x25%-900°C

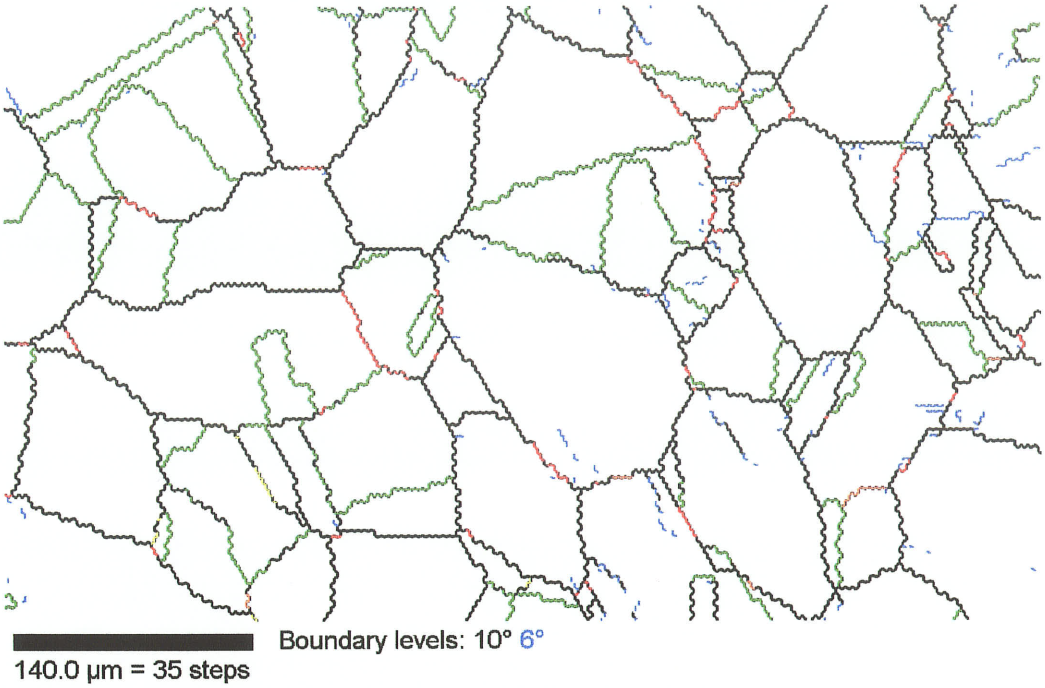

(a)

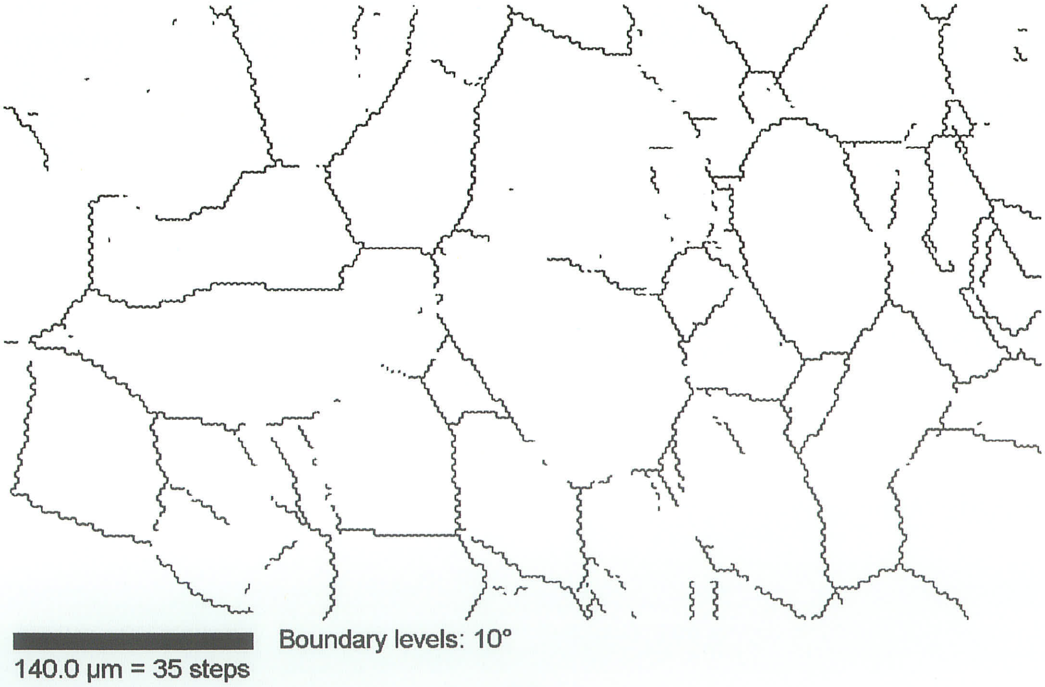

(b)

APPENDIX D

Fsp Profiles for Processed Materials

Figure D1 - Fsp Profiles for 10% and 25% Cold Rolled and Annealed at 600°C Ni-200

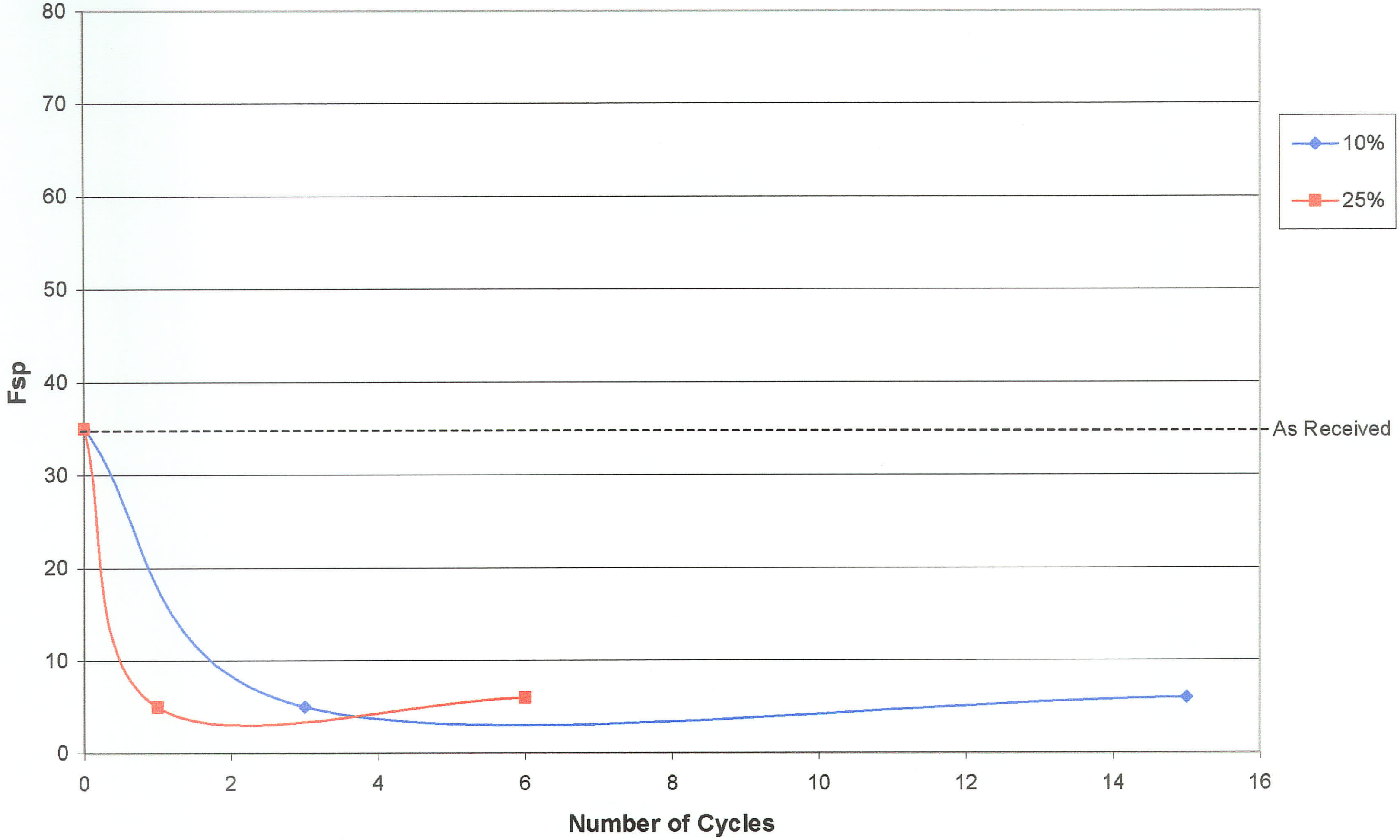

Figure D2 - Fsp Profiles for 10% and 25% Cold Rolled and Annealed at 700°C Ni-200

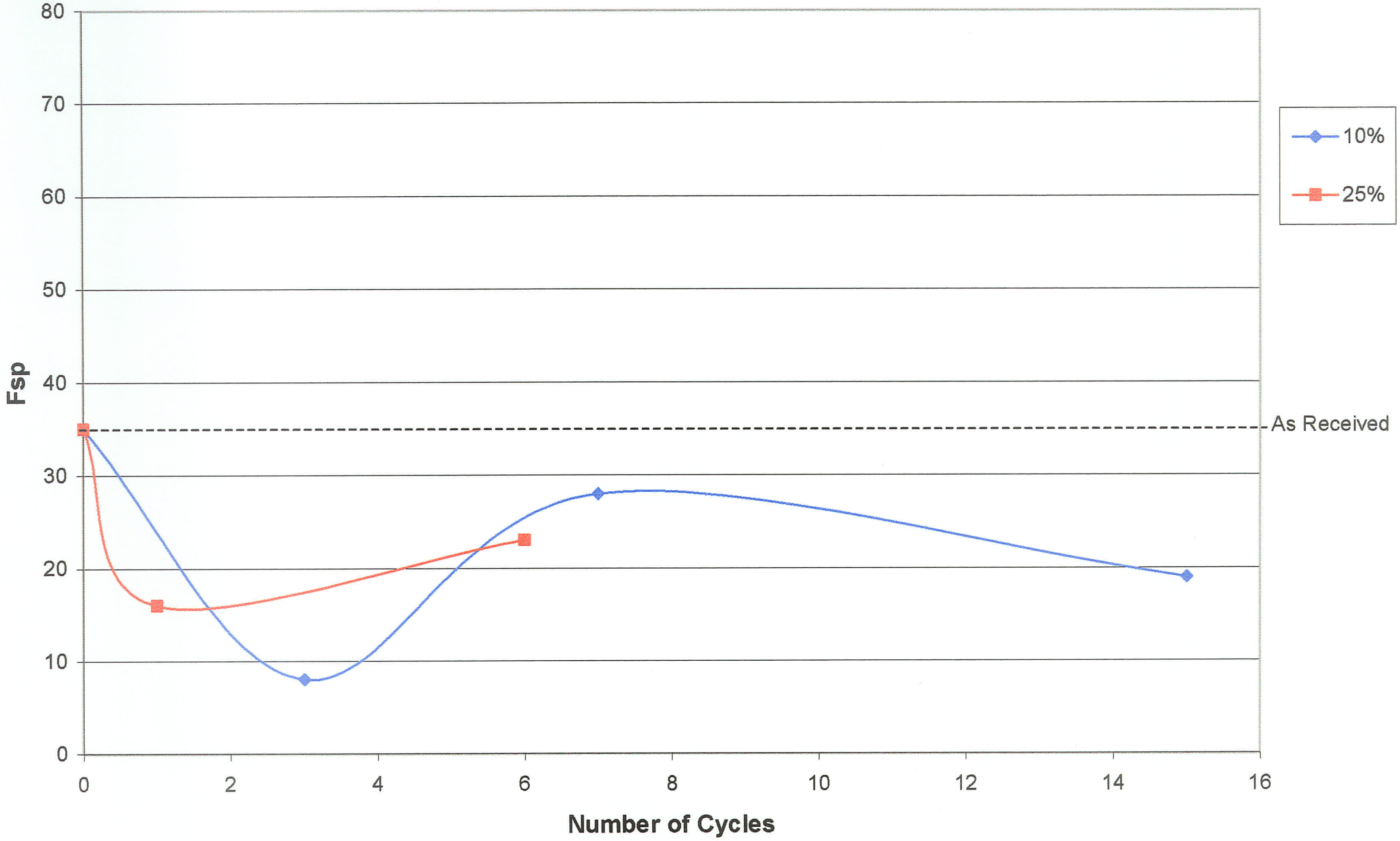

Figure D3 - Fsp Profiles for 5, 18, and 20% Cold Rolled and Annealed at 750°C Ni-200

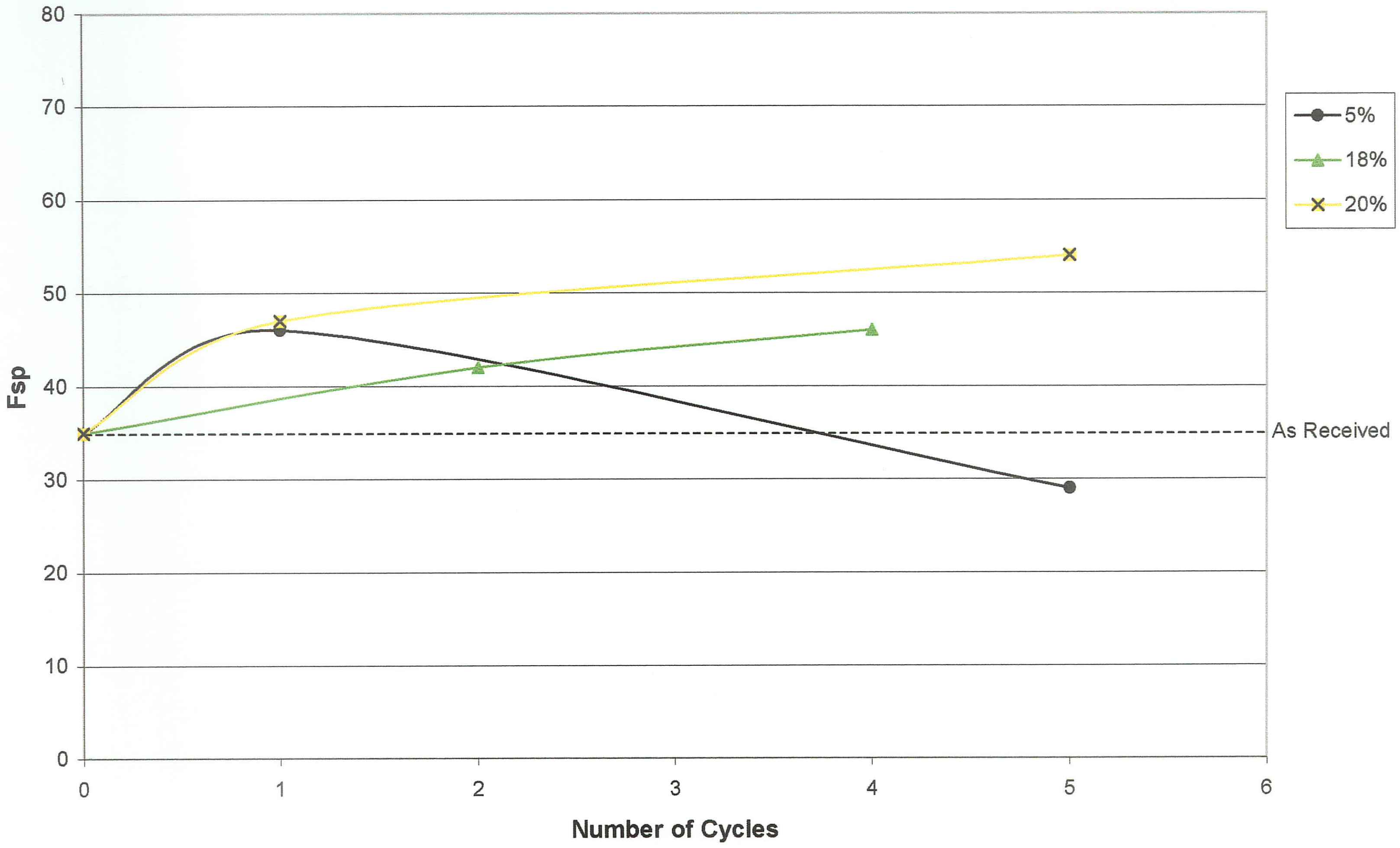

Figure D4 - Fsp Profiles for 5, 18, and 25% Cold Rolled and Annealed at 800°C Ni-200

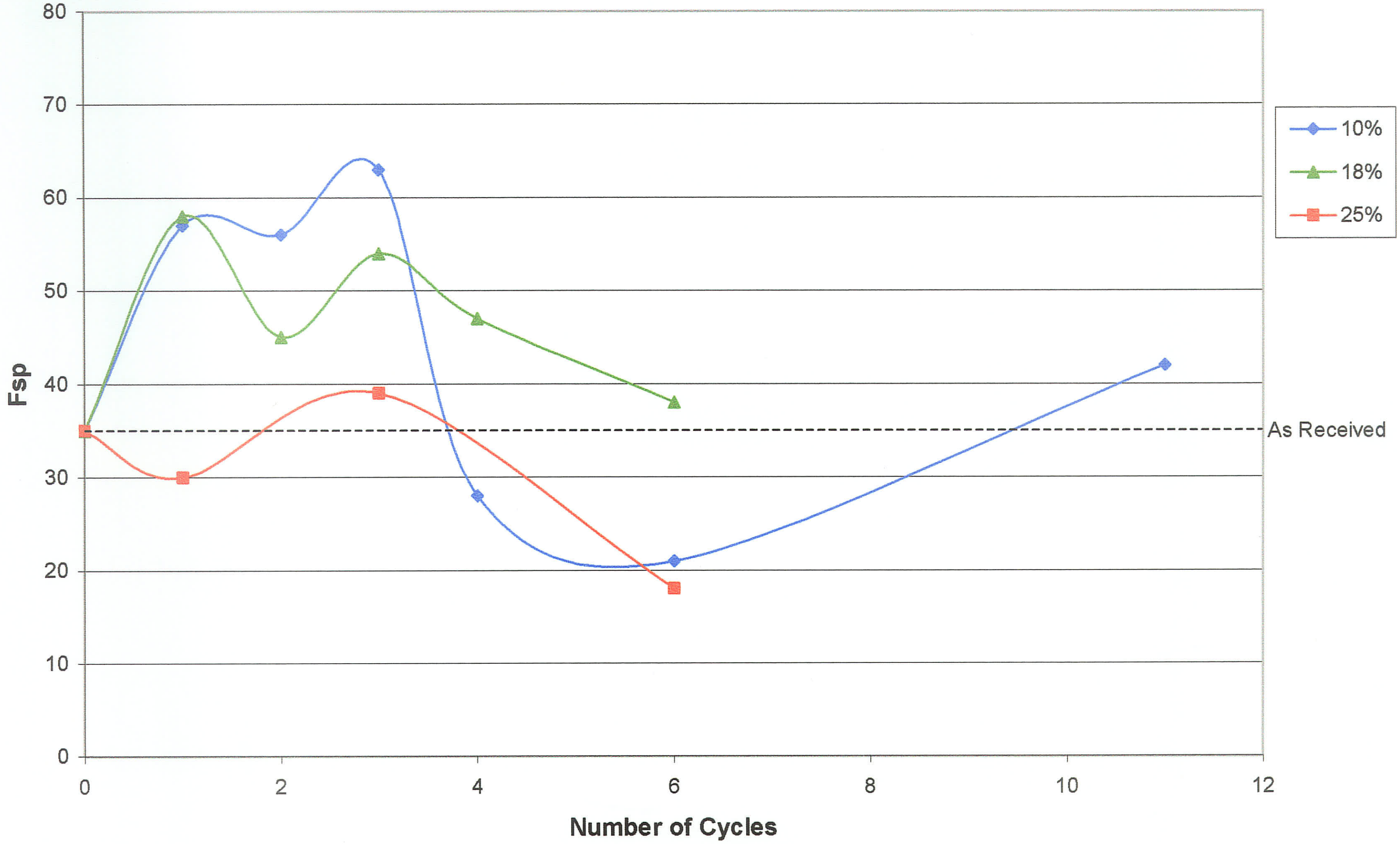

Figure D5 - Fsp and Grain Size for 10% Cold Rolled and Annealed at 800°C Ni-200

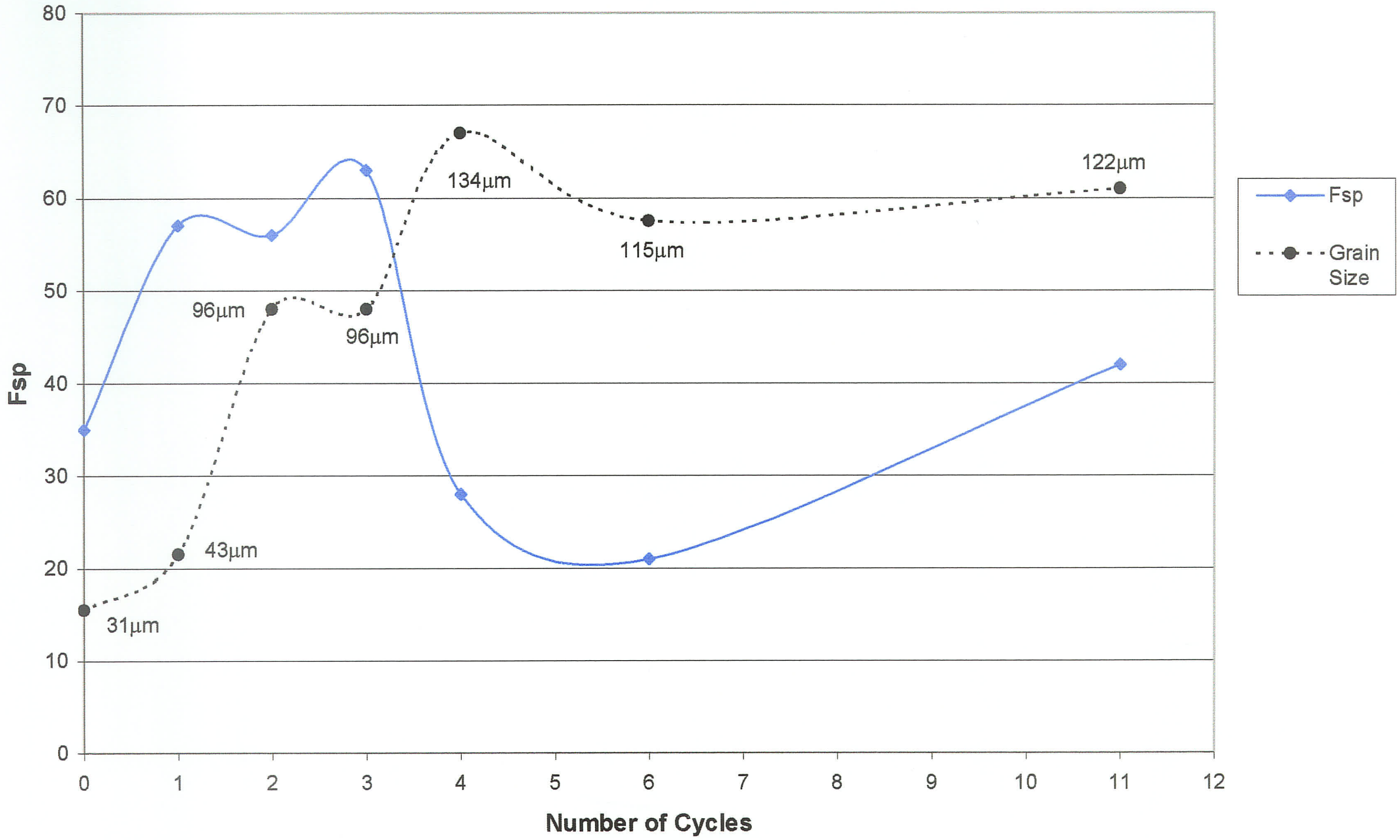

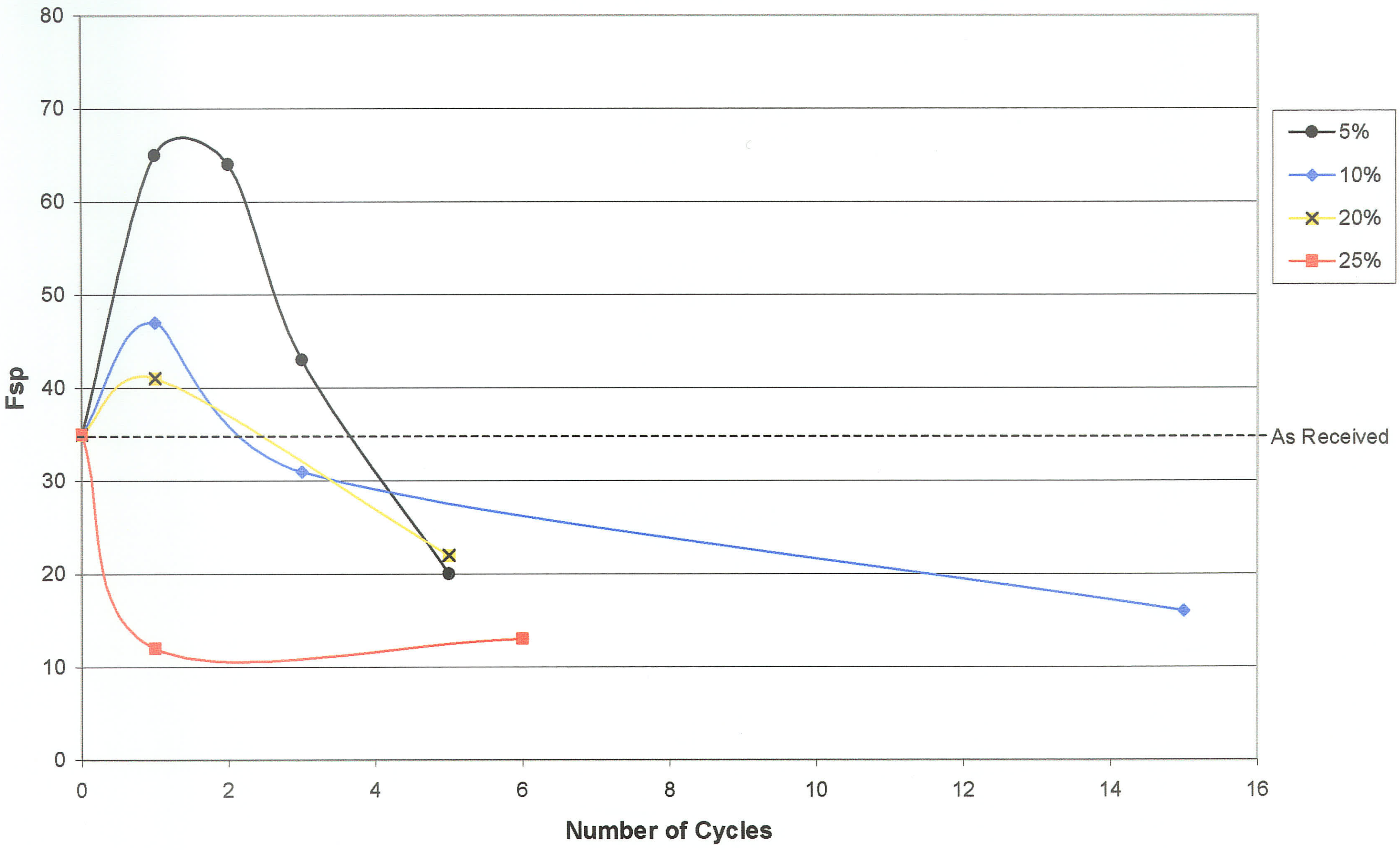

Figure D6 - Fsp Profiles for 5, 10, 20, and 25% Cold Rolled and Annealed at 900°C Ni-200

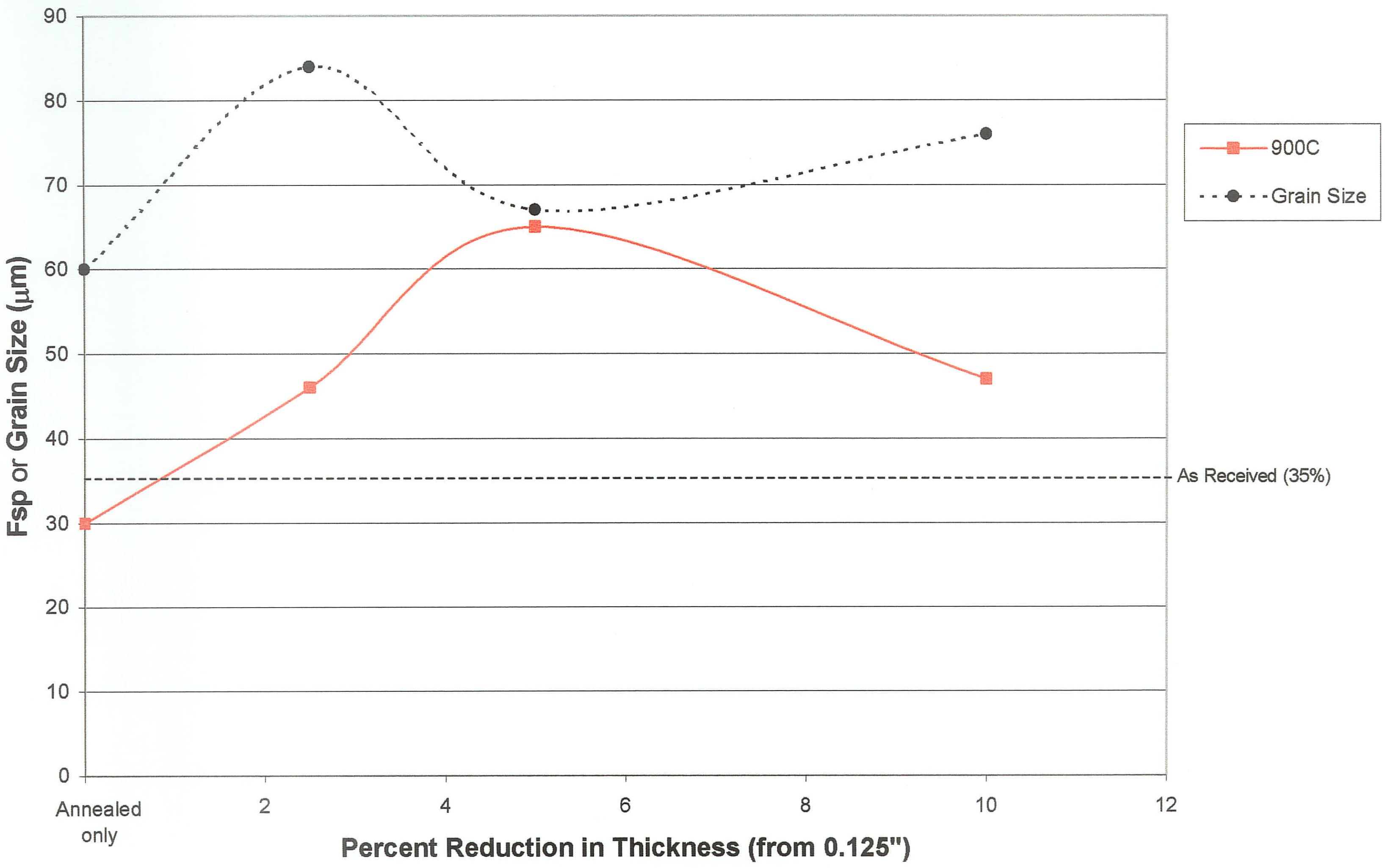

Figure D7 - Fsp and Grain Sizes for One-Step Cold Rolled and Annealed at 900°C Ni-200

Figure D8 - Fsp Profiles for 5% Cold Rolled and Annealed Ni-200

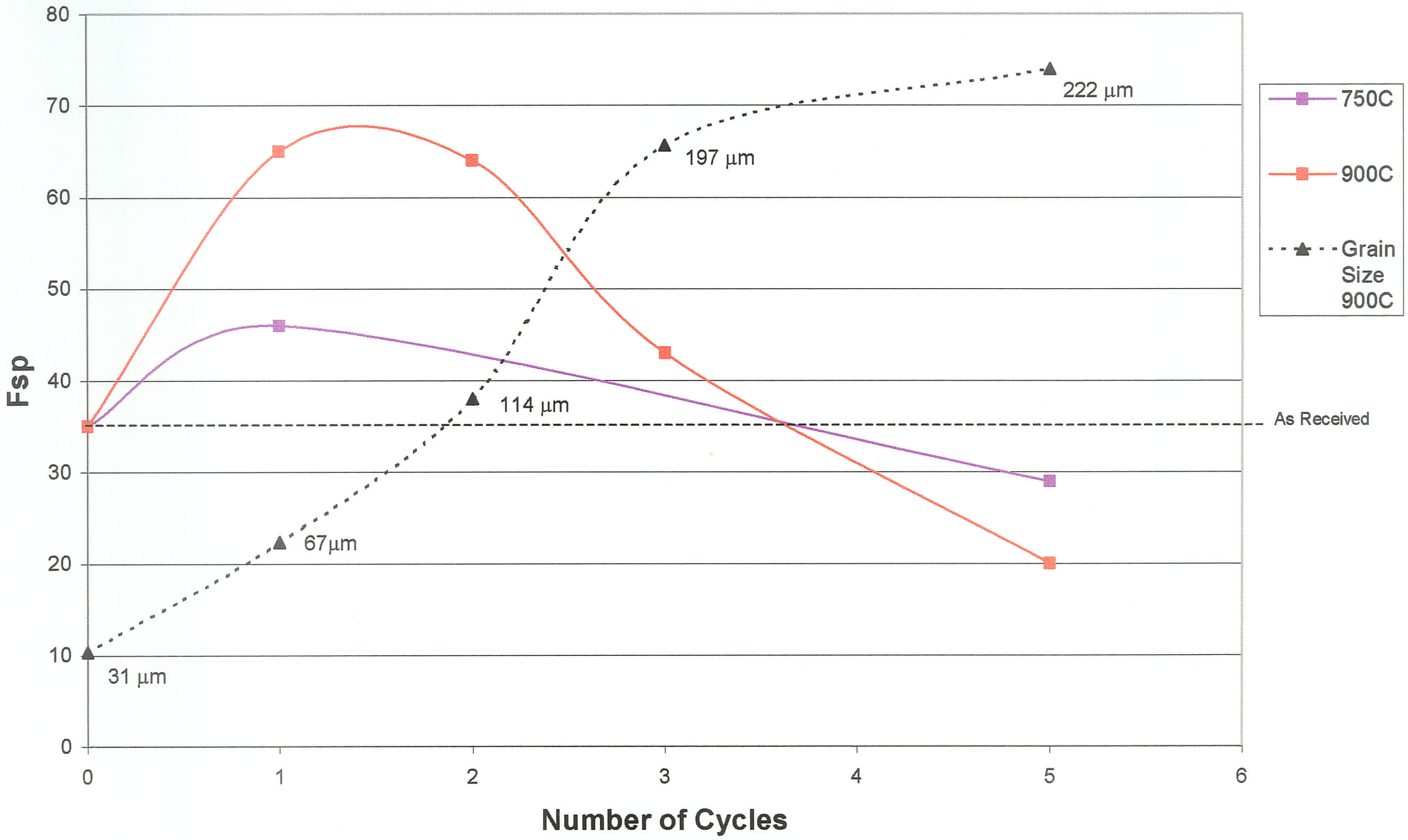

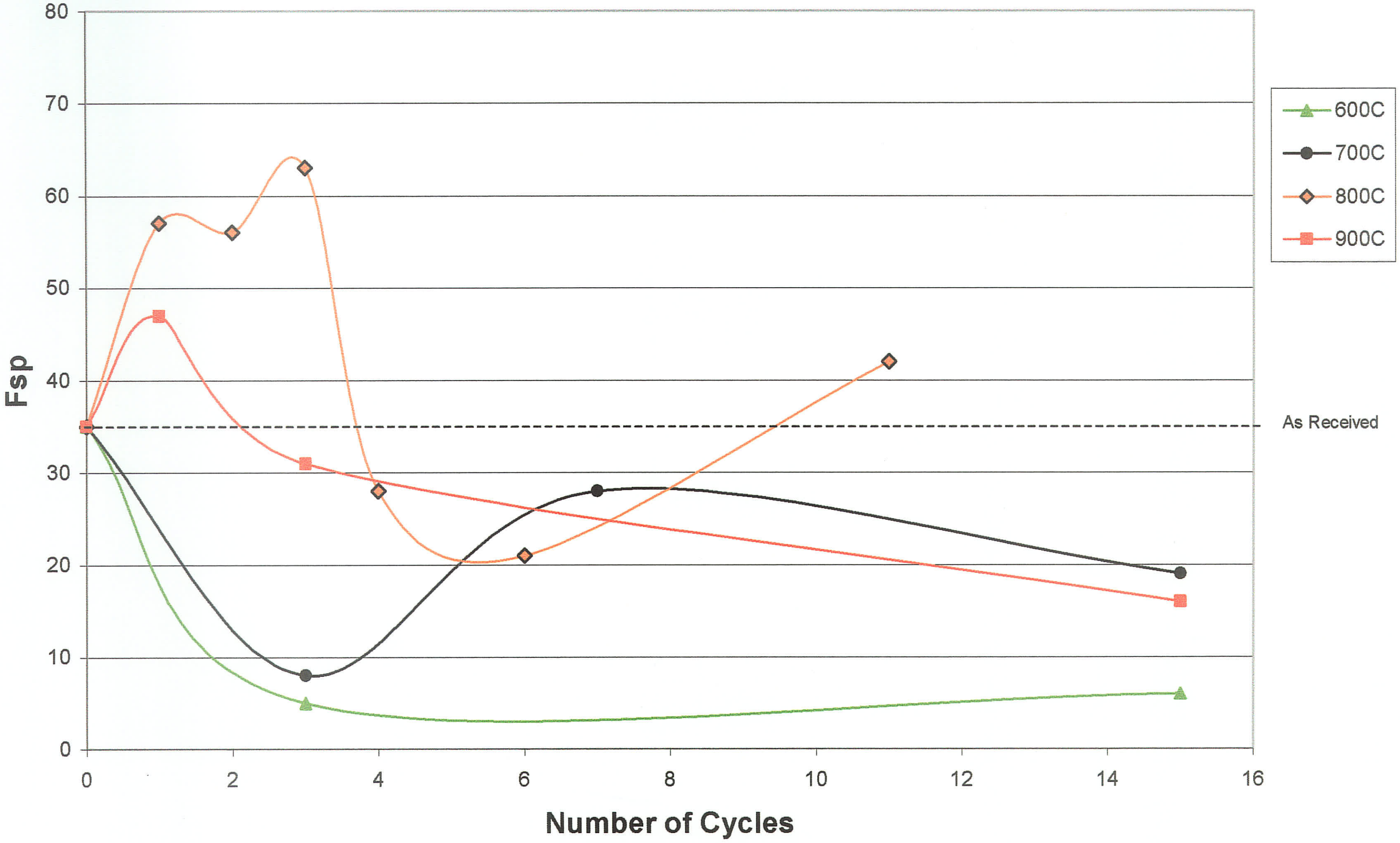

Figure D9 - Fsp Profiles for 10% Cold Rolled and Annealed Ni-200

Figure D10 - Fsp Profiles for 18% Cold Rolled and Annealed Ni-200

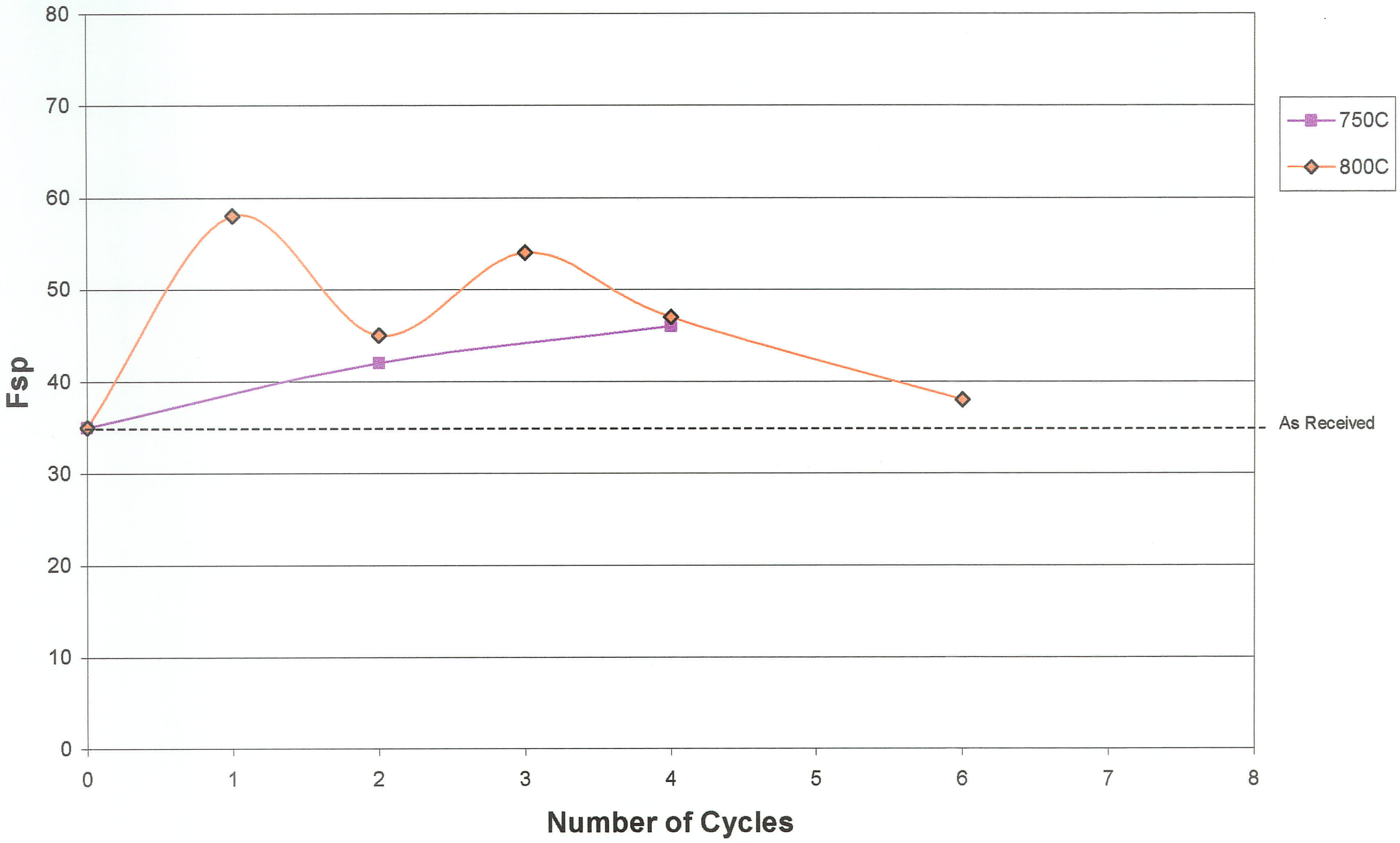

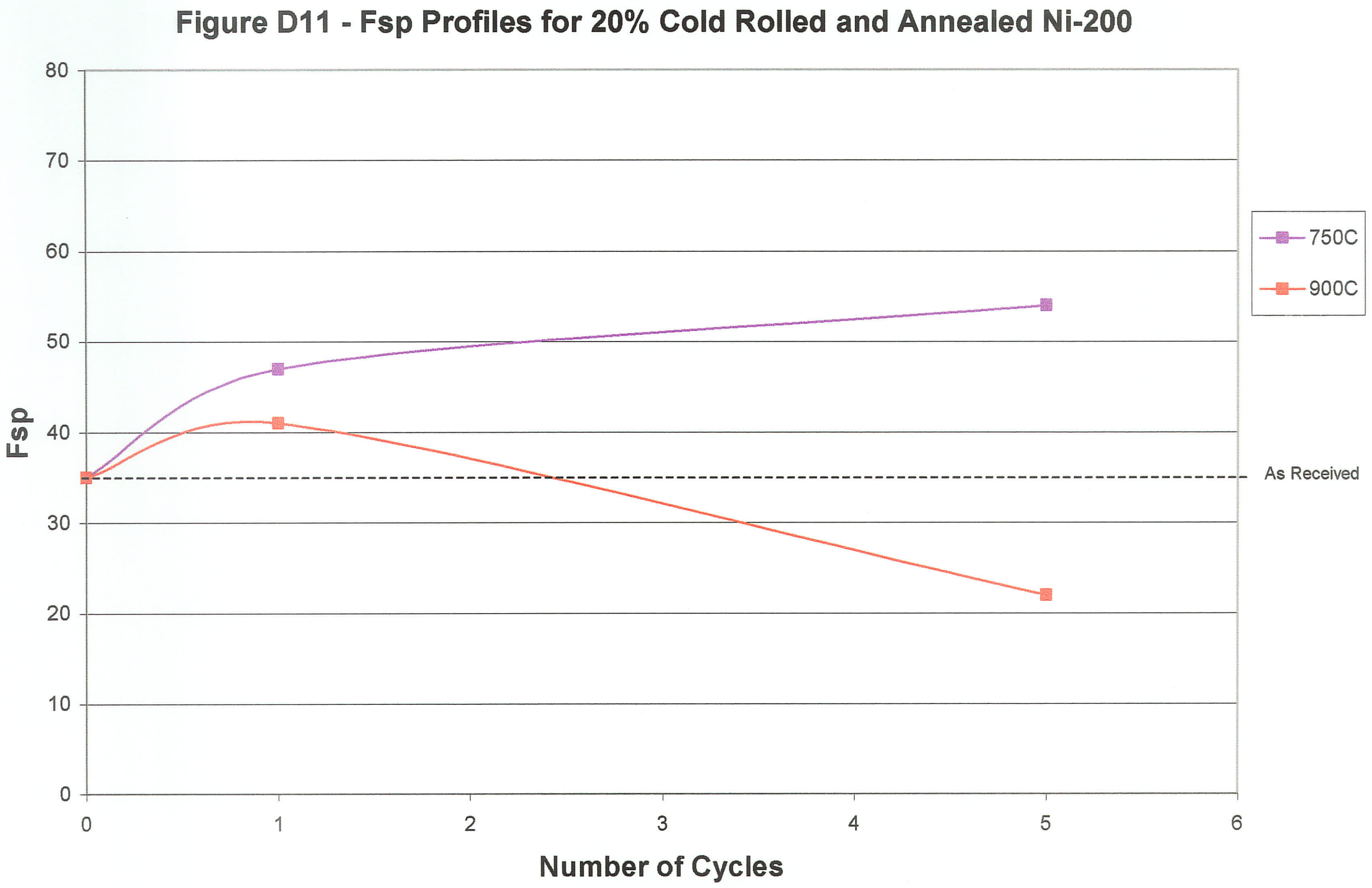
Figure D11 - Fsp Profiles for 20% Cold Rolled and Annealed Ni-200
Fsp
80
70
60
50
40
30
20
10
0
0
1
2
3
4
5
6
Number of Cycles
750C
900C
As Received

Figure D12 - Fsp Profiles for 25% Cold Rolled and Annealed Ni-200

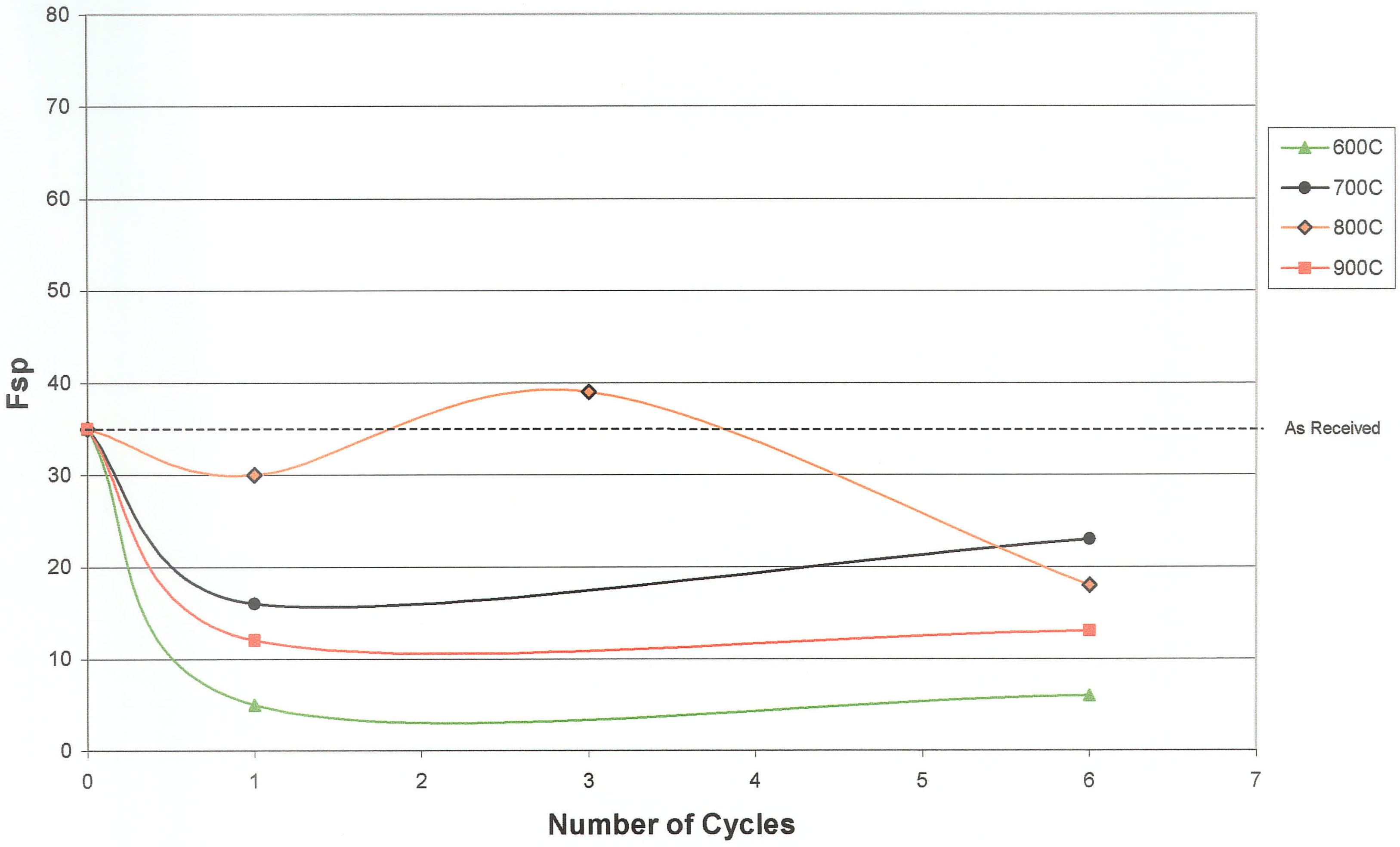

APPENDIX E

OIM Operating Procedures

**Disclaimer: The author has NOT had formal training on any of the software discussed and is in no way responsible for individuals using the equipment required for OIM operation. Prior training on the SEM is assumed by users of this document. The procedure described is unique to the current software and apparatus on the JEOL 5900 SEM at the U of MB.

Set-up:

- The sample should be mounted such that it is at the edge of the mount. If the sample was mounted in the center, the top should be cut off as shown in the figure E1 below. This is done to allow the stage to be brought into position without striking the detector in the SEM.

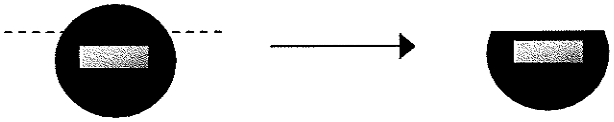

Figure E1 – Front view of sample without and with top cut off

- An excellent polish is needed to ensure a good electron backscatter diffraction (EBSD) pattern (i.e. NOT etched, scratched, no surface topography). Image quality is directly related to the quality of the sample surface.

➢ Side note on polishing: if the sample is not polished properly (i.e. polished to at least 0.05 μm polishing compound such as the blue colloidal silica for at least 10 minutes) the image will be poor. The EBSD pattern is generated from approximately the top 10 nm of the sample, thus an excellent polish is absolutely critical to ensure a completely strain free surface. Vibratory polishing with alumina compound (0.05μm) for up to about 30 minutes was found to produce excellent surface finishes. Electro-polishing is also acceptable, but it was found that mechanical polishing produced satisfactory results.

- Turn on the DSP-2000, the MSC box and the MTI box. Log on to the computer and open the OIM DC (Orientation Image Microscopy, Data Collection) software.

- Insert the sample in the special brass sample holder (which is inclined at 70°) with the cut off portion at the top. Tighten setscrew, but ensure that the back of the sample remains flat against the holder. Deviations significantly alter the data. The reason for the high angle tilt is to minimize the number of electrons absorbed by the specimen and therefore maximizing the fraction diffracted and available for detection.

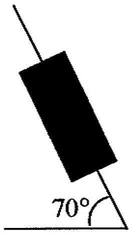

Figure E2 – Side view of inclined sample

- Insert the special holder into the standard aluminum sample holder. Note that due to a guide pin, it will only fit one way. Use copper tape and a small amount of graphite paste to ensure electrical contact is made between the sample surface and the two holders.
- Move the SEM stage down (Z direction) as far as possible (until beeping is heard). Set the stage X and Y values to negative values (ex. -5). Push **forward** on the MSC box to insert the camera into the chamber. It will stop automatically when in position.
- Using the extraction tool, carefully insert the sample assembly into the chamber without striking any of the internal microscope components or the camera (the sample should now be facing the back of the chamber).
- Rotate (R) the stage to 50° (from 12 o'clock position looking in the direction of the electron beam). The sample should now be facing the cylindrical camera in the back right hand side of the chamber as seen in figure E3. Adjust the stage X and Y values such that the sample will be directly under the beam (simplifies 'finding' the sample later).

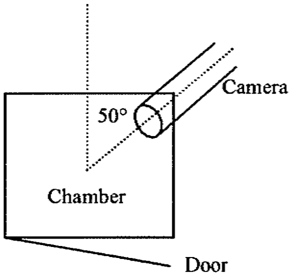

Figure E3 – Plan view of SEM chamber showing camera position

- Bring the sample up (Z) so that the beam-sample interaction point is about 2/3 up the face of the camera as seen in figure E4 on the following page. If you can't get this close, just get as close as possible *without* hitting the backscatter electron detector on the column. Once the height is adjusted, switch the selector to XY so that the stage cannot be accidentally moved up further.

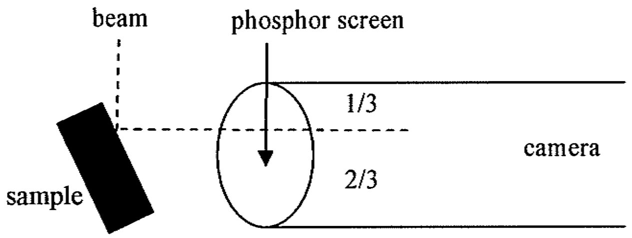

Figure E4 – Optimal position of sample with respect to camera

- Carefully and slowly close the SEM chamber door and evacuate the chamber.
- Set the accelerating **voltage** to 20 kV and the **spot size** to 50 (use SEI mode).
- When ready, turn on HT, find the sample and focus the image (use scan 2).
- Notice that the image of the sample is diagonal across the screen due to the sample rotation (i.e. a ball would roll to the top right hand corner of the screen).
- Using **scan rotation**, rotate the *image* to 50° (note that this is an electronic rotation only, the sample does not physically move). Now the ball would roll from left to right (X direction). This is done so that the OIM software knows which direction the sample is tilted so that it can compensate when controlling the traverse of the beam. Note that this makes it a little tricky to find a desired sight of interest since the image is rotated (i.e. X and Y controls move on a diagonal now rather than up, down, and side to side).
- Increase the magnification such that only the metallic sample is visible (i.e. no mounting compound in view). This provides many grains in view to capture a suitable background pattern later.
- In the OIM DC software, click on the camera icon. There should be another window that opens with a fuzzy grey circle on it (you should still be using scan 2, rapid scan).

DSP 2000 Operating Instructions:

- On the DSP 2000, adjust the **gain** and **black level** such that all of the red indicator lights are on *except* for the top and bottom ones (they should not be pulsing, but steadily lit –if not, again make sure only the sample is in field of view).
- Set the **Int** mode to **Auto** and select the number of frames to be averaged (**64**) on both the DSP 2000 and the left drop-down menu on the OIM DC software.
- Make sure that the **Live** and **Int** toggles are selected and adjust the signal intensity on the right-hand portion of the MTI box to smooth out any gradients seen in the image: horizontally, vertically, diagonally, and parabolically.
- Press **clear** to delete all the buffers previously stored.
- Press **B** from the Load/Act column. This will load a background image into buffer "B". The signal will automatically switch from **Live** to **Proc** and will show the frozen image collected (there should NOT be an EBSD pattern on the screen yet, if there is, you are

Performing a Scan:

- Use the SEM controls (X and Y) to find the area on the sample you wish to scan and focus the image to the center of the screen.
- In the OIM DC software, go to the **scan** tab, switch the toggle switch on the MSC box to OIM instead of SEM and push **capture SEM** (it will ask for SEM magnification). The SEM image should appear in the box as seen on the SEM screen (note that the top and bottom portions of the SEM image will be cropped). Note that this gives the OIM software complete control over the SEM (i.e. the SEM will be "locked" just as it is during an EDS x-ray scan).
- Using the mouse, click and drag to draw a box over the area you wish to scan. A window will pop up when you let go of the mouse button and you can specify a file name, step size, and estimate the time to scan based on a given step size, scan size, and number of frames averaged (4 works well, as mentioned previously).

** Note that if you draw a perfectly square box, the X and Y dimensions are significantly different (X being much larger than Y). This is due to the incline of the sample (70°), which is compensated for by the software (see figure E6).

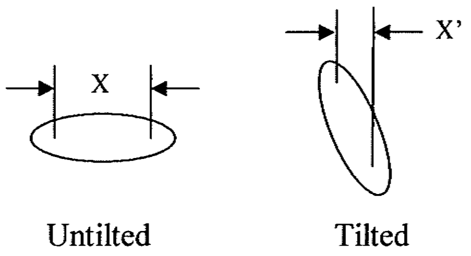

Note that X >> X'

Figure E6 – Projected distances showing difference between tilted and untilted samples

- Set the **step size** such that the beam will strike each grain at least 5 times (you should have an idea of the grain size). The smaller the step size the better the 'resolution', but it will take a longer time to perform the scan.
- Once the settings have been made, click OK. Now push **start** and the scan will begin.
- The beam will traverse across the surface of the sample stepping at specified distances.
- Each step is represented by a colored dot inside the box drawn earlier. The color changes when a different orientation is detected (i.e. different grain).
- The scan progress will be shown in the lower right portion of the screen. With the current software (OIM DC 3.5) and computer, it should be collecting 4.3 points per second.
- Go to the **data** tab, click on the **IQ/CI** button and observe the numbers being collected. The **confidence index** should be fluctuating between 0.4 and 0.8, while the **image quality** should be about 200-600. If IQ numbers are much lower, either adjust the contrast to obtain a better image (high contrast works best), or re-polish your sample. (The CI parameter ranges in value from 0 to 1. Patterns indexed with CI values greater than 0.1 are correctly indexed 95% of the time.)

scanning at too high a magnification, therefore decrease the magnification and repeat previous steps).
- Adjust the **contrast** and **brightness** in the post-processing column on the right such that an even grey image is collected within the circle. Note that when the contrast is increased too much, a white circle begins to appear in the center of the screen. If it is off-center, the gradients were not evened out properly, go back and repeat previous steps (this may require a few iterations until experience is gained).
- Select a smaller number of frames (**4**) on both the DSP 2000 and the drop-down menu on the OIM DC software, and push the toggle to select **Avg** instead of **Int** and push **A/B** from the right hand column of the display controls. Select **A** from the Load/Act column.
- Increase the magnification on the SEM and put it in spot mode (click freeze, go to the image menu, beam controller, spot mode, and set point).
- Adjust the post processing knobs to optimize the image (contrast should be high – contrast knob between 3 o'clock and maximum, brightness at about 9 o'clock). Low contrast results in low Image Quality (IQ) values during scans.
- There should be an electron backscatter diffraction (EBSD) pattern (or Kikuchi pattern) in the circle as seen in figure E5 below. If there is not a pattern visible, push cancel and set it on a different spot (you could be on a grain boundary or something). If still no pattern, something is wrong (perhaps a poor sample surface quality or severely distorted lattice?). Notice that when you move the spot (intersection of lines), a different pattern is visible due the different lattice of another grain.

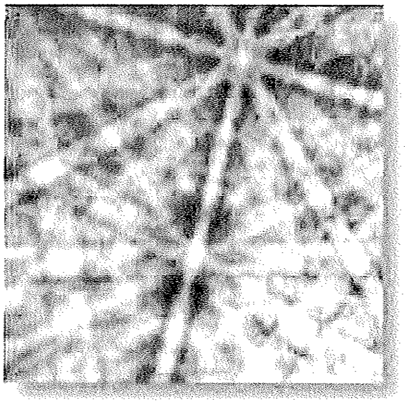

Figure E5 - Example of EBSD pattern

- Capture the pattern by clicking the black and white **capture pattern** icon.
- Go to **calibration** and click on **pattern auto** and follow the directions. Make sure the working distance is set to the appropriate value and continue. The pattern will be indexed and the CI and Fit can be observed. Now click on **Tune** and run through the steps again. This will improve the fit. The CI should be as high as possible (0.6 to 0.8 or better) and the fit should be as low as possible (less than 1 is very good). A proper calibration is essential for a successful scan.

- Note that sometimes the CI and IQ values drop to zero or close to zero. This is normal since the EBSD pattern is not well defined when the electron beam strikes a grain boundary or other discontinuity.
- Also note the options in the upper right portion of the screen. You can watch the computer index the pattern or monitor the Hough transforms, but turning it off increases the speed slightly.

OIM Analysis:

- Open the OIM Analysis software.
- Go to the File menu and click Open.
- Change the file type to scan files (.osc).
- Open the scan file you wish to analyze (this was specified when you drew the box to select the scan area in the data collection software). Default location is C:/programfiles/TEXSEM/OIMDataCollection3.5
- Observe the number of points collected as well as the average Confidence Index and the average Image Quality. Make sure these numbers are satisfactory.
- Double click on **All Data** and observe the numbers.
- Explore quick map options by clicking on the icons at the top of the screen. Right click on the actual map, select properties and choose the settings you desire.
- Right click on the Data icon in the project tree and explore data representation options.

Grain Boundary Analysis
- Click on the grain boundary quick map. This produces a map of the data collected with the grey scale shading based on image quality (light is high IQ, dark is low IQ) and grains colored according to their rotation angles (this is a default setting).
- Right click on the image and go to properties and observe the selections. To add CSLs, go to the drop down menu, click on CSL, then add, then specify type, color, line thickness, etc. Once done, click ok and observe the modifications. Also, the statistics are shown on the bottom portion of the screen.
- To make a "connectivity map" follow the above procedure, but color CSL boundaries white, and remove the IQ grayscale (select "none"). This will create a white background image with only black random boundaries observable.